Measurement of Hard Exclusive Electroproduction of π^0 Meson Cross Section in Hall A of JLab with CEBAF at 12 GeV

A dissertation presented to

the faculty of

the College of Arts and Science of Ohio University

In partial fulfillment

of the requirements for the degree

Doctor of Philosophy

Mongi Dlamini

December 2018

This dissertation titled

Measurement of Hard Exclusive Electroproduction of π^0 Meson Cross Section in Hall A of JLab with CEBAF at 12 GeV

by

MONGI DLAMINI

has been approved for

the Department of Physics and Astronomy

and the College of Arts and Science by

Julie Roche

Professor of Physics and Astronomy

Joseph Shields

Interim Dean, College of Arts and Sciences

Abstract

DLAMINI, MONGI, Ph.D., December 2018, Physics and Astronomy

Measurement of Hard Exclusive Electroproduction of π^0 Meson Cross Section in Hall A of JLab with CEBAF at 12 GeV (227 pp.)

Director of Dissertation: Julie Roche

A complete description of nucleon structure requires the simultaneous knowledge of both the spatial and momentum information of the ultimate constituents of the nucleon, the quarks and gluons. Generalized Parton Distributions (GPDs) provide such tools to describe nucleon structure. GPDs are measurable through hard exclusive processes like Deeply Virtual Compton Scattering (DVCS) and Deeply Virtual Meson Production (DVMP). GPDs can describe hard exclusive processes only if Bjorken factorization is achieved during the hard scattering process. While DVCS data have given hints of the factorization regime being attained, such hints have not been observed for DVMP data. Testing for factorization in DVMP processes is the topic of this thesis. Exclusive π^0 electroproduction has been measured by experiment E12-06-114 in Hall A of JLab. Cross sections have been measured at three fixed Bjorken-x (x_B): 0.35, 0.48 and 0.6 in the Q^2 range 3 to 9 GeV^2. In this document we present an analysis of a subset of the data: x_B = 0.35 in the Q^2 range 3.1 to 4.5 GeV^2. The different structure functions: unseparated cross section ($\sigma_T + \epsilon\sigma_L$), longitudinal-transverse interference (σ_{LT}), transverse-transverse interference (σ_{TT}), and the polarized response ($\sigma_{LT'}$) terms were extracted. The data was compared to a transversity GPD model. The model fails to reproduce the data even though the order of magnitude is in agreement for both model and data. We observe a strong disagreement between the data and the model for σ_{LT} in terms of both magnitude and the cross section sign. Our results are in a larger and wider Q^2 domain but they are in agreement with existing measurements.

Acknowledgments

I would like to express my utmost gratitude to my supervisors: Julie Roche and Paul King. Not only did they give me the opportunity to work in DVCS but they also invested all their resources in terms of expertise, time, patience, motivation and financial support. They have guided me since my first encounter with this field of nuclear physics up to this point. I have worked extensively in particular with Julie Roche and I have always envied her enthusiasm, deep understanding of physics and the ease with which she disintegrates a complex problem into small units easy to deal with. I am grateful for the opportunities Julie has availed to me in terms of exposure to a large scientific community and world class experimental facilities like JLab. Through working with Julie I have gained valuable knowledge which I think no single school program can offer and I will always be indebted to her.

My gratitude also goes to members of the Hall A DVCS Collaboration who have and continue to play significant roles in building me up as a scientist. I will always be grateful for the warmth with which I was welcomed into the group and the interest they always have about my work. Special thanks to Carlos Muñoz-Camacho, Charles Hyde and Alexandre Camsonne who have always followed my work and had ideas on how to I could make my work better. I would also like to thank my senior (and former) student colleague in the collaboration, Maxime Defurne for all the help and discussions concerning my work.

During my thesis years, I spent a significant part of my time onsite at Jefferson Lab. During that time, I worked with and around members of the Hall A Collaboration. I would like to thank the Hall A staff and collaborators, in particular our leader Cynthia Keppel, for her warm welcome in the Hall A Collaboration and the financial support she facilitated for me during one of my extended stays at JLab.

I would also like to thank members of my committee: Professors Charlotte Elster, Carl Brune, and Jennifer Hines. Thank you for investing your time and expertise in my training as a scientist.

I have also worked with an amazing set of student colleagues whom I've grown to know as my friends. I will always reminisce the discussions, especially during our marathon with beam-less shifts at the Lab. It has been a pleasure to work with and alongside: my colleagues both at Ohio and in the DVCS collaboration, Bishnu Karki and Gulakhshan Hamad, my colleagues in the DVCS Collaboration, Hashir Rashad, Alexa Johnson and Frederic Georges.

Table of Contents

List of Tables

List of Figures

Figure Page

NOMENCLATURE

ARS	Analog Ring Sampler
BCM	Beam Current Monitors
BH	Beithe-Heitler
BPM	Beam Position Monitors
CEBAF	Continuous Electron Beam Accelerator Facility
CER	Cherenkov
CFF	Compton Form Factors
CLAS	CEBAF Large Acceptance Spetrometer
CODA	CEBAF Online Data Acquisition
COMPASS	Common Muon and Proton Apparatus for Structure and Spectroscopy
CPU	Central Processing Unit
DA	Distribution Amplitude
DAQ	Data Acquisition
DIS	Deep Inelastic Scattering
DVCS	Deeply Virtual Compton Scattering
DVMP	Deeply Virtual Meson Production
EB	Event Builder
ER	Event Recorder

GPD	Generalized Parton Distribution
HERA	Hadron-Electron Ring Accelerator
HRS	High Resolution Spectrometer
LHRS	Left High Resolution Spectrometer
PAC	Program Advisory Committee
PID	Particle Identification
PMT	Photo-Multiplier Tube
pQCD	Perturbative Quantum Chromodynamics
QCD	Quantum Chromodynamics
QED	Quantum Electrodynamics
ROC	Read Out Controller
TJNAF	Thomas Jefferson National Accelerator Facility
UV	Ultra-Violet
VGG	Vanderhaeghen-Guichon-Guidal

Introduction

Electrons, protons and neutrons are the building blocks of the visible matter of the universe. The electron was discovered in 1897 by J.J. Thompson, the proton in 1919 by E. Rutherford and the neutron in 1932 by J. Chadwick. Electrons are structure-less and their interaction with matter is described by a mathematical framework known as Quantum Electrodynamics (QED). Protons and neutrons are building blocks of the nucleus and are collectively called nucleons. Until 1933, nucleons were thought to be structure-less like electrons. This picture changed when O. Stern (1933) measured the magnetic moment of the proton and found it to be approximately twice as large as predicted for elementary particles of spin $\frac{1}{2}$ and mass m.

Experimental and theoretical efforts have led to the description of nucleons as extended bodies composed of quarks and gluons, and as part of a class of particles called hadrons. The mathematical framework which describes the dynamics of hadrons from the interactions of quarks via the exchange of gluons is called Quantum Chromodynamics (QCD) and the QCD force (the strong force) is responsible for keeping nucleons and nuclei as a unit. Interactions governed by the strong force are called strong interactions. The QCD Lagrangian (a mathematical formulation which contains information about the dynamics of a system) is [1]:

$$L = \frac{-1}{4} G^a_{\mu\nu} G^{a\mu\nu} + \sum_f \bar{\psi}_f (i\partial\!\!\!/ + gA\!\!\!/ - m_f)\psi_f, \tag{0.1}$$

where:

- ψ_f is a quark field, a function of space-time,
- $G^{a\mu\nu}$ represents a gluon field strength tensor,
- $A\!\!\!/$ is a gauge invariant derivative,

- m_f is the quark mass.

Unlike photons, the force carriers of the electromagnetic (QED) interactions, gluons also interact among themselves and that self-interaction is represented by the gluon field tensor term (first term) in Eq.(0.1). The quark field term (second term) describes the quark contribution in QCD interactions. As it can be seen in Eq.(0.1), the QCD Lagrangian is derived in terms of quark and gluon degrees of freedom. However, in the non perturbative scale in QCD one never realizes free quarks and gluons but instead encounters hadrons. This brings a challenge to design experimental techniques to study the behaviour of particles which can not be isolated from one another. As a result we still have many mysteries about QCD and strong interactions in general. One interesting aspect of QCD is that compared to the other forces of nature (weak, electromagnetic, and gravitational), the strong coupling *constant* (α_s) varies drastically as a function of the energy scale or momentum transfer [2, 3]. Figure 0.1 shows the status of the current experimental measurements and theoretical calculation of the running of α_s. This principle of a running α_s leads to two important consequences:

1. Asymptotic freedom: at very short distances (high energy transfers), α_s becomes small. A small α_s means strong interactions get suppressed, reducing the interaction between quarks and gluons. In this configuration a relativistic lepton probe can interact with just one “isolated” nucleon constituent as the rest of the nucleon appears to be relatively “frozen”. This allows a perturbative treatment of QCD and an experimental access window where QCD calculations have been tested [4].

2. Confinement: at large distances (comparable to hadron size), the strong coupling constant increases [5]. As a result, there are no free quarks. Understanding QCD in

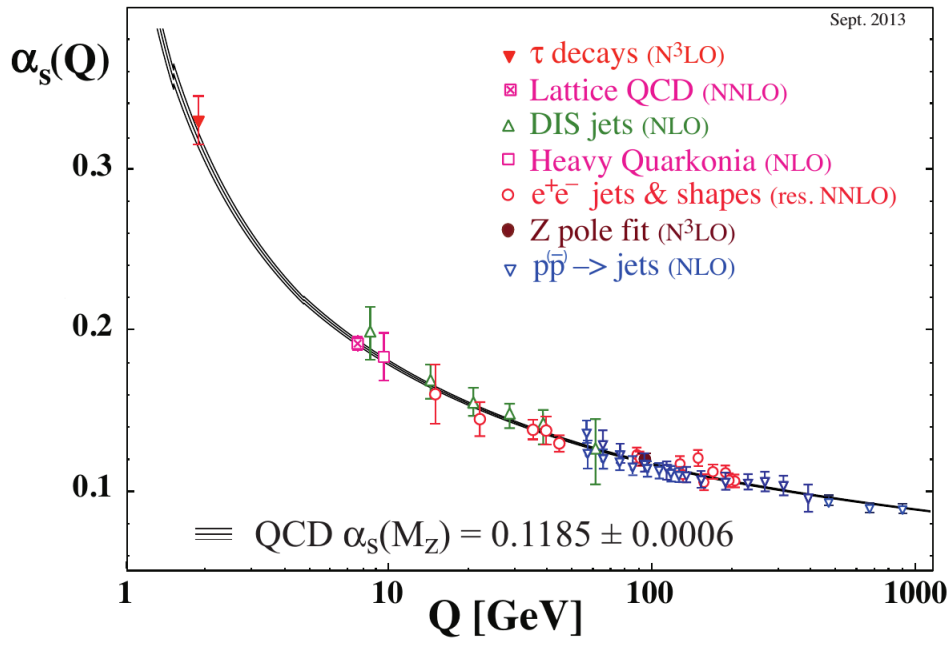

Figure 0.1: Experimental measurements and theoretical calculation of the strong coupling constant α_s as a function of the momentum transfer in QCD processes. This figure was taken from Ref. [3]. See re-use permission (1) in Appendix C.

the confinement regime is a challenge that has become an important occupation in nuclear physics.

In as much as QCD explains how the constituents of nucleons interact, there is still a number of outstanding questions related to the nucleon system:

- How is the nucleon (and other hadrons) constructed from the basic QCD degrees of freedom, quarks and gluons?
- What does the interior of a nucleon look like in terms of quark-gluon distribution?
- How much of the nucleon spin is carried by the quarks and how much by the gluons?

- How does mass arise from the interaction of essentially massless quarks and gluons?

In the absence of analytical answers to these and many other questions, experimental advances and nucleon structure models play a significant role in investigating nucleon systems [6].

Many frameworks have been formulated to investigate the structure of nucleons based on their ultimate constituents. The parton model describes the nucleon as an extended body made of 3 valence quarks and a sea of fluctuating quarks and gluons [6, 7]. These nucleon constituents are called partons and each parton is understood to possess a fraction of the nucleon's momentum and to contribute to a fraction of the nucleon's spin. GPDs build on the parton model to introduce functions which parametrize the nucleon structure by presenting the correlation between position and momentum of quarks and gluons. The GPD framework provides an access to a three dimensional tomography of the partonic structure of the nucleon. A clean way to measure GPDs is the Deeply Virtual Compton Scattering (DVCS) process [1]. DVCS is a process where a lepton scatters off a quark via the exchange of a virtual photon. The quark absorbs the virtual photon and later emits a real photon as the quark gets re-absorbed by the parent nucleon. GPDs can also be accessed via Deeply Virtual Meson Production (DVMP) which proceeds the same way as DVCS but instead of a real photon, a meson (quark-antiquark bound state) is produced in the final state.

Pioneer DVCS experiments were conducted about two decades ago and they confirmed the feasibility of measuring the DVCS process. These measurements were performed by the H1 and ZEUS collaborations at HERA, the HERMES collaboration at DESY and the CLAS collaboration at the Thomas Jefferson National Accelerator Facility (TJNAF, aka JLab). These original experiments resulted in low statistical significance because they were run in already experimental facilities, not dedicated DVCS set-ups [4]. Later on, the HERMES collaboration performed dedicated experiments and extended the

measurement of DVCS asymmetries to intermediate regions in momentum fraction x_B with an impressive collection of target and beam polarization states [8]. At JLab, the Hall A collaboration [9] and CLAS in Hall B [10] measured absolute cross sections in the valence x_B region, however at low photon virtuality (Q^2).

Experiment E00-110 [9] was the first generation of DVCS in Hall A and it was conducted in 2004. A second generation DVCS experiment was conducted in Hall A in 2010. These pioneer experiments (both 2004 and 2010) confirmed the feasibility of experiments of this kind and even though they were at low Q^2 they both showed hints of the validity of the GPD formalism in parametrizing proton structure for the electro-production of photons (DVCS). However, results from the second generation [11] are in contradiction with assumptions of the GPD formalism for the π^0 electro-production cross section. It is found that the cross section is dominated by a contribution from transversely polarized photons [11], something which the GPD formalism claims is only possible at next to leading order. Recent beam spin asymmetries by CLAS [12] and π^0 muon production cross section at COMPASS [13] are also in agreement with the findings by Defurne et al. [11]. This leaves the interpretation of π^0 (neutral pseudoscalar mesons in general) electro-production in the GPD formalism with more questions and introduces the case of the participation of some elusive structure functions know as transversity GPDs at leading order, something not expected according to the GPD formalism. These findings make the electro-production of π^0 a good hunting ground for the elusive transversity GPDs and a catalyst for the extension of the GPD formalism.

Experiment E12-06-114 is the basis for this thesis. It utilized the same (but expanded apparatus) as the earlier generations of DVCS experiments in Hall A of JLab. Moreover, this experiment was conducted with the recently upgraded electron beam energy (from 6 GeV to 12 GeV). A higher energy is necessary to attain the QCD configuration at which the GPD formalism is valid. A wider energy range is necessary to perform measurements

as a function momentum transfer and hence pin down the validity of the GPDs as the appropriate objects to parametrize proton structure. This experiment received the highest scientific rating by the JLab Program Advisory Committee. It is one of the first experiments to take place after the new energy upgrade because it is considered as having a high impact in the field of nuclear physics research [6].

I joined the DVCS experiment in the Fall of 2013 and participated in the commissioning of the apparatus for the 12 GeV experiment. In the spring of 2014, we started collecting our first data point which also happens to be the point of investigation of this thesis. Despite some accelerator challenges associated with the CEBAF's new upgrade, we managed to collect more data points in the Spring and Fall of 2016. All of these data are undergoing analysis and we are looking forward to the results and their impact on this field of nuclear physics. This thesis presents in particular the electro-production cross section of π^0 at momentum fraction $x_B = 0.36$, photon virtuality (Q^2) range of 3.1 to 4.47 GeV^2 and center of mass energy (W) of 2.58 to 3.0 GeV. This document is organized as follows:

- Chapter 1 is an introduction of the theoretical framework and background in the study of the nucleon structure in the parton picture. The Generalized Parton Distribution framework is also presented. In this chapter the experimental context of nucleon structure study, with particular emphasis on DVCS and DVMP (in particular π^0 production), is also presented.

- Chapter 2 presents an overview of the apparatus of the experiment (Experiment E12-06-114). This includes an overview of the standard Hall A equipment at JLab and the additional DVCS electromagnetic calorimeter. A brief overview of the accelerator facility is also given.

- Chapter 3 is about the analysis of one vital component of this experiment, the electromagnetic calorimeter used to detect DVCS photons and pions. This chapter introduces the tools used in interpreting the calorimeter data. Characterization and calibration of this detector are also discussed. I have spent a considerable amount of time working on the calorimeter from its operation in the hall, calibration and offline data analysis.

- Chapter 4 introduces and discusses the Monte-Carlo simulation used in the analysis to compute the acceptance of the Hall A spectrometer. In this chapter we also introduce the procedure used to fit and extract the cross section. I worked from a standard DVCS simulation, optimized and calibrated the simulation's calorimeter resolution to the data.

- Chapter 5 discusses the data analysis in terms of identifying the DVMP (π^0) channel and presents the results obtained. I wrote computer programs to select exclusive π^0 events and eventually extract the cross section.

  Both the DVCS and Hall A collaborations are big and each final result embodies contributions from a lot of people. I have summarized the aspects of experiment E12-06-114 leading to the results presented in this document by the flowchart in Fig. 0.2. My contributions to the experiment are represented by the boxes with red text in the flowchart.

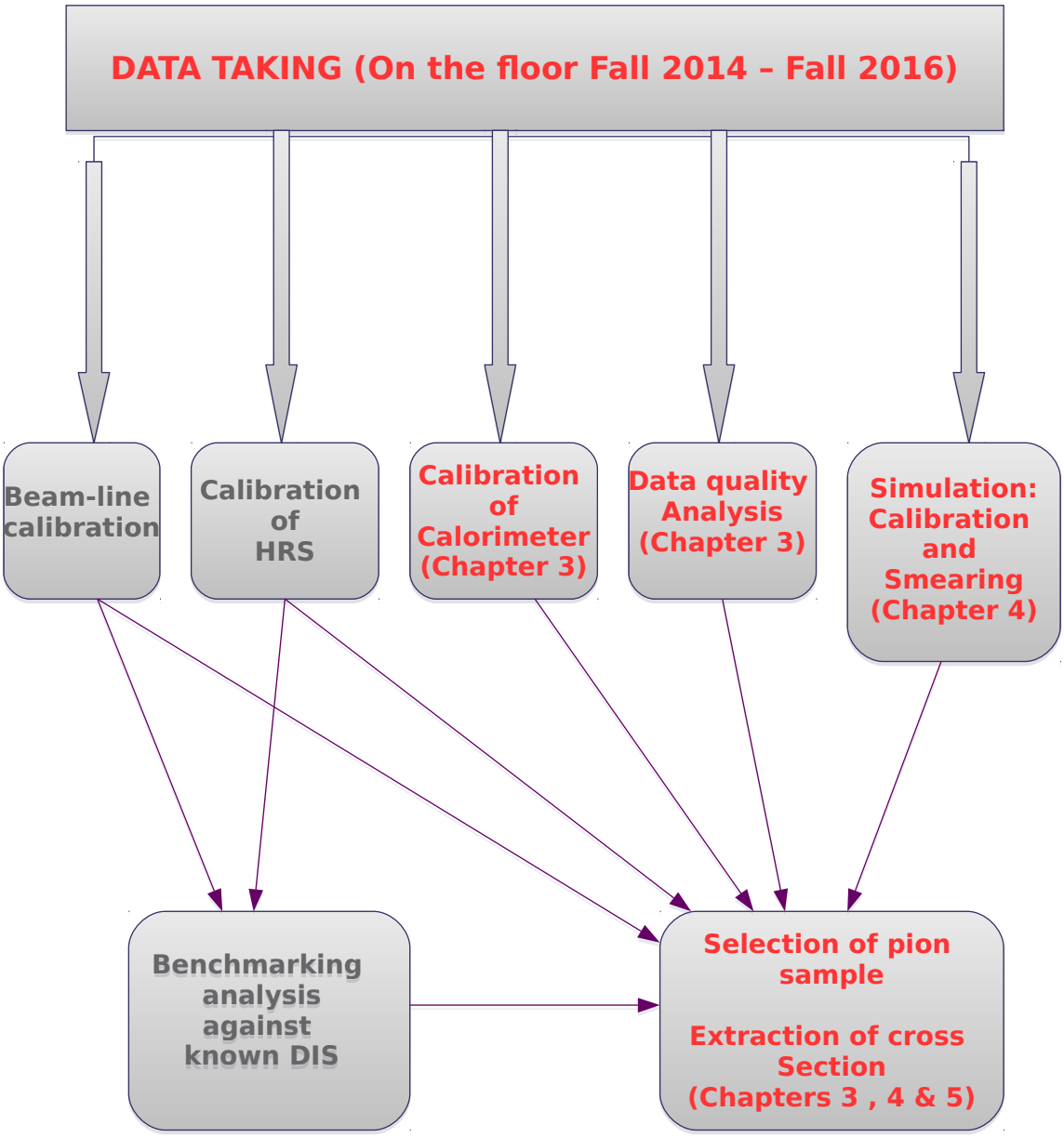

Figure 0.2: A flowchart of the aspect of experiment E12-06-114 leading to the results presented in this document and my contributions to the process. My contributions are indicated by the boxes with red text.

1 Nucleon structure via electron scattering

There are basically three methods employed by physicists to study the structure of nucleons and hadrons in general;

- through the scattering of high energy structureless particles off hadrons,
- through the study of the excitation spectrum of hadrons through the production of resonant states, also known as hadron spectroscopy and
- through the collision of energetic ion beams, also known as heavy-ion collision.

All these methods have played significant and complimentary roles in informing on nucleon structure and QCD in general. As a structureless electromagnetic probe, the electron has been and continues to be an excellent tool to study hadrons. Three main reasons make the electron the ideal tool for taking ”pictures” of the internal landscape of nucleons:

- QED is a well understood interaction,
- the QED coupling constant is small, $\alpha_{QED} \approx \frac{1}{137}$, and this allows a perturbative treatment of QED governed processes and
- electrons can be accelerated in well-defined mono-energetic beams and be accurately detected.

This knowledge of QED gives us a well defined and controllable interaction for our probe. It was through electron scattering experiments in the 1950s and 1960s that the composite structure of the proton (and hadrons in general) was revealed. In electron scattering, two techniques have been historically used to probe hadron structure. In one method called elastic scattering, the electron scatters off a hadron, leaving it intact in the process. This approach gives access to the electric and magnetic current spatial

distributions of the hadron constituents. In the second technique, Deep Inelastic Scattering (DIS), the hit hadron breaks up into a number of fragments. DIS gives access to parton distribution functions which tell us the probability to find partons carrying a fraction of the longitudinal momentum of the hadron.

These two methods have revealed significant information about nucleon structure, for example, from elastic scattering experiments we have been able to infer the size of the proton [14]. DIS experiments have made it possible to perform a flavor decomposition of the momentum distributions in nucleons. However, using these two, one gets either spatial or longitudinal momentum distribution of the hadron constituents and no access to their correlation. A correlation between the spatial and momentum distribution can provide an insight that none of the two techniques can independently give. In the last two decades, a new technique (Deeply Virtual Exclusive Processes) was introduced. In this technique, an electron scatters off a nucleon, which recoils and produces a photon in the process. Interpreted in the formalism of structure functions called Generalized Parton Distributions (GPDs), this approach combines the information accessible in the two methods mentioned above to provide a description which can be interpreted as giving a three-dimensional tomography of the nucleons interior. This is a new and exciting era in QCD studies and promises to open a new window that will help us understand QCD confinement better.

In the following sections, a brief review of these electron techniques in probing the structure of hadrons is given.

1.1 Elastic scattering

Two particles scatter elastically if both remain intact to make the final state. In 1911, Rutherford conducted elastic scattering experiments using alpha particles off a gold foil [15] and to derive the cross section of the interaction, he assumed a point-like target and a non-relativistic scattered particle to get:

$$\left(\frac{d\sigma}{d\Omega}\right)_{Rutherford} = \frac{\alpha}{4E^2 \sin^4\left(\frac{\theta_e}{2}\right)}, \tag{1.1}$$

where α is the fine structure coupling constant, E is the energy of the incident particle and θ_e is the angle of the scattered particle. For relativistic electron projectiles, Eq. (1.1) is modified by the Mott cross section given by:

$$\left(\frac{d\sigma}{d\Omega}\right)_{Mott} = \frac{\alpha}{4E^2 \sin^4\left(\frac{\theta_e}{2}\right)} \cos^2\left(\frac{\theta_e}{2}\right). \tag{1.2}$$

All these relations (above) hold for a point-like and spin-less target and as a result the experimental cross section was not in agreement with them. For a non-point-like and spin-less target (extended target), the cross section is modified to incorporate objects that encode the structure of the target as follows:

$$\frac{d\sigma}{d\Omega} = \left(\frac{d\sigma}{d\Omega}\right)_{Mott} \cdot |F(\Delta)|^2, \tag{1.3}$$

where F(Δ) is a form factor acknowledging the structure of the target and Δ is the momentum transferred to the target. An illustration of electron elastic scattering off a proton together with a definition of the relevant kinematic variables is shown in figure 1.1. The scattering occurs through the exchange of a virtual photon emitted by the incident electron. Electron elastic scattering factorizes the non-perturbative (soft structure) structure of a hadron into form factors. For low Q^2, form factors represent, via a Fourier transform, the spatial distribution of electromagnetic currents in the nucleon, in the plane transverse to the nucleon's direction [16].

The form factors are defined as the matrix elements of the QCD density matrix between nucleon states of different four-momenta (in space-time coordinates) of the electromagnetic current operator [17]:

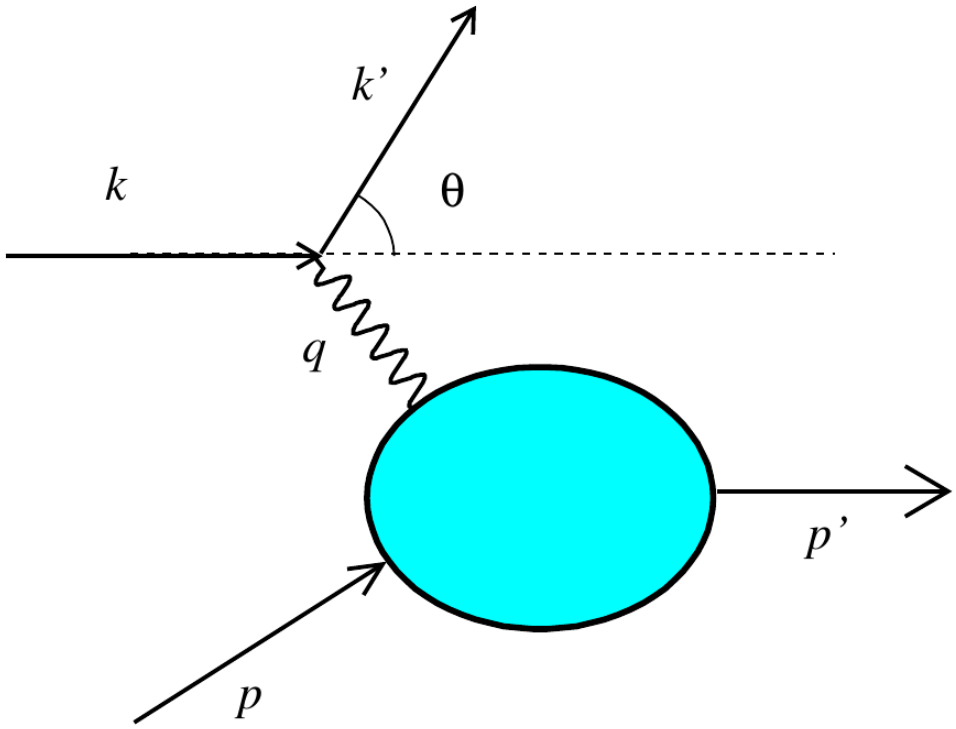

Figure 1.1: A diagram demonstrating elastic scattering of an electron off a hadron (proton). **k** represents the 4-momentum of the incident (projectile) electron, **k'** is the scattered electron 4-momentum, **p** is the target proton and **p'** is the recoil proton. **q** is the 4-momentum of the exchanged virtual photon. We also define $Q^2 = -q^2 = -(\mathbf{k'} - \mathbf{k})^2$ as the virtuality of the exchanged photon. High virtuality is associated with short wavelengths and a high resolution of the probing virtual photon.

$$j^{\mu}(x) = \sum_{q=u,d,..} Q_q \bar{\psi}_q(x) \gamma^{\mu} \psi_q(x), \tag{1.4}$$

where Q_q represents the charge of the quark involved in the process ($Q_u = Q_c = \frac{+2}{3}$ for up and charm quarks and $Q_d = Q_s = \frac{-1}{3}$ for down and strange quarks). ψ_q is the field of

a quark of a particular flavor and γ^{μ} is the field operator. The form factors F_1 and F_2 then encode nucleon structure information related to the following operation:

$$\langle p'|j^{\mu}(0)|p\rangle = \bar{N}(p')\left\{F_1(Q^2)\gamma_{\mu} + F_2(Q^2)\frac{i\sigma_{\mu\nu}q^{\nu}}{2M_N}\right\}N(p), \tag{1.5}$$

where N and $\bar{N}$ are the initial and final nucleon spinors and M_N is the nucleon mass.

The matrix elements encode the probability amplitude of finding a quark at a certain space-time coordinate in a nucleon with an initial momentum *p* and creating another quark at the same space-time coordinate but with a different momentum *p'*. These matrix elements are called "local" since the initial and final quark are created or annihilated at the same space-time point [18]. The process is also called non-forward because the nucleon undergoes a change of momentum. Since the nucleon is a spin one-half particle, two functions parametrize the nucleon structure in this regime, $F_1(Q^2)$ and $F_2(Q^2)$, the Dirac and Pauli form factors, respectively. These functions depend on Q^2 only. $F_1(Q^2)$ is related to the charge distribution in the nucleon and $F_2(Q^2)$ accounts for the presence of an anomalous magnetic moment in the nucleon [19]. In the limit where Q^2 goes to zero, where the lepton probe sees the nucleon as a whole, the following relations hold for the neutron and the proton:

$$\begin{aligned} F_1^n(0) &= 0 \quad F_2^n(0) = -1.9130\,\mu_N \\ F_1^p(0) &= 1 \quad F_2^p(0) = 1.7928\,\mu_N \end{aligned} \tag{1.6}$$

Since the proton has unit charge and the neutron has zero, $F_1(Q^2)$ is unity and zero for these systems, respectively. The magnetic moment of a point-like proton, in this Q^2 limit is expected to be unity, as it should be related to the charge distribution. By a similar argument, it is expected to be zero for a point-like neutron. Thus the discovery of the anomalous magnetic moments of the nucleons was a strong indication that nucleons were

not elementary. $F_1(Q^2)$ is related to the electromagnetic charge density in the transverse plane of an unpolarized nucleon through a Fourier transform [19]:

$$\rho(b_\perp) = \int \frac{d^2q}{2\pi} e^{(iq.b_\perp)} F_1(Q^2), \tag{1.7}$$

where $b_\perp$ is an impact parameter representing the transverse distance of a parton from the center of mass of the nucleon. $F_2(Q^2)$ is connected to the quark density in the transverse plane of a transversely polarized nucleon[19]. In this regime, the unpolarized cross section is given by [19]:

$$\frac{d^2\sigma}{d\Omega} = \frac{\alpha^2}{4E^2 \sin^4(\frac{\theta_e}{2})} \frac{E'}{E} \left\{ \left(F_1(Q^2) - \frac{Q^2}{4M^2} F_2^2(Q^2) \right) \cos^2(\frac{\theta_e}{2}) - \frac{Q^2}{2M^2} \left(F_1(Q^2) + F_2(^2) \right)^2 \sin^2(\frac{\theta_e}{2}) \right\}. \tag{1.8}$$

Introducing the Sachs electric form factor $G_E(Q^2)$ and magnetic form factor $G_M(Q^2)$ to parametrize nucleon structure, Rosenbluth [20] parametrizes the elastic cross section as follows:

$$\frac{d\sigma}{d\Omega} = \frac{\alpha}{4E^2 \sin^2\left(\frac{\theta_e}{2}\right)} \frac{E'}{E} \left[\frac{G_E^2(Q^2) + \tau G_M^2(Q^2)}{1+\tau} \cos^2\left(\frac{\theta_e}{2}\right) + 2\tau G_M^2(Q^2) \sin^2\left(\frac{\theta_e}{2}\right) \right], \tag{1.9}$$

where $\tau = \frac{-\Delta^2}{4M^2}$ and M is the mass of the nucleon. The Pauli and Dirac form factors are related to the Sachs form factors through:

$$\begin{aligned} F_1(Q^2) &= \frac{G_E(Q^2) + \tau G_M(Q^2)}{2\tau} \\ F_2(Q^2) &= \frac{G_M(Q^2) - G_E(Q^2)}{1+\tau} \end{aligned} \tag{1.10}$$

A compilation of the world data for G_{Ep} and G_{Mp} obtained by the Rosenbluth separation method is shown in figure 1.2.

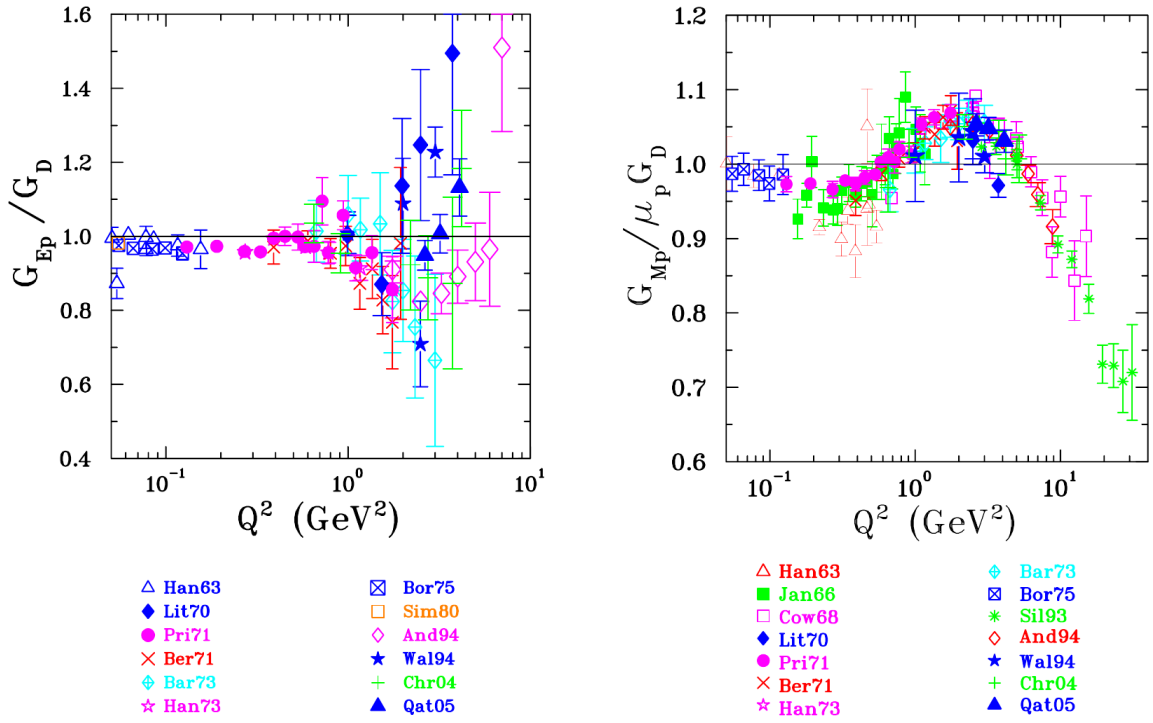

Figure 1.2: World data for the Sachs electric form factor $G_E(Q^2)$ (left panel) and magnetic form factor $G_M(Q^2)$ (right panel) obtained using the Rosenbluth method. These figures were taken from Ref. [21].

See re-use permission (2) in Appendix C.

As briefly mentioned in the introductory section, electron elastic scattering measurements have been used to calculate the proton charge radius as a derivative of the Sachs electric form factor $G_E(Q^2)$ [22]:

$$R_p^2 = -6 \left. \frac{dG_E(Q^2)}{dQ^2} \right|_{Q^2=0} . \tag{1.11}$$

Using an extrapolation to estimate $G_E(Q^2)$ at $Q^2 = 0$, a radius of $R_p^2 = 0.8798$ fm was found [14]. Even though this result is in good agreement with studies done with the hyperfine structure of hydrogen, it is in a 6-σ disagreement with results of studies done

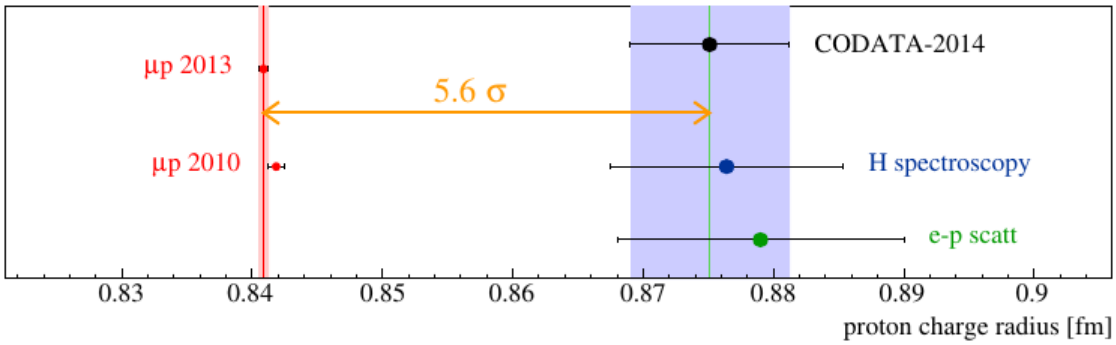

Figure 1.3: Measurements of the proton charge radius using different techniques. The red points show measurements using munoic hydrogen, the blue point is from hydrogen spectroscopy and the green point is from electron-proton scattering. As seen in the figure, the electron-proton scattering and hydrogen spectroscopy measurements are in good agreement but not with the munoic hydrogen results [14]. This figure was taken from Ref. [22]. See re-use permission (1) in Appendix C.

with the hyperfine structure of munoic hydrogen [22] (see figure 1.3). This discrepancy is called the proton radius puzzle and as of at the writing of this document (Summer 2018) it is yet to be resolved.

1.2 Deep Inelastic Scattering (DIS)

In electron-proton scattering at large momentum transfer, the proton is highly likely to break into smaller units which are difficult to all measure at once but a lot can be learned by only measuring the scattered electron ($ep \rightarrow e'X$). This process is called Deep Inelastic Scattering (DIS).

At this point we define three more kinematic variables in addition to those introduced in the previous section (section 1.1):

- the invariant mass of the hadronic final state $W^2 = (p + q)^2$,

- the longitudinal momentum fraction of the nucleon $x = \frac{Q^2}{2p \cdot q}$ and
- the energy of the exchanged virtual photon $\nu = k' - k$.

DIS is deep in the sense that the photon virtuality Q^2 is much larger than the squared proton mass M^2 and inelastic in the sense that the hadronic final state invariant mass W^2 is also much larger than M^2 [19]. At these energy scales, the virtual photon has a shorter wavelength and spatial resolution (a photon of virtuality Q^2 can "see" a short-distance region of the nucleon with a spatial resolution of the order $\Delta b_\perp \sim \frac{1}{Q^2}$ [19]) relative to the size of the probed nucleon. At such short distances, the picture of the nucleon appears to be frozen and the probe is sensitive to the substructure of the nucleon. At first order the QCD concepts of asymptotic freedom and factorization allow us to consider the probe to be interacting with one sub-particle.

DIS factorizes the scattering process into a short-distance (hard) interaction part representing a perturbatively calculable (QED) scattering of point-like objects and a long distance (soft or non-perturbative) QCD interaction part representing the non-elementary (nucleon structure) response of the nucleon to the probe. In DIS the nucleon structure is parametrized in terms of structure functions known as Parton Distribution Functions(PDFs). PDFs are objects representing the longitudinal momentum and spin distribution of partons in a fast moving nucleon. In this formalism, the assumption is that the transverse momentum of the partons in the fast moving nucleon is negligibly small. Two[1] spin independent structure functions parametrize the total (unpolarized) cross section in this regime [19]:

[1] Note that the dimensionless structure functions F_1 and F_2 in Eq.(1.12) are different from the elastic Pauli and Dirac form factors in Eq.(1.8)

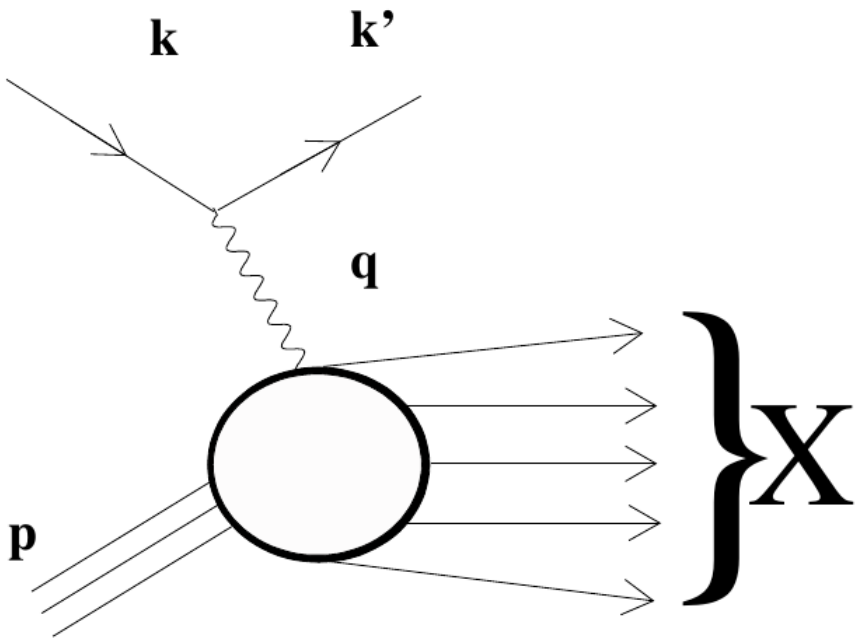

Figure 1.4: A cartoon illustrating deep inelastic scattering, $ep \rightarrow eX$. An electron (k) scatters off a proton (p) via the exchange of a virtual photon (q). The scattered electron (k') is detected and the recoil nucleon breaks up into many fragments (X) that are not detected.

$$\begin{aligned} W_1(\nu, Q^2) &= \sum_q e_q^2 \frac{q(x)}{2M} \equiv \frac{1}{M} F_1(x) \\ W_2(\nu, Q^2) &= \sum_q e_q^2 x q(x) \equiv F_2(x), \end{aligned} \tag{1.12}$$

where e_q is the charge of the quark and $q(x)$ is a parton distribution function which gives the probability to hit a sub-particle q carrying momentum fraction x of the parent nucleon. For both longitudinally polarized beam and target, the difference in the cross section for opposite spin projections of the nucleon gives access to the polarized structure functions g_1 and g_2:

$$g_1(x) = \frac{1}{2}\sum_q e_q^2 \Delta q(x),$$
$$g_2(x) = q_+(x) - q_-(x), \tag{1.13}$$

where $q_\pm$ are spin dependent parton distribution functions. The unpolarized DIS cross section can be expressed as [4]:

$$\frac{d^2\sigma}{d\Omega d\nu} = \frac{\alpha^2}{4E^2 \sin^4\left(\frac{\theta_e}{2}\right)} \frac{E'}{E} \left\{ W_2 \cos^2\left(\frac{\theta_e}{2}\right) + 2W_1 \sin^2\left(\frac{\theta_e}{2}\right) \right\}$$

(1.14)

The structure functions are the matrix elements of the QCD density matrix corresponding to the probability amplitude to find a quark at one point in space-time in a nucleon with some momentum and placing it at a different space-time point but keeping the same momentum. They (PDFs) are obtained as one-dimensional Fourier transforms in the light-like coordinate y^- (at zero values of the other coordinates) as [16]:

$$q(x) = \frac{p^+}{4\pi} \int dy^- e^{ixp^+y^-} \left\langle p|\bar{\psi}_q(0)\gamma^+\psi_q(y)|p\right\rangle,$$
$$\Delta q(x) = \frac{p^+}{4\pi} \int dy^- e^{ixp^+y^-} \left\langle pS_\parallel|\bar{\psi}_q(0)\gamma^+\gamma^5\psi_q(y)|pS_\parallel\right\rangle, \tag{1.15}$$

where p^+ is a light-cone four momentum vector: given a vector $p^\mu = (p^0, p^1, p^2, p^3)$, its light-cone components are defined by $p^\pm = \frac{1}{\sqrt{2}}(p^0 \pm p^3)$ and $p^\perp = (p^1, p^2)$.[2] $S_\parallel$ represents the longitudinal projection of the nucleon's spin. It is often useful to define two light-like vectors:

$$p_1 = \frac{\Lambda}{\sqrt{2}}(1, 0, 0, 1)$$
$$p_2 = \frac{1}{\Lambda\sqrt{2}}(1, 0, 0, -1), \tag{1.16}$$

[2] p^μ is then written as $p^\mu = (p^+, p^\perp, p^-)$. The scalar product of two light-cone vectors is defined as: $v \cdot w = v^+w^- + v^-w^+ - v^\perp \cdot w^\perp$

where Λ is a normalization parameter. The vectors p_1, p_2 satisfy the following conditions: $p_1^2 = p_2^2 = 0$ and $p_1 \cdot p_2 = 1$.

The DIS structure functions correspond to the forward limit of the optical theorem[3] as illustrated in figure 1.5. These matrix elements are called "non-local" because two different space-time points are involved in the process. The elements are also called forward because unlike the elastic form factors, the nucleon does not change momentum in the process. The DIS process is easily defined in a reference frame where the initial and final and final nucleons are collinear along the z-axis (the infinite momentum or the light-cone frame) [18].

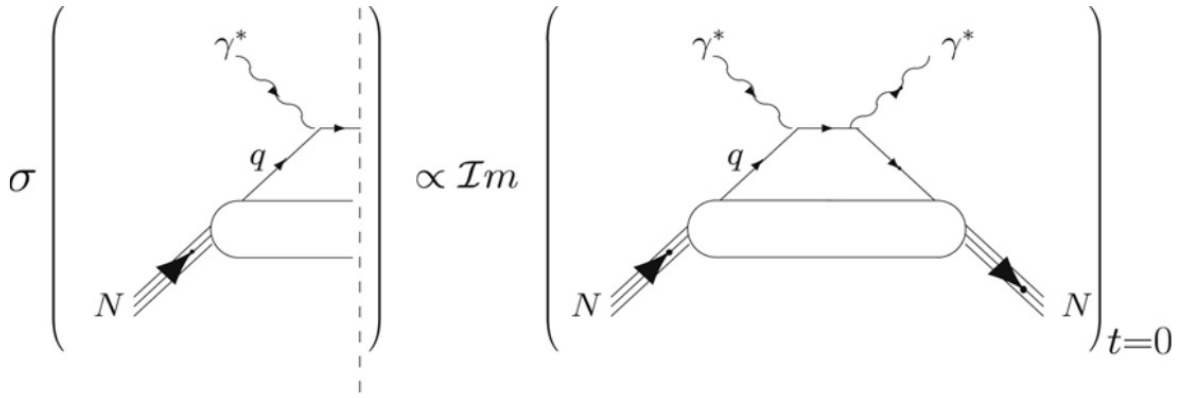

Figure 1.5: The optical theorem connects the imaginary part of the forward scattering amplitude of a process to the corresponding total cross section [18]. This figure was taken from Ref. [16]. See re-use permission (3) in Appendix C.

The structure functions have been experimentally measured extensively for the proton and some of the world data for F_2^p are shown in Figs. 1.6 and 1.7. In the limit

[3] The optical theorem relates the imaginary part of the forward scattering amplitude of the scattering process to total cross section.

where (Q^2, ν) goes to infinity, the Bjorken regime, these structure functions cease to vary with Q^2, a property called scaling. In the Bjorken picture, scaling means quarks become point-like objects at very short distances. The scaling property is, however, violated in QCD by gluon radiation at low parton momentum fraction x, as Q^2 increases [19].

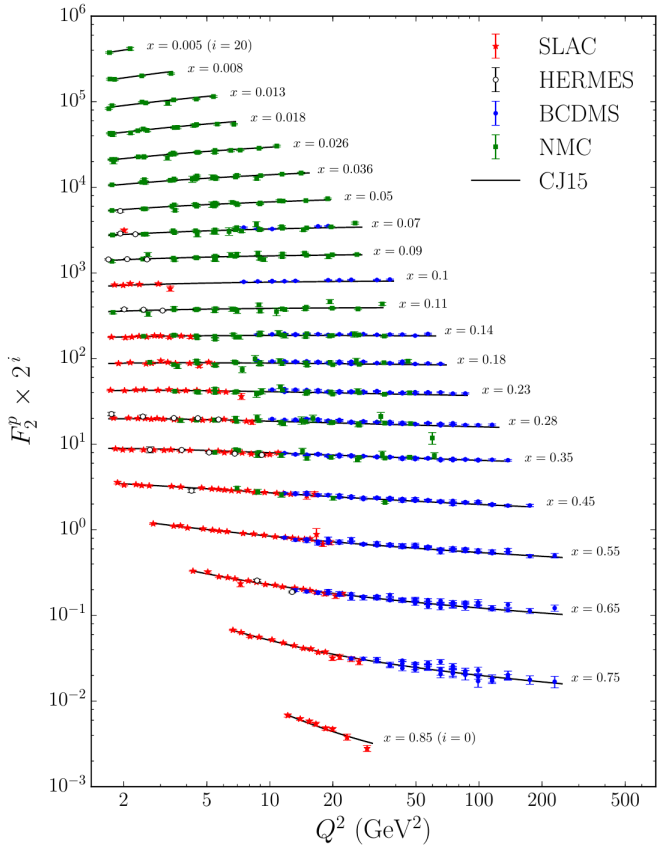

Figure 1.6: The unpolarized proton structure function F_2 data measured from different facilities in the world at fixed values of x over a large Q^2 range. The experimental measurements are represented by the points and the horizontal line across all points corresponding to a fixed x are fit by the CTEQ-Jefferson Lab Collaboration. This figure was taken from Ref. [23]. See re-use permission (4) in Appendix C.

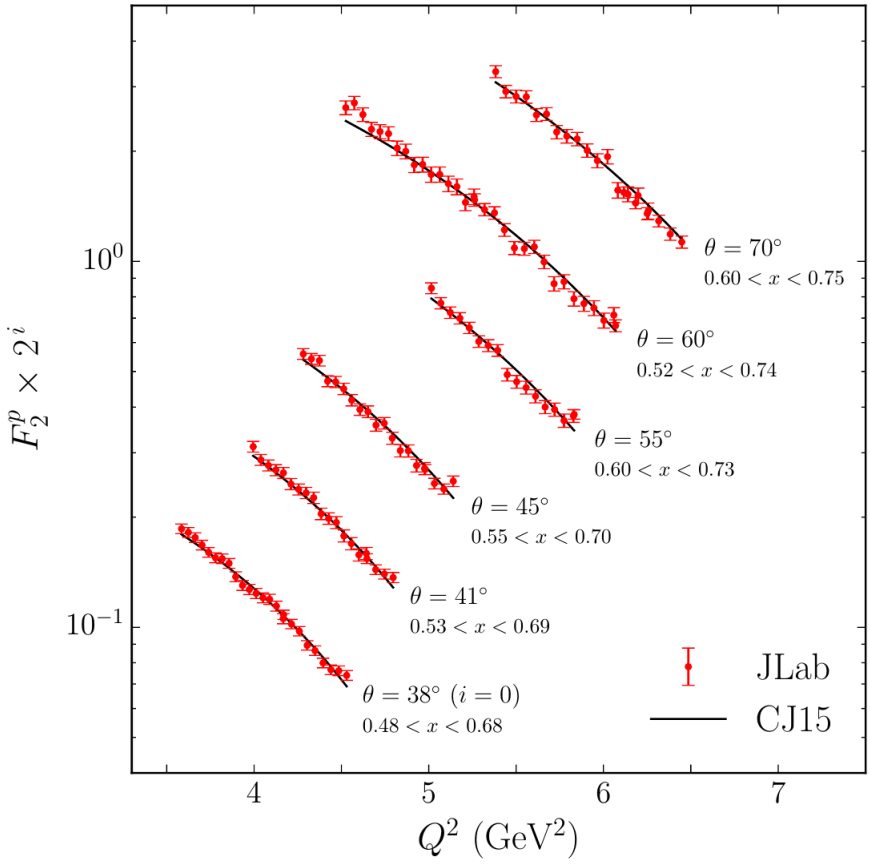

Figure 1.7: Proton structure function F_2^p from Hall C of Jefferson Lab with a fitting by the JLab CJ15 group. This figure was taken from Ref. [23]. See re-use permission (4) in Appendix C.

Fits have been performed on the F_2 structure function to extract parton distribution functions (PDFs) over a wide range in x. At large x, the u and d valence quarks are seen to dominate whilst the contribution from the sea is seen to take over at low x. This is illustrated in Fig. 1.8 obtained from work done by the CTEQ-Jefferson Lab Collaboration [23].

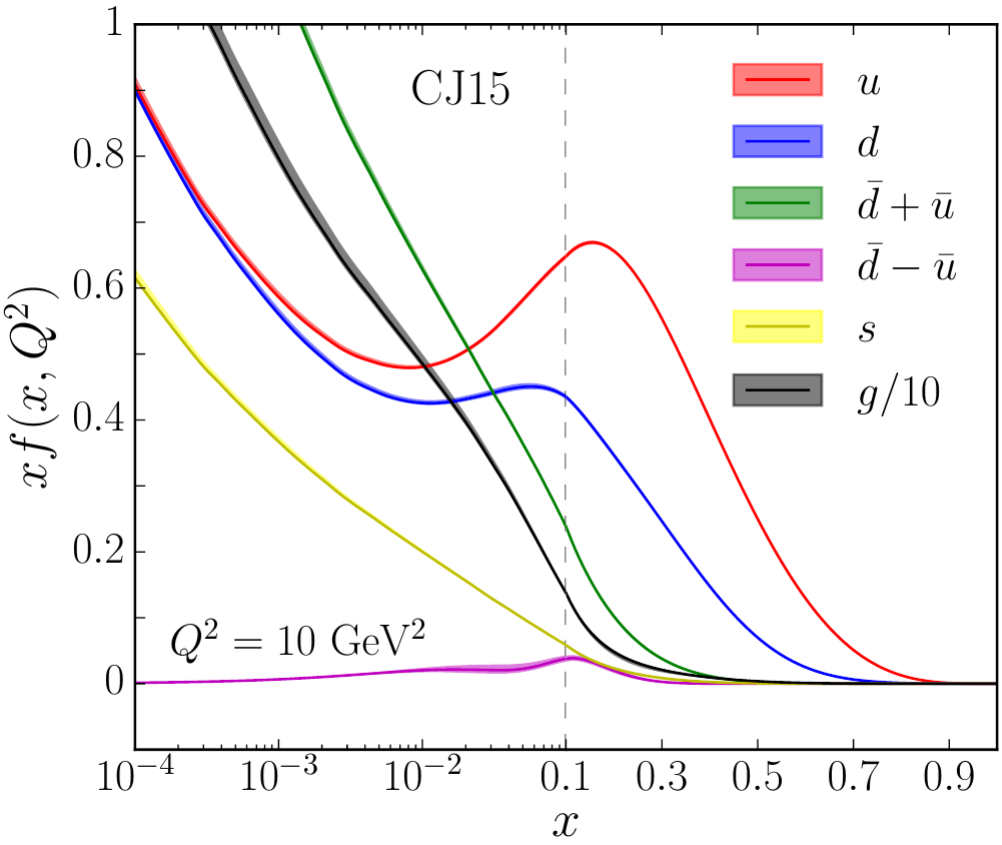

Figure 1.8: Unpolarized parton distribution functions as a function of the Bjorken variable (x) fitted for the different quark constituents of the proton. This figure was taken from Ref. [23]. See re-use permission (4) in Appendix C.

Each of these two processes (DIS and elastic scattering) lacks information contained in the other. The PDFs do not contain information about the spatial distribution of the contents of the nucleon whilst the Form Factors do not carry any information concerning the dynamics of the constituents. Therefore, none of them can provide a full picture of the nucleon's interior.

1.3 Generalized Parton Distributions

1.3.1 The Wigner distribution and GPDs

The quantities measured in elastic scattering and DIS probe only the diagonal elements of the QCD density matrix in position space and in momentum space, respectively [25]. The off-diagonal elements are interesting in that they represent the correlation between momentum and position space. A phase-space distribution which allows the simultaneous access to knowledge of both position and momentum is easily attainable for a classical system but not so easy to conceive for a quantum mechanical ensemble because of the uncertainty principle. In spite of that, the first quantum mechanical phase-space distribution was introduced by Wigner as early as 1932, the Wigner distribution [26]. The Wigner distribution cannot however be treated as a genuine joint probability for position and momentum because it is not always positive. The patches of negative probability arise due to the interference of quantum phases. The quantum-mechanical uncertainty principle restricts the amount of localization that the Wigner distribution can have. This leads to a "fuzzy" phase-space description of a system compared to the sharp determination of its position and momentum observables separately [25]. The Wigner distribution has been adapted and used in different areas of study such as in this case of nucleon structure. This is a function that provides a five-dimensional (two position and three momentum) description of the nucleon. The quantum definition of the Wigner quasi-probability is given by [25]:

$$W(\mathbf{r},\mathbf{p}) = \int_{-\infty}^{+\infty} \frac{d^3\mathbf{R}}{(2\pi\hbar)^3} e^{-ip\cdot\mathbf{R}/\hbar} \psi^*(\mathbf{r} - \frac{1}{2}\mathbf{R})\psi(\mathbf{r} + \frac{1}{2}\mathbf{R}) \tag{1.17}$$

The marginal projections of the Wigner distribution lead to its space and momentum classical limits. This means the spatial distribution can be reached by simply integrating

the Wigner distribution over the momentum variables. In a similar way, integrating the Wigner distribution over the coordinate variables leads to the momentum distribution.

In field theory, an equivalent to the quantum Wigner distribution is obtained by promoting the wave functions of quantum-mechanical states to field operators [25]. In the light-cone frame, the virtual photon momentum q^μ and the average momentum of the nucleon P^μ are collinear along the z-axis. In this frame, the Wigner operator is defined by [25, 77]:

$$\widehat{W}^\Gamma(\vec{b}_\perp, \vec{k}_\perp, x) = \frac{1}{2}\int \frac{dz^- d^2 z_\perp}{(2\pi)^3} e^{i\cdot(xp^+ z^- - \vec{k}_\perp\cdot\vec{z}_\perp)} \psi^*(y - \frac{z}{2})\Gamma\mathbb{L}\psi(y + \frac{z}{2})\Big|_{z^+=0}, \tag{1.18}$$

with $\vec{b}_\perp$ as the parton position, $\vec{k}_\perp$ is the nucleon 4-momentum in the light-cone frame and $\mathbb{L}$ is the Wilson line to ensure gauge invariance. The parameters $z^\pm, z_\perp$, and $p^\pm$ are light-cone variables. The Wigner distributions for a field theoretical system are then defined as the matrix element of the Wigner operator sandwiched between nucleon states [77]:

$$W^\Gamma(\vec{b}_\perp, \vec{k}_\perp, x) = \int \frac{d^2\Delta_\perp}{(2\pi)^2} \left\langle p'|\widehat{W}^\Gamma(\vec{b}_\perp, \vec{k}_\perp, x)|p\right\rangle, \tag{1.19}$$

with p and p' being the initial and final nucleon momentum vector. Eq.(1.19) is the most general phase-space distribution and there is no known experiment that measures the function [17]. The only way we know how to probe the single particle distributions is through high-energy processes where the leading observables are associated with components of quark (gluon) fields which can be selected by operators $\Gamma = \gamma^+, \gamma^+\gamma_5$ or $\sigma^{+\perp}$ [17]. Using the connection between GPDs and helicity amplitudes and applying parity constraints we get eight GPDs at leading order and twist [27]. Four GPDs correspond to processes which do not flip the helicity of the quark (chiral-even GPDs): H^q, E^q, $\tilde{E}^q$ and $\tilde{H}^q$. The other four correspond to processes which flip the helicity of the quark (chiral-odd GPDs): H_T^q, E_T^q, $\tilde{E}_T^q$ and $\tilde{H}_T^q$ [27].

Integrating the Wigner distributions over $\vec{k}_\perp$ yields generalized parton distributions. Using the conventions of Goeke, Polyakov and Vanderhaegen [**?**] we define the quark GPDs by integrating equation 1.19:

$$\int \frac{d^2\vec{k}_\perp}{(2\pi)^2} W^\Gamma(\vec{b}_\perp, \vec{k}_\perp, x) = \frac{\vec{P}^+}{2\pi} \int dz^- e^{ixP^+z^-} \langle p'|\bar{\psi}_q(\frac{-z}{2})\Gamma\psi_q(\frac{z}{2})|p\rangle|_{z^+=\vec{z}_\perp=0}$$

(1.20)

The right hand side of equation 1.3.1 can be interpreted as a Fourier integral along a light-cone distance z^- of a quark-quark correlation function [**?**]. This represents the process of taking a quark out of an incoming nucleon *N(p)* at a space-time point $\frac{-z}{2}$ and restoring it back to the nucleon *N(p')* at a space-time point $\frac{z}{2}$. All this happens at equal light-cone time ($z^+ = 0$) and zero transverse separation between the quarks. Since this process occurs at different points in space-time and the nucleon's momentum is changed, GPDs are called "non-local" and "no-forward".

1.3.1.1 Chiral-even GPDs

Taking $\Gamma = \gamma^+$ and $\gamma^+\gamma_5$ on the right hand side of equation 1.3.1, we get the helicity conserving GPDs:

$$\begin{aligned}\frac{\vec{P}^+}{2\pi} \int dz^- e^{ixP^+z^-} \langle p'|\bar{\psi}_q(\frac{-z}{2})\Gamma\psi_q(\frac{z}{2})|p\rangle|_{z^+=\vec{z}_\perp=0} = \\ \frac{1}{4}\Big\{(\gamma^-)_{\alpha\beta}\Big[H^q(x,\xi,t)\bar{N}(p')\gamma^+N(p) + E^q(x,\xi,t)\bar{N}(p')i\sigma^{+k}\frac{\Delta k}{2M_N}N(p)\Big] \\ + (\gamma_5\gamma^-)_{\alpha\beta}\Big[\tilde{H}^q(x,\xi,t)\bar{N}(p')\gamma^+\gamma_5 N(p) + \tilde{E}^q(x,\xi,t)\bar{N}(p')\gamma_5\frac{\Delta^+}{2M_N}N(p)\Big]\Big\}.\end{aligned} \tag{1.21}$$

The right hand side of Eq.(1.21) is a parametrization of the non-perturbative nucleon structure in terms of GPD functions. In this case nucleon structure is encoded in four

GPDs: $H(x,\xi,t)$ and $E(x,\xi,t)$ corresponding to $\Gamma = \gamma^+$, $\tilde{E}(x,\xi,t)$ and $\tilde{H}(x,\xi,t)$ corresponding to $\Gamma = \gamma^+\gamma_5$ [16, 17]. In this framework, x represents the longitudinal momentum fraction of the nucleon carried by a quark. ξ represents the skewness parameter for the longitudinal fraction of the momentum transfer to the nucleon ($\Delta_\parallel$). t ($= \Delta^2$) is the squared 4-momentum transfer between the initial and the final nucleon, $\Delta = p' - p$ ($= \Delta_\parallel + \Delta_\perp$) in Fig. 1.11. Since t is not a longitudinal parameter like x and ξ, it takes into account that there can also be a transverse component of the momentum transfer [16]. As illustrated in equation 1.3.1, GPD functions are classified according to whether they correspond to a vector operator $(\gamma^-)_{\alpha\beta}$ or an axial-vector operator $(\gamma_5^-)_{\alpha\beta}$ for the active quark. This can be seen in figure 1.9 where the initial and final helicities of both the nucleon and the active quark are shown.

The four GPDs can be summarized as follows:

- H parametrizes a vector transition,
- E parametrizes a tensor transition,
- $\tilde{H}$ parametrizes an axial-vector transition and
- $\tilde{E}$ parametrizes a pseudoscalar transition.

GPDs H and E correspond to averages over quark helicity (see figure 1.9) and are not sensitive to the quark helicity and thus are called unpolarized GPDs. GPDs $\tilde{H}$ and $\tilde{E}$ on the other hand involve differences of quark helicities and are therefore quark helicity sensitive and called polarized GPDs. Furthermore, GPDs H and $\tilde{H}$ conserve proton helicity yet E and $\tilde{E}$ do not. Overall, the four GPDs parametrize the four independent helicity-spin combinations of the nucleon-quark system (conserving quark helicity) [16].

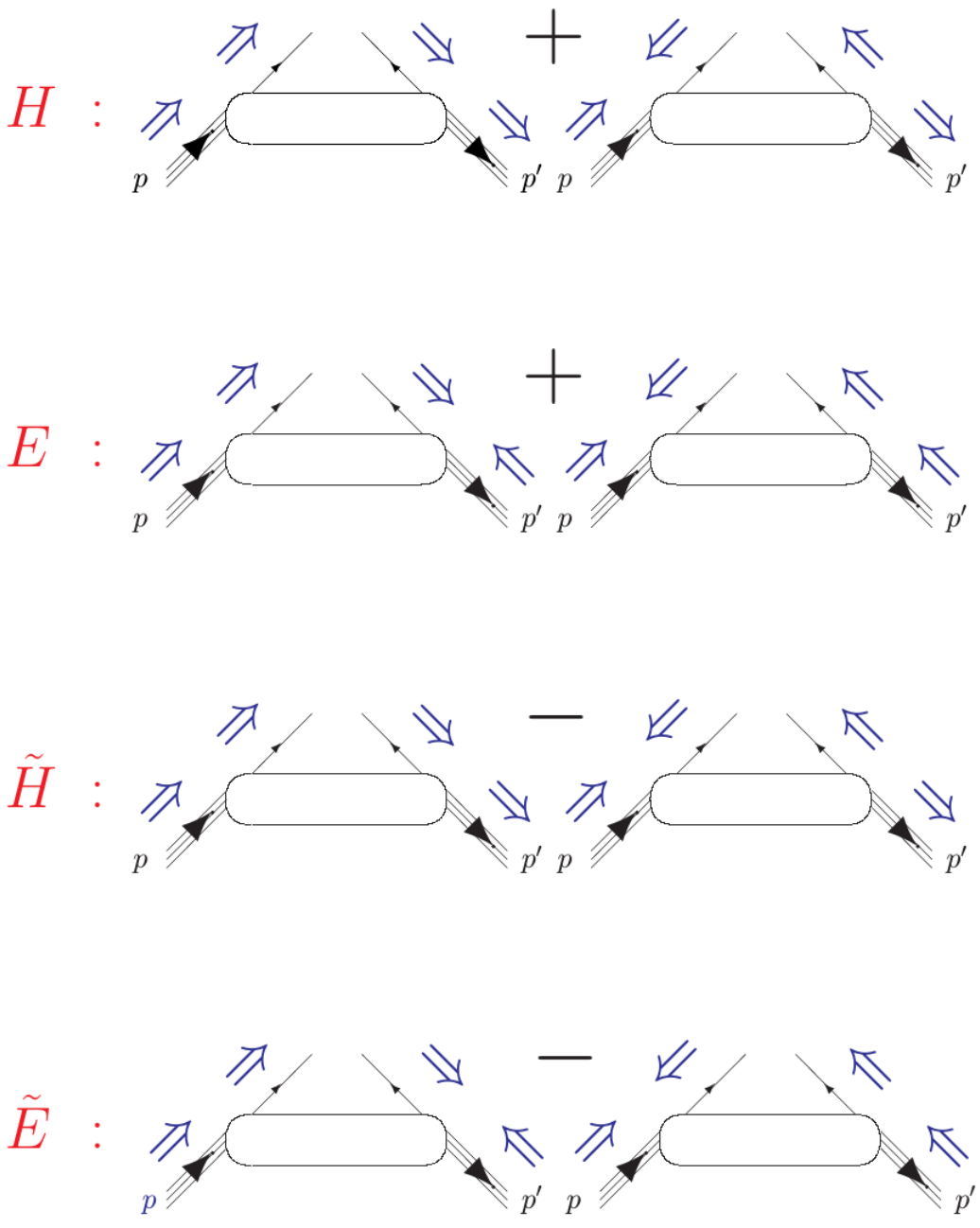

Figure 1.9: Nucleon and active quark helicities corresponding to the four GPDs at leading twist and order. This figure was taken from Ref. [16]. See re-use permission (3) in Appendix C.

1.3.1.2 Transversity GPDs

Up to this point we have only discussed chiral-even quark GPDs at leading order and twist. To complete the picture (at leading order and twist) we now turn to the chiral-odd GPDs. Using the conventions of Diehl [27], chiral-odd GPDs are given by:

$$\begin{aligned}\frac{1}{4\pi}\int dz^- e^{ixP^+z^-}\langle p'|\bar{\psi}_q(\frac{-z}{2})i\sigma^{+i}\psi_q(\frac{z}{2})|p\rangle|_{z^+=\vec{z}=0} \\ = \frac{1}{2P^+}\bar{N}(p')\Big[H_T^q(x,\xi,t)i\sigma^{+i} + \tilde{H}_T^q(x,\xi,t)\frac{P^+\Delta^i - \Delta^+P^i}{M_N^2} \\ + E_T^q(x,\xi,t)\frac{\gamma^+\Delta^i - \Delta^+\gamma^i}{2M_N} + \tilde{E}_T^q(x,\xi,t)\frac{\gamma^+P^i - P^+\gamma^i}{M_N}\Big]N(p),\end{aligned} \tag{1.22}$$

with the introduction of the chirality flipping operator $\Gamma = \sigma^{+\perp}$ instead of the chiral-even operators γ^+ and $\gamma^+\gamma_5$. The chiral-odd GPDs describe the transverse structure of the nucleon and the nucleon tensor charge. They are generally referred to as "transversity GPDs". In the forward limit (limit where the momentum transfer to the proton $t\to 0$) only GPD H_T^q can be measured and in this limit it is equal to the transversity distribution of the quarks, $h_1(x)$ [28]. $h_1(x)$ cannot be measured directly in inclusive DIS because the quark coupling to the photon conserves chirality [27]. Easy access to transversity functions is possible through exclusive electroproduction of neutral pseudoscalar mesons (π^0 mesons) as discussed in section 1.3.3.3.

1.3.1.3 Basic properties of GPDs

First moments and connection to the Form Factors

The Fourier transform of the GPDs with respect to the transverse component of the momentum transfer, $\Delta_\perp$, is related to the transverse position $b_\perp$ and the latter gives the transverse spatial distribution of partons as a function of x. This enables GPDs to combine the spatial information with the longitudinal momentum information to give a 3-D picture of the interior of the nucleon. Since the GPDs unify a wealth of information, their

moments in the momentum fraction x integrates out some kinematic dependencies and bring us back to a 1-D representation of the nucleon's interior. The first moments of the GPDs simplify to the elastic form factors [17]:

$$\begin{aligned} \int_{-1}^{+1} dx H^q(x,\xi,t) &= F_1^q(t) \quad \int_{-1}^{+1} dx E^q(x,\xi,t) = F_2^q(t) \;\forall\; \xi \\ \int_{-1}^{+1} dx \tilde{H}^q(x,\xi,t) &= g_A^q(t) \quad \int_{-1}^{+1} dx \tilde{E}^q(x,\xi,t) = h_A^q(t) \;\forall\; \xi, \end{aligned} \tag{1.23}$$

where F_1^q and F_2^q are the electromagnetic Dirac and Pauli form factors, respectively. g_A^q is the axial form factor and h_A is the pseudoscalar form factor. The relations in Eq.(1.23) are independent of ξ. This is a consequence of Lorentz invariance: integrating the matrix elements of Eq.(1.21) over x removes all reference to the particular light-cone direction with respect to which ξ is defined, therefore the result is ξ independent [27].

Second moment and connection to quark orbital angular momentum

The second moment of the GPDs is related to the spin structure of the nucleon. Understanding the partitioning of the nucleon's spin according to its fundamental building blocks has been a long unresolved and interesting topic in QCD and is now famously known as "the spin puzzle". An earlier and naive approach to understanding the source of the nucleon's spin assigned the sum of the spins of the valence quarks to add up to the total spin of the nucleon but later experiments proved otherwise. According to a gauge-invariant nucleon spin decomposition by Ji [26], the spin can be broken down into:

$$\frac{1}{2} = J = J^q + J^g \tag{1.24}$$

In equation 1.3.1.3, J^q is the contribution of the total angular momentum of quarks to the nucleon spin and J^g is a similar contribution from the gluons. The quark contribution can be decomposed further as:

$$J^q = \frac{1}{2}\,\Delta\,\Sigma + L_q,$$

(1.25)

where $\frac{1}{2}\Delta\Sigma$ is the quark intrinsic spin and L_q is the quark orbital angular momentum contribution to the spin. The second moment of the GPDs, evaluated at zero momentum transfer ($t = 0$), is then related to J^q via Ji's sum rule [26]:

$$\begin{aligned} J^q = \frac{1}{2}\int_{-1}^{+1} x dx\big[H^q(x,\xi,t=0) + E^q(x,\xi,t=0)\big]\;\forall\;\xi \\ = \frac{1}{2}\Delta\Sigma^q + L^q \end{aligned} \tag{1.26}$$

The spin contribution ($\Delta\Sigma^q$) is measurable in DIS experiments and has been found to contribute 20 to 30 % to the nucleon spin [26]. With $\Delta\Sigma^q$ measurable, this means measuring the second moment of the GPDs can, via the sum rule, lead to the determination of the quark orbital momentum contribution to the nucleon spin. However, there is still a huge question on how to go about decomposing the total angular momentum of the gluon (J^g) into the orbital angular momentum part L_g and the spin part Δg in such a way that both can be related to observables [26]. Δg has been directly measured experimentally and is consistent with zero even though it was extracted with large uncertainty [26]. Regardless, equation 1.26 opens the door to pinning down the quark orbital contribution to the nucleon's spin and hence closing the quark's case in the spin puzzle. A lot of work has been done in the extraction of GPD H in proton targets but GPD

E has not been extensively studied. With an active global GPD program it is both promising and exciting that in the future we will have all the role players in equation 1.26 and close the quark case in the spin puzzle.

Forward limit and connections to the PDFs

In the forward limit (momentum transfer to the proton, t, goes to zero), the GPDs reduce to the known parton distributions:

$$H_q(x,0,0) = q(x),$$

$$\tilde{H}_q(x,0,0) = \Delta q(x),$$

where $q(x)$ and $\Delta q(x)$ are the unpolarized and polarized quark densities.

Relative to the chiral-even GPDs, little is known about the transversity GPDs yet. They have been both experimentally and theoretically elusive in that they are difficult to interpret. Their known constraint is the forward limit of H_T:

$$H_T(x,0,0) = \delta_T q_f(x), \tag{1.28}$$

where $\delta_T q_f(x)$ is the transversity distribution function. Chiral-odd GPDs promise to be a rich avenue for describing some exclusive processes such a electroproduction of neutral mesons as discussed in section 1.3.3.3.

Polynomiality condition

Finally, the polynomiality condition is the more general rule of the x moments of GPDs. GPD polynomiality states that the x^n moment of GPDs should be a polynomial in ξ of order n or $n+1$ (if n is even or odd, respectively) [16]:

$$\begin{aligned} if\ n\ is\ even\ &: \int_{-1}^{+1} x^n dx H(x,\xi,t) = a_0 + a_2\xi^2 + a_4\xi^4 + ... + a_n\xi^n, \\ if\ n\ is\ odd\ &: \int_{-1}^{+1} x^n dx H(x,\xi,t) = a_0 + a_1\xi^2 + a_4\xi^4 + ... + a_{n+1}\xi^{n+1}. \end{aligned} \tag{1.29}$$

The same rules apply for the other GPDs $\tilde{H}$, $\tilde{E}$ and E. The polynomiality condition is a consequence of time reversal invariance which dictates that $H(x,\xi,t) = H(x,-\xi,t)$ [16].

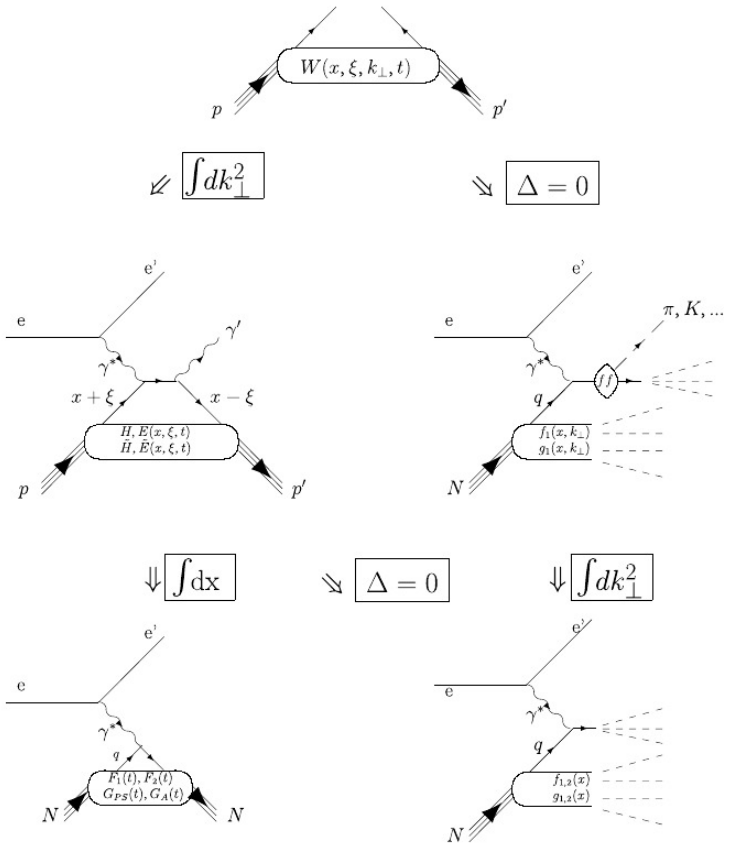

Figure 1.10: Relationship between the Wigner distributions, GPDs, Form Factors and Parton Distribution Functions. This figure was taken from Ref. [16]. See re-use permission (3) in Appendix C.

1.3.2 Factorization and the Handbag Dominance

Factorization theorems enable us to apply calculations to many QCD processes, order by order in a renormalizable perturbation series [29, 30]. At this point we recall the

challenge of QCD, its Lagrangian is formulated in terms of quarks and gluons yet at low energies in QCD (long distances) we encounter hadronic degrees of freedom. Therefore, from the Lagrangian we are not able to compute and predict the long distance properties of hadrons. However, at short distances, asymptotic freedom allows us to "see" one parton at a time. Basically we can compute scattering off a single parton but our ability to do so vanishes for a family (long distances in QCD) of partons. In an asymptotically free configuration, we understand each constituent parton to be carrying a definite momentum fraction x of the hadron. Therefore, an energetic electron probe in contact with the hadron can also be understood as interacting with a parton of definite momentum instead of the whole hadron. In the center of mass frame, the hadron is contracted in the direction of the collision and its internal interactions are time dilated before and after the hard scattering process and thus they can not interfere with the interaction of the active parton with the electron probe [30]. Therefore, factorization enables us to treat electron-nucleon high energy scattering processes as a product of two parts: a hard scattering part which is perturbatively calculable in QED and the second part describes the response of the hadronic system to the probe, the non-perturbative part, and in deep scattering processes, this is described by the structure functions. The factorization proof for the DVCS process is given by Collins and Freund [33].

A good demonstration of factorization is its application in DIS. In the Bjorken limit, scaling is achieved and the electron probe can be understood to be elastically interacting with one parton only. The DIS cross section can be thought of as a product of probabilities which can be written as:

$$\sigma_{DIS}(x, Q^2) = \sum_i q_i(x)\sigma_{eq\to eq}(x, Q^2), \tag{1.30}$$

where in Eq.(1.30) the parton distribution functions $q_i(x)$ encode the non-perturbative part of the interaction (the QCD part) and $\sigma_{eq\to eq}(x, Q^2)$ represents the perturbatively calculable QED part of the cross section.

In as much as a hadron has a sea of quarks and gluons, most of the hadron's momentum is shared among a small number of its constituents hence a probing particle will only interact with one parton interaction. The probability of coherent scattering for a system of n of partons is suppressed by the n^{th} power of photon's virtuality:

$$P_n \sim \left(\frac{|\delta z_\perp|^2}{\pi R - N^2}\right)^n \sim \frac{1}{(Q^2 \pi R_N^2)^n}, \tag{1.31}$$

where $\pi R - N^2$ is the transverse area of the nucleon and z is the distance of the probe from the nucleon (determined by the probe virtuality Q^2). Therefore, at leading order, we have one photon scattering off cleanly from a single parton and according to the factorization theorem this is known as the handbag approximation. The handbag approximation for DVCS is illustrated by the cartoon in Figure 1.11. A quark absorbs a photon at time t_0 and as a results accelerates. It then re-emits a photon at a later time $t'>t_0$ and merges with the parent nucleon. The short distance and time structure of the process is accessible in the Bjorken limit ($Q^2 \longrightarrow \infty$ or rather high virtualities) at a fixed Bjorken variable $x_B = \frac{Q^2}{2\vec{p}\cdot\vec{q}}$. The handbag approximation predicts that the electroproduction process will be dominated by longitudinally polarized photons and only quark helicity conserving GPDs participate in parametrizing the nucleon's soft structure at leading order and twist [33].

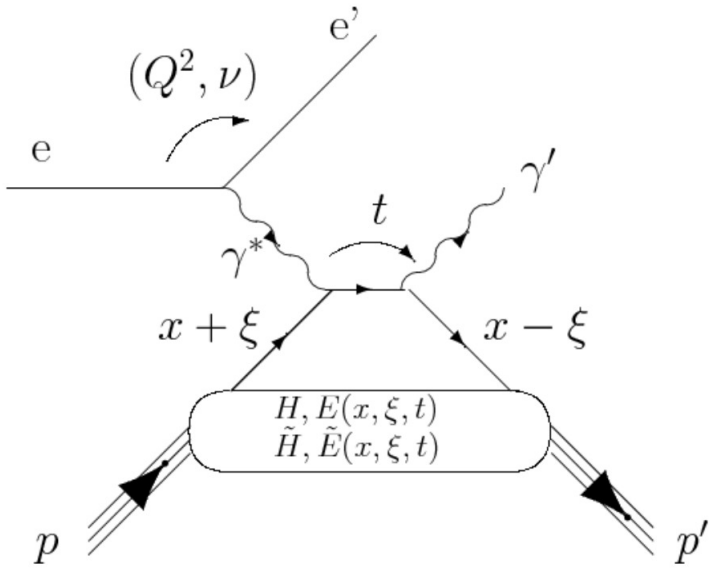

Figure 1.11: The "handbag" diagram for DVCS. The momentum four-vectors of the incident and scattered electron are *e* and *e'*, respectively. The momentum four-vectors of the virtual (incident) and real (scattered) photon are represented by γ^* and γ. t is the invariant momentum transfer to the nucleon which has initial and final momentum four-vectors p and p'. ξ is the longitudinal momentum fraction transferred to the nucleon and x is the longitudinal momentum fraction carried by a struck parton. The functions H, $\tilde{H}$, E and $\tilde{E}$ are GPDs factorizing the strong interactions in DES, as explained in the text. This figure was taken from [16]. See re-use permission (3) in Appendix C.

1.3.3 Accessing GPDs via Deep Exclusive Processes

1.3.3.1 Deeply Virtual Compton Scattering

Electroproduction of a photon can occur through two processes. The Bethe-Heitler (BH) is a process where the photon is emitted along one of the electron lines, before or after the interaction vertex, as shown in figure 1.12. This process is completely calculable if one knows the nucleon form factors. The photon can also be emitted by the nucleon

(from this point on, the nucleon under study is specifically a proton) and this is the DVCS process. The five-fold differential cross section is given by [4]:

$$\frac{d\sigma^{ep\to ep\gamma}}{dQ^2 dx_B d\phi_e dt d\phi} = \frac{\alpha^3 x_B y}{16\pi^2 Q^2 \sqrt{1+4x_B^2 M^2/Q^2}} \left|\frac{\mathcal{T}}{e^3}\right|^2 \tag{1.32}$$

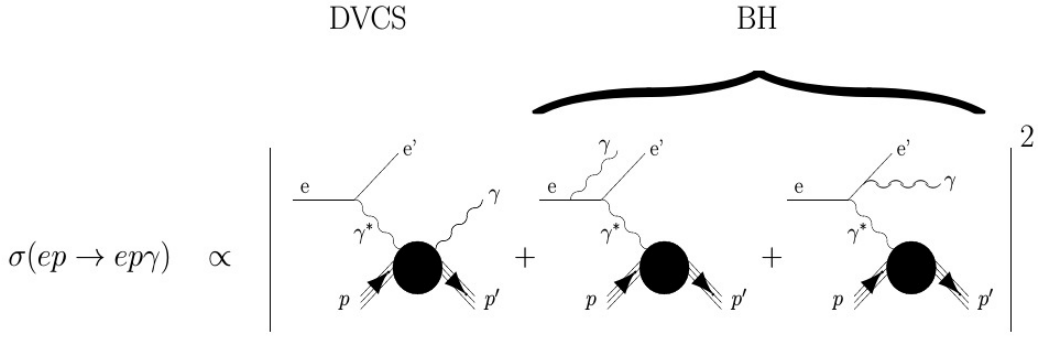

Figure 1.12: Mechanisms that can lead to electroproduction of a real photon,the DVCS and the Bethe-Heitler processes illustrated in the diagrams. This figure was taken from Ref.[16]. See re-use permission (3) in Appendix C.

Besides the photon virtuality Q^2 and the momentum transfer t, the cross section also depends on the DIS scaling (Bjorken) variable $x_B = Q^2/(2M_p\nu)$, where $\nu = E - E'$ is the electron energy transfer. It also depends on the fraction of the electron energy lost in the nucleon rest frame, $y = \frac{\nu}{E}$, the electron azimuthal angle with respect to the horizontal plane, around the beam-line direction, ϕ_e, the angle between the leptonic plane and the hadronic plane, ϕ, as shown in figure 1.13.

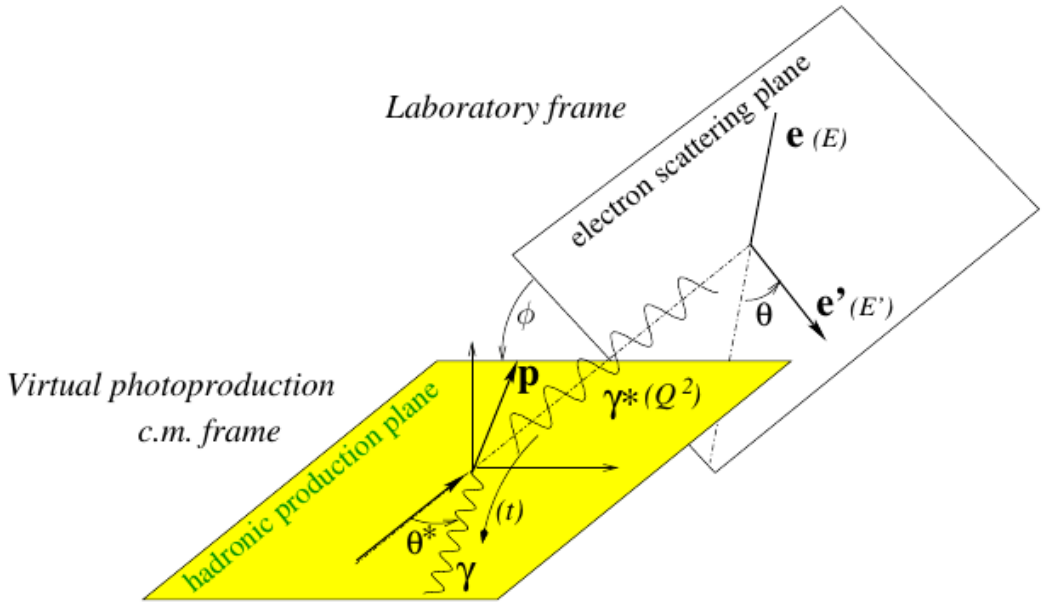

Figure 1.13: Description of reference frames for the DVCS reaction, according to the Trento convention. This figure was taken from Ref. [16]. See re-use permission (3) in Appendix C.

Since the DVCS amplitude interferes with the BH amplitude, see figure 1.12, this results in a total amplitude, $\mathcal{T}$, which is a superposition of the BH and DVCS amplitudes:

$$\begin{aligned} |\mathcal{T}|^2 &= |\mathcal{T}_{\mathcal{DVCS}}|^2 + |\mathcal{T}_{\mathcal{BH}}|^2 + \mathcal{I} \\ \mathcal{I} &= \mathcal{T}^{\dagger}_{\mathcal{DVCS}}\mathcal{T}_{\mathcal{BH}} + \mathcal{T}^{\dagger}_{\mathcal{BH}}\mathcal{T}_{\mathcal{DVCS}} \end{aligned} \tag{1.33}$$

where $\mathcal{T}_{\mathcal{BH}}$ and $\mathcal{T}_{\mathcal{DVCS}}$ are the BH and DVCS amplitudes respectively. $\mathcal{I}$ is the interference between the BH and DVCS processes. The cross section is proportional to the square of the amplitude, with the contribution from the DVCS process containing information about the GPDs and the BH contribution encoding Form Factor information. The terms contributing to the amplitude ($\mathcal{T}_{\mathcal{BH}}$, $\mathcal{T}_{\mathcal{DVCS}}$ and $\mathcal{I}$) can be expanded into finite sums of Fourier harmonics, where different terms of the sum correspond to different twist

levels (twist-two, twist-three, etc.). A calculation at a twist level in the perturbative Feynman expansion of the amplitude can be defined as a suppression of each expansion term by powers of $\frac{1}{Q^2}$ [4]. Up to twist-3, the terms in the cross section can be harmonically expanded as [32]:

$$|\mathcal{T}_{\mathcal{BH}}|^2 = \frac{e^6}{x_B^2 y^2 (1+\epsilon^2)^2 \Delta^2 \mathcal{P}_1(\phi)\mathcal{P}_2(\phi)} \left\{ C_0^{BH} + \sum_{n=1}^{2} C_n^{BH} \cos(n\phi) + \mathcal{S}_1^{BH} \sin(\phi) \right\} \tag{1.34}$$

$$\mathcal{I} = \frac{\pm e^6}{x_B y^3 \Delta^2 \mathcal{P}_1(\phi)\mathcal{P}_2(\phi)} \left\{ C_0^{\mathcal{I}} + \sum_{n=1}^{3} [C_n^{\mathcal{I}} \cos(n\phi) + \mathcal{S}_n^{\mathcal{I}} \sin(n\phi)] \right\} \tag{1.35}$$

$$|\mathcal{T}_{\mathcal{DVCS}}|^2 = \frac{e^6}{y^2 Q^2} \left\{ C_0^{DVCS} + \sum_{n=1}^{2} [C_n^{DVCS} \cos(n\phi) + \mathcal{S}_n^{DVCS} \sin(n\phi)] \right\}, \tag{1.36}$$

where the (±) in the interference term represents a sign convention for negatively(-) and positively(+) charged lepton probes. Furthermore, $\mathcal{P}_1(\phi)$ and $\mathcal{P}_2(\phi)$ are the Bethe-Heitler electron propagators expressed as [31]:

$$Q^2\mathcal{P}_1 = (k - q')^2 = Q^2 + 2k\Delta, \tag{1.37}$$

$$Q^2\mathcal{P}_2 = (k - \Delta)^2 = -2k\Delta + \Delta^2, \tag{1.38}$$

with *q'* and *k* representing the virtual photon and the incoming electron 4-vectors, respectively. Δ is the momentum transfer to the nucleon.

It is worth noting that even though the GPDs depend on three variables x, ξ and t, only the last two variables (ξ and t) can be accessed by measuring the kinematics of the scattered electron and the final state photon and proton [16]. The variable x is not experimentally accessible as a result of the closed loop in the DVCS process. GPDs, therefore, can not be measured directly in an experiment. Instead, Compton Form Factors

(CFF), which depend on two variables, ξ and t can be measured [16]. The connection between the experimental observables containing GPDs (that is to say, CFFs) and the DVCS amplitude is carried by the coefficients of the expansion terms of the Fourier harmonics (see equations 1.34, 1.35 and 1.36). The C's are linear combinations of the CFFs weighted by form factors, which are integrals of the GPDs.

Since the GPDs also encode nucleon helicity information, they can be toggled using beam-target spin degrees of freedom. Thus the use of polarized beams and or targets allows access to different linear combinations of GPDs, depending on the choice of polarization configuration. In this case, one can either calculate the total (unpolarized) cross section or a helicity correlated difference of cross sections. For polarized experiments (either beam or target or both polarized), the difference of cross sections are sensitive to BH-DVCS interference terms [16], giving a linear combination of the electromagnetic Form Factors F_1, F_2 and the CFFs. In general, single spin observables (either beam or target polarized, but not both) are sensitive to the imaginary part of the CFFs while double spin observables (both beam and target polarized) are sensitive to real part of the CFFs [16]. The total cross section is sensitive to the real part of the DVCS amplitude whilst the cross section difference is sensitive to the interference of the Bethe Heitler and the imaginary part, assuming a small DVCS term contribution:

$$\begin{aligned} d\vec{\sigma} - d\vec{\sigma} &= 2 \cdot \mathcal{T}_{\mathcal{BH}} \cdot Im(\mathcal{T}_{\mathcal{DVCS}}) + [|\mathcal{T}^{\rightarrow}_{\mathcal{DVCS}}|^2 - |\mathcal{T}^{\leftarrow}_{\mathcal{DVCS}}|^2] \\ d\vec{\sigma} + d\vec{\sigma} &= |\mathcal{T}_{\mathcal{BH}}|^2 + 2 \cdot \mathcal{T}_{\mathcal{BH}} \cdot Re(_{\mathcal{DVCS}}) + |\mathcal{T}_{\mathcal{DVCS}}|^2, \end{aligned} \tag{1.39}$$

with the arrows representing a polarized beam.

It is also interesting to note that different targets give different access to the GPDs. This is because different targets bring the possibility of accessing different reaction channels which avail different combinations of GPDs. Furthermore, for the same target, different target-beam spin orientations will give access to different linear combinations of

the GPDs. In particular, the difference of polarized cross sections on a neutron target is understood to access a linear combination of GPDs in which the GPD E dominates. Since the GPD E is one of the arguments into Ji's sum rule, this makes the neutron an interesting laboratory for future DVCS experiments. Since free neutrons can not last the duration of these experiments, a simple source of polarized neutrons would be useful. Due to its spin structure, polarized ^{3}He is the ideal source of free polarized neutrons and is promising to be the focus for future DVCS experiments. My experiment, however, used an unpolarized liquid hydrogen (proton) target.

1.3.3.2 Hard Meson ElectroProduction

GPDs encode the structure of the nucleon regardless of the probe and the reaction that is being used as a tool and technique of probing. As a consequence, GPDs are called universal quantities and in addition to DVCS, they are also accessible through hard electroproduction of mesons (Deeply Virtual Meson Production, aka DVMP). The quantum numbers of the meson in the final state makes it possible to probe and separate the contributions from different GPDs and allow for the flavor decomposition of the underlying GPDs. As an example, Collins et al. [30] predicted that at leading order and twist, longitudinally polarized vector meson channels (ρ_L, ω_L and ϕ_L) are sensitive to the unpolarized GPDs (H and E) only. On the other hand, pseudo-scalar meson ($\pi^{\pm}, \pi^0, \eta, K^{\pm}, K^0$, etc) channels are sensitive to the polarized GPDs ($\tilde{H}$ and $\tilde{E}$). This makes hard meson production a good tool to disentangle the different GPDs and is usually seen as complimentary to DVCS. Table 1.1 gives examples of hard exclusive production processes of mesons with their quantum numbers (J^{PC}) on a proton target and the different flavor decompositions accessible for each process. DVMP also provides an experimental window to access transversity GPDs as illustrated in figure 1.14.

GPDs	Meson (J^{PC})	Flavor Sensitivity
	$\pi^0(0^{-+})$	2(u-$\bar{u}$) - (d-$\bar{d}$)
H_T, E_T	$\pi^+(0^{--})$	(u-$\bar{u}$) + (d-$\bar{d}$)
	$\eta(0^{-+})$	2(u-$\bar{u}$) -(d-$\bar{d}$) +2(s-$\bar{s}$)

Table 1.1: Examples of hard exclusive production of mesons with their quantum numbers (J^{PC}) on a proton target and the different flavor decompositions accessible for each process.

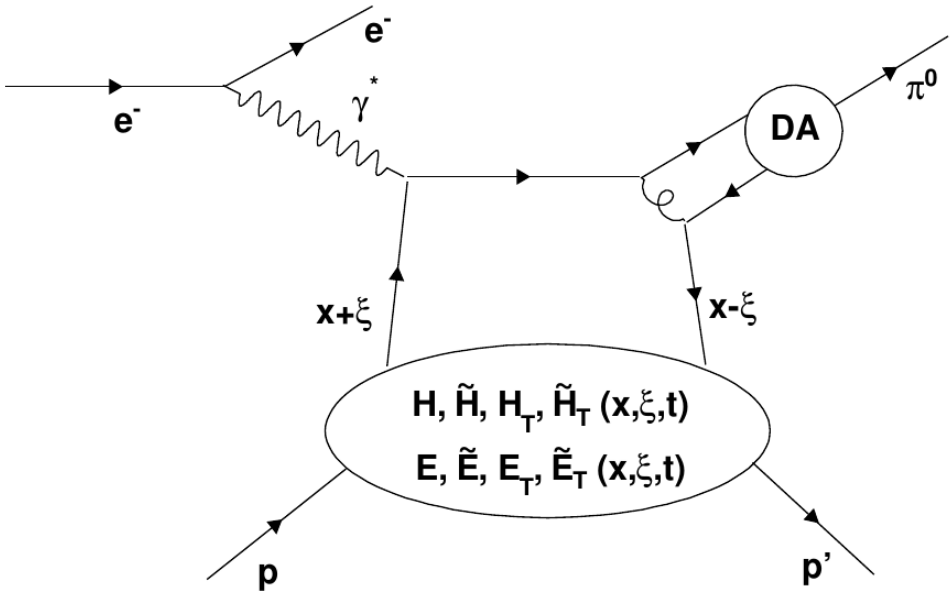

Figure 1.14: A leading twist and order diagram of the electroproduction of a π^0 meson. As opposed to the DVCS reaction, the hard part has the pion distribution amplitude (DA) which is a non-perturbative object. The objects H_T, $\tilde{H}_T$, E_T and $\tilde{E}_T$ are called transversity GPDs. They are chiral-odd GPDs appearing at next to leading order (twist-3) when considering the transverse momentum of the quark entering the meson with respect to the mesons momentum. For this kind of reaction, factorization has been proven for longitudinally polarized virtual photons only [30].

The possibilities availed by DVMP come at an experimental and theoretical price. Unlike in DVCS, the hard part in meson production has a soft or rather strongly interacting system in the form of the meson in the final state, see figure 1.14. This introduces the need for a different factorization scheme for the perturbative expansion of the meson production amplitude. Hitherto, a factorization theorem has only been derived for longitudinally polarized photons. Derivation of a factorization theorem requires a

demonstration that the theory does not have Ultra-Violet (UV) divergences. In the case of the longitudinal photons, the main source of UV divergences has been the contribution (to the amplitude) from soft quark exchanges, the so called end points. It has been demonstrated by Collin et al. [30] that for longitudinally polarized photons, the end point contribution terms are suppressed by a factor of $\frac{1}{Q^2}$. At large Q^2 this power suppression is deemed sufficient to obtain a factorization theorem. It has, however, not been experimentally or otherwise determined what the exact lower Q^2 limit is for the factorization to hold. In the case of transversely polarized photons, it is also demonstrated by Collin et al. [30] that the amplitude is suppressed by one power of Q ($\frac{1}{Q}$).

The factorization proof for DVMP is given by Collins-Frankfurt-Strikman [29] and they have predicted that in the handbag approximation the cross section is dominated by longitudinally polarized photons (σ_L). The contribution from transversely polarized photons (σ_T) is understood to be suppressed by a factor of $\frac{1}{Q^2}$ relative to the longitudinal contribution to the cross section. In general, according to the handbag approximation σ_L is expected to scale as $\frac{1}{Q^6}$ whilst σ_T scales as $\frac{1}{Q^8}$.

The differential cross section for exclusive meson electroproduction for a longitudinally polarized beam and unpolarized target is given by [35]:

$$\frac{d^4\sigma}{dtd\phi dQ^2dx_B} = \frac{1}{2\pi}\Gamma_{\gamma^*}(Q^2, x_B, E)\Big[\frac{d\sigma_T}{dt} + \epsilon^*\frac{d\sigma_L}{dt} + \sqrt{2\epsilon^*(1+\epsilon^*)}\frac{d\sigma_{TL}}{dt}\cos(\phi) + \epsilon^*\frac{d\sigma_{TT}}{dt}\cos(2\phi) + h\sqrt{2\epsilon^*(1-\epsilon^*)}\frac{d\sigma_{TL'}}{dt}\sin(\phi)\Big], \tag{1.40}$$

where $\Gamma_{\gamma^*}(Q^2, x_B, E) = \frac{\alpha}{8\pi}\frac{Q^2}{M^2k^2}\frac{1-x_B}{x_B}\frac{1}{1-\epsilon}$ is the virtual photon flux, $\epsilon^* = \frac{1-y-\frac{Q^2}{2k^2}}{1-y+\frac{y^2}{2}+\frac{Q^2}{4k^2}}$ is the virtual photon flux's degree of polarization, h (=±1) is the helicity of the lepton probe, the electron in our case, k and k' are the initial and scattered electron energy.

1.3.3.3 Hard Electroproduction of Pseudoscalar Mesons

According to the handbag formalism the electroproduction process is expected to be dominated by longitudinally polarized virtual photons. The longitudinal amplitude for pseudoscalar mesons involves the chiral-even GPDs $\tilde{H}$ and $\tilde{E}$ [27]. At leading order the pion hard electroproduction amplitude is [**?**]:

$$\mathcal{M}^L = -ie\frac{4}{9}\frac{1}{Q}\Big[\int_0^1 dx\frac{\Phi_\pi(x)}{x}\Big]\frac{1}{2}(4\pi\alpha_s)\cdot\Big\{A_{\pi N}\bar{N}(p')n\gamma_s N(p) + B_{\pi N}\bar{N}(p')\gamma_s\frac{\Delta\cdot n}{2m_N}N(p)\Big\}, \tag{1.41}$$

where:

α_s is the strong coupling constant,

$$A_{\pi^0 p} = \int_{-1}^{+1} dx\Big(e_u\tilde{H}^u - e_d\tilde{H}^d\Big)\Big\{\frac{1}{x-\xi+i\epsilon} + \frac{1}{x+\xi-i\epsilon}\Big\}, \tag{1.42}$$

$$B_{\pi^0 p} = \int_{-1}^{+1} dx\frac{1}{\sqrt{2}}\Big(e_u\tilde{E}^u - e_d\tilde{E}^d\Big)\Big\{\frac{1}{x-\xi+i\epsilon} + \frac{1}{x+\xi-i\epsilon}\Big\} \tag{1.43}$$

and $\Phi_\pi(x)$ is the chiral-even (twist-2) pion distribution amplitude (DA), a non-perturbative object which encodes the meson structure.

Using data for the $\pi^0 \to \gamma\gamma$ transition form factor, $\Phi(x)$ has been found to take the form [**?**]:

$$\Phi_\pi(x) = \sqrt{2}f_\pi 6x(1-x), \tag{1.44}$$

$f_\pi = 0.0924$ GeV from π^0 weak decay.

At this point we recall the ultimate goal of nucleon structure study: to parametrize the non-perturbative structure of nucleons (or hadrons in general) in terms of GPD

functions. The handbag formalism gives us eight GPDs for nucleon soft structure parametrization at leading order and twist: four chiral-even and four chiral-odd. The first goal of nucleon structure experiments is to test the validity of the handbag formalism in parametrizing nucleon structure. In order to test the relevance of the handbag formalism we have to confirm that the predicted dominance of the longitudinal cross section (over the transverse cross section) can be experimentally observed. As predicted for electroproduction at high Q^2, the handbag approximation is in agreement with experimental data for photoproduction [10, 34] and for vector meson production [36]. In the case of pseudoscalar meson production, models based on the handbag formalism are found to under predict the data by an order of magnitude for π^+ [37]. This implies that the data are not in the region of asymptotic freedom where the handbag formalism applies.

A more stringent test of the handbag formalism validity is the Q^2-dependence of the separated longitudinal and transverse meson cross section terms. In the regime where the handbag formalism applies, σ_T is predicted to scale as Q^{-8}, σ_L is expected to scale as Q^{-6} and $\sigma_L \gg \sigma_T$. Separated cross section terms for π^+ data from JLab's Hall C show that the data is not in the regime where the handbag formalism holds [36, 38]. As shown in the left panel of figure 1.15, σ_T is completely off and does not scale as predicted at low Q^2 and small t whilst σ_L does. Even though σ_L does scale as predicted and is found to be larger than σ_T at small t, this is consistent with σ_L being boosted by a dominant meson pole in this region [36] and such cannot be interpreted as the handbag dominance. Going to higher Q^2 and t (right panel of figure 1.15) we see σ_T dominating over σ_L, consistent with a vanishing pion pole. A larger σ_T (than σ_L) is also another indication that the handbag formalism is insufficient in this experimental regime. Concerning the scaling at high Q^2, σ_L continues to scale as predicted but σ_T still does not scale according to predictions. It is however worth noting that the high Q^2 plot has only two data points and σ_T might scale well.

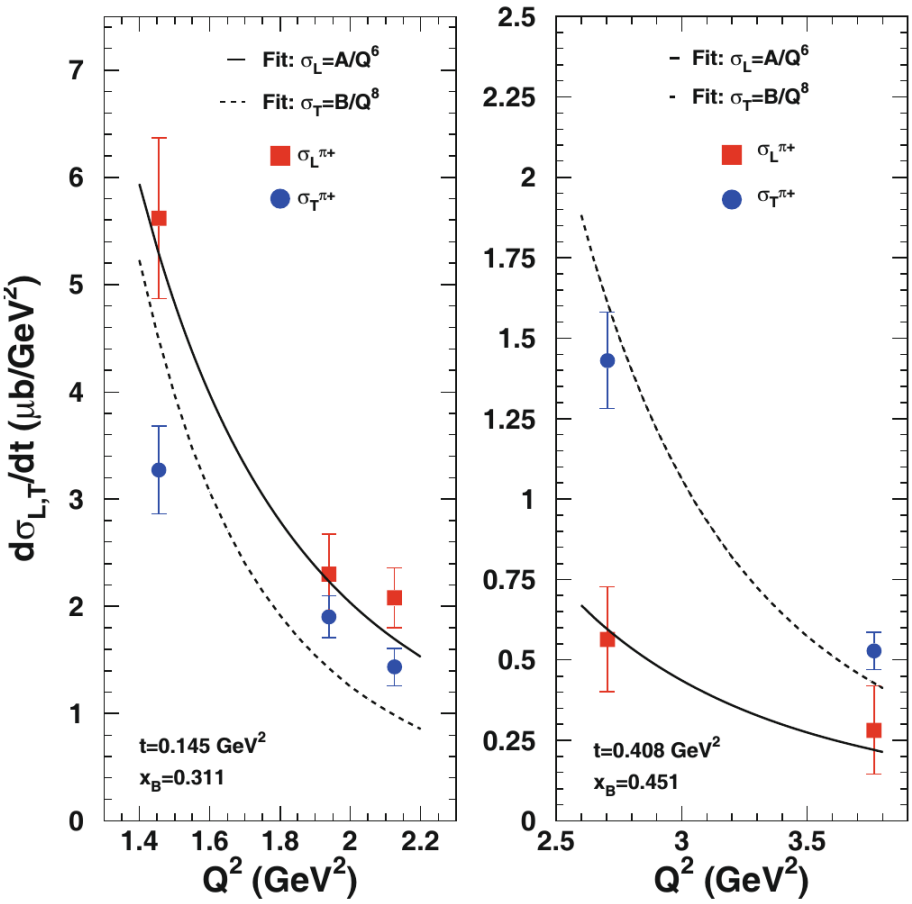

Figure 1.15: Longitudinal and transverse π^+ electroproduction cross sections for fixed momentum transfer t and longitudinal momentum fraction x_B. Solid lines show a $\frac{A}{Q^6}$ fit to σ_L and the dashed lines represent a $\frac{B}{Q^8}$ fit to σ_T. This figure was taken from Ref. [36]. See re-use permission (6) in Appendix C.

1.3.3.4 Pseudoscalar Mesons, Twist-3 DA and Transversity GPDs

The discrepancy between experimental data and the handbag approximation suggests a strong participation of transversely polarized photons in the pseudoscalar meson electroproduction channels at leading order in pQCD. This has inspired models assuming

a transverse factorization and the proposition that for pseudoscalar meson production, the chiral-odd meson DA appearing at twist-3 couples with tranversity GPDs [39, 40]. Chiral-odd DAs arise at twist-3 when considering the transverse momentum of the quark (with respect to the meson's momentum) entering the meson. Even though the twist-3 pion wave function should be kinematically suppressed compared to the twist-2 amplitude, it comes with a transverse response term which is boosted by the mass factor $\mu_\pi = \frac{\mu_\pi^2}{m_u+m_d}$ (m_u and m_d are the bare masses for the up and down quarks) which increases the meson production cross section [36]. Including transversity GPDs in the models has been able to describe the π^+ HERMES [41] cross sections and the interference terms of the π^0 JLab CLAS data [37]. Figure 1.16 shows the CLAS data being well described by the transversity models of Goloskokov and Kroll [39] and Goldstein et al. [40].

The transversity GPDs can be accessed only if we can isolate the transverse from the longitudinal contributions to the cross section. The participating GPDs in meson production for transverse photons are H_T, characterizing quark distributions involved in nucleon helicity flip processes, and $\bar{E}_T$ ($= 2\tilde{H}_T + E_T$), characterizing quark distributions involved in nucleon non-helicity flip processes [37]. In their model, Goldstein et al. [40] have found the following relation and a way of accessing the transversity GPDs H_T, $\tilde{H}_T$ and E_T from measuring σ_T and σ_{TT}:

$$\begin{aligned} \frac{d\sigma_T}{dt} &= \frac{4\pi\alpha}{2k'}\frac{\mu_\pi^2}{Q^8}\left[(1-\xi)\left|\langle H_T\rangle\right|^2 - \frac{t'}{8m^2}\left|\langle 2\tilde{H}_T + E_T\rangle\right|^2\right], \\ \frac{d\sigma_{TT}}{dt} &= \frac{4\pi\alpha}{2k'}\frac{\mu_\pi^2}{Q^8}\frac{t'}{16m^2}\left|\langle 2\tilde{H}_T + E_T\rangle\right|^2, \end{aligned} \tag{1.45}$$

where in this case k' prime is the phase space factor;

$$k' = \frac{16\pi}{Q^2}\left(\frac{1}{x_B} - 1\right)\sqrt{(W^2 - m^2) + Q^4 + 2W^2Q^2 + 2Q^2m^2} \tag{1.46}$$

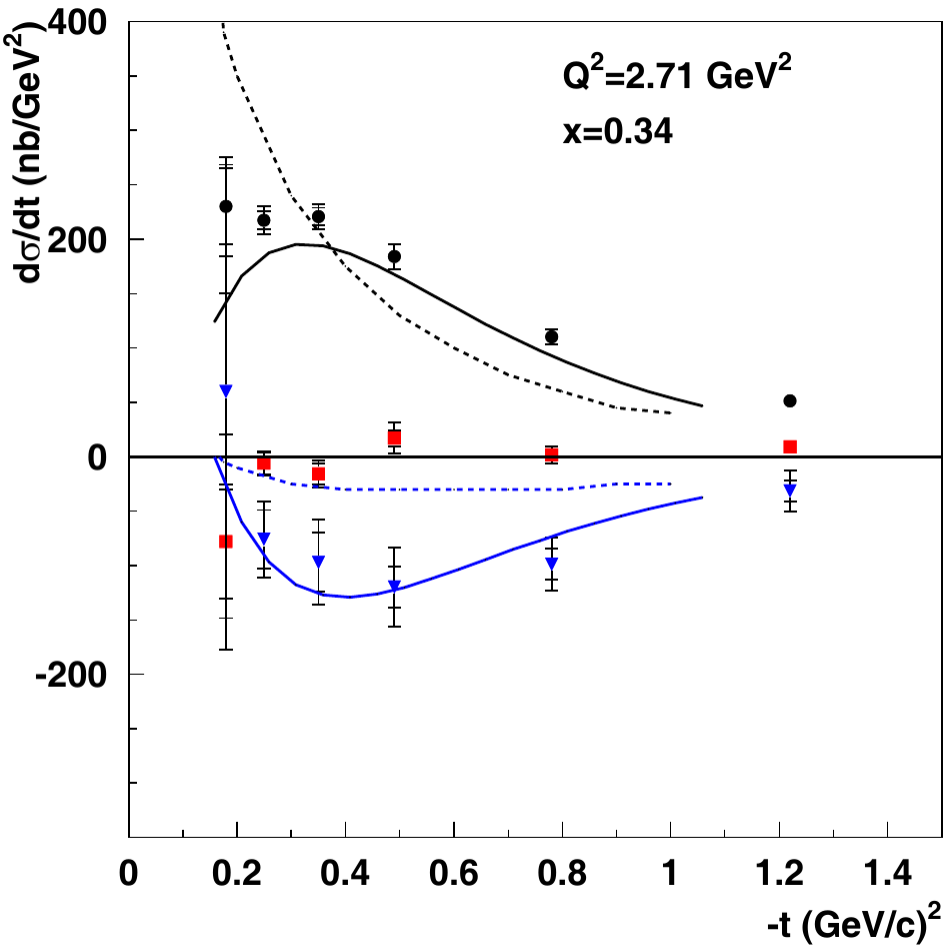

Figure 1.16: σ_{TT} and σ_{LT} interference terms of the π^0 CLAS [37] cross section compared to transversity GPD models by Goloskokov and Kroll [39] (solid curves) and Goldstein et al. [40] (dashed curves). Black symbols represent the $\sigma_T + \epsilon\sigma_L$, blue symbols represent σ_{TT} and the red are representive of σ_{LT}. This figure was taken from Ref. [36]. See re-use permission (6) in Appendix C.

1.3.4 Existing Exclusive Hard Electroproduction Measurements

1.3.4.1 Pseudoscalar Meson Production Experiments

The first JLab π^0 electroproduction measurements were published by the Hall A collaboration [42]. In 2014, the CLAS collaboration [43] published the results of the measurement of π^0 electroproduction using a wider CLAS kinematic coverage shown in figure 1.18. Both the HALL A and CLAS results do not have the longitudinal and transverse components of the cross section separated but strongly contradict the handbag approximation. These results show a large transverse-transverse interference term in the π^0 production cross section implying that in this experimental regime transversely polarized photons play a significant role in the transition at leading order and twist.

The most recent results on pion production are shown in Figure 1.17 and were published by the JLab Hall A collaboration presenting a Rosenbluth separation of the cross section at x_B = 0.36 and Q^2 (1.5, 1.75 and 2) GeV^2 [11]. Even though the σ_L term of the cross section is found to be consistent with zero, the interference cross section term, σ_{LT} is non-zero. This implies a non-negligible σ_L contribution. Also, σ_T is found to be much larger than σ_L, in contrast to the asymptotic prediction of the handbag factorization.

Other results which support the presence of a significant σ_{LT} interference come from beam spin asymmetries measurements with Hall B's CLAS detector [12] where a non-zero beam spin asymmetry, indicating an L-T interference, was observed. Recent results from COMPASS [13] (see figure 1.20) using a muon beam to produce neutral pions also show a large transverse-transverse (σ_{TT}) and a small σ_{LT} contribution to the cross section. In all these results the handbag approximation fails and this is a strong suggestion of the participation of transversely polarized photons and the helicity flip GPDs at leading

order for π^0 (in general pseudoscalar meson) leptoproduction. Transversely polarized photons invite transversity GPDs and are predicted to start contributing at next to leading order. These results have contradicted the handbag approximation and instead they have made lepton production of π^0 mesons a good hunting ground for the transversity GPDs.

Up until now, the range of applicability of the handbag formalism in DVMP is still in question. Instead pseudoscalar mesons (in particular π^0) electroproduction has been identified by Goldstein et al. [44], Goloskokov and Kroll [39] as sensitive to the helicity flip processes and hence the chiral-odd GPDs, at leading order in the handbag formalism. π^+ electroproduction is another channel sensitive to helicity flip GPDs but its disadvantage is the presence of a dominant pion-pole term which makes the interpretation of the data complicated [37]. The pion-pole is absent in π^0 electroproduction.

Using the advantage of the 12 GeV upgrade, experiment E12-06-114 (of this thesis) is the first JLab experiment to measure π^0 cross sections over a wider kinematic range in Q^2 (from 3 to 9 GeV^2) and more points in x_B (from 0.36 to 0.6). This thesis will, however, focus on data at x_B = 0.36 taken at three different points in Q^2: 3.2, 3.6 and 4.47 GeV^2. We present in this document the cross section measured at the first Q^2 point, 3.2 GeV^2. Even though this data doesnot offer a complete separation of the longitudinal (σ_L) and transverse (σ_T) contributions to the cross section, the unseparated cross section ($\sigma_U = \sigma_T + \epsilon\sigma_L$) is a good observable to test against the predictions by handbag approximation models. In addition to the unseparated cross section, the data offers interference terms σ_{LT} (longitudinal-transverse interference) and σ_{TT} (transverse-transverse interference). These interference terms offer additional experimental observables to be compared against handbag and transversity models.

1.3.4.2 DVCS Experiments

Since the last decade, DVCS cross sections have been measured and are still planned to be measured in two distinct kinematic regimes: the quark-gluon sea, at low x_B, and the valence region at higher x_B, as shown in figure 1.21.

The HERA collider performed of the pioneer DVCS experiments. At HERA, the H1 and ZEUS collaborations operated with 27.5 GeV positrons and 820 GeV protons at center of mass energy 30< W <130 GeV and 8< Q^2 < 85 GeV^2 [47]. They measured the unpolarized cross section of the $ep \rightarrow ep\gamma$ process. At such high energies (low x_B) the DVCS process is sensitive to the quark-gluon sea, hence gluon GPDs. HERA had the capability to use both electrons and positrons as a probe enabling the H1 collaboration to measure a variety of beam spin asymetries.

The HERMES experiments at HERA used an electron beam as well as a positron beam to measure DVCS beam spin asymmetries on fixed gaseous targets (hydrogen and deuterium). Longitudinally and transversely polarized target asymmetries, beam-charge asymmetries and all associated beam-spin/target-spin/beam-charge double asymmetries [48]. The HERMES Q^2 range was from 1 GeV^2 to 6 GeV^2 and x_B in the range 0.04 to 0.2. The average momentum transfer was $\langle -t \rangle$ = 0.27 GeV^2, using a 27.5 GeV positron/electron beam. For the first measurements exclusivity was implemented by a missing mass cut on the recoil nucleon. DVCS asymmetries and moments results from the HERMES data were found to be in agreement with the handbag formalism [16]. This agreement even though in a small band in Q^2, is a strong sign of the dominance of the handbag diagram over higher twists in the case of DVCS. For the last two running years of HERA, a recoil detector was installed to improve the selection of DVCS events by direct measurement of the recoil protons [48].

The CEBAF Large Acceptance Spetrometer (CLAS) collaboration in Hall B of JLab also measured electron beam spin asymmetries off a fixed hydrogen target covering kinematics in the Q^2 range 1 to 4.8 GeV^2, x_B range 0.1 to 0.6 using a 6 GeV polarized electron beam. A 20 to 30 % asymmetry was observed. The asymmetries indicate a $\sin\phi$ behavior as expected from the handbag formalism. This result suggests sensitivity to the handbag description of the DVCS process and an indication that the GPD formalism might be a valid description of nucleon structure. Unpolarized and beam-polarized cross sections have recently been published by CLAS [10] increasing our confidence in the knowledge of the GPD H. The latest CLAS results also support the models predicting an increasing proton size at lower Bjorken momentum fraction.

The JLab Hall A collaboration measured both unpolarized and the difference of polarized cross sections with W≈2 GeV, using a polarized electron beam on a fixed proton target. Four-fold beam-polarized and unpolarized cross sections were measured, $\frac{d^4\sigma}{dx_B dt d\phi dQ^2}$ [9], see figure 1.22. Measurements were done at four values of momentu transfer to the proton $-t$: 0.17,0.23, 0.28 and 0.33 GeV^2 for kinematics $\langle x_B \rangle$ = 0.36 and $\langle Q^2 \rangle$ = 2.3 GeV^2. In addition, beam polarized cross sections were measured at $\langle Q^2 \rangle$ = 1.5 GeV^2 and $\langle Q^2 \rangle$ = 1.9 GeV^2. These data have made a contribution to provide constraints in extracting the real and imaginary parts of the GPD H [19]. Early conclusions show that the valence quarks (high x) seem to remain at the center of the nucleon while the sea and gluons (low x) can extend towards the ”surface” of the nucleon. CFFs have also been extracted from this data, indicating early scaling properties.

The first Hall A DVCS results have shown early signs of validation of the GPD formalism and the handbag picture of DVCS but are limited to a narrow kinematic region, small Q^2 (less than or equal to 2.3 GeV^2) and x_B (less than or equal to 0.36). The

experiment on which this thesis is based explored a wider range in both Q^2 and x_B, thus testing the precision with which the handbag amplitude dominates (or does not) over higher twist amplitudes. This was made possible by the new (and wide, x_B up to 0.6 and Q^2 up to 9 GeV^2) kinematic region availed by the 12 GeV era at JLab.

Future DVCS experiments in Hall B and Hall C will also explore previously non-explored regions. At CERN, COMPASS is set up to study DVCS at the sea quark and gluon regime (at very low x_B). An Electron Ion Collider proposal is still in circulation and should it materialize, it will offer possibilities to measure kinematics which can not be reached using fixed targets. The EIC will be fundamental in measuring DVCS observables at low x and probe gluon GPDs. All these efforts will contribute to constrain existing GPD models even further and extracting with confidence, nucleon information in the GPD formalism.

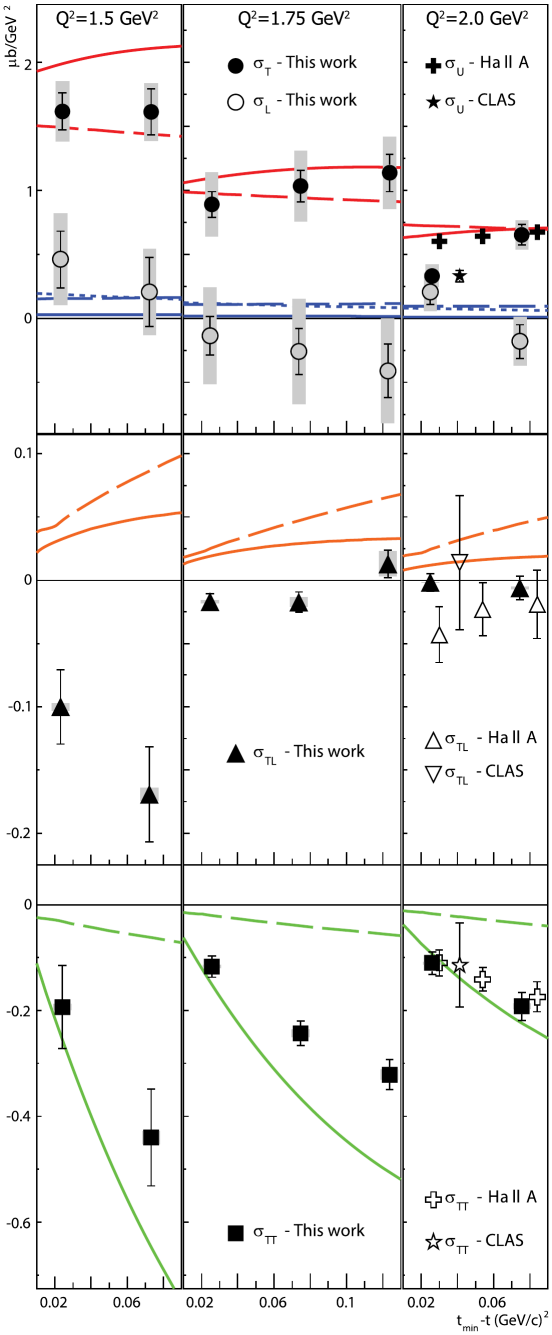

Figure 1.17: Hall A Rosenbluth results: $d\sigma_T$ (full circles), $d\sigma_L$ (open circles), $d\sigma_{TL}$ (triangles), and $d\sigma_{TT}$ (squares) as a function of momentum transfer t_{min} for Q2=1.5 (left), 1.75 (center), and 2GeV^2 (right) at x_BB=0.36 [11]. Solid lines are predictions by Ref. [39] and long dashed lines from Ref. [40]. The short-dashed lines are predictions from the VGG model [45]. This figure was taken from Ref. [11]. See re-use permission (7) in Appendix C.

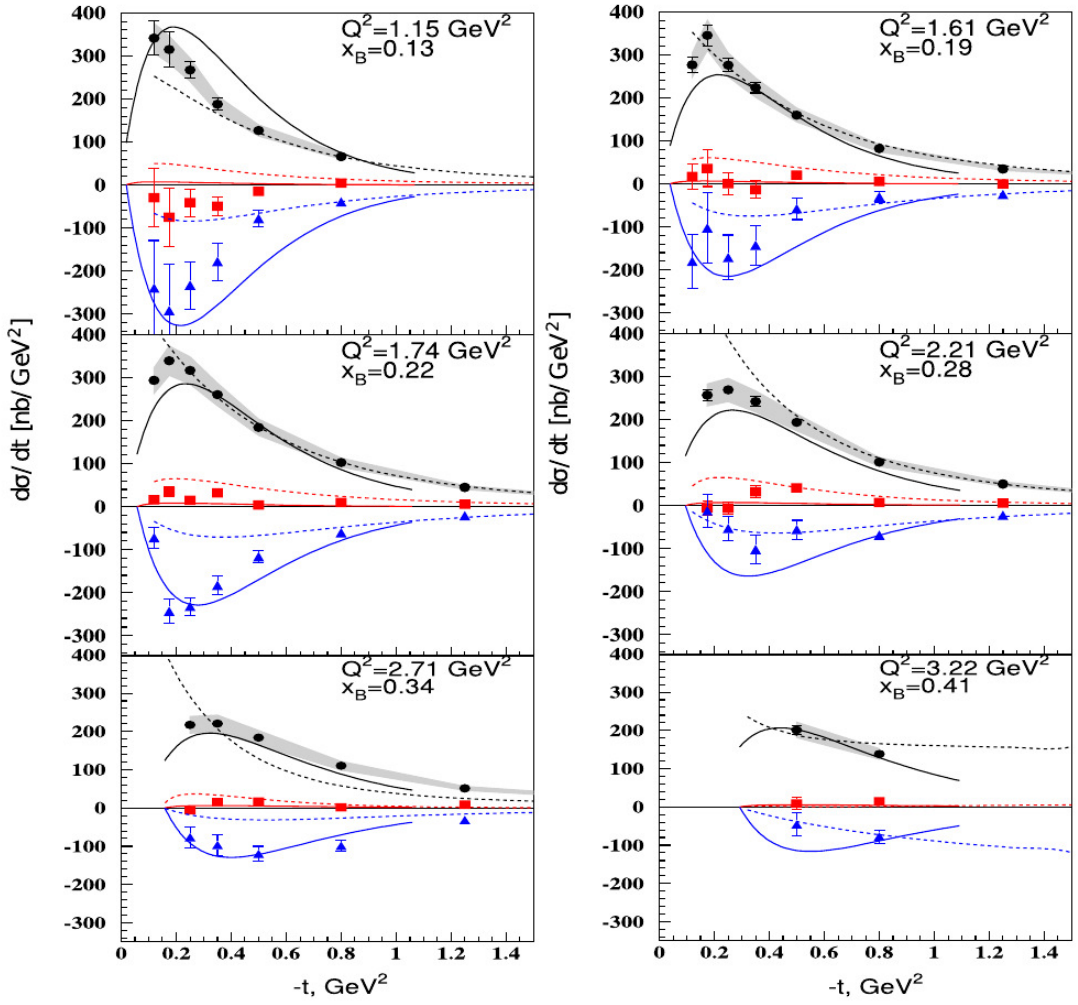

Figure 1.18: The extracted structure functions as a function of momentum transfer to the proton, t. The black (solid circles) represent $\frac{d\sigma_U}{dt} = \frac{d\sigma_T}{dt} + \frac{\epsilon d\sigma_L}{dt}$, the blue (triangles) represent $\frac{d\sigma_{TT}}{dt}$; and the red (squares) $\frac{d\sigma_{LT}}{dt}$. The curves (of the corresponding color) are model predictions of these cross section responses. Solid curves are from model prediction by Goloskokov and Kroll [39] and the dashed lines are predictions by Goldstein, Gonzalez-Hernandez and Liuti [28]. This figure was taken from Ref. [43]. See re-use permission (7) in Appendix C.

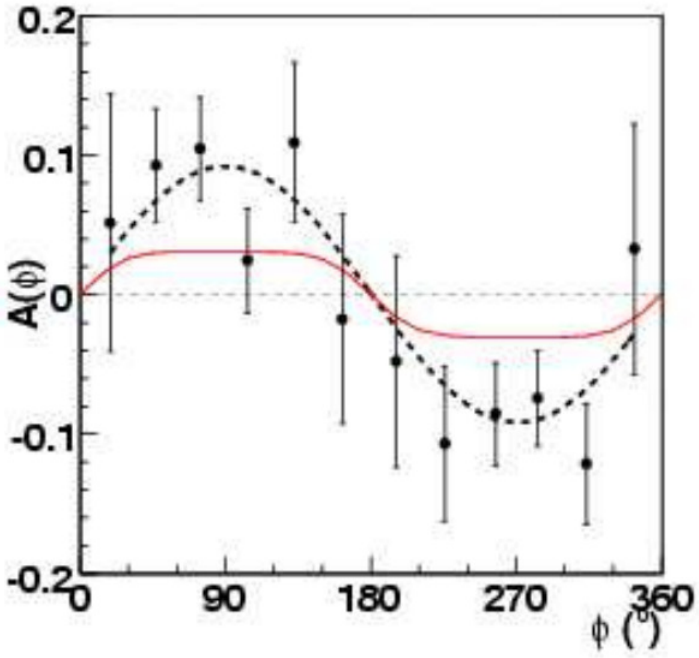

Figure 1.19: CLAS result for the π^0 photoproduction beam spin asymmetries (BSA) as a function of the angle between the lepton and the hadronic planes, ϕ [12]. The black dashed curve is a fit with $A(\phi) \approx \alpha \sin\phi$ and the red curve is a prediction by the JML model [49] based on Reggeion exchange and hadronic degrees of freedom. This figure was taken from Ref. [12]. See re-use permission (8) in Appendix C.

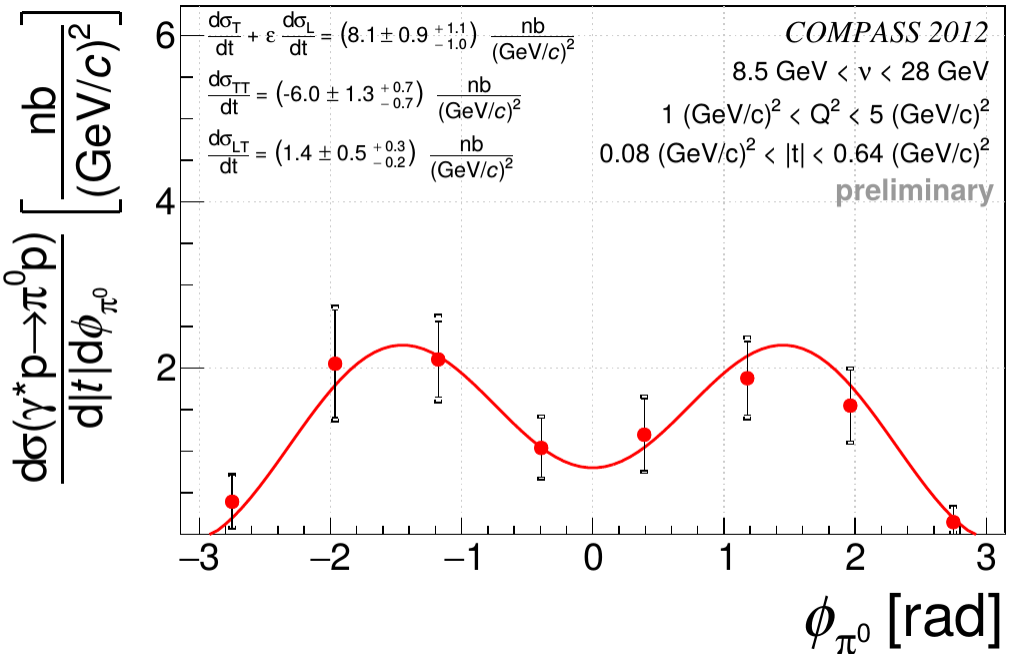

Figure 1.20: COMPASS result for the π^0 muon production cross section as a function of the angle between the lepton and the hadronic planes, ϕ. The red dots show the measured cross section for each bin in ϕ. A binned maximum likelihood fit was used to extract the amplitude of the modulations and the result is shown by the red curve. This figure was taken from Ref. [13]. See re-use permission (8) in Appendix C.

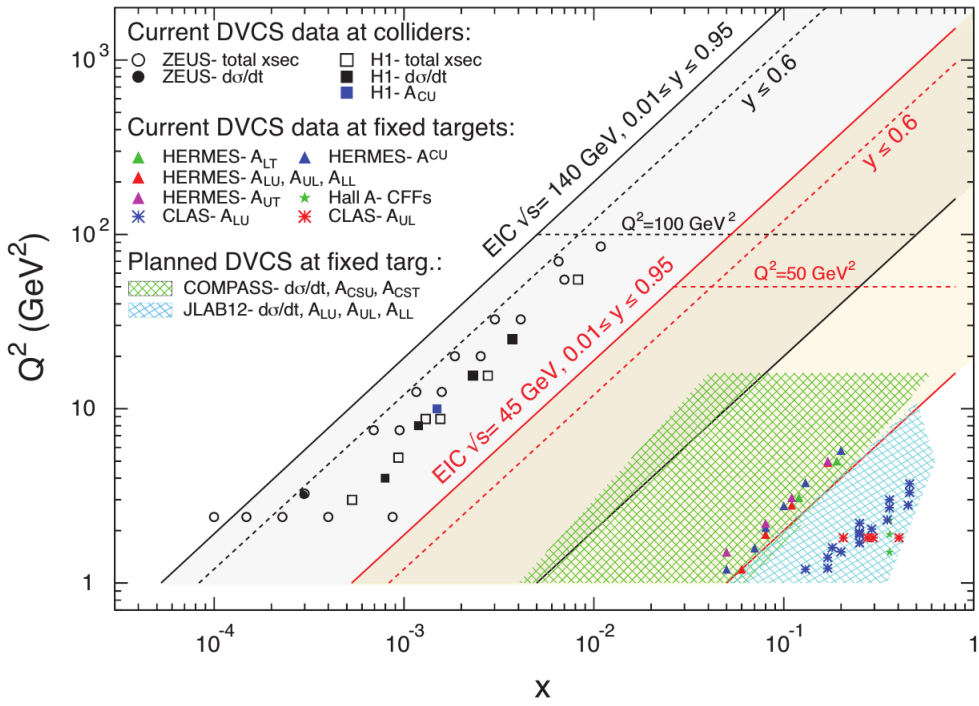

Figure 1.21: The kinematic domain, Q^2 as a function of x_B for past (H1, ZEUS, HERMES, TJNAF at 6 GeV) and future (COMPASS, TJNAF at 12 GeV) DVCS measurements. This figure was taken from Ref. [46].

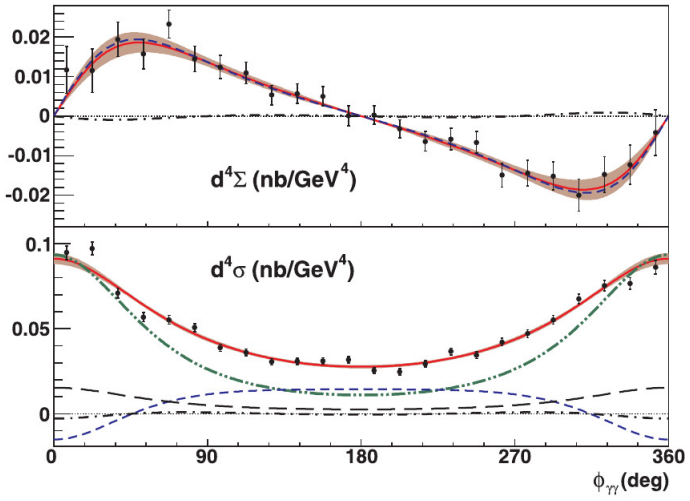

Figure 1.22: DVCS Hall A results: Helicity dependent cross section (top panel) and helicity independent cross section (bottom panel) shown as a function of the azimuthal angle ϕ. These are the first (2004) DVCS results from Hall A of JLab and they proved the feasibility of such (DVCS) experiments in Hall A kinematics. This figure was taken from Ref. [9]. See re-use permission (5) in Appendix C.

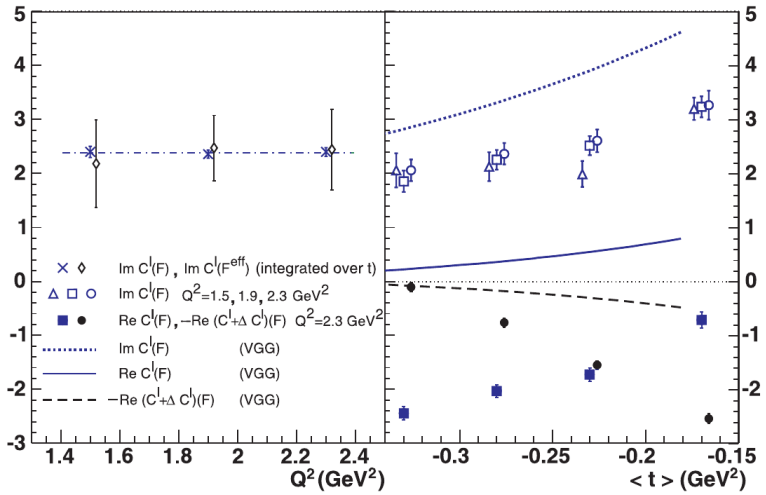

Figure 1.23: DVCS Hall A results: Compton Form Factors (CFF) extracted from the 2004 DVCS experiment in Hall A. In the limited Q^2 coverage of the 2004 experiment, the CFF's show some early signs of scaling. This figure was taken from Ref. [9]. See re-use permission (5) in Appendix C.

2 The E12-06-114 Experiment

Experiment E12-06-114 is the third generation DVCS experiment in Hall A of JLab. The first experiment was conducted in 2004 and it was a pioneer experiment. The second generation was conducted in 2010. The first experiments confirmed the feasibility of DVCS experiments in JLab (in particular Hall A) kinematics and they showed hints of the validity of the GPD formalism in parametrizing proton structure in the case of electrophoton production. The E12-06-114 experiment utilized the same apparatus as the earlier generations, with an expanded calorimeter since the second (2010) generation. However, this experiment was done with a recently upgraded electron beam energy (from 6 GeV to 12 GeV). A higher and wider energy range is necessary to further test the validity of the GPDs as the appropriate functions to parametrize proton structure in the deep inelastic region. This experiment received the highest scientific rating by the JLab Program Advisory Committee (PAC) and was one of the first experiments to take place after the 12 GeV upgrade.

In this chapter, we introduce the experimental set-up, beginning with the experiment detail, the accelerator facility and then the hall which housed the experiment.

2.1 Experiment overview

As briefly mentioned in the introduction, experiment E12-06-114 is a third generation of DVCS experiment in Hall A. The first experiment, E00-110 was a pioneer experiment that used exclusive electron scattering to measure helicity-dependent and helicity-independent cross sections for the DVCS ($ep \rightarrow ep\gamma$) process off a proton target. This experiment was conducted in Hall A of the Thomas Jefferson National Accelerator Facility (TJNAF, aka JLab). The experiment was conducted at a fixed x_B of 0.36 and a narrow Q^2 range between 1.5 to 2.3 GeV^2. Conducted with a maximum beam energy of 5.5 GeV, this meant the experiment was limited in the kinematic ranges of x_B and Q^2 it

could cover. However, even with these limitations, the experiment was successful in demonstrating the feasibility of measuring GPDs at kinematics possible at JLab. This experiment also endorsed the methodology employed to measure GPDs and motivated other similar experiments at JLab.

The most recent experiment, E12-06-114, used the same technique as E00-110 but this time with a newly upgraded facility offering higher beam energies than before and without a proton detector. Longitudinally polarized electron beams of 6.6, 8.8, and 11 GeV [4] were fired to scatter off a 15 cm liquid hydrogen target. The scattered electrons were counted using the left arm of Hall A's High Resolution Spectrometer. The produced DVCS photon was registered using a 39 cm by 48 cm Lead-Fluoride (PbF_2) electromagnetic calorimeter. The recoil proton was not detected but a missing mass reconstruction of the DVCS reaction was used to distinguish DVCS events. With the 12 GeV upgrade, the experiment had a wider Q^2 coverage ranging from 3 to 9 GeV^2. In addition, a Q^2 scan was performed at different values of x_B, i.e, 0.36, 0.48 and 0.6. The experimental set-up is shown by the cartoon in figure 2.1 and the kinematic coverage of the experiment is shown in table 2.1.

The experiment ran from the Fall of 2014 to the Fall of 2016. A total of 50 PAC days were initially approved for the experiment. This means that assuming a 100% efficiency of the accelerator facility, we were supposed to run for 50 days. However, being the first experiment after the 12 GeV upgrade, we found that the accelerator had a relatively low efficiency. This meant that we had to spend more time running than it had been planned (about 130 days instead of 50). The low efficiency also came with the misfortune of not covering all kinematic settings as planned. For example, we ended up not having time to

[4] These are nominal energies

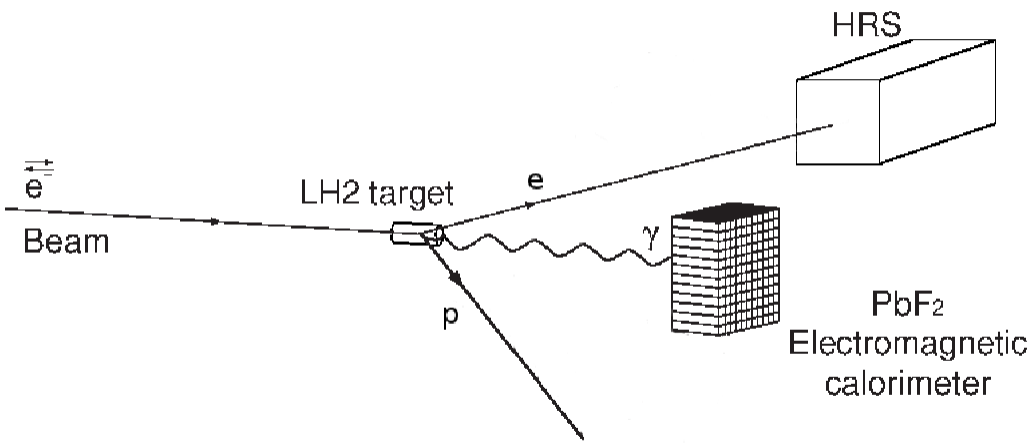

Figure 2.1: A cartoon showing the experimental set-up of E12-06-114 in Hall A of JLab.

collect data for two kinematics at x_B of 0.6. Also, in some kinematics we collected lower statistics than projected. This was even complicated by the changing beam energies (per pass) for different run schedule periods. The drifting beam energies made it impossible to go back to an old experimental kinematic setting and fill for the low statistics at a later period. Figure 2.2 shows predictions of the VGG GPD model [45] for the proton structure functions. The imaginary part of $C_0^{\mathcal{I}}$ in equation 1.35 is shown as a function of Q^2 for the different points of x_B that were taken. The Q^2 dependence of the structure function (and other structure functions in general) is known as scaling behaviour. The results from the model predict a scaling for this structure function, thus validating the GPD handbag formalism for the electroproduction of photons (DVCS) over the wide arm in Q^2 shown in the figure. Once complete analysis of the acquired E12-06-114 is complete, it will be interesting to see how much the data agrees with this conjecture by the VGG model. In the case of neutral meson (π^0) electroproduction, existing data has so far contradicted the

x_B	Name	DAQ period	Q^2 GeV^2	E_{beam} GeV	$E_{scattered}$ GeV	E_{photon} GeV	DAQ rate Hz
0.36	kin36_1	Fall 2014	3.2	7.35	1.925	5.06	120
	kin36_2	Fall 2016	3.6	8.52	2.92	5.83	220
	kin36_3	Fall 2016	4.47	10.62	3.99	6.9	635
0.48	kin48_1	Spring 2016	2.7	4.48	1.49	2.83	216
	kin48_2	Spring 2016	4.37	8.84	3.99	4.66	180
	kin48_3	Spring 2016	5.33	8.84	2.92	5.74	200
	kin48_4	Spring 2016	6.9	11.02	3.36	7.47	90
0.6	kin60_1	Fall 2016	5.54	8.52	3.92	4.57	84
	kin60_3	Fall 2016	8.4	10.62	3.9	6.75	70

Table 2.1: Experiment E12-06-114 kinematic coverage. Also shown in the table are the dates around which data acquisition was done for each kinematic.

handbag formalism. The understanding is that the data is not yet in the regime where the handbag formalism applies for pseudoscalar mesons. As an experiment which extended the kinematic arm in Q^2, E12-06-114 results will provide further tests of the handbag formalism in pseudoscalar meson production.

Experiment Goals

The principal goal of the experiment was to measure precise helicity-dependent and helicity-independent cross section of the DVCS process, which is related to the CFFs. This was performed at fixed kinematic points x_B over a large range in Q^2. The measured absolute cross sections will be useful in revealing many properties about the proton system, such as:

- Scaling tests of DVCS cross sections. Earlier DVCS experiments confirmed the scaling property but over a narrow range in Q^2(between 1.4 and 2.4 GeV^2 [16]). Experiment E12-06-114 tests the scaling property for a Q^2 range between 3 and 9 GeV^2. Passing this test will prove that the GPD formalism is appropriate to describe nucleon structure.

- To separately measure the Real and Imaginary parts of the DVCS amplitude. The angular harmonics which are sums of CFFs (and FFs) enable access to the Real and Imaginary parts of different combinations of CFFs and FFs. Therefore, a precise measurement of cross section will lead to improved knowledge of Real and Imaginary amplitudes of the DVCS and BH process.

- The 12 GeV upgrade also came with the advantage of a large kinematic coverage in Q^2, x_B and t. A wide kinematic range is necessary to map out the proton at many points and provide data that will be useful in extracting GPD parametrizations. Such measurements are likely to improve current GPD models and eventually reduce the model dependence of the GPD parametrizations.

- Measurement of $e\vec{p} \rightarrow ep\pi^0$ cross section. This tests the factorization dominance of neutral meson (in general pseudoscalar mesons) electro-production. Up to this point, existing data is not yet in the regime of factorization dominance. The extended kinematics associated with this experiment are an important search for the point beyond which factorization holds or else prove the participation of transversity GPDs at leading order for pseudoscalar mesons.

Exclusivity of the DVCS reaction

An exclusive experiment is one in which all particles in the final state are detected and DVCS is in this subset of experiments. The DVCS process is a three body final state

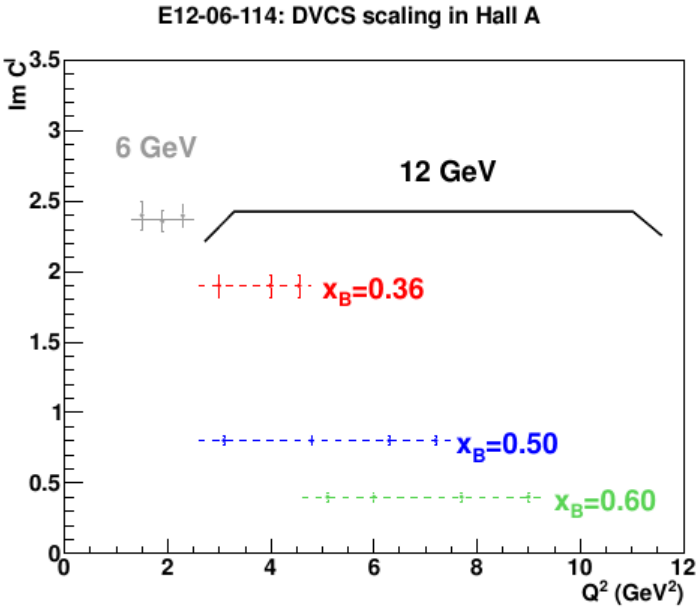

Figure 2.2: DVCS scaling in Hall A of JLab. The Q^2 domain possible with the 6 GeV beam is shown in gray and the kinematic coverage of the 12 GeV beam is shown in black. Also shown are the kinematic variable (x_B) points at which the Q^2 scan was performed. This figure was taken from [16]. See re-use permission (3) in Appendix C.

channel. The photon was detected by the DVCS calorimeter, the electron by the spectrometer, and the recoil proton was not detected. Instead, exclusivity of the DVCS process was ensured by the H(e,e'γ)X missing mass (M_X^2) technique. The missing mass technique entails using momentum conservation to reconstruct the energy (missing mass) of the undetected particle. The missing mass peak (in the missing mass distribution) is called the exclusivity peak because it is the one which completes the requirements for exclusivity in our case. There are also other competing reactions that make the DVCS not easy to identify. The main competing channels are:

- π^0 production ($ep \rightarrow e'p'\pi^0$). The π^0 decays into two photons and is easier to identify if the decay is symmetrical (see figure 2.3) and both photons are detected by

the calorimeter. In an asymmetrical π^0 decay, one of the decay photons will be more energetic than the other [4] and will look more like a DVCS photon. The missing mass can not tell the difference between this and the DVCS process. However, in the case of π^0 production this not a problem because we are indeed looking for pions.

- associated DVCS (non-resonant) [4] ($ep \rightarrow e'N\gamma\pi$). An additional pion is produced and the lower its momentum is, the closer the missing mass of this reaction gets to the DVCS one.

- associated DVCS (resonant) [4] ($ep \rightarrow e'(\Delta or N^*)\gamma$). Here, the resonance decays into a pion and a nucleon. Since the first resonance is the $\Delta(1232)$, it means the minimum missing mass squared for this process is about 1.5 GeV^2.

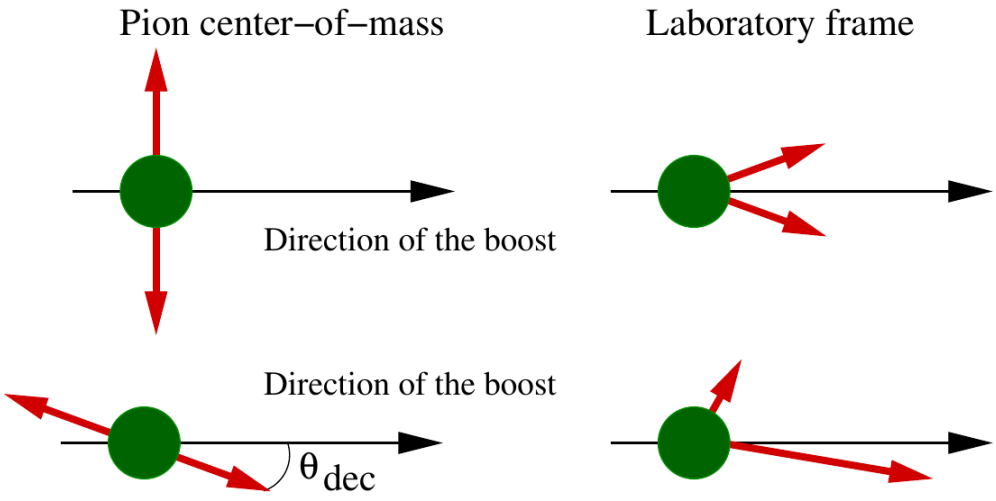

Figure 2.3: A demonstration of two different kinds of π^0 decays. When the π^0 decays with both photons emitted perpendicular to the direction of the boost in the π^0 center of mass, the decay is symmetric (top panel) otherwise (bottom panel) it is asymmetric.

The M_X^2 technique is based on using the information from the spectrometer and the calorimeter to compute the missing mass squared of the recoil proton as follows:

$$M^2_{ep->e'\gamma X} = (k + p - k' - q)^2, \tag{2.1}$$

where *k, p, k'* and *q* are the 4-momentum vectors of the incident electron, the target proton, the scattered electron and the real photon, respectively. In the case of π^0 production, *q* is the 4-momentum vector of the pion reconstructed from the two photons detected by the calorimeter. An example of the missing mass spectrum is shown in figure 2.4. To ensure exclusivity, a cut is then applied in the missing mass as shown in the figure. Since the proton does not break up in the process, M_X^2 should ideally be the mass of the proton (0.88 GeV^2). In reality, M_X^2 is on average 0.88 GeV^2 and is dominated by the energy resolution of the calorimeter.

2.2 The Continuous Electron Beam Accelerator Facility(CEBAF)

The CEBAF at the TJNAF produces polarized electron beams and recently (in 2014) got an upgrade from a 6 GeV maximum beam energy to 12 GeV, after circulating the beam five times. The accelerator has two superconducting linacs, North and South, connected by arcs with steering magnets to guide the electron beam from one linac to the other. CEBAF is designed to supply a continuous instead of a pulsed beam. This is made possible by the use of superconducting radio frequency (SRF) technology which uses liquid helium to cool Niobium cavities to about 2 Kelvin (niobium has a 9 K superconduction transition point) [51]. At this temperature, the cavities have a relatively low electrical resistance (power load), leading to a very efficient electron acceleration.

To extract electrons, a gallium arsenide doped with phosphorus (GaAsP) cathode source is secured in a vacuum chamber and hit with a laser [52] in a process called optical

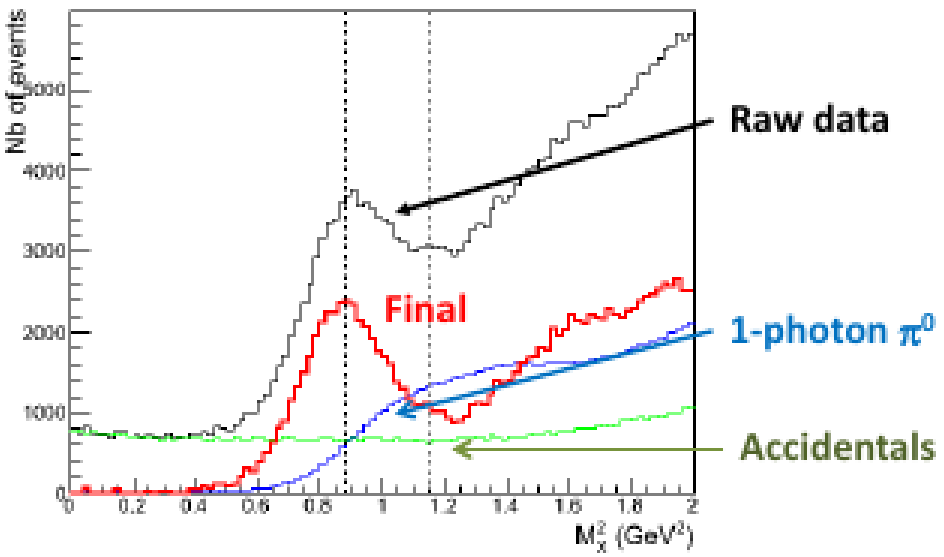

Figure 2.4: $ep \rightarrow epX$ missing mass squared. The peak (at 0.88 GeV^2) is the recoil proton mass squared and its width is dominated by the energy resolution of the calorimeter. The black spectrum is the missing mass plot of all electron-photon coincidence events. The green spectrum represents accidental electron-photon coincidences (background) and the blue plot represents a contamination by π^0 events which have only one photon detected. Subtracting the accidentals and the π^0 contamination results in the red plot. This figure was taken from [50].

pumping. This propels valence electrons of the GaAsP to fill the conduction band resulting in photoemission. Beam polarization is achieved by polarizing the laser (photon beam) used for optical pumping. The choice of the polarization of the laser dictates the polarization of the electron beam also. To polarize the laser, it is passed through a voltage controlled wave plate, which polarizes the photons circularly [52]. Changing the sign of the voltage applied to the wave plate switches the direction of polarization(±). A maximum of 88% beam polarization has been achieved [56].

The extracted electrons are swept from the cathode surface using a potential difference and are accelerated up to 45 MeV before being injected into the North linac as demonstrated in figure 2.5. After the 12 GeV upgrade, the electron beam can be accelerated to 1.1 GeV maximum energy in one linac. At the end of the first linac, the beam is steered into the South linac where it is again accelerated. This makes one pass. The beam can now be extracted to experimental halls or can be recirculated for a second pass, up to a maximum of 5 passes.

In addition to the original experimental halls A, B and C, a new experimental hall (hall D) has been constructed with the 12 GeV upgrade. This hall (hall D) is located in such a way that it receives beam that has been accelerated through one more linac than the beam to the other halls. As a result of the 12 GeV upgrade, halls A, B, and C will receive a maximum of 11 GeV while hall D has half a pass more beam circulation and will receive the maximum 12 GeV. All the halls can receive beams of different energies and currents simultaneously. This is made possible by radio frequency separators and magnets that split and steer the beam into the different halls. The maximum beam current the CEBAF accelerator can provide is 180 μA [53].

Why is CEBAF the ideal facility for this experiment?

There are many high energy accelerators in the world, all of which have made significant contributions to the field and are still in operation. However, CEBAF outshines them as the ideal facility for experiment E12-06-114 because of the following reasons:

- CEBAF has a high duty factor. The duty factor is defined as the ratio of the duration of a pulse (pulse width) to the time between consecutive pulses. In other words, the duty factor tells how much continuous (high duty factor) or pulsed (low duty factor) an electron beam is. To accelerate high energy electrons, enormous currents are needed to generate the necessary electric fields. Since most accelerators do not have

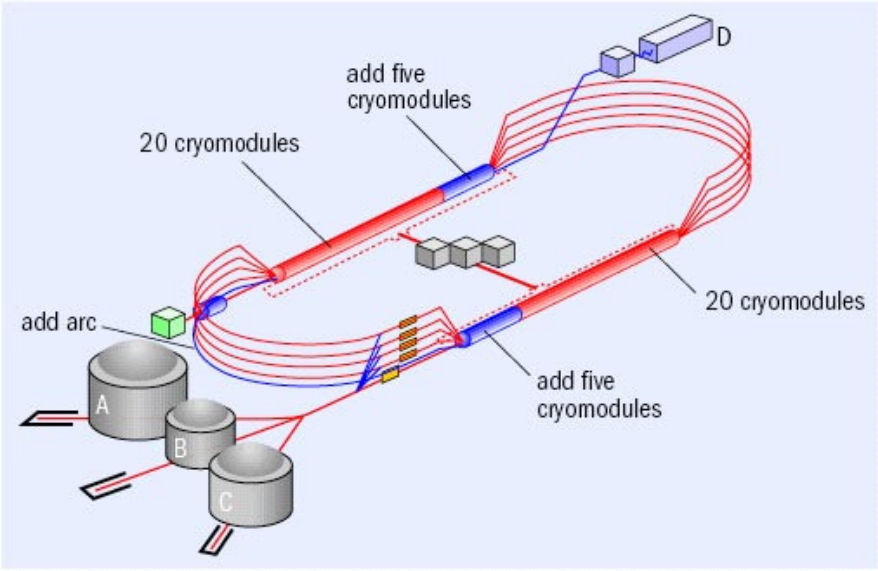

Figure 2.5: CEBAF with the 12 GeV upgrade. The injector is represented by the green box close to hall A and it is viewed by the North linac. The beam is injected into the North linac and passed to the South linac for a complete pass. The two linacs initially had 20 cyromodules each. With the 12 GeV upgrade, 5 cryomodules have been added to each linac and a new hall D has been installed in addition to the already existing halls A,B and C.

the technology to support large currents for an extended period of time, the common way to circumvent this is to operate the machine for short time intervals to allow for cooling between the pulses and inherently having a low duty factor. With the superconducting radio frequency cavity technology, CEBAF beats this obstacle and is able to supply a high current over an extended time period. A high duty factor (close to unity) is necessary for a coincidence experiment like E12-06-114 where we detect the scattered electron in coincidence with a photon.

A high duty factor accelerator delivers its electrons evenly spread over time so that few are at the target area at the same time. This helps to suppress, identify and separate the number of accidental coincidences. This is in contrast with low duty factor machines where a large pulse (many incident electrons) is sent onto the target within a narrow time interval. This will consequently result in a huge number of interactions at or around the same time and many detectors may not have the necessary time resolution to distinguish accidentals from true coincidences. An illustration of the effect of the duty factor on the suppression of accidental events is demonstrated in figure 2.6.

- CEBAF has a very high electron polarization of about 88% maximum.
- CEBAF has a high current supply and this connects to a high luminosity of $\sim 10^{37} cm^{-2}\ \mathrm{s}^{-1}$ in experimental Hall A. With the 12 GeV upgrade, the facility also has a high enough beam energy to meet the kinematic coverage projected for the experiment.

2.3 Experimental Hall A

The layout of the hall is shown in figure. 2.7 and it consists of several components dedicated to the transport, control and measurement of the properties of the electron beam before and after scattering off a target. The hall also has dedicated detectors to measure the products of experimental reactions.

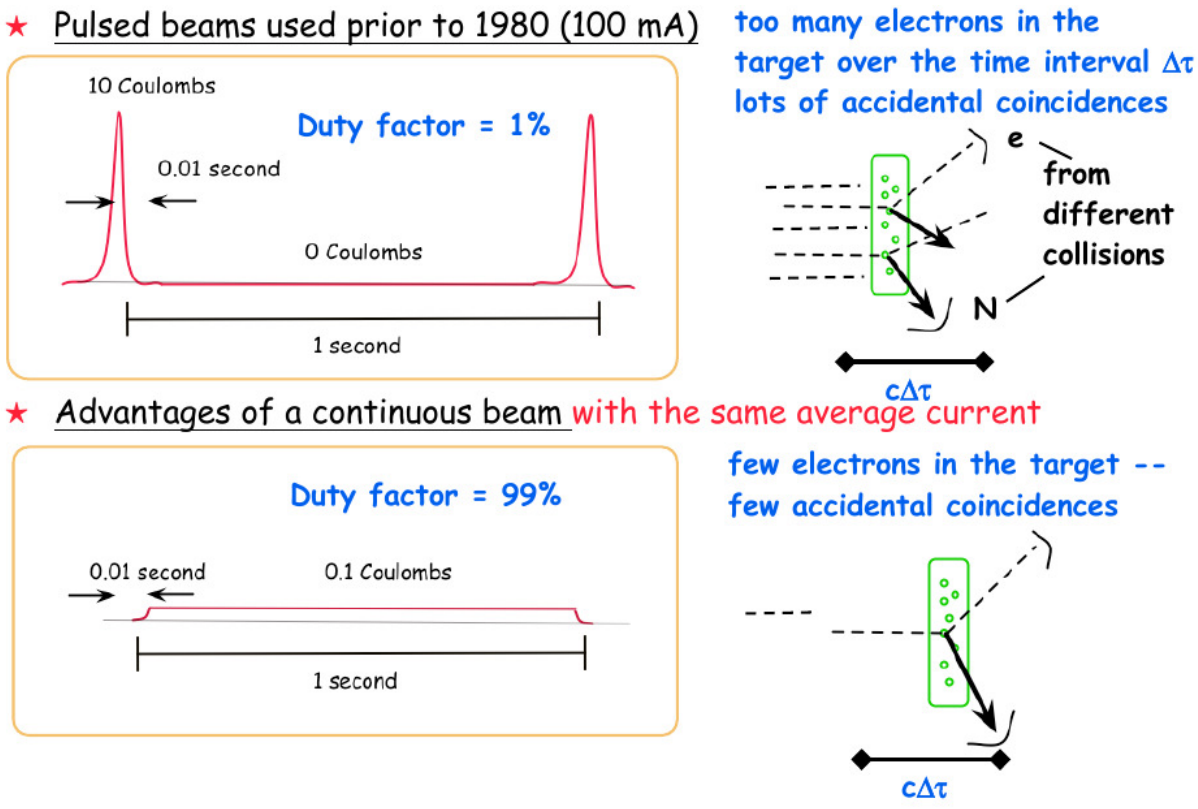

Figure 2.6: An illustration (by F. Gross [54]) of the duty factor for an accelerator and its impact on the level of contamination by from accidental coincidences. This figure was taken from Ref. [54]. See re-use permission (1) in Appendix C.

2.3.1 The beamline

The beamline instrumentation has equipment dedicated to the transportation of the electron beam before and after the target whilst measuring the applicable properties of the beam at the same time. Special attention is paid to the control and measurement of the beam energy, current, position, direction, size and polarization. In each of these and other cases, two or more independent techniques or devices are employed to provide confidence in absolute measurements and also for redundancy, just in case one device fails.

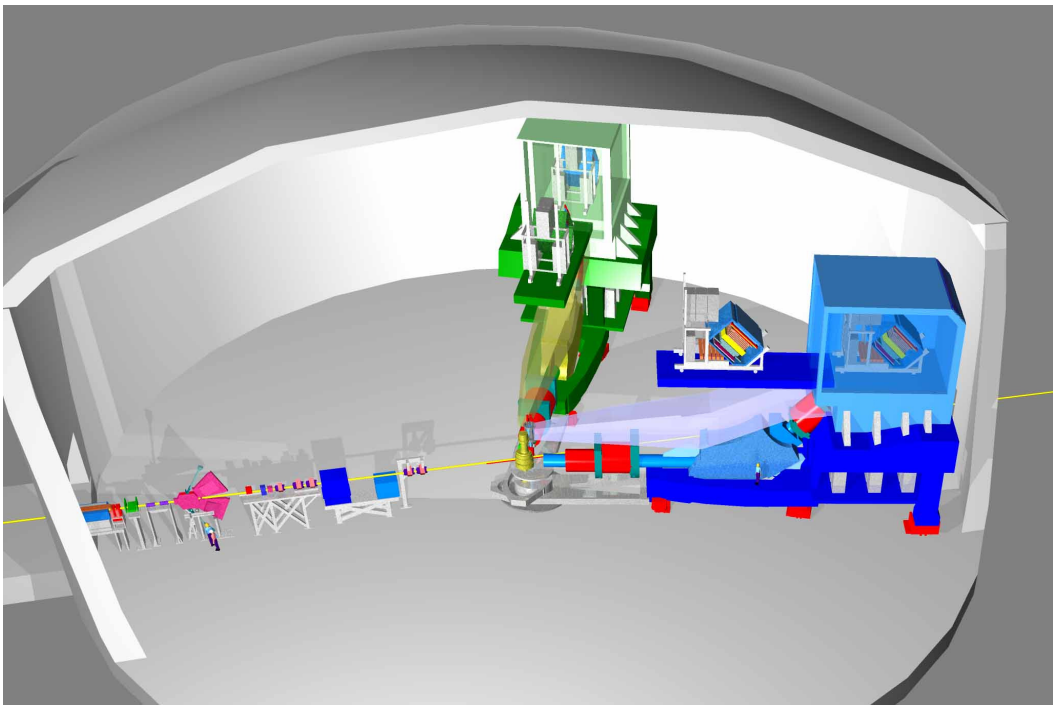

Figure 2.7: A schematic showing the layout inside JLab's Hall A. The green and yellow structure on the left represents the left arm of the High Resolution Spectrometer (HRS). The blue and cyan structure on the right represents the right arm (RHRS). The yellow structure where the two arms seem to meet is the target chamber. The yellow line that runs straight represents the beamline running from the beam entrance to the hall (bottom left corner). Between the beam entrance and the target chamber, there is a series of beamline instruments (BPMs,BCMs, polarimeters, etc.) used to transport and measure properties of the beam as discussed in the text.

In the following subsections, we will briefly talk about the beamline components that were applicable to experiment E12-06-114.

2.3.1.1 Beam polarimetry

To measure the polarization of the beam, the hall has two independent polarimeters: the Compton and the Møller polarimeters. The principles of operation for both polarimeters are based on QED processes, hence the asymmetries they detect (in order to measure the polarization) can be computed from first principles.

The Compton was however not available during part of the data taking periods because of poor laser alignment issues. During that time, the Møller polarimeter was the only technique available for polarimetry. It is for this reason that I will discuss the Møller polarimetry only in this section.

Møller polarimeter: The Møller polarimeter is based on the principle of Møller scattering of a polarized beam of electrons off polarized atomic electrons in a ferromagnetic foil. The foil acts as a target of polarized atomic electrons. Two different methods can be used to magnetize the ferromagnetic target. One technique is called the ”low field” method and uses a weak magnetic field of about 20 mT [55] to magnetize a ferromagnetic target tilted at a small angle to the beam. The foil can also be tilted at different angles in the horizontal plane making the target polarization to have both longitudinal and transverse components. This method has a polarization precision of $\sim$ 1.7% [55]. The other method is called the ”high field” technique and here the target is placed perpendicular to the beam and polarized perpendicular to its plane using a strong magnetic field of about 3 T [55]. The high field method has a better precision of $\sim$ 0.9%. The low field method was used for the data taken in the Fall of 2014 only and this is because by then the equipment had not been optimized for the 11 GeV upgrade [55]. The rest of the measurements were done using the high field technique.

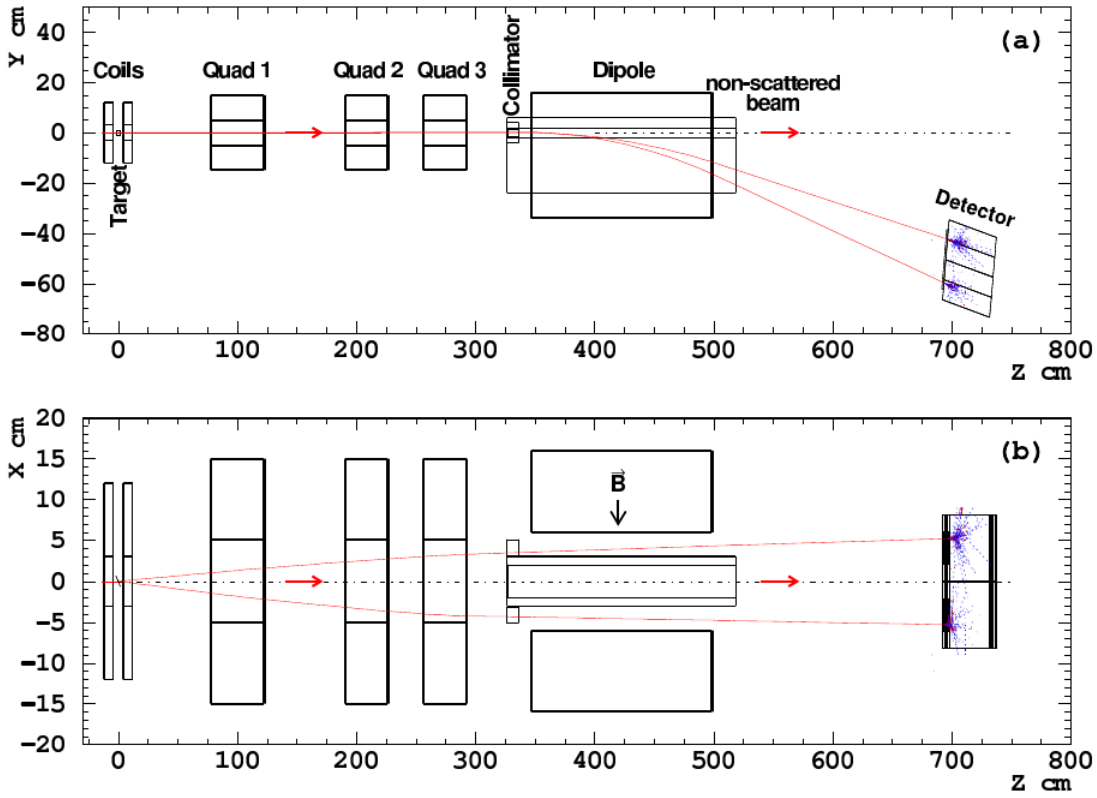

Figure 2.8: A schematic of the Møller polarimeter. (a) shows the side view and (b) shows the top view.

The Møller scattering cross section depends on both the beam and target polarization. Møller scattered electrons are detected using a dedicated magnetic spectrometer (shown in figure 2.8) that has a sequence of three quadrupole magnets and a dipole. The detector is equipped with lead-glass calorimeter modules that are split in to two arms to detect a coincidence of two scattered electrons. The beam polarization is determined from the helicity-driven asymmetry of the coincidence counting rate. A summary of the Møller measurements and polarization results is shown in table 2.2. An average 86% beam polarization was measured.

One disadvantage about the Møller is that it is invasive. This is because the scattering of an electron off a thick (greater than 1μm) heavy atom (iron) target is smeared and results in a change of the effective polarization of the electron. Therefore, the measurement can not be conducted in parallel with normal production running. Polarization measurements were usually arranged at regular intervals, especially after we sanctioned a change in the beam energy.

Date mm-dd-yyyy	E_{beam} GeV	Polarization %	Stat. Error %	Sys. Error %	Technique
12-08-2014	7.375	+84.58	±0.25	±2.2	low field
02-17-2016	4.477	+86.68	±0.10	±1.0	high field
02-29-2016	8.837	+86.95	±0.20	±1.0	high field
03-31-2016	10.985	+86.79	±0.14	±1.0	high field
04-19-2016	10.982	+88.19	±0.13	±1.0	high field
10-31-2016	8.495	+86.75	±0.10	±1.0	high field
11-28-2016	10.590	+85.39	±0.11	±1.0	high field
12-07-2016	10.591	+84.18	±0.10	±1.0	high field
12-19-2016	8.498	+86.20	±0.10	±1.0	high field

Table 2.2: A summary of the Møller measurements for experiment E12-06-114 [56].

2.3.1.2 Beam position monitors

The hall is equipped with Beam Position Monitors (BPMs) to determine the position and direction of the beam at the target. The are two BPMs upstream of the target, one 7.524 m and the other 1.286 m from the target. Each BPM has a set of four antennas

set-up around the beam so that the beam induces a current in each of them. The relative position of the beam with respect to the antennas is found by comparing the intensity in each antenna. The absolute position is found by calibrating the BPMs against wire scanners called superharps located next to each BPM. Using the BPMs, the beam position and angle can be determined to within 140 μm and 30 μrad, respectively [52].

Also located upstream is a raster system which is used to spread the beam out. The beam can be rastered by several millimetres, usually 4 mm $\times$ 4 mm for cryogenic targets, both in the x and y directions perpendicular to the beam direction.

2.3.1.3 Beam current monitors

The hall is also equipped with Beam Current Monitors (BCMs) to determine the current or charge sent onto the target. The BCMs are located upstream the target, between the polarimeters and they are designed to provide a stable, low noise and non-destructive beam current measurement. BCMs consist of two RF cavities and an Unser monitor. The Unser monitor is a Parametric Current Transformer which provides an absolute reference [52]. It is calibrated by passing a known current through a wire inside the beam pipe. However, the pedestal of the output signal of the Unser monitor drifts significantly in minutes and thus it can only be useful for calibration purposes, not for monitoring the beam current over extended periods.

To determine the current, the two resonant RF cavities on either side of the Unser Monitor are tuned to the frequency of the beam. In this way, the resulting voltage output from the cavities is proportional to the beam current. The constant of proportionality and the relevant offset is determined from a dedicated BCM calibration done against the Unser.

2.3.1.4 Beam energy measurement

The Arc method was used to measure the beam energy. The Arc method uses the deflection of the beam in the magnetic field of the arc between the accelerator and the hall

to measure the absolute energy. During this measurement, the beam is tuned in dispersive mode and eight dipoles are used to steer it in the arc. The integral of the magnetic field of the eight dipoles employed to bend the beam is measured using Nuclear Magnetic Resonance technique. The bending angle is also measured using the BPMs. The momentum (p) of the beam is then related to the magnetic field integral if the eight dipoles and the bend angle by (to leading order):

$$p = k\frac{\int \vec{B} \cdot \vec{dl}}{\theta}, \tag{2.2}$$

where k = 0.299792 GeV rad. T^{-1} $m^{-1}c^{-1}$ [57]. The precision in the energy measurement is $\frac{\delta E}{E} = 10^{-4}$ [57]. Results of the beam energy measurements done by D. Higinbotham [57] are summarized in table 2.3.

Date mm-dd-yyyy	No. of passes	$E_{measured}$ in Hall A GeV	$E_{calculated}$ from accelerator settings GeV
10-17-2016	1	2.222	2.218
10-26-2016	3	6.427	6.407
12-20-2016	4	8.520	8.497
12-01-2016	5	10.587	10.589

Table 2.3: A summary of the Hall A beam energy measurements for experiment E12-06-114 [57].

2.3.2 The target system

There is a scattering chamber which houses the various targets in use and this chamber is kept under vacuum during production. The chamber is made of a 1cm thick

cylindrical shell of aluminium. A 500 μm thick exit window made out of kapton is installed (in place aluminium) towards the entrance of the spectrometers. The window provides a path of a smaller radiation length (compared to aluminium) to minimize energy lost by the scattered particles as they exit the target chamber. Inside the scattering chamber, there is a target ladder on which the cryogenic and other (solid) targets are mounted. The target ladder has target control and motion sub-systems installed inside the chamber.

The cryogenic target

Together with its cooling, gas handling, pressure and temperature monitoring sub-systems, the cryogenic target system is mounted inside the scattering chamber. The cryogenic target had one loop filled with liquid hydrogen (LH_2). The target cell is a 15 cm long cylindrical with a diameter of 63.5 mm. The side-walls of the aluminium container are 178 μm while entrance and exit windows are 71 μm and 102 μm thick, respectively. The upstream window consists of a ring holder that has a 19 mm inner radius designed to be large enough for the beam to pass through. Under normal operating conditions, the LH_2 target density is approximately 0.0723g/cm^3 at an average pressure of approximately 0.17 MPa and temperature of 19 Kelvin. The target coolant is helium supplied by the End Station Refrigeration (ESR). To minimize warming the target and increasing its density fluctuations due to the small size of the beam spot ($\sim$ 100 μm) being too focused, the beam is rastered on the target. Beam rastering is a requirement for all currents above 5 μA on the target. The cryogenic target can take up to 130 μA of rastered beam current, equivalent to 700 W of power deposited.

Besides the cryogenic target, there are also solid targets:

- **Carbon**: a 1mm thick sheet of carbon used for optics studies.

- **BeO**: is used to locate the beam spot at the target using a camera installed in the scattering chamber. It is very useful when getting beam for the first time in a long while.

- **Optics**: a set of 1mm thick carbon sheets used for optics calibration of spectrometer. This target had 5 carbon sheets in 2014 and it was modified to 7 sheets in 2016.

- **Dummy target**: Aluminium foils used to study target wall effects. The dummy target cell is designed exactly as that of the cryogenic target in length and cell thickness. The only difference is that it is not filled with anything inside.

- **Raster target**: a 10 cm long cylindrical hollow tube made of aluminium walls. The raster target is used for beam centering, especially to check if the beam is not coming at angle relative to the x-z place. Well centered beam coming at no angle will pass through the tube without scrapping the walls of the target.

- **Empty**: no target but a good position to place the target while beam is still being driven into the hall.

2.3.3 The High Resolution Spectrometers (HRS)

The equipment of central importance in Hall A are two identical High Resolution Spectrometers (HRS) used to detect scattered particles, for example, electrons. The two spectrometers are abbreviated LHRS and RHRS for the left and right, respectively. Each spectrometer is made up of a detector package following three superconducting quadrupole magnets and one dipole magnet. The magnet configuration is shown in figure 2.9 and is known as the QQDQ configuration [52]. The quadrupoles are used to focus scattered charged particles as they are transported to the detectors in the hut. The dipole uses the bending of a charged particle in a magnetic field to determine its momentum. The spectrometers have a maximum central momentum 4.3 GeV. In the

momentum range of 0.8 to 4.0 GeV, both spectrometers have a nominal precision of $\frac{\delta P}{P} \approx 2 \cdot 10^{-4}$ and angular (horizontal) resolution better than 2 milliradians. The transverse position resolution is approximately 1 mm, for both spectrometers. Only the LHRS was used for experiment E12-06-114 and its detector package will be discussed here.

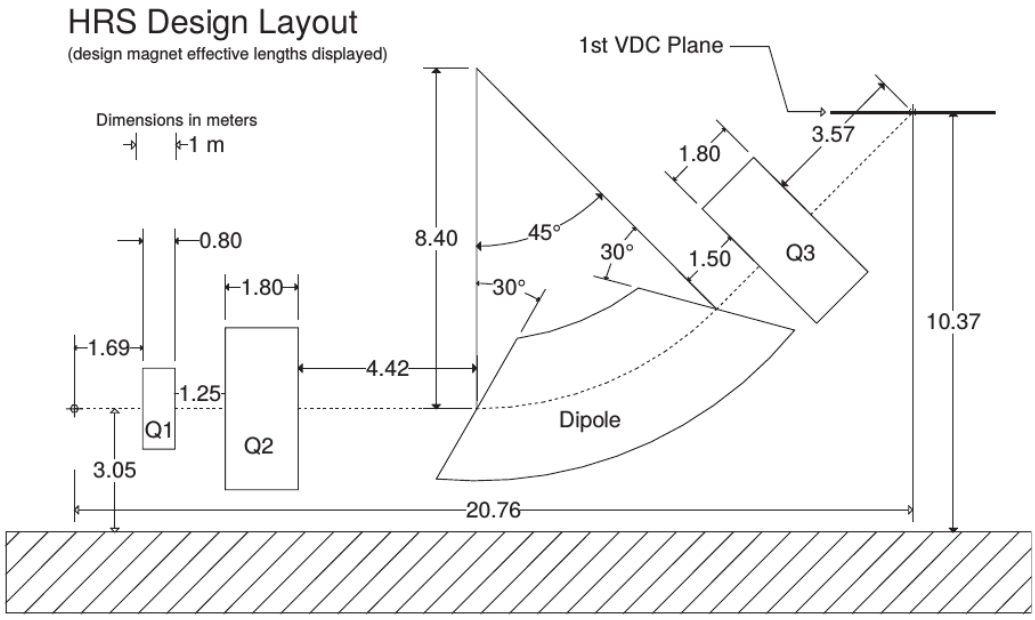

Figure 2.9: Cross section view of the HRS showing the magnet set-up ($Q_1Q_2DQ_1$ arrangement) for each spectrometer. This figure was taken from Ref. [52]. See re-use permission (10) in Appendix C.

The Q_1 Magnet Status

The core components of the spectrometer are its superconducting magnets because they are responsible for transporting particles from the target area and focusing them in the focal plane where there is the detector stack. There are four magnets: three

quadrupoles and a dipole in a Q_1, Q_2, D and Q_3 configuration. All these magnets were superconducting (before Fall 2016) and cooled using helium from the ESR.

Of these magnets, Q_1 was malfunctioning and its power supply could not support currents to reach a central momentum setting beyond 3.2 GeV, meaning the magnet could not reach its full operating capability. Since the momentum setting of the spectrometer depends on all the magnets, this limitation in Q_1 compromised the momentum acceptance of the whole spectrometer from the original 4.3 GeV to 3.2 GeV for the maximum central momentum. In the Fall of 2014, this was not a problem because the kinematic point we did was below the 3.2 GeV limit, see table 2.1 (the momentum setting of the spectrometer is given by the column showing the scattered electron energy). However, in the Spring of 2016, some of our kinematics required a momentum setting beyond the Q_1 limitation. To go around this issue, Q_1 was set at a lower current than required to support the necessary magnetic field for a momentum setting above 3.2 GeV. Setting a lower current is called detuning the magnet and it compromises the magnetic field and hence the bending of particles in the field compared to the other properly functioning magnets. Moreover, for each detune setting, a new calibration is required for the optics transportation matrix of the spectrometer.

In the Fall of 2016, the superconducting Q_1 was replaced by a water cooled Short Orbit Spectrometer (SOS) quadrupole which had formerly been used in Hall C. However, studies by E. Christy [58] showed that the quadrupole was saturated for all our kinematic settings in Fall 2016. This is demonstrated in figure 2.10 where the set momentum is plotted against the relative field per unit momentum. In the non-saturated region, the ratio of the relative field is constant with the set momentum. However, beyond 2.75 GeV, the ratio drops. Unfortunately, all of our kinematics in Fall 2014 were above 2.75 GeV.

The LHRS Detector Package

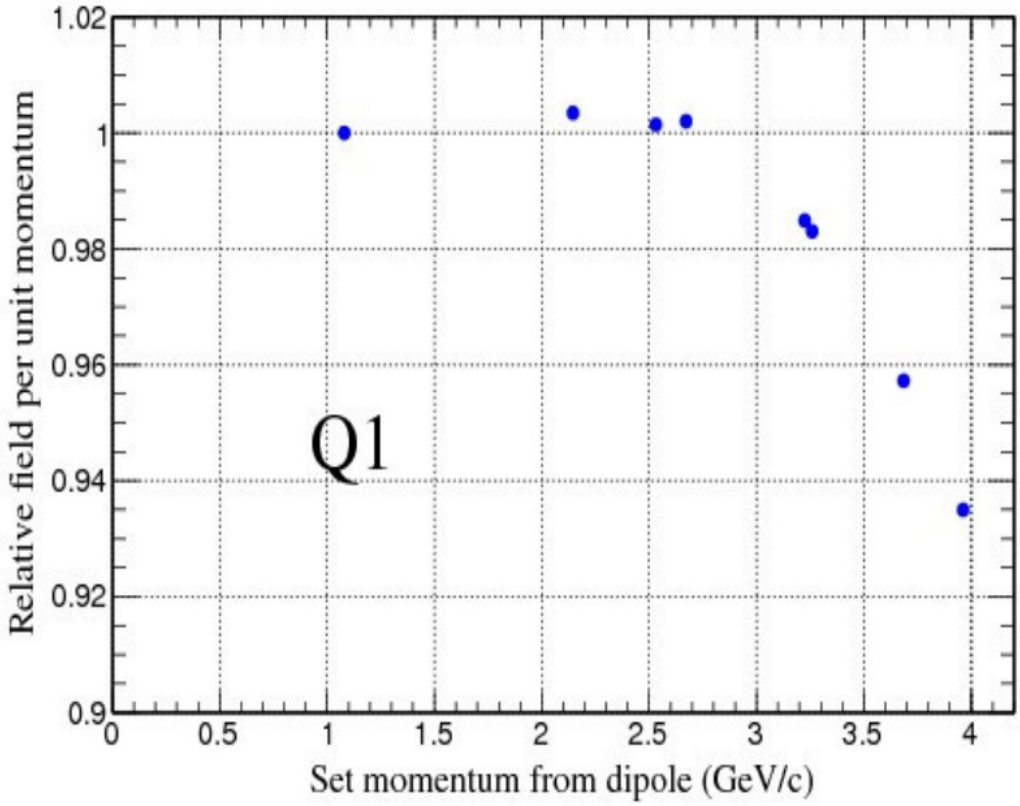

Figure 2.10: Saturation of the SOS Q_1 used for the Fall 2016 kinematics [58]. Saturation started beyond 2.75 GeV where the ratio of the relative field per unit momentum drops below one. In a non-saturated field, the ratio should stay constant.

A cartoon of the detector package is shown in figure 2.11, for the left arm. There is a similar set-up for the right arm, with slight differences in the design of the component detectors. The detector stack is discussed below:

Vertical Drift Chambers: Each detector package is equipped with a pair of vertical drift chambers (VDC), a detector used to provide charged particle tracking by measuring the position and angle of the trajectory. Each VDC chamber has two wire planes (called U

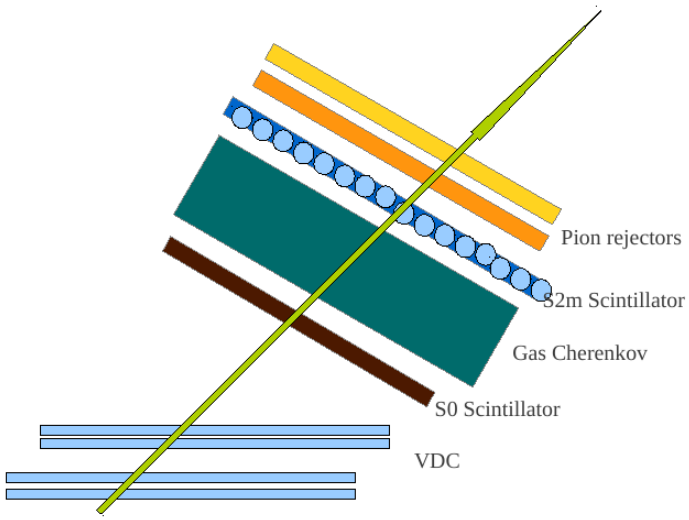

Figure 2.11: Cross section view of the HRS detector package. The arrow shows the nominal particle trajectory through the detector stack.

(lower) and V (upper)) separated by 335 mm. Each plane has a total of 368 wires, spaced 4.28 mm apart [52, 59]. The spectrometer momentum resolution depends directly on how well the position and the angle of the particle can be measured. The VDCs have a position resolution $\sigma_{x(y)} \approx 100\mu$m and angular resolution $\sigma_{\theta(\phi)} \approx 0.5$ milliradians [52, 59].

S2m scintillator: S2m is an array of 16 overlapping scintillator paddles each of 5 mm thickness. The scintillator material is BICRON plastic [60]. Each paddle has its scintillation magnified and read out by two PMTS in a left and right configuration. In coincidence with the gas Cherenkov (to be discussed below), the S2m was used to form the trigger signal to start data acquisition (DAQ) for the DVCS data. This detector was also used in coincidence with the S0 to study the efficiency of the gas Cherenkov.

Gas Cherenkov: This is a 150 cm long box filled with carbon-dioxide at atmospheric pressure and is used for particle identification. The gas Cherenkov detector is mounted between the S0 and the S2m and it provides particle identification by producing Cherenkov light [52]. The Cherenkov allows electron identification with an efficiency above 99% and has a pion suppression threshold of 4.8 GeV [52]. It has ten spherical mirrors to focus Cherenkov light. Each of the mirrors is viewed by a PMT. The final signal from the Cherenkov is given by the sum of the ten PMTs. The threshold to accept a Cherenkov signal was set at 15 mV and this was too low to suppress noise. A higher threshold was used to clean the signal during analysis. During the experiment, the Cherenkov formed the trigger in coincidence with the S2m as mentioned above.

Pion rejectors: Particle identification is also provided by a set of two electromagnetic calorimeters (shower detectors). The pion rejectors are a set of two layers each of 34 Lead (Pb) glass blocks. These are mounted after the S2m and are made of lead glass blocks to induce showers of pair production and bremsstrahlung radiation for a total collection of electron energy, while discriminating pions. Together with the gas Cherenkov detectors, the showers provide, on average, above 98% and a suppression factor of $2 \cdot 10^5$ for a pion of momentum above 2 GeV [52].

S0 scintillator: The S0 is one scintillator paddle made of BICRON plastic and it is mounted just before the gas Cherenkov. This detector was used in coincidence with the S2m to form a trigger during elastic calibration of the DVCS electromagnetic calorimeter (see chapter 3). Since the spectrometer was detecting elastic protons during the calibration, only the scintillators were ideal for the detection. Being massive, the proton can not surpass the speed of light in the carbon-dioxide medium and hence the Cherenkov was not useful. Also, protons are minimum ionizing and deposit less energy (a small signal) in the pion rejectors. The S0 was also used in coincidence with S2m (gas Cherenkov) to form a trigger to study the efficiency of the gas Cherenkov (S2m).

2.3.4 The Electromagnetic calorimeter

The DVCS electromagnetic calorimeter is not part of the hall A standard equipment but part of the DVCS set-up to detect the real photons in the final state of the DVCS reaction. It is made of 13×16 lead-fluoride (PbF_2) blocks each measuring $3 \times\ 3 \times\ 18.6$ cm^3. The front face of the calorimeter with the blocks stacked is shown in figure 2.12. The calorimeter uses the electromagnetic shower principle to degrade the initial photon into secondary positron-electron pair showers. The secondaries then produce Cherenkov light which is collected by photo-multiplier tubes. Each PbF_2 block is viewed by one PMT. Properties of PbF_2 include:

- A large density (7.7 g/cm^3) making the detector very compact, hence a short radiation length (0.95 cm).
- Moliére radius of 2.22 cm providing approximately total energy absorption within 9 calorimeter blocks [4].
- Very fast rise time, total pulse width < 20 ns (se figure 2.14).
- Reasonable secondary photon yield, Monte-Carlo simulations estimate 1000 Cherenkov photons per 1 GeV [4] and hence sufficient energy resolution, $\frac{\sigma_E}{E} \approx \frac{5.3}{\sqrt{(E(GeV)}}$ [61]

The DVCS calorimeter is a central part of this thesis and a more detailed attention is paid to it in chapter 3.

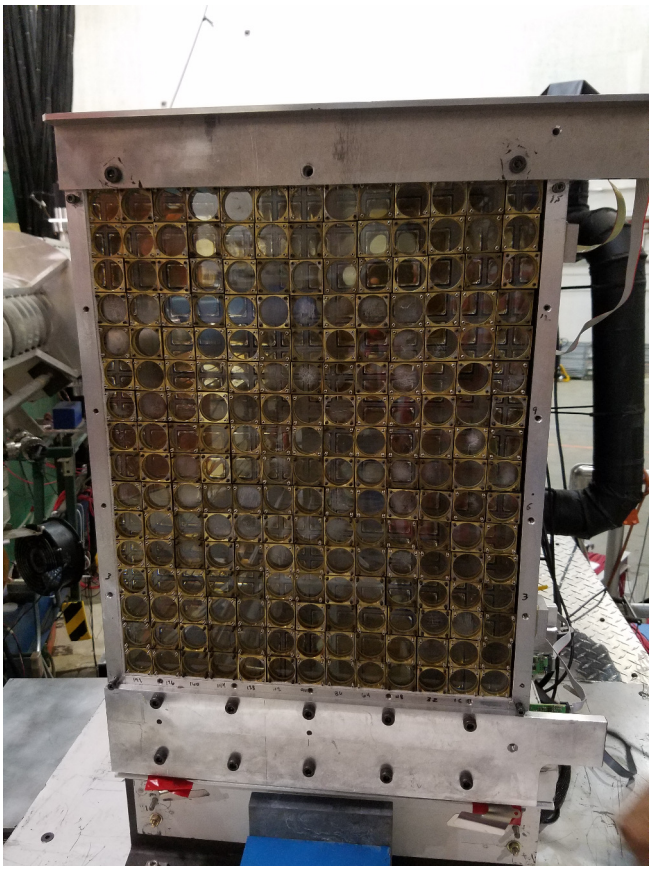

Figure 2.12: The front face of the DVCS calorimeter showing the 208 PbF_2 blocks already stacked.

2.4 Data Acquisition

2.4.1 Standard Hall A Data Acquisition

The data acquisition process used the Cebaf Online Data Acquisition (CODA) system developed by the Jefferson Lab Data Acquisition Group [52]. The system consists of several data processing crates, each with a number of modules, all coordinated by CODA. Examples of hardware coordinated by CODA include VME digitization crates, front-end Fastbus crates, ethernet networks and a number of Unix computers. An example

of how a CODA configuration works is shown in figure 2.13. Once the electronics modules have processed and recorded the signal, it is sent to the VME crates where there are CPUs running a CODA program called Read Out Controller (ROC) to read data out the VME crates [60]. An Event Builder (EB) collects data from all the applicable ROCs and the Event Recorder (ER) handles recording onto the disks. CODA supports all these and allows users to set experimental configurations such as choosing detectors that will form a trigger or triggers (in the case of multiple triggers) and the pre-scale factors for each trigger.

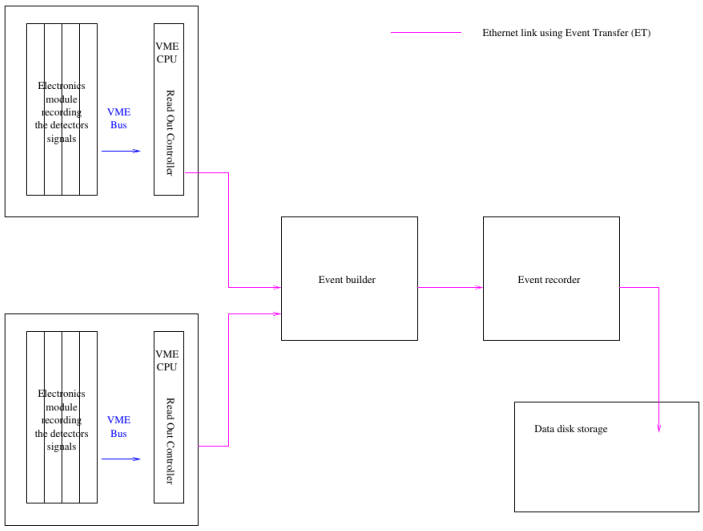

Figure 2.13: Schematic of a CODA configuration [60].

The DVCS experiment used the coincidence of a scattered electron and a photon to trigger data acquisition. The scattered electrons were measured using the LHRS which used a coincidence of the S2m and the gas Cherenkov sum to form an electron trigger.

2.4.2 Dedicated DVCS DAQ

2.4.2.1 The Analog Ring Sampler

Hall A has a high luminosity (10^{37} s^{-1} cm^{-2}) and some kinematic settings which will require the calorimeter to be at small angles and close to the target resulting in very high event rates (see table 2.1). Such high rates are associated with large pile-up events (like the ones shown in figure 2.14) which would make the ordinary ADCs not reliable in terms of time and energy resolution. For better rejection of pile-up events and better time and energy resolution, an Analog Ring Sampler chip was designed. The ARS is a system of an array of 128 capacitor cells which continuously sample the signal at 1GHz [4]. Once sampling is completed, the signal is stored in capacitors, digitized and ready to be sent as a valid photon signal to trigger data acquisition. Once a trigger is issued, the capacitor array is read out, cleared and the previous 128 samples are stored.

The ARS produces huge amounts of data, for instance, at a coincidence rate of 50 Hz, a data rate of 2 Mbytes/s is produced [4]. This requires a large amount of time (128 μs) to be read out. Therefore, reading out all triggered events for the ARS would induce a large dead time for data acquisition. In order to avoid this problem by recording only interesting events, a special trigger module was designed for the experiment.

2.4.2.2 DVCS trigger module

The DVCS trigger module was a level 2^5 type of trigger. The first level trigger was a coincidence between the S2m and the gas Cherenkov. As mentioned earlier, the DVCS calorimeter was close to the beamline and target which were main sources of noise.

[5] A trigger is a system that uses a programmed criteria to decide (select) which events in a detector should be recorded. Triggers are usually designed in levels. A level 1 trigger selects data that becomes an input to a level 2 trigger. In this experiment, the HRS trigger is the level 1 and the DVCS trigger acts secondary to it.

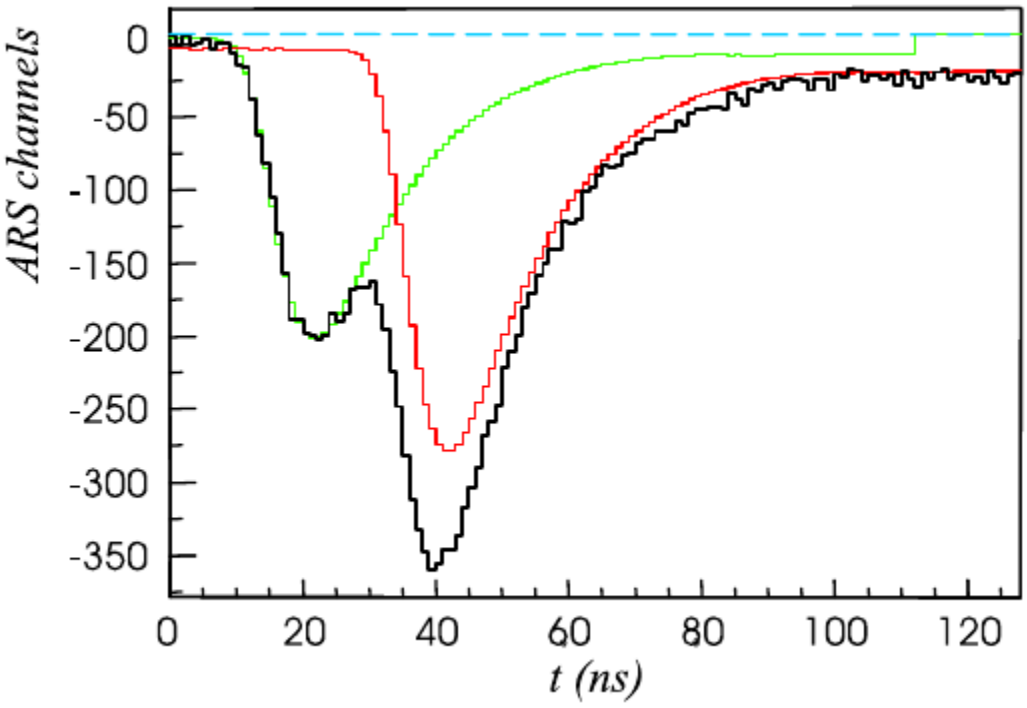

Figure 2.14: An example of ARS signals recorded in a 128 ns window. The ARS take a snapshot of the signals every nano-second and provide a good time and energy resolution for subtracting pile-up events like the one shown in this figure. This figure was taken from Ref.[4].

Therefore, a lot of time was invested in reading the ARS because proper selection of photons is important. To make the DVCS trigger, once the HRS has an electron event, all the ARS were stopped but not read [4]. An integration based on a 2×2 block "tower" of the pedestal subtracted ADC signals was done for all possible combinations of the calorimeter PMTs. It takes the trigger 340 ns to search for possible 2×2 block towers. An

above threshold[6] tower indicates a DVCS photon in the calorimeter and the ARS were readout, leading to a final DVCS trigger sent to record the event. The amount of time it took to make the decision to save (or not to save) an event is 800 ns. A schematic of the DVCS trigger logic is shown in figure 2.15. The trigger could be set on single detector mode and trigger on one specific detector. The trigger was also designed such that it was able to bypass the cluster finding algorithm in what is called the auto validation mode. The auto validation mode was employed especially to acquire deep inelastic (DIS) data. The trigger module also supported multiple simultaneous triggers in different modes of auto validation and with different pre-scale factors. A typical DAQ trigger setting would have atleast 3 simultaneous triggers: the standard DVCS non-auto validated trigger formed by the S2m and Cherenkov prescaled by 1 (taking every seen event), a DIS trigger formed by an auto validated S2m and Cherenkov prescaled atleast by 2 (taking one out of 2 seen events) depending on the kinematic and an auto validated clock trigger prescaled by 16384.

[6] The threshold for the DAQ was set at the beginning of the run. Setting the threshold is a compromise between the expected photon energy in that kinematic and the DAQ rate which is proportional to the dead time.

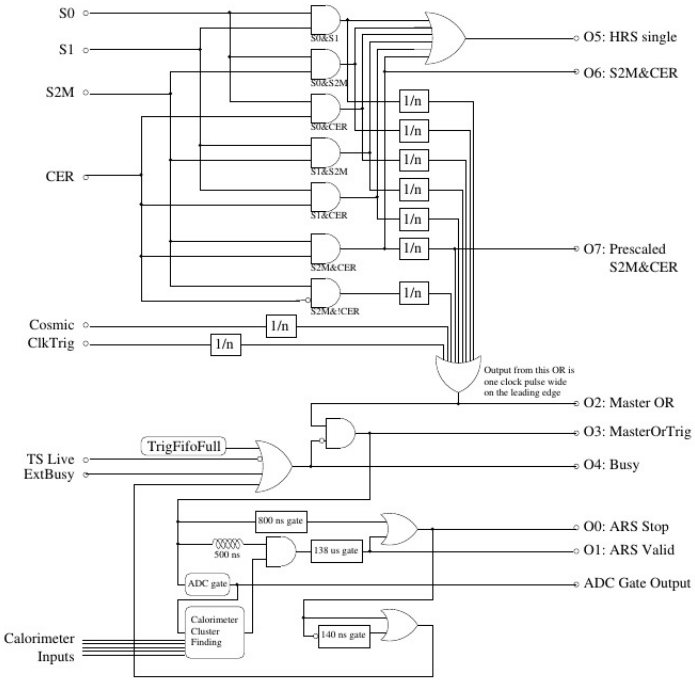

Figure 2.15: The logic for the dedicated DVCS trigger.

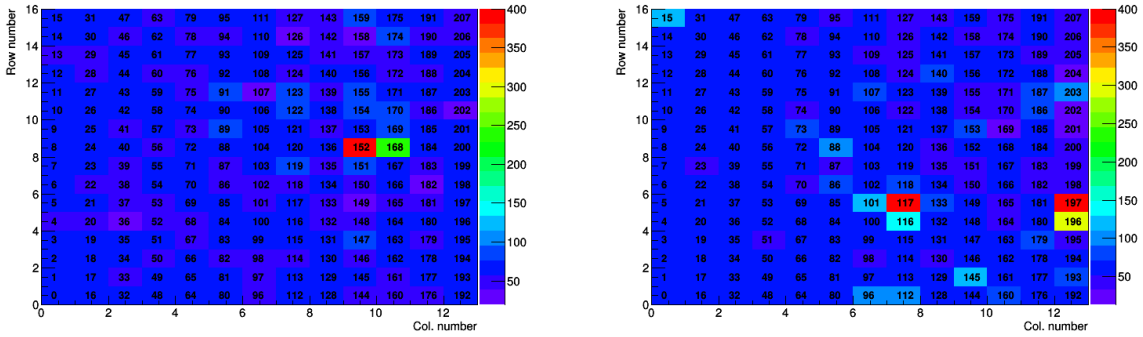

Figure 2.16: Calorimeter showing block numbers and the size of the ADC signal in each channel. Most channels show the pedestal, which is about 60 ADC channels. The right panel shows the case where once cluster has been found and the left is an example of a two cluster (likely a pion) event.

3 Calorimeter Data Analysis and Calibration

The DVCS calorimeter is used to detect the photon (photons) in the final state of the DVCS (DVMP) process. During the experiment the kinematic settings were such that the calorimeter was placed very close to the target and the beamline. Both the target and the beamline are major sources of background radiation in the experimental hall. The accurate analysis of the data is central to the success of the experiment and a proper analysis of the calorimeter data is essential.

The calorimeter data analysis is performed in two steps. The first step is the analysis of the recorded ARS waveforms to extract time and energy information. This is achieved by comparing the signal in each calorimeter channel to a block specific reference shape. This step is called waveform analysis. The waveform analysis algorithm was developed by C. Munoz-Camacho [4] for the first DVCS experiment in 2004. It was later used to analyze data from the second (2010) experiment and has been optimized for the analysis of experiment E12-06-114. In this chapter the waveform analysis procedure has been classified under "General Analysis Algorithms" and will be extensively discussed in section 3.1.1. In addition to its general description, the optimization of the waveform analysis algorithm will be discussed. As briefly mentioned above, central to waveform analysis are the reference shapes for each calorimeter channel. The reference shapes were extracted and updated for each period of data acquisition (Fall 2014, Spring 2016 and Fall 2016). Monitoring the stability of reference shapes for all channels, extracting and updating them was part of my responsibilities for experiment E12-06-114. A detailed discussion of reference shapes will be presented in section 3.2.1.

The second step of calorimeter data analysis is to integrate the information across all calorimeter blocks to get centers of energy deposition, their position and eventually the total energy deposited. This step is called clustering. Clustering is important because it selects the areas of the calorimeter that had a significant energy deposition and also

assigns each calorimeter block to the corresponding electromagnetic shower in the calorimeter. The clustering algorithm was also developed by C. Munoz-Camacho [4] for the 2004 data. It has been used for analysis of the 2010 data and was also used for experiment E12-06-114. The clustering algorithm is therefore part of the "General Analysis Algorithms" and will be discussed in detail in section 3.1.2.

A very important aspect in the interpretation of the calorimeter data (and the whole experiment) is calibration of the calorimeter. Calibration is necessary to convert the signal amplitudes obtained from waveform analysis into units of energy. Several elastic calibrations were performed for each data acquisition period and I analyzed all the calibration data and eventually produced calibration coefficients to convert signal amplitude to units of energy for each calorimeter channel. A detailed discussion of the calibration tools, procedure, and results is presented in section 3.4.2. In addition to extraction of calibration coefficients, elastic data is useful in studying energy and angular (position) resolution of the calorimeter. Calorimeter resolution was studied for all elastic data collected and the procedure and results are also discussed and presented in section 3.4.2.

3.1 General Analysis Algorithms

3.1.1 Waveform analysis

As briefly mentioned in the introduction, the waveform analysis is necessary to extract the amplitude and arrival time of a signal for each channel of the calorimeter. To achieve this, each signal is fitted against a channel specific reference shape. The basis of the waveform analysis algorithm is the assumption that the signal shape is independent of its amplitude [4]. The waveform analysis also uses the fact that the signal off a PMT is linear and each pulse can be related to another pulse from the same PMT by a scaling

factor. Based on these assumptions, all signals can be expressed as a scaled translation (in a time window) of a reference shape.

In an ideal situation (no noise), for a signal with a known arrival time $t = 0$, the amplitude would be one which minimizes the functional:

$$\chi^2 = \sum_{i=0}^{127} (x_i - ah_i)^2, \tag{3.1}$$

x_i is the signal, a is the amplitude and h is the reference shape. The subscript i runs through the 128 ns of the ARS time window (see chapter 2), comparing the signal to the reference shape in steps of one nanosecond. However, the signal time is unknown and the functional in (3.1) has a time dependence:

$$\chi^2(t) = \sum_{i=0}^{127} (x_i - a(t)h_{i-t})^2 \tag{3.2}$$

To search for the signal in the ARS time window, the reference shape is shifted, in 1 ns steps, from its original position across the window until the best fit is found. The best fit is obtained where the χ^2 is minimal and this also defines the arrival time of the signal. The arrival time is then expressed as the difference (in time) between the position of the minimum of the reference shape and the position where the best fit was found. To minimize the χ^2 functional, we take the derivative of equation (3.2) with respect to the amplitude and search for minima:

$$\frac{\partial \chi^2(t)}{\partial a(t)} = -2 \sum_{i=0}^{127} (x_i - a(t)h_{i-t})h_{i-t},$$

solving for the amplitude results in:

$$a(t) = \frac{\sum_{i=0}^{127} x_i h_{i-t}}{\sum_{i=0}^{127} h_{i-t}^2}. \tag{3.4}$$

The waveform algorithm is computer-time consuming. To improve its time efficiency and also reduce the impact of accidental events, the algorithm has been optimised to search for signals in a 80 ns segment of the ARS window. This "new window" has been set such that it is centered about the average arrival time for physics events. From this point on, we will use $[i_{min}, i_{max}]$ to denote the limits of the effective ARS analysis window.

3.1.1.1 Baseline fitting

The first part of the waveform analysis is to check if there is a physical signal present or not. This is done using the baseline fitting, by defining a baseline b and minimizing the functional:

$$\chi^2 = \sum_{i=i_{min}}^{i_{max}} (x_i - b)^2, \tag{3.5}$$

which minimizes to:

$$b = \frac{1}{(i_{max} - i_{min})} \sum_{i=i_{min}}^{i_{max}} x_i. \tag{3.6}$$

If the χ^2 is less than a set global threshold χ_0^2, the baseline fit is considered sufficient and the event is ignored (no signal). Else if χ^2 is larger, the baseline fit is considered not good enough and a one pulse fit will be implemented. An example of the outcome of a baseline fit is shown in figure 3.1.

3.1.1.2 One-Pulse fitting

The one pulse fit is implemented if the baseline fit χ^2 in equation (3.5) is larger than χ_0^2 and this algorithm searches for the possibility of having just one signal. In this case, we minimize the functional:

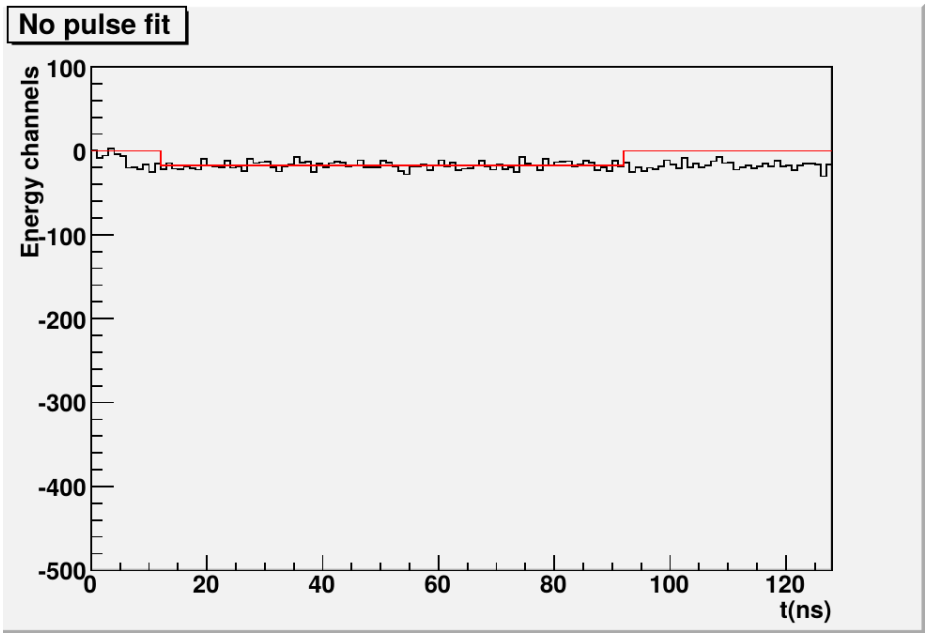

Figure 3.1: An example of a baseline (noise) fit. The PMT signal is shown in black and the fit is shown in red.

$$\chi^2(t_1) = \sum_{i=i_{min}}^{i_{max}} (x_i - a_1(t_1)h_{i-t1} - b(t_1))^2. \tag{3.7}$$

The minimization is done with respect to the amplitude a_1 and also the baseline b and it yields:

$$\frac{\partial \chi^2}{\partial a_1} = -2 \sum_{i=i_{min}}^{i_{max}} (x_i - a_1(t_1)h_{i-t1} - b(t_1))h_{i-t_1},$$

(3.8)

$$\frac{\partial \chi^2}{\partial b} = -2 \sum_{i=i_{min}}^{i_{max}} (x_i - a_1(t_1)h_{i-t1} - b(t_1)). \tag{3.9}$$

This set of equations can also be written as:

$$\begin{bmatrix} \sum_{i=i_{min}}^{i_{max}} x_i h_{i-t1} \\ \sum_{i=i_{min}}^{i_{max}} x_i \end{bmatrix} = \begin{bmatrix} \sum_{i=i_{min}}^{i_{max}} h_{i-t_1}^2 & \sum_{i=i_{min}}^{i_{max}} h_{i-t1} \\ \sum_{i=i_{min}}^{i_{max}} h_{i-t1} & \sum_{i=i_{min}}^{i_{max}} 1 \end{bmatrix} \begin{bmatrix} a_1(t_1) \\ b(t_1) \end{bmatrix} \tag{3.10}$$

Similar to the case of the baseline fit, we also evaluate the χ^2 against a preset χ_1^2 to test its goodness. If $\chi_0^2 < \chi^2 < \chi_1^2$, the one pulse fit is deemed sufficient. Else if $\chi^2 > \chi_1^2$, a two pulse fitting algorithm is invoked. An example of a one pulse fitting is shown in figure 3.2.

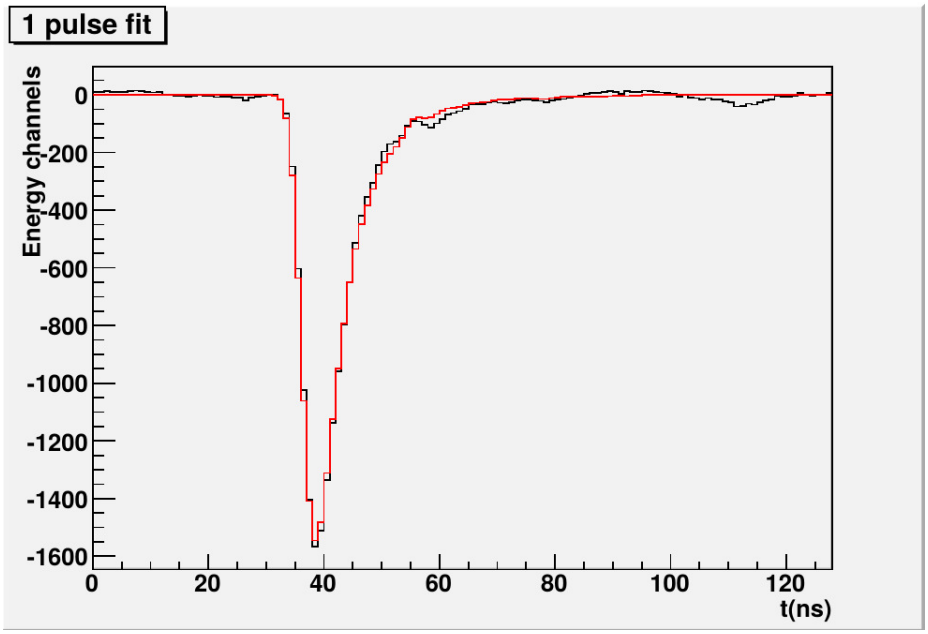

Figure 3.2: A one pulse fit (red) of the PMT signal (black).

3.1.1.3 Two-Pulse fitting

The two pulse fit is employed if the χ^2 in equation (3.7) is larger than χ_1^2 indicating that the one pulse fit is not adequate to reproduce the signal. In that case, the two pulse fit will try to search for a second pulse. Therefore, the function to be minimized is:

$$\chi^2(t_1,t_2) = \sum_{i=i_{min}}^{i_{max}} (x_i - a_1(t_1,t_2)h_{i-t1} - a_2(t_1,t_2)h_{i-t2} - b(t_1))^2, \tag{3.11}$$

The minimized set of equations can be expressed as:

$$\begin{bmatrix} \sum_{i=i_{min}}^{i_{max}} x_i h_{i-t_1} \\ \sum_{i=i_{min}}^{i_{max}} x_i h_{i-t_2} \\ \sum_{i=i_{min}}^{i_{max}} x_i \end{bmatrix} = \begin{bmatrix} \sum_{i=i_{min}}^{i_{max}} h_{i-t_1}^2 & \sum_{i=i_{min}}^{i_{max}} h_{i-t_1}h_{i-t_2} & \sum_{i=i_{min}}^{i_{max}} h_{i-t_1} \\ \sum_{i=i_{min}}^{i_{max}} h_{i-t_1}h_{i-t_2} & \sum_{i=i_{min}}^{i_{max}} h_{i-t_2}^2 & \sum_{i=i_{min}}^{i_{max}} h_{i-t_2} \\ \sum_{i=i_{min}}^{i_{max}} h_{i-t_1} & \sum_{i=i_{min}}^{i_{max}} h_{i-t_2} & \sum_{i=i_{min}}^{i_{max}} 1 \end{bmatrix} \begin{bmatrix} a_1(t_1,t_2) \\ a_2(t_1,t_2) \\ b(t_1,t_2) \end{bmatrix} \tag{3.12}$$

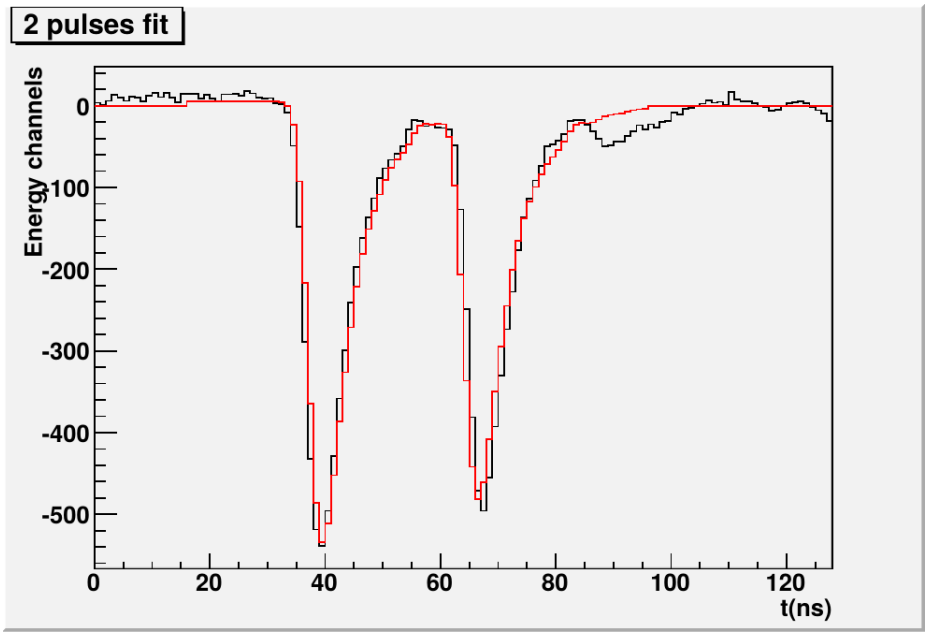

Figure 3.3: An outcome of a two pulse fit (red) of a PMT signal (black).

3.1.2 The clustering algorithm

Most of the photon energy is contained within one particular central block, the rest is well contained in a few neighbouring blocks. When one photon hits the calorimeter most

blocks record noise and only a few (≈ 9) blocks record an actual signal. The group of blocks recording a signal coming from the same incident particle is called a cluster. In addition, multiple particles can be detected by the calorimeter during a single event, be it from the same or different reactions. Once they hit the calorimeter, each of these particles will generate electromagnetic showers which may overlap. The clustering algorithm comes in handy in the spatial separation of such events and assigns each participating calorimeter block to its cluster. An example of a multi-particle event is π^0 production where the pion decays into two photons. In the case both photons hit the calorimeter, the clustering algorithm is useful in disentangling the two electromagnetic showers associated with the event.

Using an energy threshold that is set differently for each kinematic, the clustering algorithm looks for the energy sum of a combination of four neighbouring blocks. This is done for every combination of four adjacent blocks using an algorithm called cellular automata [62]. To construct the clusters, the algorithm first looks for the main impact block, also called the local maxima, see figure 3.4. With the impact block identified, the algorithm then checks the amplitude of the neighbouring blocks to form a cluster. To be added to a cluster, the condition is that a neighbouring block should have a lower amplitude than the local maxima. For each cluster, the total energy is computed as follows:

$$E_{cluster} = \sum_i C_i A_i,$$

where C_i and A_i are the calibration coefficient and signal amplitude for block i, respectively. The index i loops over all the blocks identified to belong to a cluster.

The point of impact x is calculated as a weighted sum block positions. The weighting factor is a logarithm of the relative energy deposited in each block:

15	31	47	63	79	95	111
14	30	46	62	78	94	110
13	29	45	61	77	93	109
12	28	44	60	76	92	108
11	27	43	59	75	91	107
10	26	42	58	74	90	106
9	25	41	57	73	89	105
8	24	40	56	72	88	104
7	23	39	55	71	87	103
6	22	38	54	70	86	102
5	21	37	53	69	85	101

Figure 3.4: Illustration of the clustering algorithm with the selected blocks of impact in violet and the local maxima shown in red for each cluster.

$$x_{cluster} = \frac{\sum_i w_i x_i}{\sum_i w_i}, \qquad w_i = max\left\{0, W_0 + log\left(\frac{E_i}{E}\right)\right\} \tag{3.14}$$

The logarithmic weighting factor accounts for the fact that the electromagnetic shower decreases exponentially with distance. Therefore, the further a block is from the impact point, the less it contributes to the total cluster energy. The term W_0 makes it possible to further adjust the weight of each block as a function of reconstructed energy. As W_0 goes to infinity, the weight distribution is uniform but for small W_0, blocks with a relatively higher energy dominate. Since clustering is performed after the waveform analysis, W_0 is adjusted for each waveform analyzed calorimeter signal after the minimization.

The computation of the position presented above assumes the electromagnetic shower begins at the surface of the calorimeter, which is not the case. The shower starts at a certain depth a correction has to be applied to cater for that. Furthermore, depending on the distance between the calorimeter and the 15 cm target, particles from different

interaction points (along the target) may have significantly different propagation lengths before hitting the calorimeter. The final corrected hit position is then:

$$x_{corr} = x\left(1 - \frac{a}{\sqrt{L^2 + x^2}}\right), \tag{3.15}$$

where a (has been estimated to be about 7 cm from simulation and elastic data) is the depth at which the shower starts and L is the distance from the vertex to the calorimeter point of impact.

The time of arrival of each photon event (event time) is also defined as the time of the cluster. To calculate the cluster time, we weigh the arrival times of each signal (channel) composing the cluster as follows:

$$T_{cluster} = \frac{\sum_i A_i t_i}{\sum_i A_i}, \tag{3.16}$$

A_i is the amplitude of signal in channel i and t_i is the arrival time of the signal.

3.2 Analysis for Experiment E12-06-114

3.2.1 Reference shapes

In the interest of waveform analysis, each of the 208 calorimeter blocks has a reference signal extracted and assigned to it. The reference shapes were extracted from elastic calibration data. This is because elastic data were acquired at low current (5 μA) and less susceptible to pileup. Moreover, the elastic reaction channel is very constrained and suffers less accidentals (noise) than production data. To select even a cleaner sample, we chose signals with a high energy deposition in the calorimeter. For each calorimeter block, the first signal is weighted by its amplitude. Afterwards, an iterative, averaging process follows where other signals are added to the first with a weight of their amplitude. As the amplitudes are averaged, the signals are also shifted in time to superimpose pulses

arriving not exactly at the same times. A set of 208 reference shapes corresponding to 208 PMTs was created.

Since the Fall of 2014, five elastic calibrations have been done. Reference pulses were extracted from each elastic calibration data. The decision on which shapes to use for each production data acquisition period was based on how much the shapes have changed from one calibration data to the next. In general there were no significant changes in most shapes across all calibration data. In a few cases (5 calorimeter channels) some channels have visibly non-negligible changes like reflections in the signal as shown in figure 3.5 and obviously the same shape cannot be used for data corresponding to the two different periods of data acquisition.

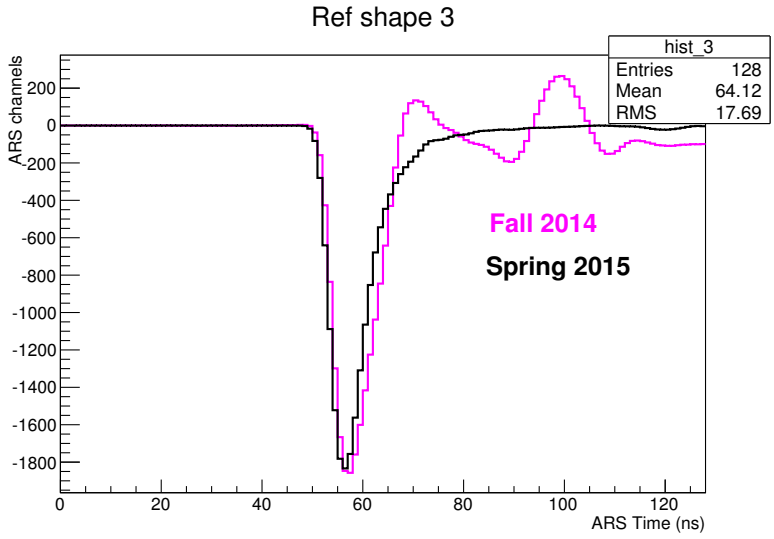

Figure 3.5: A comparison of the reference pulse extracted for trigger number 3 from the Fall of 2014 and Spring 2015 data sets. A reflection caused some bumps at the trailing tail of the pulse in the Fall. This had been fixed for the Spring run.

A study was done to investigate by how much these reference shapes differ from one block to the next. As a reminder, a different shape is used for each calorimeter block (PMT). To understand if it is necessary to use 208 different reference shapes, properties of the shapes such as the Full Width at Half Maximum (FWHM), rise times (leading edge) and fall times (trailing edge) were compared. Using the integral binning of 1ns (ARS sampling rate), it is difficult to see the differences. Instead, a linear interpolation was implemented to get a fraction of a nanosecond precision. Shown in figure 3.6 are the results after the linear interpolation. Overall, even though the differences are small, one can notice variations from one block to the next.

3.2.2 Waveform Analysis Optimization

The waveform analysis procedure entails fitting the ARS signal for either zero, one or two pulses for each event. As already explained in earlier sections, the decision on how many pulses to search for (and then fit) is based on the progressive computation of a χ^2, starting from a baseline fit χ^2_0. It is therefore necessary to study and optimize the waveform analysis to search for the optimum χ^2 values for each threshold χ^2_0, and χ^2_1.

To determine the optimal values of the thresholds χ^2_0, and χ^2_1 , we studied the effect of these values on several parameters such as:

- The energy resolution of the calorimeter,
- The reconstructed means and resolutions of the exclusivity peaks (proton missing mass and π^0 invariant mass),
- The $ep \rightarrow ep$ elastic invariant mass W^2,
- The number of π^0-like events as a function of the total number of events,

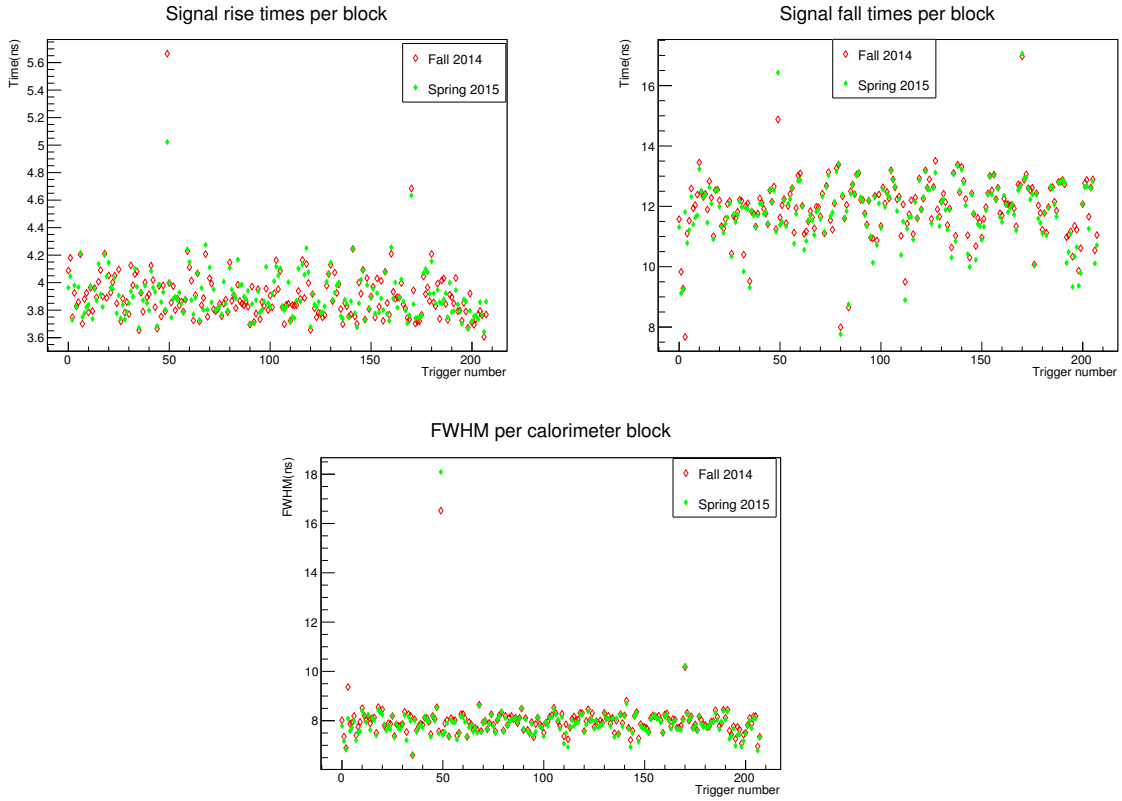

Figure 3.6: Properties of the reference shapes for all calorimeter blocks. Top panel: Rise times (left) and fall times as a function of trigger number.
Bottom panel: Full Width at Half Maximum for all blocks. All the blocks have similar signals except for blocks 49 and 170.

- The computation time.

The value of χ_0^2 has the biggest impact on the energy resolution because it decides which events have to be considered as background and which events have a signal above background. Figure 3.7 shows results of the study of the effect of different values of χ_0^2 on the energy resolution and the resolution of the elastic $ep \rightarrow ep$ reaction. The final optimal value of χ_0^2 was set to 60 MeV and 300 MeV for χ_1^2. For a χ^2 greater than 300 MeV, a two pulse fit will be triggered.

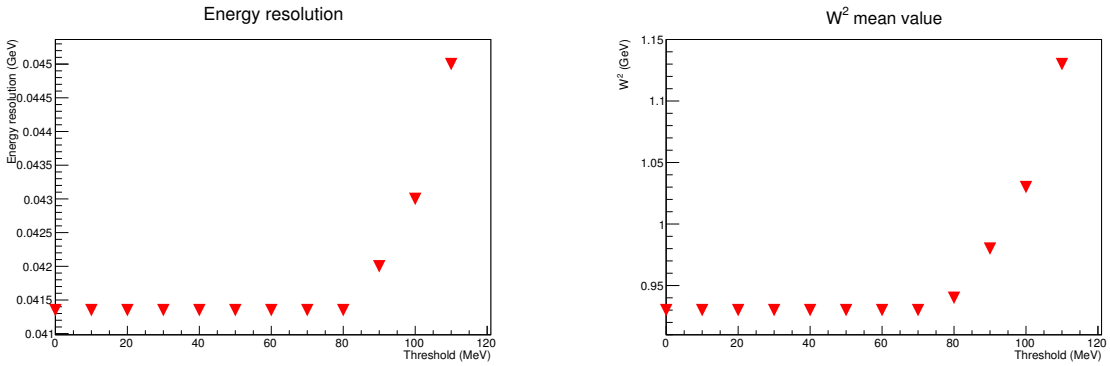

Figure 3.7: The energy resolution (GeV) as a function of the fit parameter χ_0^2 (left panel) and the elastic invariant mass W^2 as a function of χ^2 (right panel). This figure was adapted from F. Georges in his report to the Hall A DVCS collaboration [68].

3.3 Calorimeter-HRS Coincidence Time Calibration and Optimization

The ability to determine the time of arrival of each of the detected particles in the detectors is a vital component of this experiment. Our ability to measure time with a good resolution plays a significant role in suppressing accidental events and improving the energy resolution of the calorimeter. Since the spectrometer has an excellent momentum resolution, the limiting factor in the measurement of the missing mass is the calorimeter energy resolution. How well the photon energy is measured significantly determines how well the recoil proton's missing mass is reconstructed. To improve the ability to determine the desired photon's energy, one way is to apply corrections and optimize the distribution of the HRS-Calorimeter coincidence times for each calorimeter block. An additional calibration is done to get the signals to arrive within the same time window for all channels, nicely isolating purely accidental events from accidental plus DVCS events. This results in a global time window enabling us to apply a global calorimeter timing in the selection of analysis events, instead of a channel-dependent event selection criteria.

To apply the timing corrections, properties of the electron signal propagation in the spectrometer and the photon signal propagation in the calorimeter that will introduce differences in coincidence times from one event to the next were considered. The following are the properties studied and corrected for:

- Jitter in the trigger that stops the ARS,
- Arrival time as a function of each calorimeter block (calibration),
- Time as a function of each S2m scintillator paddles (16 of them),
- Distance (time) of light propagation from the hit point in a paddle to the timing phototube,
- Electron path length as determined by the relative momentum and vertical angle of the electron.

3.3.1 Trigger Jitter Correction

An ideal timing signal should have a fixed period and similarly a fixed starting point over time [63]. In reality, all timing signals have some statistical fluctuations which are inherent to the detector. As a result of these random fluctuations, two identical signals will not always trigger at the same point but instead will have a time variation which is dependent on the amplitude of the fluctuations [63]. The variations of the timing signals rising and falling edges as compared to the ideal signal are defined as jitter. In PMT signals, jitter is caused by factors such as:

- Variations in the number of photons in the detector,
- Gain variations in the PMT and
- Transit time of photons through the detector.

In this experiment, the timing of the electron was set by the S2m scintillators and a correction needs to be applied to minimize the amplitude and the effects of the fluctuations in the S2m arrival time with respect to the signal which sets the trigger (the ARS stop). The jitter correction is applied for each event by considering the difference between the S2m signal timing and the trigger signal timing given by (in nanoseconds):

$$t_{corr} = t_{raw} + (t_{S2m} - t_{trigger})/10, \tag{3.17}$$

where t_{corr} is the corrected time, t_{raw} is the coincidence time for an event, t_{S2m} is the S2m signal time and $t_{trigger}$ is the trigger signal time for an event event. The factor of 10 accounts for the fact that the S2m TDCs have a better time resolution (100 picoseconds) than the ARS (1 nanosecond). An example of the average widths of the arrival time before the jitter corrections is shown in the top left panel of figure 3.13. The trigger jitter correction is the most significant step in the coincidence time optimization. This can be seen by the improvement introduced to the time distributions (after its implementation) and shown in the top right panel of figure 3.13.

3.3.2 Calorimeter Time Calibration

Each calorimeter block has a cable which transmits the signal from the block's PMT to the DVCS trigger. The cable length varied from one calorimeter channel to the next and this introduced differences in the signal propagation times across channels. An optimization was done to correct for this difference for all the production data. A 150 MeV cut (on the photon) was applied to select good photon events. The mean of the arrival times for all the events passing the selection criteria in each channel was considered as the channel time. These channel arrival times were then used to calibrate the event time such that the coincidence peak was centered around zero for each calorimeter channel. After this calibration all channels have their times aligned and hence a global time requirement

can be imposed for event selection during data analysis. The left panel of figure 3.8 shows these arrival times for each calorimeter block and a calibrated time spectrum for all blocks considered at once is shown on the right panel. Since the different kinematics have the calorimeter at different distances from the target, the arrival times for each channel vary from one setting to the next and the propagation of the electron in the spectrometer is also kinematic dependent. This makes it necessary to apply an independent calibration for each kinematic. After this calibration, the next goal is then to improve the dispersion of the time spectrum by applying several corrections as detailed in the following sections.

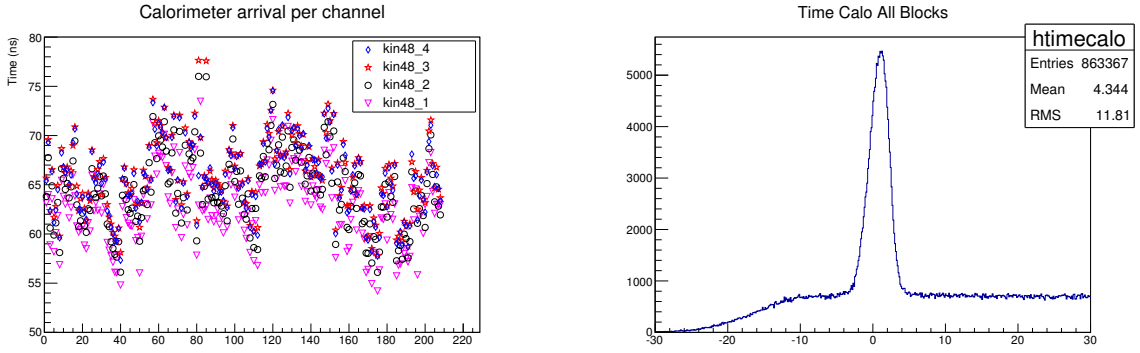

Figure 3.8: Calibration of the spectrometer-calorimeter coincidence times.Left channel: the spectrometer-calorimeter coincidence times (average coincidence time for events) as a function of calorimeter channels for a few kinematics. Since the different kinematics have the calorimeter at different distances from the target, the arrival times for each channel vary from one setting to the next. Right panel: the spectrometer-calorimeter coincidence time with all the channels considered at once after calibration using the channel-dependent arrival times (shown on the left panel). After this calibration, we have a global calorimeter time and we can apply a universal timing selection criteria to select events for final cross section analysis.

3.3.3 Correction for S2m Paddles

The detector package in the spectrometer has sixteen scintillator paddles and the electron's arrival time associated with each of them varies slightly from one to the next, depending on the momentum of the scattered electron. The time distribution of each paddle was histogrammed and the mean of each histogram was used as a correction factor to center the time distribution. Figure 3.9 shows by how much time each scintillator paddle was shifted for centering for a few kinematics. Again, the correction factor shows some dependence on the kinematic setting because of differences in the momentum setting of the HRS for each.

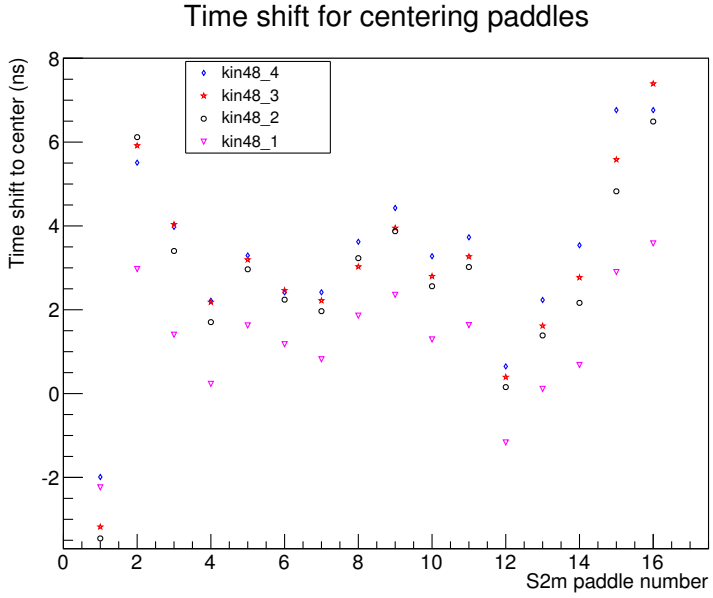

Figure 3.9: Scintillator paddle corrections: time offsets for each scintillator paddle. These were used to shift the coincidence time corresponding to each paddle to be zero-centered. A difference in the momentum setting of the spectrometer is responsible for the varying correction factors for each paddle as a function of the kinematic setting.

3.3.4 Propagation time in scintillator material

The spectrometer electronics are designed such that the right (right hand-side relative to the beam direction) phototubes set the timing for S2m. Since the scintillators are 1 meter long, different particles will fire each paddle at points that are at different distances from the right phototubes. Therefore, the scintillation signals have to spend different amounts of time propagating through the paddle material before being collected. To correct for this difference in propagation times, the correlation between the arrival times and the position of a hit along the length of the paddles (in the non-dispersive direction, y) was empirically studied. A linear correlation between the time and the position was observed and fitted using a first degree polynomial to extract the slope and the intercept. An example of the correction coefficients is shown for a few kinematics in figure 3.10. The correction for the offset (intercept) is very negligible and can be ignored. The arrival time is then corrected as follows:

$$t_{corr} = t_{raw} - (m_{S2m} \cdot y_{S2m} + c_{S2m}), \tag{3.18}$$

where t_{corr} is the corrected time, m_{S2m} is the slope of the correlation for a scintillator paddle, y_{S2m} is the y position for an event and c_{S2m} is the intercept for a paddle.

3.3.5 Electron path length in spectrometer

From one event to the next, there is a variation in the electron's momentum. Therefore, different electron events (within the same kinematic or momentum setting of the HRS) do not bend by the same amount in the magnetic field of the spectrometer. Hence the path length in the spectrometer varies with events. In essence, since the scintillator paddles are spread out in the dispersive direction relative to the electron's trajectory (x direction), each scintillator paddle gets fired by electrons of a slightly

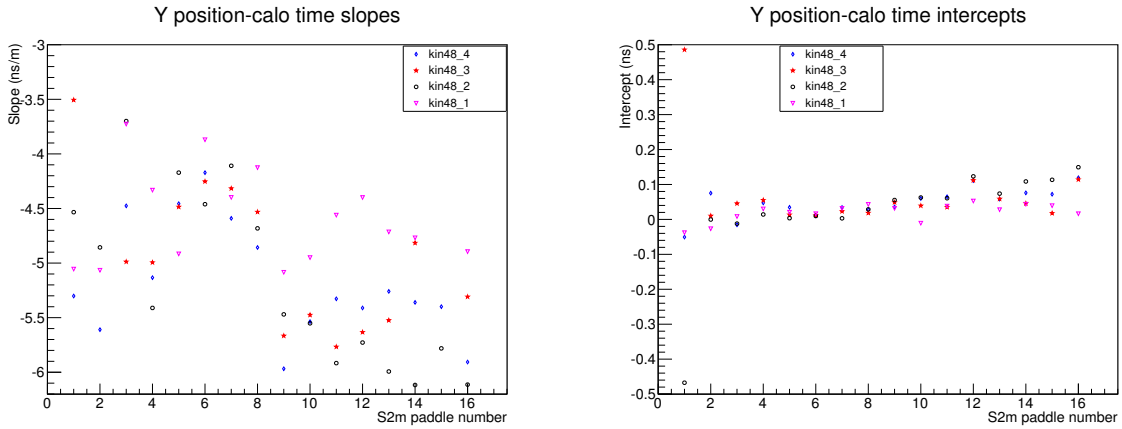

Figure 3.10: Slopes (right) and intercepts (left) for each scintillator paddle. These were extracted by empirically studying the correlation between the arrival time and the non-dispersive position (y) for each scintillator paddle. The intercepts are negligible and can be ignored.

different momentum fraction compared to other paddles and hence different electron path lengths induced by that. To correct for the differences emanating from different electron path lengths in the HRS, the correlation of the vertical angle (θ) and the arrival times was empirically studied. A linear correlation was observed and the time correction was applied in a similar fashion as the previous section. A similar study was also done as a function of the momentum of each event resulting in another linear correlation between the event momentum and the arrival time. A summary of the extracted slopes and intercepts for each scintillator paddle is shown in figures 3.11 and 3.12. The correction for both the angle and the momentum is done using the offset and the slope in the same way as done in the previous section.

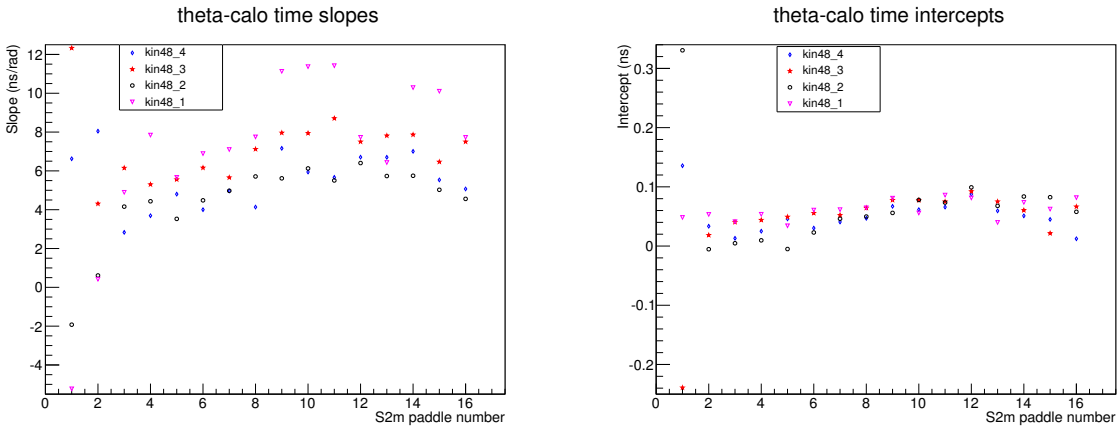

Figure 3.11: Slopes (right) and intercepts (left) corresponding to each scintillator and extracted by looking the the correlation between the theta angle and the coincidence time.

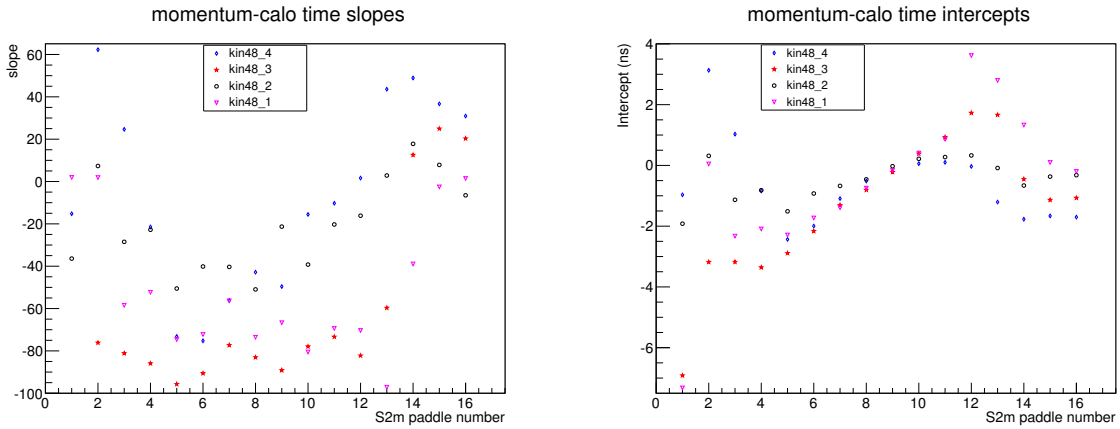

Figure 3.12: Slopes (right) and intercepts (left) corresponding to each scintillator and extracted by looking the the correlation between the momentum fraction and the coincidence time.

Fig. 3.13 shows a summary of the the amount of dispersion (standard deviation) as a function of channel number after each time correction. Starting with a maximum standard deviation of about 3 ns after the first (jitter) correction, after all corrections have been

applied, on average a sigma of about 0.85 ns is obtained at a 150 MeV cut in photon energy.

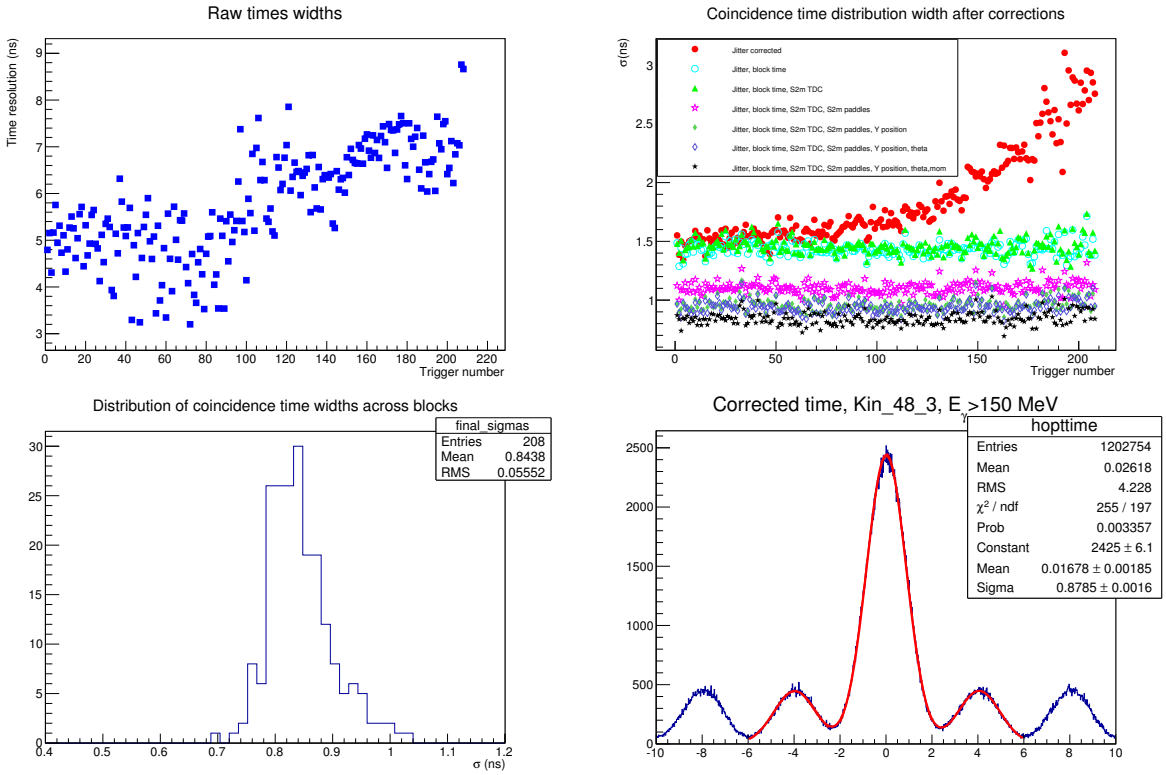

Figure 3.13: A summary of the coincidence time calibration and optimization results. Top left: widths (sigmas) of the time distribution as a function of calorimeter block before any correction is applied. Top right: widths of the time distribution per block as a series of accumulating time corrections are applied as shown in the legend. Bottom left: An example of histogramed final corrected widths for all 208 calorimeter blocks in kinematic 36_1. With an energy cut of 150 MeV, an average of 0.85 ns was achieved. Bottom right: The final calibrated and optimised calorimeter time shown for kinematic 48_3. The 4 nanoseconds beam structure can be seen in the coincidence time distribution.

3.4 Calorimeter Energy Calibration

Calibrating the calorimeter entails adjusting the high voltage of the 208 calorimeter phototubes such that for the same energy deposition, we get the same signal response across all PMTs. Balancing the gain for each channel is necessary because it allows us to set a global clustering threshold for triggering on the calorimeter during data acquisition. Calibration can be done using either the ADC or the ARS signals or both but we chose to calibrate the ARS because they have a superior energy resolution compared to the ADCs. The calorimeter was first calibrated and tested before the experiment using cosmic rays. This pre-beam adjustment of the gains of the phototubes is then followed by an absolute energy calibration using elastic electrons at the beginning and halfway through the experiment. In this section we first discuss the pre-beam calibration and later conclude by describing the procedure of and the results from the elastic calibration.

3.4.1 Cosmic ray calibration

Cosmic rays are an ionizing radiation gift from nature and they are useful in testing and calibrating a number of detectors before the experiment starts. The minimum energy deposition of cosmic rays crossing the crystals of the calorimeter vertically along the shortest distance (3 cm) is 35 MeV per block, producing about 35 Cherenkov photons on average [4] and that is enough to calibrate the phototubes. The energy deposition of ionizing particles depends on the length of the material they traverse. Therefore, to ensure a selection of events with a uniform energy deposition across all crystals, only particles that had a vertical trajectory through the calorimeter were selected. This was done by requiring that a particle fires both the top and the bottom crystals in the same column, in that way traversing the same distance in all impact blocks. The vertical cosmic cut was done offline, after all the cosmic events had been saved. Typically, the cosmic rate was 4Hz and the DAQ was run overnight for a period of 10 to 12 hours harvesting between

140k to 170k cosmics. After applying vertical and pedestal cuts, we were left with an average of 400 to 500 events per column.

An integration (above pedestal) of the ARS signals of the selected cosmic spectrum was then fitted with a Gaussian for each channel. The mean from the fit was taken as the starting point of the calibration and the high voltage for each channel was then adjusted such that the mean is shifted and well centered about 3000 (high enough to be clearly separated from the pedestal but not too high up the capacity of the ARS) integrated ARS channels.

To adjust the HV, we consider the relative gain, defined as:

$$G = \alpha HV^{\beta}, \tag{3.19}$$

where β is a block specific parameter which is on average, approximately 7 for PMTs used in this experiment. An average of four iterations was sufficient to align the gains of the PMTs to 4.5% (for the ARS) and 5.3% (for the ADCs) across all calorimeter channels. For each iteration (calibration step), the next HV values were calculated as:

$$HV_2 = HV_1 \left(\frac{G_2}{G_1}\right)^{\frac{1}{\beta}}, \tag{3.20}$$

where G_1 and HV_1 are the starting gain and high voltage respectively. G_2 and HV_2 correspond to the target gain (3000) and the high voltage set to achieve this target, respectively. After four iterations, no better calibration could be achieved. For an absolute energy calibration we next used elastic electrons using the first beam sent by CEBAF into the hall.

3.4.2 Elastic calibration

To calibrate the absolute response of the calorimeter phototubes we performed an elastic calibration at the beginning and then later stages of the experiment. During elastic

calibrations, the polarity of the HRS was set to positive to detect elastically recoiling protons. Elastic electrons were detected in the calorimeter. The calibration was challenged by a small acceptance of the HRS allowing only a small portion of the calorimeter to be illuminated. To circumvent the acceptance limitation, the vertical acceptance was increased by placing the calorimeter at 6 metres from the target. However, that does not solve the horizontal acceptance challenge and to address that the calorimeter was placed at three different (but overlapping in terms of acceptance) angles, see figure 3.14.

3.4.2.1 Procedure

In order to reconstruct the energy deposited in the calorimeter, one needs to first extract the coefficients that transform the signals from each calorimeter PMT to the energy deposited in each block. The calibration is then based on collecting this cluster energy and finding block coefficients which will reproduce the deposited energy [4]. The total energy is the sum of all depositions in the calorimeter. If we denote the signal collected from block i during event j by A_j^i and the corresponding block coefficient by C_i, the total energy deposited is given by:

$$E^j = \sum_{i=0}^{208} (C_i A_i^j) \tag{3.21}$$

The calibration coefficients are then calculated by minimizing the functional:

$$\chi^2 = \sum_{j=0}^{N_{events}} \left(E_j - \sum_{i=0}^{208} (C_i A_i^j) \right)^2 \tag{3.22}$$

where E_j is calculated using HRS information as follows:

$$E_j = E_b + M_p - E_p^i. \tag{3.23}$$

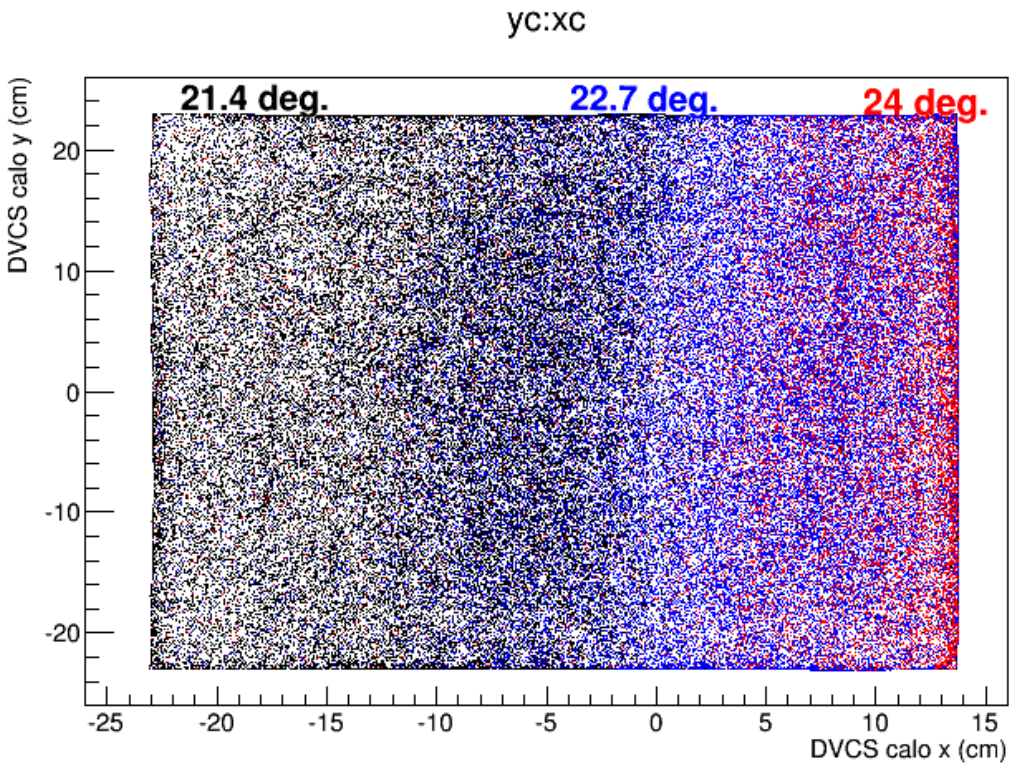

Figure 3.14: The calorimeter face showing the three different settings used to fully illuminate the calorimeter's acceptance during the elastic calibrations. For the calibration the central momentum of the HRS (P_{HRS}) was 3.0 GeV, the central angle of the HRS (θ_{HRS}) was 32.5^o, the beam energy (E_B) was 6.4 GeV and the calorimeter was placed at 6.0 m from the target.

E_j is the electron energy, E_b the beam energy, M_p the proton mass and E_p^i the recoil proton energy for event i. Minimizing equation 3.22 results in the following system of linear equations:

$$\sum_{i}^{208}\left(\sum_{j=1}^{N_{events}} A_j^k A_j^i\right) C_i = \sum_{j=1}^{N_{events}} E_j A_j^k, \tag{3.24}$$

where k goes over all calorimeter blocks.

Inverting the 208×208 matrix $\sum_{j=1}^{N_{events}} A_j^k A_j^i$ gives the calibration coefficients.

3.4.2.2 Implementation

A selection of good elastic scattering events was done on the HRS variables. A 2D graphical cut on the horizontal scattering angle (L.tr..tg_ph) and the fractional deviation of the protons' momentum from the central momentum of the HRS (L.tr.tg_dp) was used to select the "elastic line" for protons, see the left panel of figure 3.15. Vertex cuts were imposed on the selected events to suppress contributions coming from the end caps of the target cell. The cuts applied on the vertex are shown on the right panel of Fig. 3.15. Since an elastic reaction is clean, a single pulse waveform analysis was used to extract the time and energy information from the ARS.

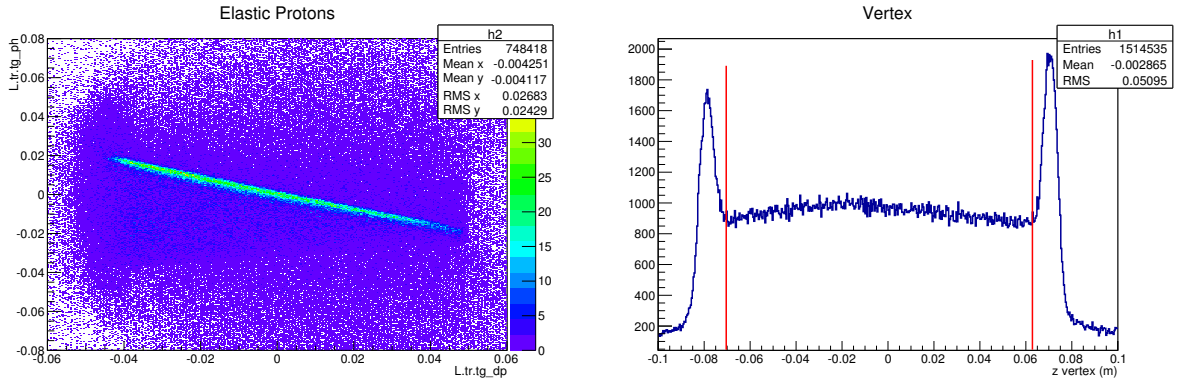

Figure 3.15: Criteria for selection of good elastic protons in the HRS. Left panel: a 2D plot of the horizontal scattering angle (L.tr..tg_ph) and the fractional deviation of the protons' momentum from the central momentum of the HRS (L.tr.tg_dp). The elastic line (elastic protons in the spectrometer) can be seen on top of background. Right panel: the reconstructed vertex z-coordinate and the applied cuts represented by the region in-between the two red vertical lines.

3.4.2.3 Energy Resolution

The calorimeter energy resolution was computed using data acquired for the elastic calibration, after the calorimeter had been calibrated. The resolution was obtained by comparing the value of the elastic electron energy obtained from the energy conservation equation (3.23) using the HRS information, E^{HRS} and the electron energy reconstructed in the calorimeter using the calibration coefficients, E^{calo}. The resolution is then computed as the width of the energy discrepancy distribution (see figure 3.16) divided by the mean reconstructed energy;

$$Energy\ resolution = \frac{E^{HRS} - E^{calo}}{\langle E^{calo} \rangle} \tag{3.25}$$

Energy calibration results

Figure 3.16 shows an example of calibration results from an elastic calibration performed in February 2015. The energy measured by the calorimeter was compared to the one measured by the HRS to get the energy resolution of the calorimeter. At an average 7 GeV electron energy, the calorimeter was found to have a 3.0% resolution. The results corresponding to other calibrations are summarized in table 3.1.

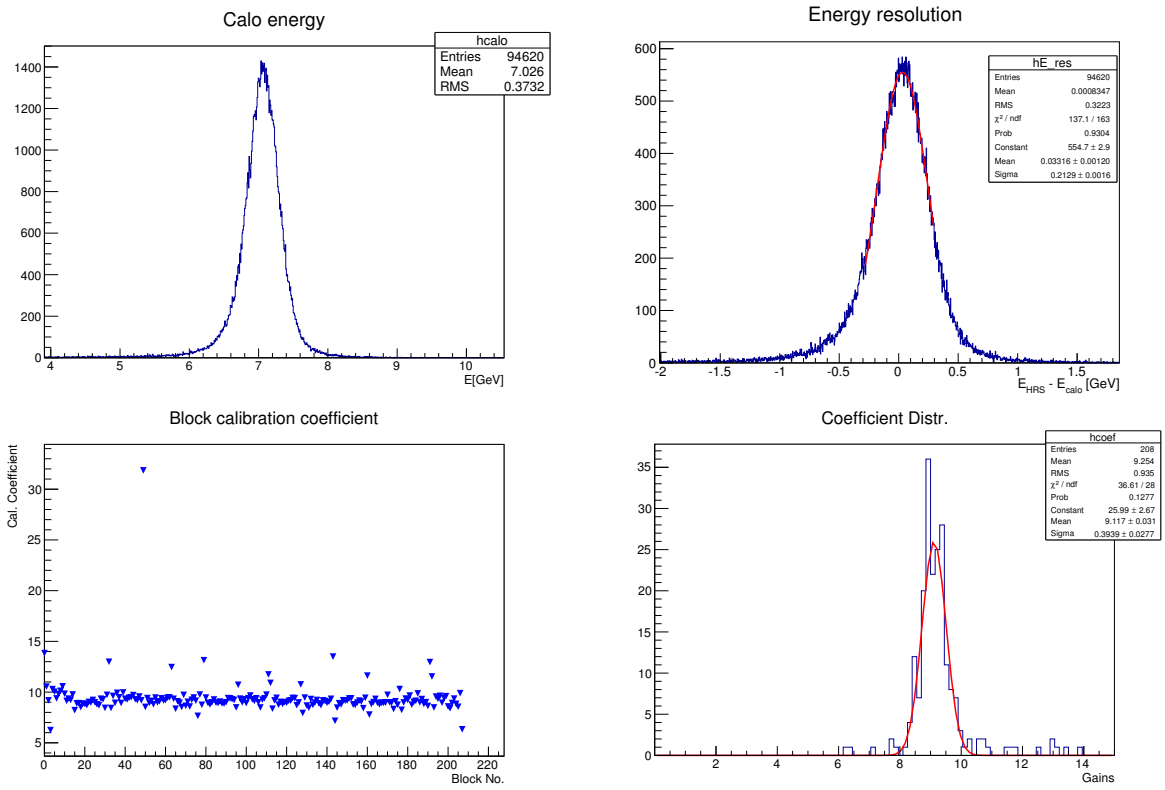

Figure 3.16: Elastic calibration results for the February 2015 calibration. Top panel: the energy of elastic electrons reconstructed in calorimeter is shown on the left. On the right is the energy resolution obtained from the elastic calibration. A 3.0% energy resolution was obtained at an average 7 GeV elastic electron. Bottom panel: a plot of the extracted calibration coefficients as a function of block number on the left and the same coefficients histogrammed on the right panel. Excluding the blocks at the edges, calibration coefficients are within 5% in agreement across all other blocks. The edge blocks have fewer neighbors and hence more susceptible to energy leaks, therefore they have higher than average calibration coefficients.

Set	E_{beam} [GeV]	$E_{electron}$ [GeV]	σ (Δ E) [GeV]	Resolution [%]	$\Delta\Phi$ [mrad]	$\Delta\theta$ [mrad]
December 2014	7.3	5.0	0.205	4.10	1.42	1.20
February 2015	9.6	7.0	0.213	3.00	1.10	1.02
February 2016	4.4	3.1	0.144	4.65	2.10	1.67
April 2016	4.4	3.1	0.153	4.94	2.03	1.71
October 2016	6.45	4.2	0.133	3.17	1.72	1.41
December 2016	6.45	4.2	0.154	2.39	1.64	1.36

Table 3.1: Summary of elastic calibrations for different elastic data sets. Columns 4 and 5 show the energy resolution in energy units and as a percentage, respectively. The last two columns show the horizontal angular resolution ($\Delta\phi$) and the vertical angular resolution ($\Delta\theta$) of the calorimeter. The definitions of both projections of angular resolution is given in section 3.4.2.5.

3.4.2.4 Trigger Calibration and Calorimeter Clustering Thresholds

Even though the absolute energy calibration is done based on the ARS signals, it is still important to perform the calibration against the trigger (ADC) signals too. As explained in chapter 2 the decision on whether or not to consider an event as having fired the calorimeter is informed by a tower formed by the trigger signals of 4 calorimeter channels. The trigger calibration is therefore important since it informs the choice of the trigger tower threshold (relative to the expected photon energy in that kinematic) set during data acquisition. The DAQ calorimeter tower threshold can be adjusted depending of factors like event rate and or dead time concerns. For example if it has been set too low and a high rate (inducing large dead times) is observed as a result, it can be increased to ease the DAQ rate.

The trigger can be calibrated using two methods. The first method is exactly the same as the one explained in 3.4.2.1, but this time using a pedestal subtracted ADC signal for the event signal. The second method calibrates the trigger signals against the already calibrated ARS signal by using the correlation between the two. Plotting the trigger signals against the calibrated ARS and fitting using using a first degree polynomial, the slope gives the calibration coefficient and the intercept is the ADC pedestal. An example of this method is shown for one channel of the calorimeter in figure 3.17. Results of the trigger calibration for all elastic data sets are shown in table 3.2.

Elastic data set	**Mean coefficient [GeV/ADC ch.]**	**Mean coefficient [ADC ch./GeV]**
December 2014	0.00424	235.8
February 2016	0.00583	171.5
April 2016	0.00911	109.7
October 2016	0.00606	165.0
December 2016	0.00610	163.9

Table 3.2: Elastic trigger calibration coefficients for different elastic data sets.

At the waveform analysis stage of data processing, clustering thresholds slightly higher than the values of the DAQ triggering thresholds were used to get a cleaner photon sample. The final values for different kinematic settings are summarized in table 3.4

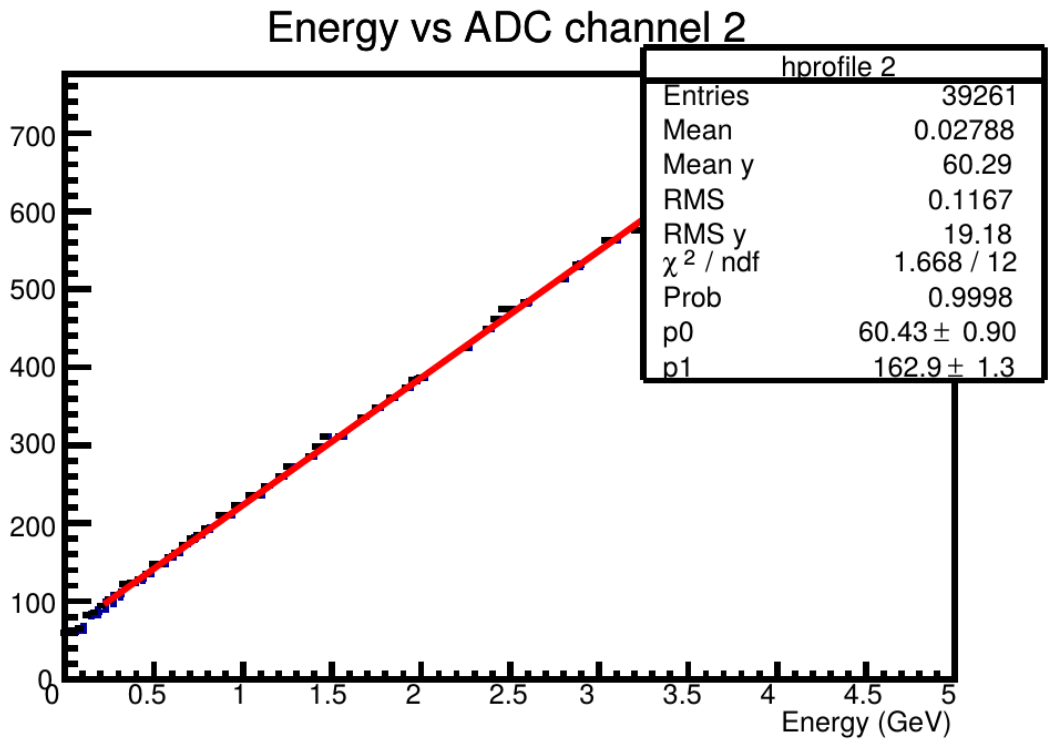

Figure 3.17: Calibrated ARS energy (horizontal axis) and the ADC signal (vertical axis) for calorimeter channel 2 from October 2016 elastic data. The blue points represent the data and the red line is a fit to the data. From the fit, the slope (calibration coefficient for this channel) is about 160 ADC channels per GeV. The ”y”-intercept (ADC pedestal) is about 60 ADC channels.

3.4.2.5 Calorimeter Angular Resolution

The energy resolution of the calorimeter has an impact on how well we can reconstruct the missing mass of the undetected proton. On the other hand, the angular resolution tells us how well (or not) we can distinguish two points of impact on the calorimeter. The angular resolution is calculated for two angles: one in the horizontal plane (ϕ) and another in the vertical plane (θ). We compute each angle using two methods. One method uses the momentum vector of the proton in the HRS and the other uses the

Kinematic setting	**DAQ threshold (GeV)**
kin36_1	1.0975
oldkin36_2	1.0975
kin48_1	0.4243
kin48_1 (run 12508)	0.8907
kin48_2	0.8907
kin48_2 (run 13000, 13183-4)	1.0073
kin48_2 (run 13001 to 13015, 13191 to 13193)	0.3076
kin48_3	1.0073
kin48_3 (run 12838)	0.4243
kin48_4 (run 13100 to 13162)	1.0073
kin48_4 (run 13279 to 13418)	1.4571
kin36_2	1.5200
kin36_3	1.5200
kin60_1	0
kin60_3	0

Table 3.3: DAQ thresholds (GeV) for each run period. The last two kinematic settings had a low DAQ event rate hence the decision to remove the tower requirement on the calorimeter to invite more statistics.

energy reconstructed in the calorimeter. The resolution is then given by the difference between the angle computed based on the HRS data and that calculated using the calorimeter data, assuming a perfect HRS momentum resolution.

run period	**TriggerSim clustering threshold (GeV)**
kin36_1	1.1
oldkin36_2	1.1
kin48_1	0.5
kin48_2	0.9
kin48_3	1.1
kin48_4 (run 13100 to 13162)	1.1
kin48_4 (run 13279 to 13418)	1.5
kin36_2	1.6
kin36_3	1.6
kin60_1	0.8
kin60_3	1.0

Table 3.4: Final values for clustering threshold, in GeV, for each run period.

Procedure

Starting from the kinematics of the elastic reaction (e + p → e' + p') and confining the electron beam on the z-axis [64]:

$$(0,0,p_z^b)_e + (0,0,0)_P = (p_x^{e'}, p_y^{e'}, (p_z^{e'})'_e + (p_x^{P'}, p_y^{P'}, p_z^{P'})'_P \tag{3.26}$$

$$(p'_{ex}, p'_{ey}, p'_{ez}) = (-p'_{Px}, -p'_{Py}, p_z^b - p'_{Pz}). \tag{3.27}$$

Since $p_z^b = E_b$ the following formulae can be written for the angles:

$$\begin{aligned}
\theta^e_{calo} &= atan\left(\frac{p'_{ex}}{p'_{ez}}\right) & \theta^e_{HRS} &= atan\left(\frac{-p'_{Px}}{E_b - p'_{Pz}}\right) \\
\phi^e_{calo} &= atan\left(\frac{p'_{ey}}{\sqrt{(p'_{ex})^2 + (p'_{ez})^2}}\right) & \phi^e_{HRS} &= atan\left(\frac{-p'_{Py}}{\sqrt{(p'_{Px})^2 + (E_b - p'_{Pz})^2}}\right),
\end{aligned} \tag{3.28}$$

and the angular resolution is given by;

$$\begin{aligned}
\Delta\theta &= \theta^e_{HRS} - \theta^e_{calo} \\
\Delta\phi &= \phi^e_{HRS} - \phi^e_{calo}
\end{aligned} \tag{3.29}$$

Table 3.1 summarizes the results of the angular resolutions for all the elastic data we acquired. In figure 3.18 we show the angular resolution for the elastic calibration performed in Fall 2014. In figure 3.18 we also shown the angular resolution calculated for each of the three calibration settings needed to fully illuminate the calorimeter during the elastic calibrations.

3.4.3 Calibration Optimization with π^0

As the calorimeter gets exposed to beam over time, its crystals undergo radiation damage and they lose their transparency, depending on how close they are to the beam. The gains of the PMTs also change over time and this gradually makes the elastic calibration coefficients invalid. The disadvantage of the elastic calibration technique is that it cannot account for gain variations between two calibrations. Moreover, the elastic calibration is a time consuming procedure which takes hours to set up. It takes a minimum of 4 hours to switch the polarity of the spectrometer from negative to positive and then an additional 4 hours to reverse it for production. This means we cannot perform elastic calibrations frequent enough to be sensitive to gain variations. Instead we use elastic calibrations to extract first order calibration coefficients for the calorimeter.

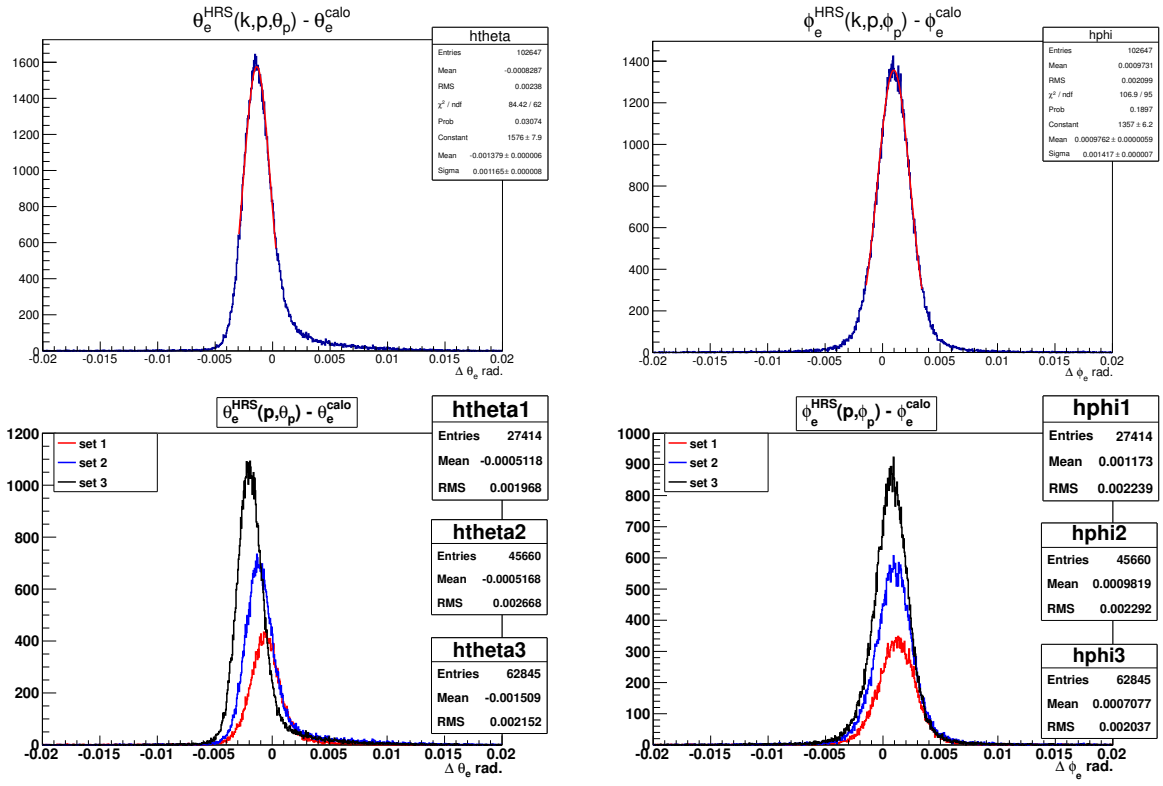

Figure 3.18: Angular resolution for the Fall 2014 elastic data. The top panels show the global resolutions across the whole calorimeter face. The bottom panels show the resolutions for 3 different regions on the calorimeter face. The calorimeter cannot be fully illuminated at one setting hence 3 settings (in the case of the 2014 data the spectrometer angle and momentum setting but for later calibrations it was the calorimeter angle) were used.

A complimentary procedure using π^0 is then used to monitor the gains and optimize the calibration coefficients for each calorimeter crystal block on a daily basis. This method relies on the detection of both exclusive photons originating from the decay of π^0 mesons and adjusting the calibration coefficients such that we recover both the π^0 invariant mass and the proton missing mass. We adjust the individual gain factors of each block by finding the extremum of the following functional [65]:

$$F = \sum_{i=1}^{N}(m_i^2 - m_0^2)^2 + 2\lambda \sum_{i=1}^{N}(m_i^2 - m_0^2), \tag{3.30}$$

where the index i loops over the total number of events N, the masses m_0 and m_i are the π^0 rest mass and the invariant mass as reconstructed by the calorimeter for each event, respectively. The first term in equation 3.30 measures the width of the reconstructed π^0 peak while the second term has the Lagrange multiplier to enforce the constraint $\langle m_i \rangle = m_0$. The π^0 invariant mass for each event is given by:

$$m_i^2 = 2E_1E_2(1 - \cos(\theta_{\gamma_1\gamma_2})), \tag{3.31}$$

where E_1, E_2 are the energies of the two daughter photons of the π^0. $\theta_{\gamma_1\gamma_2}$ is the angle between the two photons calculable from the 4-momentum vectors of both photons ($\mathbf{q}_1$, $\mathbf{q}_2$) as:

$$\cos\theta_{\gamma_1\gamma_2} = \frac{\mathbf{q}_1 \cdot \mathbf{q}_2}{E_1E_2}. \tag{3.32}$$

The calibration is performed iteratively by introducing a small block dependent gain correction factor ϵ_k such that $E_{ji}^{(k)} \rightarrow E_{ji}^{'(k)} = (1 + \epsilon_k)E_{ji}^k$. The index k represents each individual block contributing to the energy (E) of cluster j. To extract the calibration factors we minimize equation 3.30 with respect to ϵ_k:

$$\begin{aligned} \frac{\partial F}{\partial \epsilon_k} &= 2\sum_{i=1}^{N}\left(m_i^2 - m_0^2 + \lambda + \sum_k \epsilon_k \frac{\partial m_i^2}{\partial \epsilon_k}\right)\frac{\partial m_i^2}{\partial \epsilon_k} \\ &= 0. \end{aligned} \tag{3.33}$$

The solution to this set of linear equations is given by:

$$\epsilon_k = [C^{-1}]_{kk'}(D - \lambda L)_{k'}, \tag{3.34}$$

where:

$$
\begin{aligned}
C_{kk'} &= \sum_{i=1}^{N} \left(\frac{\partial m_i'^2}{\partial \epsilon_k} \frac{\partial m_i'^2}{\partial \epsilon_{k'}} \right), \\
D_k &= -\sum_{i=1}^{N} \left((m_i^2 - m_0^2) \frac{\partial m_i'^2}{\partial \epsilon_k} \right), \\
L_k &= \sum_{i=1}^{N} \frac{\partial m_i'^2}{\partial \epsilon_k}.
\end{aligned}
\tag{3.35}
$$

The effect of the calibration optimization with π^0 is illustrated in figure 3.19. After this optimization, we are able to recover better the π^0 rest mass and also gain a some improvement in the resolution.

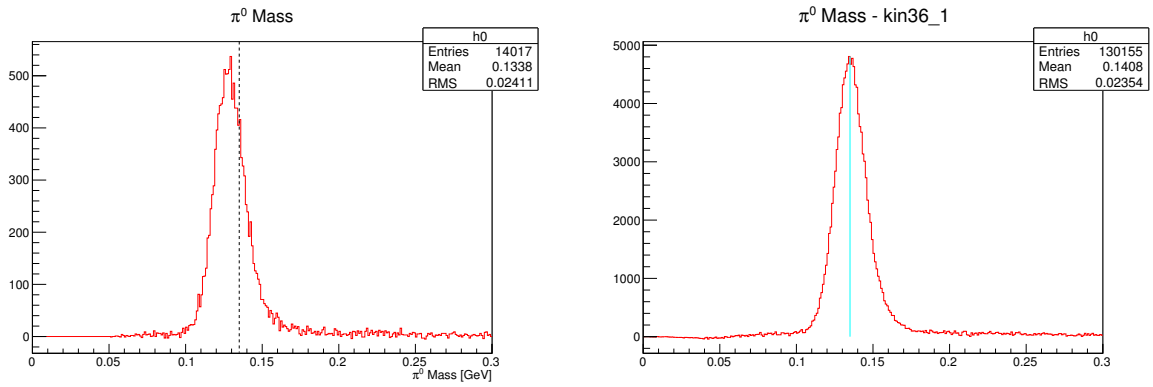

Figure 3.19: Calorimeter calibration optimization with π^0 mesons. Left panel: the π^0 rest mass reconstructed using the calibration coefficients from the elastic calibration only. Right panel: the π^0 rest mass reconstructed using both the elastic calibration coefficients and the optimal values extracted from the π^0 optimization procedure. We are able to recover better the π^0 rest mass (~ 0.135 GeV) after the optimization.

3.5 Pileup Studies

When running at higher currents, we risk a loss in energy resolution as a consequence of a high accidental rate (the accidental rate is proportional to the square of the current) and an increase in pileup events. The default analysis searches for only one cluster and fits the signal using only one pulse. However, when going to high currents, one should consider the possibility of pulse pileup and the growing significance of two clusters in the analysis. This study was done to evaluate by how much we lose on the resolution of the exclusivity peaks when the current is increased. Data at three beam currents was studied: 5 μA, 10 μA and 15 μA. To clean up the exclusivity peak, the following steps were done:

- Applying a number of cuts on the physics data, either looking at single or two cluster analysis
- Accidental subtraction
- π^0 subtraction

To account for accidentals, we looked for events in a 10 ns time window away from the main coincidence window, which was also 10 ns (see the left panel of figure 3.20).

To evaluate the significance (or lack of) of two pulse over single pulse fitting during analysis of the calorimeter data, the data at the three different currents were analyzed first by fitting a single and then fitting two pulses. To make the case for the necessity of one technique over the other, the resolution of the pion invariant mass and that of the pion production missing mass($ep \rightarrow e\gamma\gamma X$) was used. As shown in figure 3.21, the resolution of the exclusivity peak worsens quicker with increasing current for a single pulse fit than it does for the double pulse technique. Therefore, for the final waveform analysis, the two-pulse fit was implemented across all data.

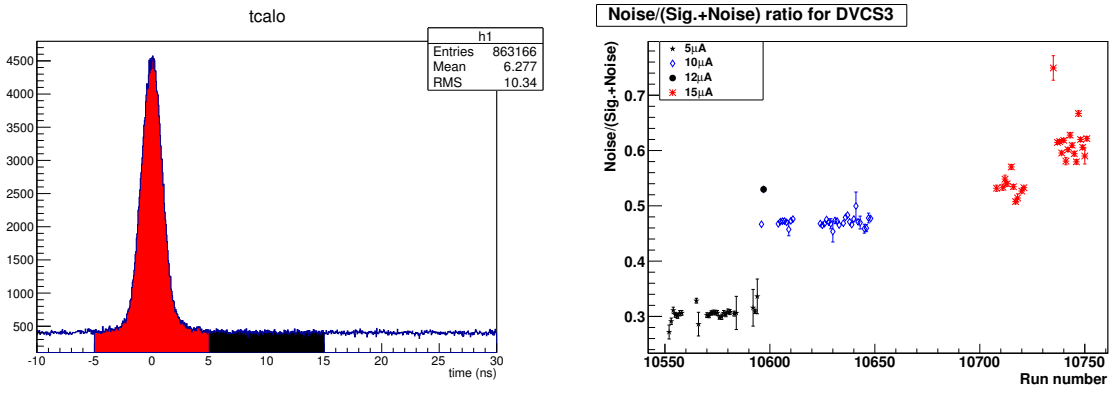

Figure 3.20: Pileup studies with different beam currents on the target. Left panel: A section of the calibrated coincidence time window illustrating the coincidence peak centered at zero (area shaded in red). Away from the coincidence peak is a flat accidental or background region. To estimate the background under the coincidence peak, we look at a time window in the background region (area shaded in black). Both the coincidence and accidental window were chosen to be the same width in time.
Right panel: Noise to signal plus noise ratio for Fall 2014 (kin36_1) data showing an increase of the background with current.

3.6 Conclusion

In this chapter we have presented and discussed the tools and methods used to analyze calorimeter data. Emphasis was put on "general" analysis tools which were developed for the first generation DVCS experiment in Hall A of JLab and then optimized for experiment E12-06-114. The "general" analysis tools include the waveform analysis algorithm used to fit calorimeter signals to extract their amplitude and time of arrival. Critical to the waveform analysis is the extraction of reference shapes (pulses) for each calorimeter channel. Extraction of reference pulses from elastic scattering data was

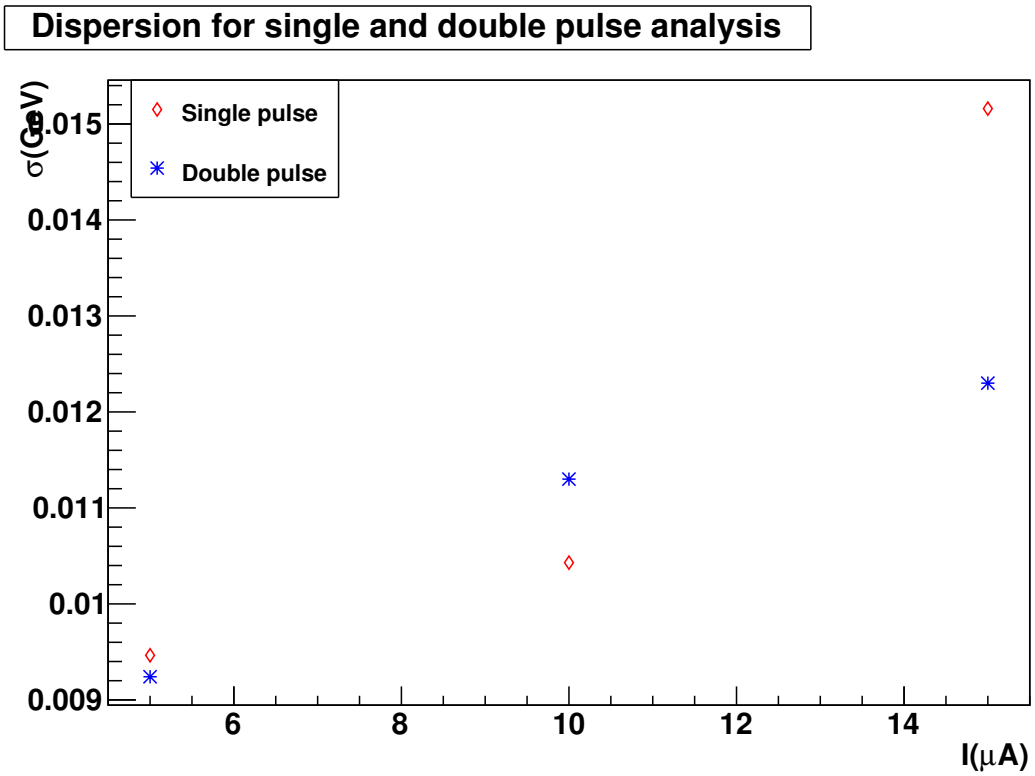

Figure 3.21: The resolution of the π^0 invariant mass as a function of beam current and the choice of one-pulse and two-pulse fitting techniques. The resolution worsens faster for single-pulse fitting (compared to two-pulse fitting) as current increases. For the final waveform analysis of all the data, the two-pulse technique was used.

discussed in section 3.2.1. I extracted, updated and monitored the evolution of reference pulses for all the periods of data acquisition. Also part of the general analysis tools is the clustering algorithm used to integrate over calorimeter data to compute cluster, their position and the total energy deposited. An important pre-requisite for clustering is a proper calibration of the response of the photomultiplier tubes of the calorimeter to energy deposited. An absolute energy calibration of the calorimeter was performed and it is discussed in section 3.4.2. I analyzed and extracted calibration coefficients for all elastic scattering calibration data acquired for experiment E12-06-114. In addition to energy

calibration, I also performed the calibration and optimization of the spectrometer-calorimeter coincidence time to improve the resolution of the coincidence time spectrum and suppress accidental coincidences, as discussed in section 3.3. The coincidence time calibration and optimization was performed for all experiment E12-06-114 data.

4 Monte-Carlo simulation

4.1 Introduction

The purpose of the simulation is to compute the experimental phase space (acceptance) covered by the detectors for each event. The acceptance of the spectrometer is a complicated hyper-volume of five variables: y_{tg} (the position of the electron in the non-dispersive direction) , ϕ_{tg} (the tangent of the angle made by the electron's trajectory to the non-dispersive direction), x_{tg} (the position of the electron in the dispersive direction), θ_{tg} (the tangent of the angle made by the electron's trajectory to the dispersive direction) and δ_{tg} (the fractional deviation of the electron's momentum from the central momentum setting of the spectrometer). The acceptance of the electromagnetic calorimeter is defined by its x and y coordinates and the photon energy.

The simulation is also used to extract the experimental cross section by a fitting procedure which will be discussed later in the chapter. The simulation is based on GEANT4, a detector simulation package written in C++ [70]. In the simulation, the detectors of interest to the experiment in the hall are implemented. This includes their positions in the hall, material used to construct them and their dimensions. Geant4 also provides and supports the fundamental particles of interest, their generation and tracking [70]. The GEANT4 toolkit also handles the interaction of the final state particles with matter, between the vertex and the detectors. Interactions before the vertex are handled by the event generator. The DVCS simulation package in GEANT4 was set up by R. Paremuzyan and M. Defurne [71] for the second generation DVCS experiment in Hall A. I adapted the existing DVCS package for the kinematics of the E12-06-114 experiment. The simulation is limited in that it can not reproduce the resolution effects of the calorimeter as seen in the experimental data. To reproduce the calorimeter resolution in

the simulation, I adapted, optimized and implemented a smearing algorithm developed by M. Defurne [46].

In this chapter we will discuss the main features of the simulation. These features include the event generator which incorporates some real radiative corrections. A brief discussion of the experimental geometry will also be given. A procedure to adjust the resolutions of the simulated calorimeter data so that they can match the experimental resolution widths is also described. The final section of this chapter is dedicated to the fitting procedure for cross section extraction.

4.2 Geometry and experimental set-up

The target cell and the scattering chamber described in section 2.3.2 are implemented in the GEANT4 code exactly the same as in the hall and they are shown for the simulation in figure 4.1. The spectrometer is not fully implemented but only its entrance window is. The entrance window in the simulation is implemented with an acceptance twice as large as the real one to make sure we fully simulate the acceptance of the spectrometer. An electron is deemed to have been detected by the spectrometer once it reaches the entrance window. An acceptance function (called the ”r-function”) is later used to determine if the detected electron is within the good acceptance region of the focal plane. Just like the real spectrometer, the entrance window is placed at a fixed distance from the target and is rotatable by an angle (from the beamline) to be placed at the corresponding position for each kinematic.

The electromagnetic calorimeter is fully implemented, including the positioning of each of the 208 crystal blocks according to a survey done for each kinematic setting in the Hall. The calorimeter also has its angle (from the beamline) and distance from the target adjustable to match that of a kinematic setting of interest.

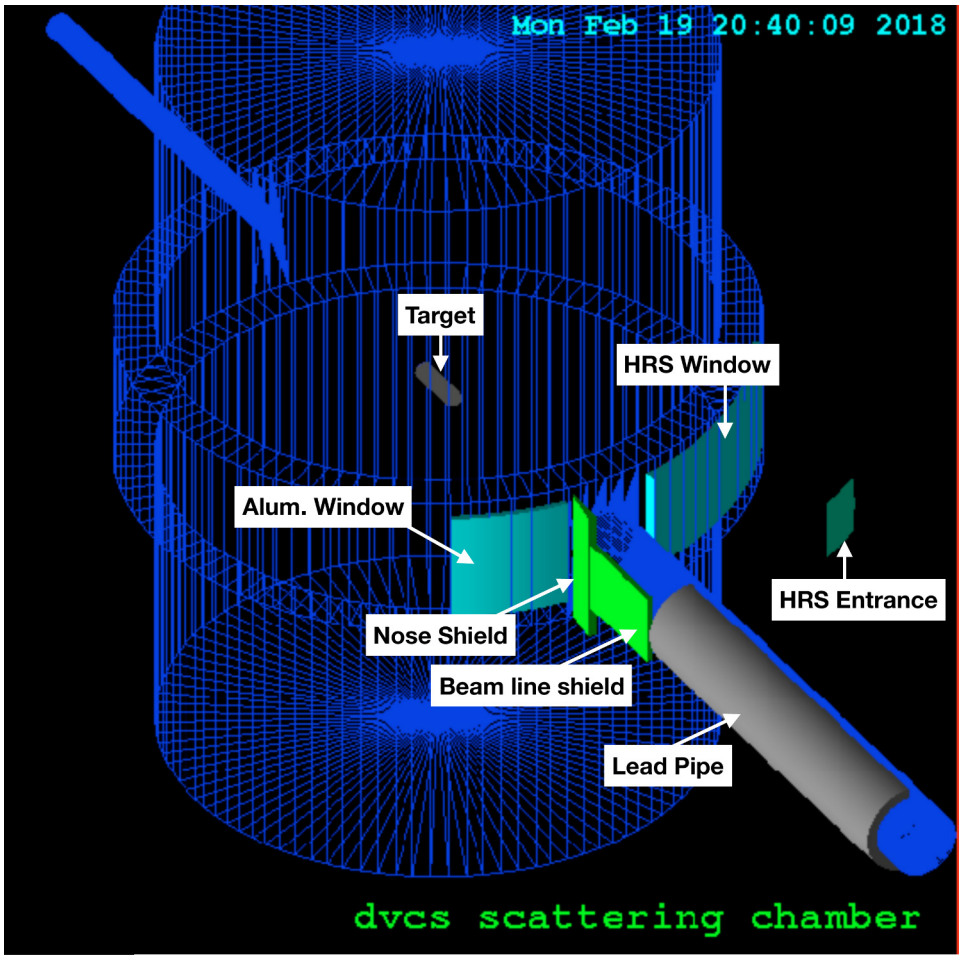

Figure 4.1: The Hall A vacuum scattering chamber as implemented in the simulation is shown here as the cylindrical mesh of blue lines. Also shown is the implementation of the beam dump (labelled Lead Pipe), the spectrometer (HRS) entrance, HRS window, some shielding and the target cell inside the scattering chamber.

The limitation of the simulation is that it cannot reproduce the correct proton missing and π^0 invariant masses and their resolutions. For this reason the simulation needs to be fine tuned to match the data as discussed in section 4.5.

4.3 QED Radiative Corrections

Radiative corrections refer to corrections for Bremsstrahlung effects, where a particle possessing an electric charge emits radiation as it decelerates in an electromagnetic field. Because of its light mass the electron is more susceptible to such interactions than the proton. There are two types of radiative corrections: real and virtual radiative corrections, see figure 4.2.

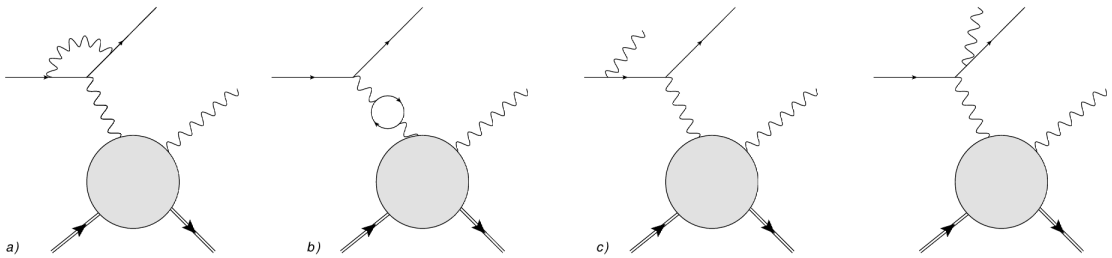

Figure 4.2: Examples of cases of real and virtual radiative effects at first order shown here for electrophoton production. (a) Virtual radiative effect: an electron emits a photon before scattering and reabsorbs it after, altering the electron's momentum on both sides of the vertex. (b) Virtual radiative effect: vacuum polarization where a virtual photon converts into an electron-positron pair. (c) Real photon emitted either before the vertex or after.

4.3.1 Real Radiative Corrections

Real radiative effects refer to Bremsstrahlung emitted by either an incident or a scattered electron. The emission of a real photon modifies the kinematics of the reaction. Real radiative corrections can be external or internal. External radiative corrections are implemented when the electron goes through matter. Internal radiative effects occur and

their corrections are applied at the point of the interaction. As briefly mentioned in the introduction, external radiative effects are handled by the GEANT4 toolkit. Let's consider an electron of initial energy E_0 incident onto a material of thickness x radiation lengths[7]. After traversing the material, the electron's energy loss will follow the distribution [63]:

$$I(E_0, \Delta E, x) = \frac{b \cdot x}{\Delta E}\left[\frac{\Delta E}{E_0}\right]^{b \cdot x}, \tag{4.1}$$

where ΔE is the energy loss by the electron, $b \approx \frac{4}{3}$[63].

Inverting equation 4.1, we get:

$$\frac{\Delta E}{E_0} = U^{\frac{1}{b \cdot x}}. \tag{4.2}$$

U is generated uniformly in range [0,1] in the simulation and the energy loss is applied for each event and each material the electron traverses.

The real radiative processes generate a radiative tail in the exclusivity quantities (proton missing mass and π^0 mass) and since this modifies the kinematics of the reaction experimentally, they have to be taken into account in the calculation of the spectrometer acceptance using the simulation [4].

4.3.2 Virtual Radiative Corrections

Virtual radiative effects occur off nuclei at the reaction vertex. Virtual radiative corrections to the Bethe-Heitler process contain vertex corrections and vacuum polarization corrections [69]. At leading order in QED, three process (shown in figure 4.2) contribute to radiative loses:

- An electron emits a photon before the vertex and re-absorbs it after. This changes the electron's momentum before and after the interaction.

[7] The radiation length is an intrinsic characteristic of a material related to the amount of energy a particle carrying an electromagnetic charge will lose by traversing a distance x of the material.

- The virtual photon splits into an electron-positron pair.
- A real soft photon is emitted. A soft photon refers to when a second photon is emitted and it has an energy much smaller than the initial and final electron energies and also much smaller than the first and energetic photon [69].

All these modifications to the interaction also get convoluted into the cross section of the reaction and have to be corrected for:

$$\sigma_{exp} = \sigma_{Born} \cdot \eta_{virt}, \tag{4.3}$$

where σ_{Born} is the Born cross section (first order theoretical cross section) and η_{virt} is the virtual radiative correction is given by [69]:

$$\eta_{virt} = \frac{e^{\delta_R^0 + \delta_{ver}}}{(1-\delta_{vac})^2}, \tag{4.4}$$

where:

$$\begin{aligned}
\delta_{vac} &= \frac{\alpha_{em}}{3\pi}\left[\ln\left(\frac{Q^2}{m_e^2}\right) - \frac{5}{3}\right], \\
\delta_{ver} &= \frac{\alpha_{em}}{3\pi}\left[\frac{3}{2}\ln\left(\frac{Q^2}{m_e^2}\right) - 2 + \frac{\pi^2}{6} - \frac{1}{2}\ln^2\left(\frac{Q^2}{m_e^2}\right)\right], \\
\delta_R^0 &= \frac{\alpha_{em}}{\pi}\left[Sp\left(\cos\frac{\theta_e}{2}\right) - \frac{\pi^2}{3} + \frac{1}{2}\ln\left(\frac{Q^2}{m_e^2}\right)\right],
\end{aligned} \tag{4.5}$$

where α_{em} is the electromagnetic fine-structure constant, δ_{vac} is the vacuum photon polarization correction, δ_{ver} is the vertex radiative correction and δ_R^0 is the finite part of the radiative correction corresponding to soft photon emission [69].

The virtual radiative effects do not modify the kinematics of the reaction [4] and they can be corrected for by applying a constant correction factor for each kinematic.

4.4 The Event Generator

As shown in the schematic in figure 4.3, the $ep \rightarrow ep\pi^0$ reaction can be divided into 2 parts. The first part is called the leptonic reaction which is describes the emission of the virtual photon. The second part is the hadronic part which handles the recoil proton and the production of the pion.

We generate the leptonic reaction first by uniformly generating events along the full target length in a solid angle larger than the real acceptance of the HRS. A reaction vertex is generated first and then radiative corrections are applied considering the material the electron has passed through and the thickness of the target material up to the vertex point. At the vertex, the scattered electron is generated. The electron horizontal angle θ_e is then generated in such a way that it covers a wider range than the real horizontal acceptance of the HRS. After that we uniformly generate the Q^2 of the reaction in the following range:

$$Q^2 \in \left[4 \cdot E_v^{ext} \cdot p_{min} \cdot \sin^2\left(\frac{\theta_{min}}{2}\right); 4 \cdot E_v^{ext} \cdot p_{max} \cdot \sin^2\left(\frac{\theta_{max}}{2}\right)\right], \tag{4.6}$$

with E_v^{ext} being the incident electron energy corrected for external radiative effects, p_{min}, p_{max}, θ_{min} and θ_{min} are the limits of the scattered electron's momentum and horizontal angle. The momentum acceptance $[p_{min}, p_{max}]$ is defined to be 5.5% around the HRS central momentum instead of the nominal 4.5%. The electron horizontal acceptance (θ_{min} and θ_{max}) is defined to be 60 milli-radians instead of the nominal 28 milli-radians.

Once the reaction Q^2 is generated, the maximum limit on the Bjorken-x variable is then calculated according to:

$$x_B^{lim} = \frac{Q^2}{(m_p + m_\pi)^2 - M^2 + Q^2}, \tag{4.7}$$

where m_p and m_π are the masses of the proton and the pion. The requirement is that the reaction invariant mass should be at the minimum equal to the combined masses of

these two particles for the reaction to be physically possible. x_B is then generated uniformly between limits defined by:

$$\begin{aligned} x_B^{min} &= Max\left(\frac{Q^2}{2M_p(E_v^{ext} - p_{min})}, 0.05\right), \\ x_B^{max} &= Min\left(\frac{Q^2}{2M_p(E_v^{ext} - p_{max})}, x_B^{lim}\right), \end{aligned} \tag{4.8}$$

The generation of Q^2 and x_B is then followed by the simulation of internal real radiative corrections. The azimuthal electron angle ϕ_e is then generated to be wider than the HRS vertical acceptance and used to rotate the scattered electron. The scattered electron is then simulated up to the entrance window of the HRS. The GEANT4 toolkit handles the transport and the associated external radiative corrections.

Next we simulate the hadronic part in the center of mass of the virtual photon-proton system. We generate the squared momentum transfer to the proton (t) uniformly between t_{min} and t_{max}:

$$t_{min} = -Q^2 \frac{2(1 - x_B)(1 - \sqrt{1 + \epsilon^2}) + \epsilon^2}{4x_B(1 - x_B)}, \tag{4.9}$$

t_{max} is fixed at -3 GeV^2 for all events. We then compute the 4-momentum vectors of the final state particles according to the π^0 production kinematics. Once calculated, the 4-vectors are then boosted in the laboratory frame and are rotated around the virtual photon by the angle ϕ_{π^0} generated uniformly in [0;2π]. The decay of the π^0 is isotropically generated in its rest frame and the decay products boosted in the laboratory frame. Finally all particles are rotated around the beam axis in order to simulate the vertical acceptance of the HRS. We finally compute the phase space, which is different for each event, as follows:

$$\Gamma_{\pi^0} = \Delta Q^2 \times \Delta x_B \times \Delta t \times \Delta \phi_{\pi^0} \times \Delta \phi_e, \tag{4.10}$$

where only $\Delta\phi_e$ (=$2 \cdot \pi$) is a constant for all events.

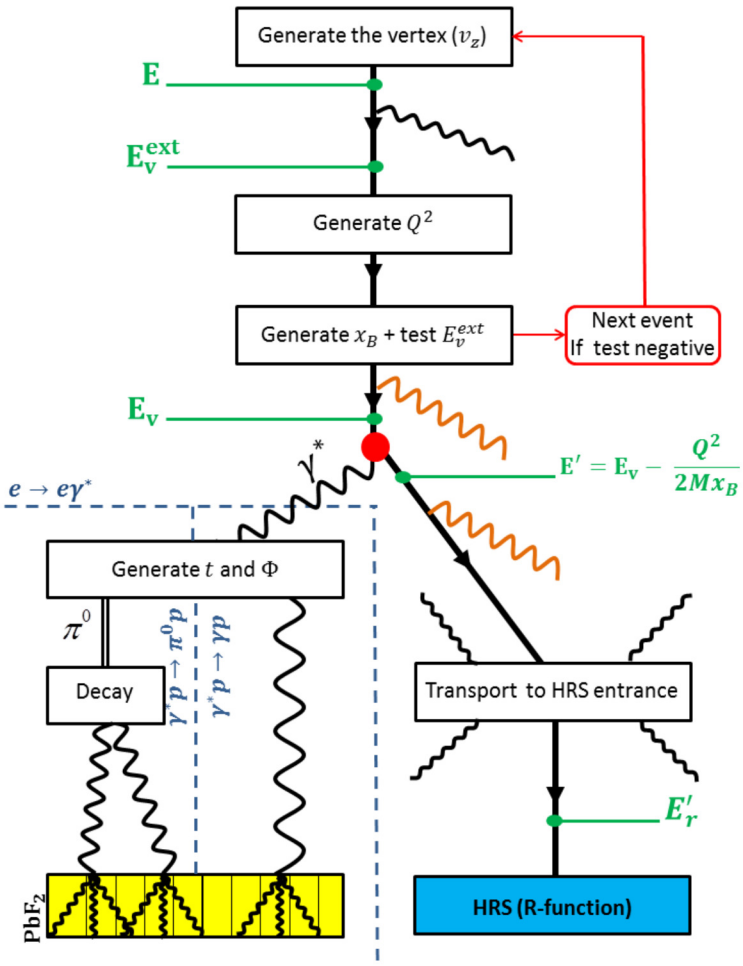

Figure 4.3: A schematic flow of the Monte-Carlo simulation.

4.5 Calibration and Smearing of Monte-Carlo Simulation

The energy and angular resolution of the calorimeter are difficult quantities to simulate. A full simulation of the energy deposited in one PbF_2 block read out by a DVCS photomultiplier tube showed that a 1 GeV photon hitting the middle of the front face of a block produces 1000 photo-electrons [4] and basically explains the energy and angular resolution measured when performing the elastic calibration (see section 3.4.2). In

practise, the number of photo-electrons deposited in the blocks per GeV of incident energy depends on the noise level, for example how close the calorimeter is from the target or the exit beam line. It also depends on the radiation dose accumulated on each block: blocks lose transmission when they accumulate radiation. This effect depends on the block as it seems to be related to the presence of defects in the crystalline structure. Leakage between the different blocks also modifies the relationship between the total energy of the incoming photon and the total energy measured by the different calorimeter blocks. All of these effects result in the measured energy being lower than the actual energy and the missing masses being higher than the physical rest masses. To correct for these effects, we chose first to simulate a ”perfect” energy deposition and then perform both a smearing and calibration based on the resolution and the energy calibration of the data.

4.5.1 Smearing procedure

The resolution of the reconstructed proton mass and the measured photon energy is dominated by the calorimeter's energy resolution which depends on the position of impact on the face of the calorimeter: blocks at different distances from the beamline experience different levels of noise. Therefore, the calorimeter was divided into 49 partially overlapping areas to perform a ”local” smearing for each area. To support interpolation of the calibration coefficients around the edges of the calorimeter, eight more points were added. We take the four-momentum vector of each photon and apply the following smearing-calibration transformation [46]:

$$\begin{bmatrix} q_x \\ q_y \\ q_z \\ E \end{bmatrix} \longrightarrow Gaus(\mu, \sigma) \times \begin{bmatrix} q_x \\ q_y \\ q_z \\ E \end{bmatrix}, \tag{4.11}$$

where μ is a calibration parameter correcting for the imperfections of the simulation in estimating the photon energy compared to the experimental data and σ is the smearing parameter accounting for the calorimeter resolution. These parameters were obtained by performing a χ^2 comparison of both the reconstructed proton mass and the measured π^0 mass between the data and the simulation. The parameters were adjusted until the best match between data and simulation was obtained. Since the smearing procedure was done for only 49 areas (plus 8 on the edges), an interpolation algorithm was used to smear data points which hit the calorimeter away from the centers of these areas. Figures 4.4 show the calibration and smearing parameters as a function of position on the calorimeter face. Figure 4.5 shows the angular resolution of the calorimeter as a function of position. The resolution can be seen worse close to the beam as a result of a high accidental rate. A comparison of the reconstructed proton mass and the π^0 mass before and after the smearing is shown in figures 4.6 and 4.7, respectively.

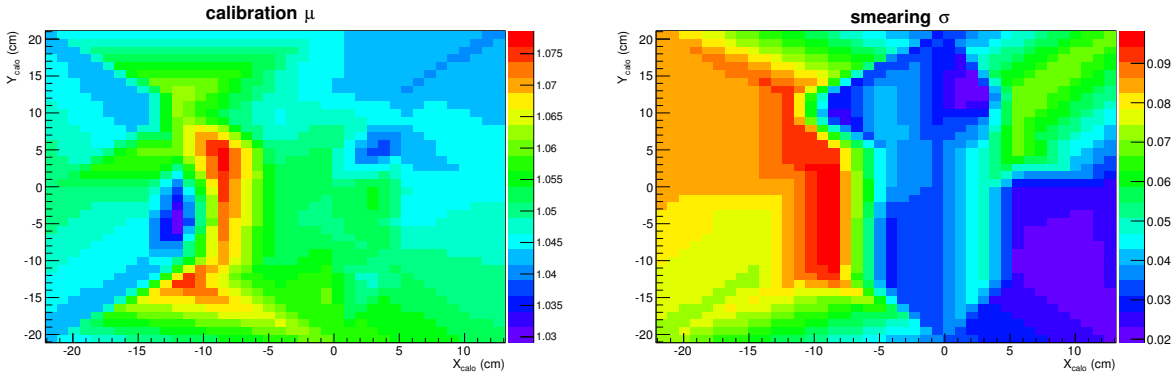

Figure 4.4: The position dependent calibration coefficient μ (in GeV) shown on the left panel and the smearing parameter σ (GeV) on the right panel.

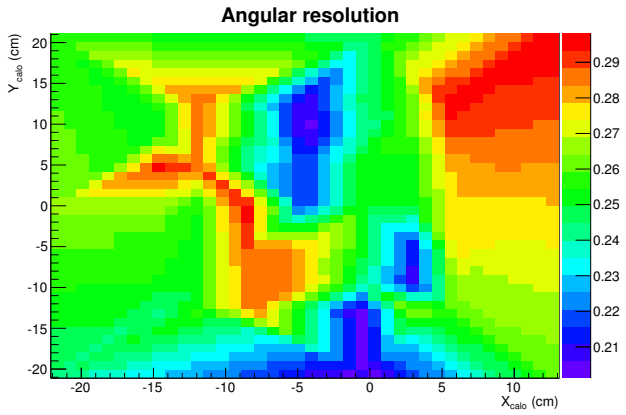

Figure 4.5: The angular resolution as a function of position on the calorimeter face. The resolution is driven by both the proximity to the beamline (worse closest to the beamline because of a high accidental rate) and the quality of the PbF_2 crystals.

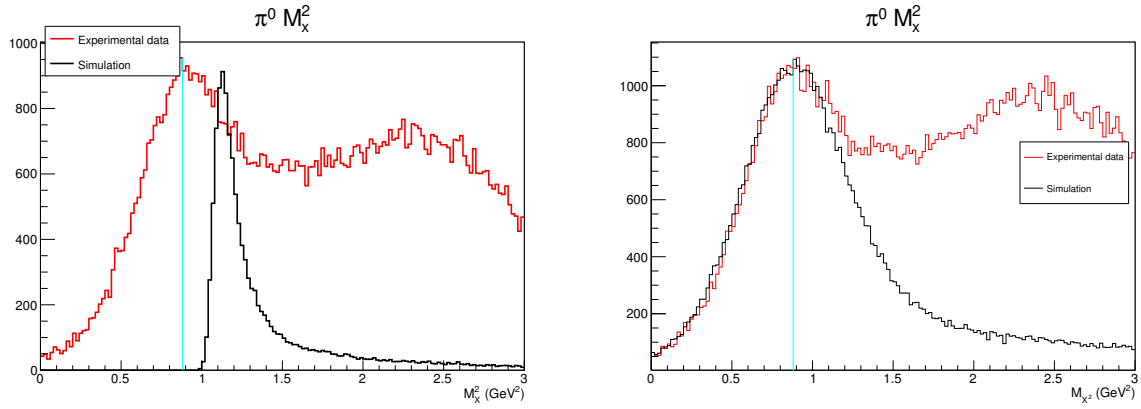

Figure 4.6: Spectrum of the π^0 production missing mass ($ep \rightarrow e\gamma\gamma X$) of the Monte-Carlo simulation compared to data. Left: Before the smearing and calibration procedure. Right: After calibration and smearing procedure.

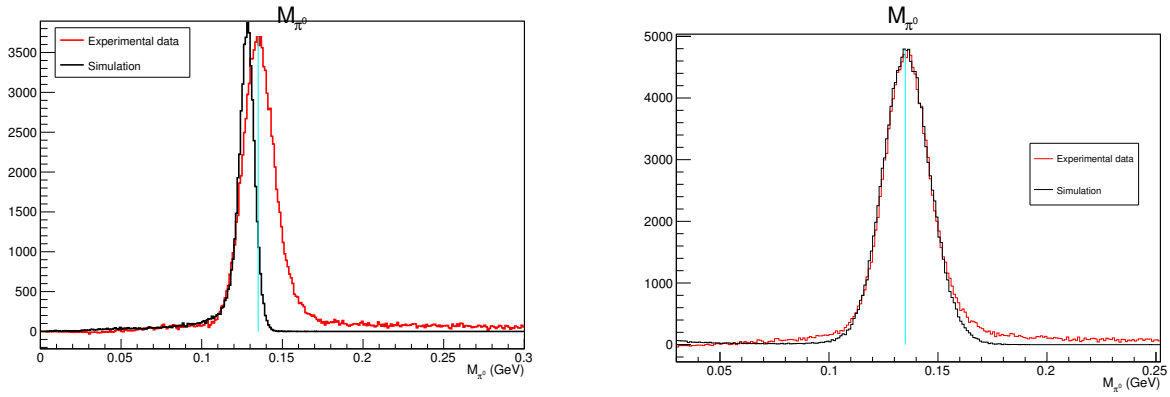

Figure 4.7: Spectrum of the π^0 invariant mass of the Monte-Carlo simulation compared to data. Left: Before the smearing and calibration. Right: After calibration and smearing.

4.6 Fitting procedure and cross section extraction

We extract the cross section by comparing the number of experimental events to a prediction by a Monte-Carlo simulation. We use the parametrization of the π^0 production cross section described in section 1.3.3.3 with the Monte-Carlo simulation to extract the different response terms to the cross section. This method brings two advantages with it [4]:

1. It integrates the kinematic dependencies over the entire acceptance of the experimental geometry.

2. It corrects for bin migration caused by the resolution effects of detectors.

4.6.1 Procedure

Let us define two types of binning:

- Reconstructed bins: based on kinematic variables as reconstructed by the detectors.
- Vertex bins: based on kinematic variables at the reaction vertex. Variables at the vertex can only be accessed in the simulation.

If there were no radiative and detector resolution effects, the reconstructed and vertex kinematics would be the same. To extract the cross section, we need both the vertex and reconstructed kinematic variables. As we know both the reconstructed and vertex variables in the simulation, we can construct a bin migration matrix K_{rv} whose elements are the probabilities for an event to belong to the vertex bin v and the reconstructed bin r. Defining N_r as the total number of events in reconstructed bin r, we have:

$$\forall r \; N_r = \sum_{v=1}^{\mathcal{V}} K_{rv} N_v, \tag{4.12}$$

where N_v is the number of events in the vertex bin v. N_v is related to the cross section:

$$N_v = \mathcal{L} \int_{\Phi_v} \frac{d^4\sigma_v}{d\Phi} d\Phi, \tag{4.13}$$

where $d\Phi$ is the four-fold phase-space factor ($dQ^2 \; dx_B \; dt \; d\phi_\pi$). We can then re-write equation 4.12 as follows:

$$N_r = \mathcal{L} \sum_{v=1}^{\mathcal{V}} K_{rv} \int_{\Phi_v^r} \frac{d^4\sigma_v}{\Phi} d\Phi. \tag{4.14}$$

Assuming a cross section which is stable over the space Φ_v, the previous equation can be written as:

$$N_r = \sum_{v=1}^{\mathcal{V}} K_{rv} \left(\mathcal{L} \int_{\Phi_v^r} d\Phi \right) \times \frac{d^4\sigma_v}{d\Phi} \tag{4.15}$$

We then use the simulation to define and compute the matrix K_{rv} by performing the integration in equation 4.15 above and we get the following result:

$$K_{rv} = \sum_{i \in r \cap v} \frac{\Gamma^i_{MC}}{N_{gen}}, \tag{4.16}$$

where i is an event in reconstructed bin r and vertex bin v, Γ^i_{MC} is the phase-space factor and N_{gen} is the number of generated events in the simulation.

Consider the parametrization of the π^0 cross section introduced by equation 1.40, it can also be compressed into the form:

$$\frac{d^4\sigma}{dQ^2 dx_B dt d\phi} = \sum_{n=1}^{N} \Gamma_n(E, Q^2, x_B, \phi) X^n, \tag{4.17}$$

where Γ_n is a known function depending on the kinematic variables and X^n is a column vector of the cross section parameters we want to extract. In our case we can extract 4 parameters as mentioned in the introduction of this section, therefore, N=4 and $X^n = \{\sigma_T + \epsilon, \sigma_{TT}, \sigma_{LT}, \sigma_{LT'}\}$. We can now use equation 4.17 in equation 4.14 to connect the number of reconstructed events to the cross section parameters X^n:

$$N_r = \sum_{v=1}^{\mathcal{V}} \sum_{n=1}^{N} K^n_{rv} X^n_v. \tag{4.18}$$

The migration probability matrix also takes the form:

$$K^n_{rv} = \sum_{i \in r \cap v} \Gamma_n(E, Q^2, x_B, \phi) \frac{\Gamma^i_{MC}}{N_{gen}} \tag{4.19}$$

An example of the migration probability matrix for the first term in the cross section parametrization of equation 1.40 is shown in figure 4.8.

We can now construct a χ^2 which will be minimized to extract X^n:

$$\chi^2 = \sum_{r=1}^{\mathcal{R}} \left(\frac{N^{exp}_r - N^{MC}_r}{\sigma^{exp}_r} \right)^2, \tag{4.20}$$

where $\mathcal{R}$ is the total number of experimental bins, N^{exp}_r represents the number of events in experimental reconstructed bin r with the error σ^{exp}_r. N^{MC}_r is the number of events in simulation reconstructed bin r.

The coefficients $\bar{X}^n$ are then defined as the values of X^n which minimizes the χ^2 of equation 4.20:

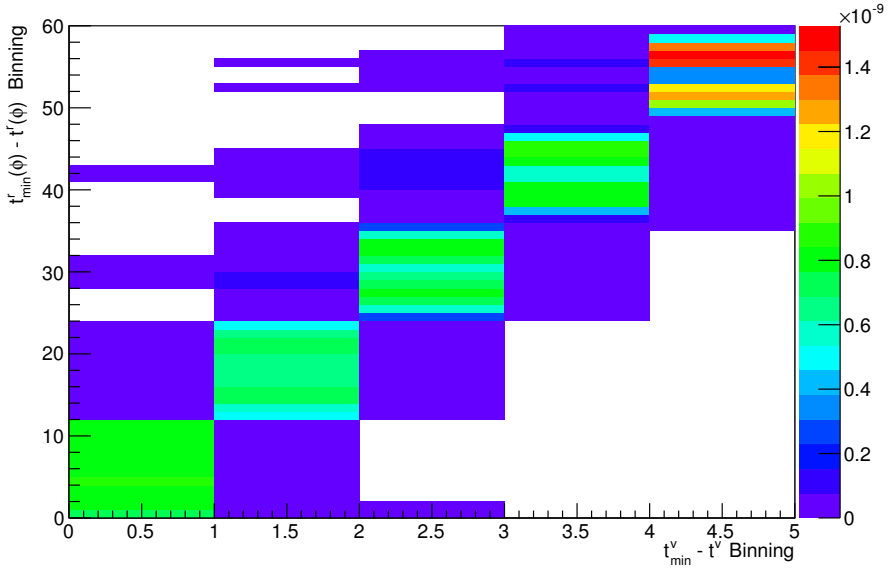

Figure 4.8: The migration probability matrix for the first term in the cross section parametrization of equation 1.40, shown here for Kin36_1. The horizontal axis shows the binning in the momentum transfer to the proton at the vertex (t^v). The vertical axis shows binning in the reconstructed momentum transfer (t^r) as a function of binning in the angle between the hadronic and the leptonic planes (ϕ). Each t^r bin is divided into 12 ϕ bins. The dense diagonal is the case where both the vertex and reconstructed kinematics fall in the same t bin and the off-diagonals are cases where $t^r \neq t^v$ (bin migration cases).

$$0 = -\frac{1}{2}\frac{\chi^2}{\partial X^n_v}\bigg|_{\bar{X}}, \tag{4.21}$$

$$0 = \sum_{v'=1}^{\mathcal{V}} \sum_{n'=1}^{N} A^{n,n'}_{v,v'} \cdot \bar{X}^{n'}_{v'} - B^n_v \; \forall v, \; n. \tag{4.22}$$

Equation 4.22 is a matrix system defined by:

$$A^{n,n'}_{v,v'} = \sum_{r=0}^{R} \mathcal{L}^2 \frac{K^n_{rv} \cdot K^{n'}_{rv'}}{(\sigma^{exp}_r)^2},$$
$$B^n_v = \sum_{r=0}^{R} \mathcal{L} \frac{K^n_{rv} \cdot N^{exp}_r}{(\sigma^{exp}_r)^2}. \tag{4.23}$$

This linear system of equations is solved by inverting matrix A and obtaining the cross section parameters:

$$\bar{X}^n_v = \sum_{v'=1}^{\mathcal{V}} \sum_{n'=1}^{N} [A^{-1}]^{n,n'\,n'}_{v,v'\,v'}, \tag{4.24}$$

where A^{-1} is the covariance matrix. The error on each extracted parameter of $\bar{X}^n$ is given by the corresponding diagonal element of A^{-1}:

$$\delta\sigma^2_n = (A^{-1})_{nn}. \tag{4.25}$$

Taking into accounts the effects of bin migration, the number of simulation counts per bin can be written as follows:

$$N^{MC} = \mathcal{L} \sum_{v,n} K^n_{rv} \cdot X^n_v. \tag{4.26}$$

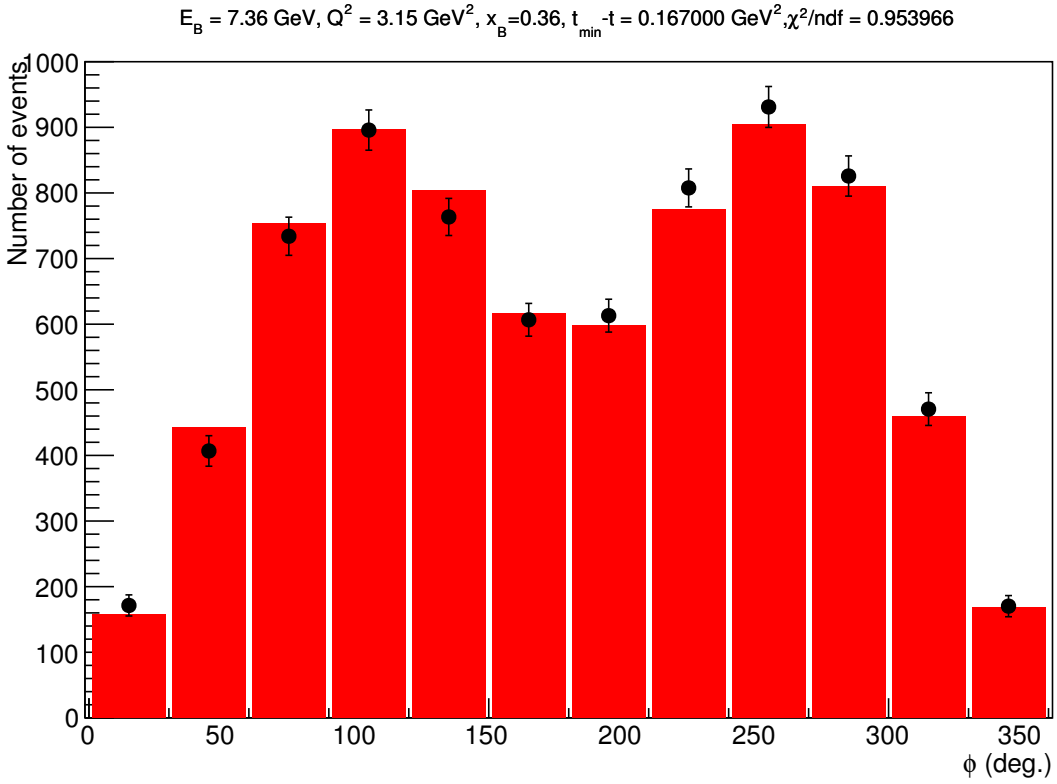

Figure 4.9: The number of events (from experiment) in a t_{min} - t bin of Kin36_1 is shown as the black points with the associated statistical errors. The red histogram represents the number of events in the same t_{min} - t bin as estimated by the Monte-Carlo simulation. The cross section is extracted by minimizing the difference between the experimental number of events and the estimate of the simulation.

5 Data Analysis and Results

Having discussed the principle of cross section extraction in chapter 4, we now focus on the analysis criteria and cuts employed to select the exclusive π^0 events from the data. We then apply the fitting procedure to extract the cross section and present the results. We present in this chapter the general event selection criteria applicable to all kinematics. We however present results for kin36_1 only. Analysis for other kinematics (kin36_2 and kin36_3) is still in progress and we show only preliminary results for these kinematics.

5.1 Selection of Exclusive π^0 Events

To select a clean π^0 sample we applied a number of cuts starting with the selection of good electron events based on the spectrometer variables only. Once a good electron was identified, a second set of cuts was applied to select good π^0 events in the calorimeter. Finally, even after these cuts, our events were still susceptible to some accidental contamination. Accidentals are uncorrelated (not coming from the same reaction) electron-π^0 events which gave a coincidence even when the basic electron and calorimeter cuts had been implemented. To remove accidental contamination, we relied on the excellent spectrometer-calorimeter timing resolution of the experiment.

5.1.1 Electron Selection

5.1.1.1 Particle Identification (PID) Cuts

As mentioned in section 2.3.3, the electron trigger was formed by the coincidence of a scintillator (S2m) and a gas Cherenkov (CER) detector. The gas Cherenkov was designed to prevent pions below 4.8 GeV/c from producing Cherenkov radiation by using a medium (carbon dioxide) with a refractive index such that the pions do not exceed the speed of light. However, the discriminator threshold of the Cherenkov was set very low (15 mV) during the experiment and a lot of pion events qualified to form a trigger. In

addition to that, unlike the scintillators which triggered on any of the sixteen paddles getting fired, the gas Cherenkov triggered on the analog sum of all the ten PMTs. To suppress pion contamination, a Cherenkov selection threshold was set at 150 channels, see 5.1.

Once the Cherenkov had been used to suppress pions, our sample was still contaminated by medium energy electrons also known as δ rays. δ rays are electrons produced by pions interacting with matter between the target and the detector stack. Since they are electrons, they produce enough Cherenkov radiation to form a trigger and also qualify as good electron events according to the gas Cherenkov detector (above 150 Cherenkov channels). To suppress δ rays, we used the electromagnetic calorimeter (also known as pion rejectors) in the spectrometer. Since electrons will lose all their energy in the calorimeter, a spectrum of the energy deposited in the calorimeter will distinguish between pion, δ and good electron events. The bottom panel of figure 5.1 shows the pion rejector spectrum showing three distinct regions: a low energy peak representing pions, a high energy peak representing a good electron signal and a flat region of δ rays in between.

5.1.1.2 Vertex and Tracking Cuts

Tracking cuts were also applied to select events with a good track in the VDCs. The Hall A Analyzer (the standard track reconstruction algorithm developed specifically for Hall A) is not well adapted to handle events for which more than one track in the VDC planes is detected. To get around this Analyzer limitation, only events for which one cluster was detected are selected [75]. To compensate for the removal of events which even though they were multi-cluster but could still have been good electron events, a tracking correction (discussed in section 5.3.1) is applied run by run.

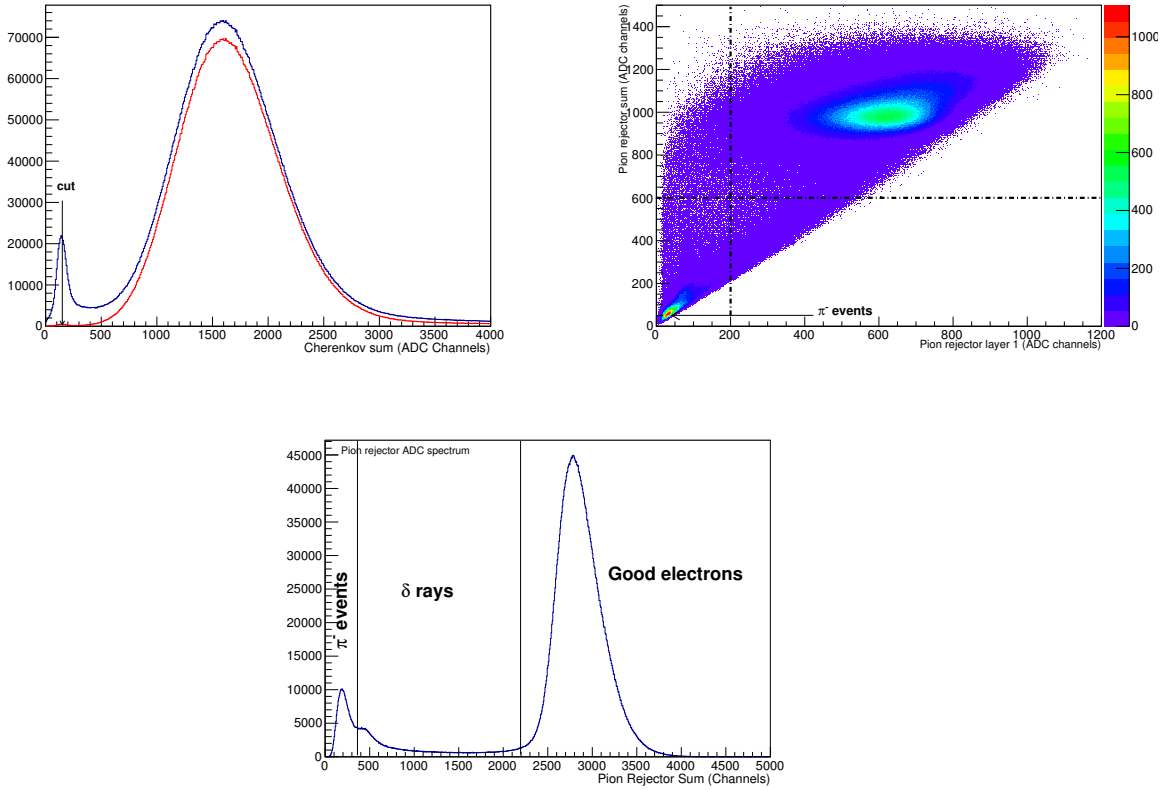

Figure 5.1: Electron PID selection. Top left: the Cherenkov ADC spectrum for π^0 events in kin36_1 without any cuts (blue) and with the pion rejector cuts (red). The minimum ionization peak (single photon peak) is centered at 150 channels as seen on the blue spectrum. Top right: the pion rejector sum plotted against the first layer of the pion rejectors. The dash-dotted lines represent cuts applied to both the pion rejector sum and the first layer of the pion rejectors. Bottom panel: energy deposited in the electromagnetic calorimeters (pion rejectors) of the spectrometer without any cuts applied. Three distinct regions can be seen and selection cuts can be easily applied to suppress pion and medium energy electron events.

Cuts along the target length (vertex cuts) were also applied to remove contributions from events which scattered off the aluminium walls and the end caps of the target cell. To define the vertex cuts for each kinematic, data taken on a dummy target were used to locate the position of the target end caps. A distribution of the z-coordinate of the interaction vertex is shown in figure 5.2.

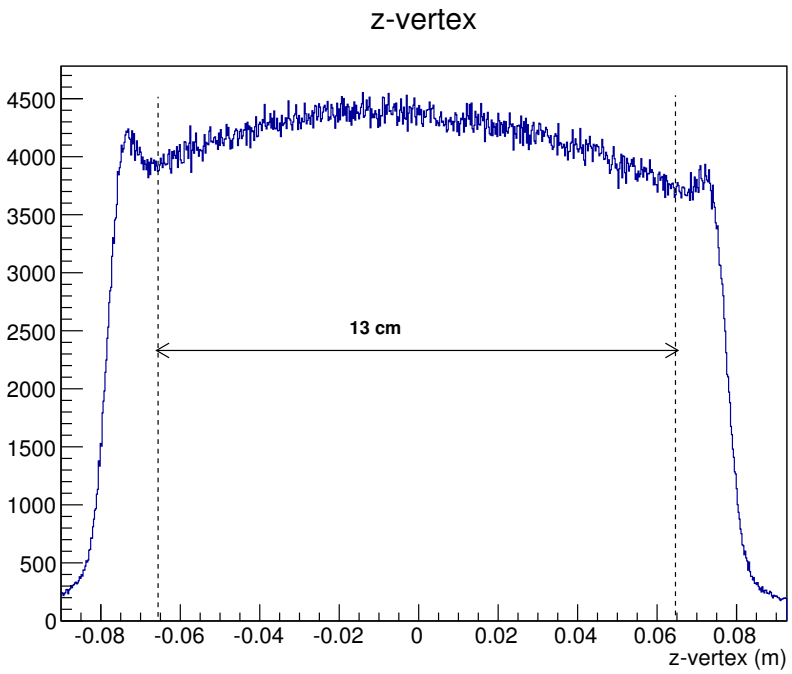

Figure 5.2: The z-coordinate of the vertex of the reaction along the target for kin36_1 shown for runs taken at 5 μA only. The peaks at the edges correspond to events scattered off the aluminium walls of the target cell. The vertical dotted lines represent the selection cuts along the vertex, only events between them were selected.

5.1.1.3 Phase Space and Acceptance (R) Cuts

Finally, ”R-cuts” were applied to select events which passed through a well understood part of the spectrometer acceptance. The ability to properly reconstruct an event depends on how well we understand the magnetic field of the spectrometer and the relevant optics transport matrix connecting the target (reaction area) and the detector stack. Usually, the magnetic field and hence the acceptance is poorly understood at the fringes. To complicate matters, the acceptance of the spectrometer is a region defined by 5 kinematic variables. Making a cut in each variable independently would not work because the variables are correlated. To get around this problem, an R-function was used. The 5-dimensional R-function takes as its arguments variables y_{tg}, ϕ_{tg}, x_{tg}, θ_{tg} and δ_{tg}, as defined in figure 5.4 and chapter 4. With these inputs, the R-function returns an R-value defined as the minimum distance from a test point to the boundary of a polygon in a plane [72]. In this analysis we used R-cuts implemented by Johnson [76]. A summary of the applied R-cuts is given in table 5.4 for each kinematic. The phase space of this kinematic with and without the acceptance cuts is shown in figure 5.3.

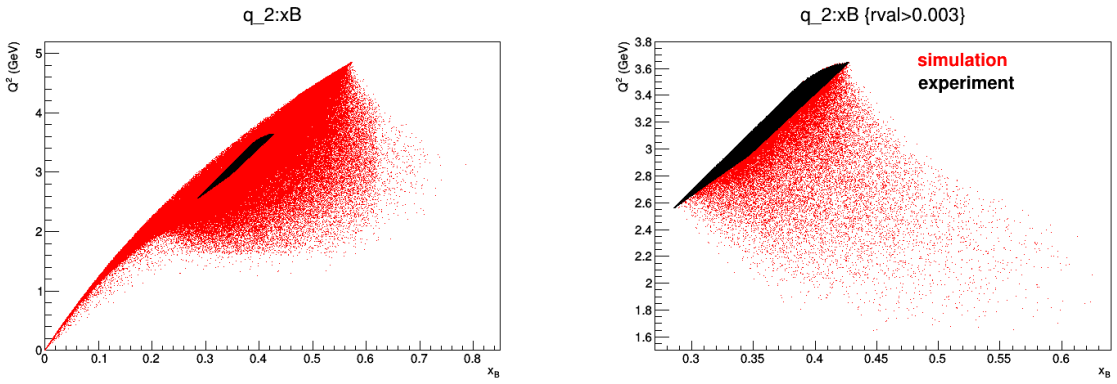

Figure 5.3: Phase space of kin36_1 shown for both simulation and the experimental data. Left panel: with no R-cuts. Right panel: with R-cuts implemented.

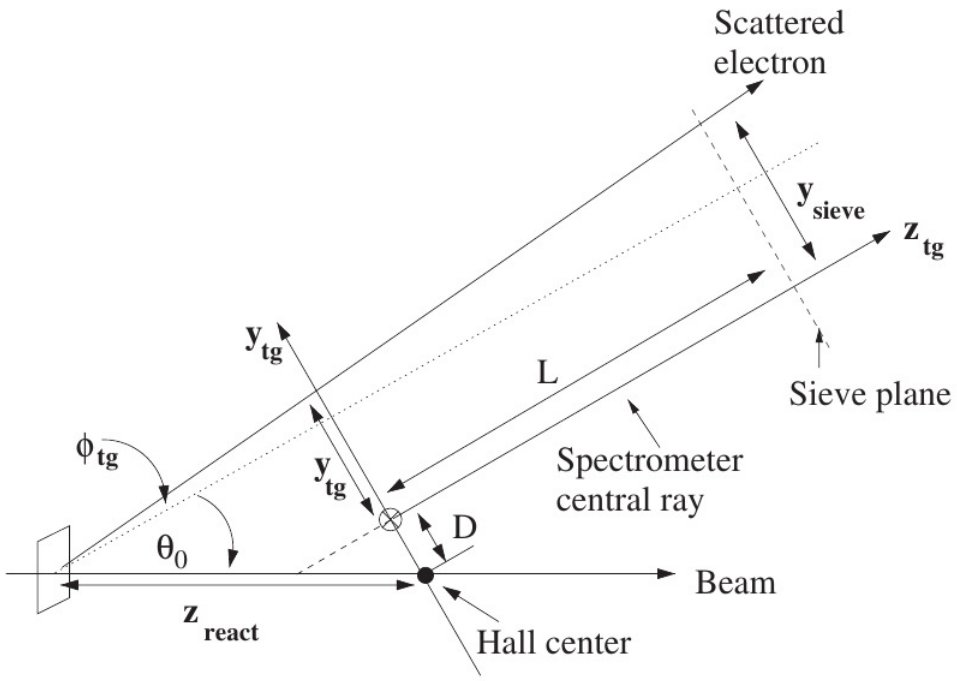

Figure 5.4: Hall A coordinates for scattered electron into the spectrometer and the variables which define the spectrometer acceptance as shown in Ref. [52]. L is the distance from the hall center to the entrance of the spectrometer, D is the displacement of the spectrometer axis from its ideal position. θ_0 is the spectrometer central angle setting.

5.1.2 π^0 Selection

From the events with a good electron, we then selected events with two clusters above a set software energy threshold. The software threshold was driven by two factors:

- The hardware threshold set during data acquisition determined the lowest software threshold we could apply. Looking for clusters below the hardware threshold would be similar to searching for clusters from background signals.

- The expected pion energy for a particular kinematic. If a pion decays symmetrically, each daughter photon will carry half of the pion's initial energy and we set our software high enough to stay clear off background and not too close to the expected photon energy. To accommodate the case of asymmetrical decays, we imposed the "above threshold" energy cuts just for one of the two photons and loosened the energy requirement on the second one.

Table 5.1 summarizes the hardware and software thresholds for the different kinematics. It is worth noting that the hardware threshold was set during DAQ and could not be changed at the analysis stage.

Table 5.1: Clustering thresholds for the kinematics

Information	Kin36_1	Kin36_2	Kin36_3
Hardware threshold (GeV)	1.1	1.48	1.48
Expected π^0 energy (GeV)	4.5	5.2	6.5
Software threshold(GeV)	1.2	1.5	1.5

After two cluster events were identified, we applied cuts on both the invariant mass of the π^0 and the missing mass of the recoil proton to isolate the $ep \rightarrow e\gamma\gamma X$ reaction. The invariant mass and the missing mass are correlated because of fluctuations due to the calorimeter's imperfections in measuring the energy of the photons, which in turn correlates fluctuations in the proton missing and the π^0 invariant mass. To remove this correlation, we adapted an empirical approach from M.Mazouz [97]:

$$M_X^2 = M_X^2\big|_{raw} + C \cdot (m_{\gamma\gamma} - m_{\pi^0}), \tag{5.1}$$

where $M_X^2\big|_{raw}$ and M_X^2 is the proton missing mass before and after the decorrelation procedure. $m_{\gamma\gamma}$ is the ideal π^0 invariant mass and m_{π^0} is the average π^0 invariant mass as measured by the calorimeter. C is an empirical correction factor obtained by studying the fluctuations of the π^0 production missing mass as a function of the energy of the two photons measured by the calorimeter:

$$C = \frac{2E_1E_2}{m_{\pi^0}(E_1+E_2)}\left(m_{\pi^0}^2 - 2\sqrt{2}\left(\nu + M - q\cos(\theta_{\pi\gamma^*})\right)\right), \tag{5.2}$$

where E_1, E_2 are the photon energies, ν is the energy transfer to the virtual photon, M is the proton mass, q is the π^0 momentum 4-vector and $\theta_{\pi\gamma^*}$ is the angle between the π^0 and the virtual photon. Calculation of C was done for each event and an average value was used for the final correction. Removal of the correlation enabled us to apply one dimensional cuts on both variables as shown in figure 5.5.

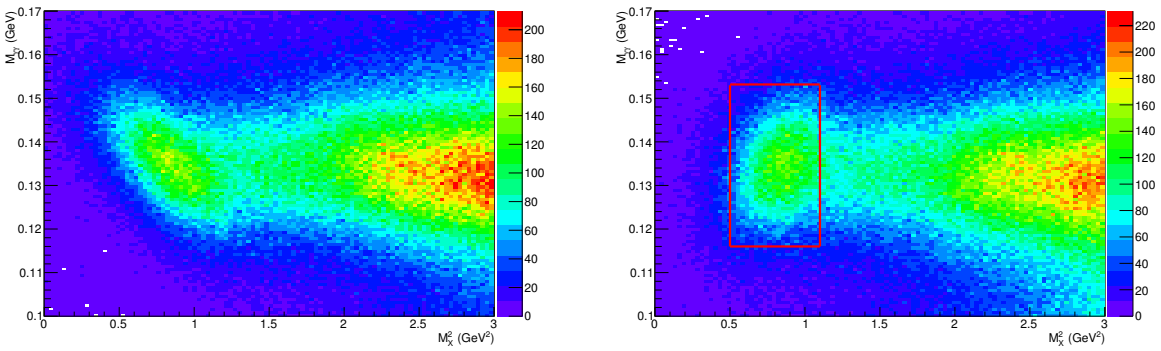

Figure 5.5: π^0 selection based on energy and momentum conservation. Left panel: raw invariant mass against missing mass distribution for kin36_1. Right panel: the invariant mass vs. missing mass distribution after corrections and removal of the correlation. The red box illustrates the selection cuts given in table 5.2.

Table 5.2: π^0 Exclusivity cuts for all kinematics.

Kin36_1	Kin36_2	Kin36_3
M_X^2[0.5,1.10]	M_X^2[0.5,1.15]	M_X^2[0.5,1.15]
M_{π^0}[0.116,0.153]	M_{π^0}[0.124,0.146]	M_{π^0}[0.1,0.155]
E^γ >1.1 GeV	E^γ >1.5 GeV	E^γ >1.5 GeV

Table 5.3: Coincidence Selection Cuts. These are the same for all kinematics.

Cut Name	Cut Details
Triple coincidence (T_{ccc})[-3,3]	$\|t^{\gamma^1}\|$ <=3,$\|t^{\gamma^2}\|$ <=3
Accidental π^0 (T_{acc})[-11,-5]	$\|t^{\gamma^1} + 8\|$ <=3,$\|t^{\gamma^2} + 8\|$ <=3
Accidental photon (T_{cac})[-11,-5],[-3,3]	$\|t^{\gamma^1}\|$ <=3, $\|t^{\gamma^2} + 8\|$ <=3
Triple accidentals (T_{aaa})[-11,-5],[5,11]	$\|t^{\gamma^1} + 8\|$ <=3,$\|t^{\gamma^2} - 8\|$ <=2
Calorimeter edge x[-21,12],y[-21,21]	3 cm from edge

5.2 Accidental Subtraction

Our reaction channel is a two-body final state but the π^0 decays into two photons. In the end we detect three particles in coincidence, the scattered electron and the two photons. To select true coincidence events, we applied additional cuts on the arrival times of the photons as detailed in table 5.3. Timing corrections discussed in section 3.3 were implemented such that in the end we have the timing of each photon with respect to the scattered electron as shown in figure 5.6. True coincidences are within the electron's arrival timing window centered around (0,0) in figure 5.6. The time window was set to be ±3 ns wide (chosen to be $\pm 3\sigma$, where σ is the calorimeter-spectrometer corrected time

resolution, see section 3.3). Unfortunately, the sample in the [-3,3] ns window is still contaminated by accidentals. To remove contamination by accidentals, we studied several time windows which describe the time distributions of both photons (the calorimeter) with respect to the electron (spectrometer), see figure 5.6. There are three contributions to the accidentals:

$$N^{ACC}_{e'\gamma_1\gamma_2.} = N_{aaa} + N_{cac} + N_{acc},$$

(5.3)

where the subscript *a* denotes an accidental particle and the subscript *c* stands for a particle in coincidence (and the order is scattered electron,"first" and "second" photon, as denoted on the left hand side of equation 5.2). Therefore, the right-hand side of equation can be broken down as:

1. N_{aaa} represents the number of purely uncorrelated signals detected for all three particles. This is the baseline background of the experiment represented by the points away from the vertical, horizontal and diagonal bands (in time box R_1) in figure 5.6.

2. N_{cac} represents the number of events which have the electron in coincidence with only one photon, the other photon is accidental. This sample is represented by either the vertical or horizontal band in figure 5.6.

3. N_{acc} represents the number of events where the two photons are correlated and the electron is an accidental. These events can be seen occupying the diagonal band, away from the peak at the origin in figure 5.6.

To estimate each term that makes up the accidentals, we looked at the following time windows which were defined to have the same width as our main coincidence window (also summarized in table 5.3):

- We applied selection cuts to two-photon events in the time range [-11,-5] ns (time box R_3 in figure 5.6) on both photons to get $N_{acc} + N_{aaa}$.
- We applied cuts to select one photon in the range [-3,3] ns and another in in the range [-11,-5] ns (time box R_4 in figure 5.6) to get $N_{cac} + N_{aaa}$.
- To compensate for a possible double correction for N_{aaa}, we looked at events passing the analysis cuts but with one photon in the range [-11,-5] ns and the other photon in the range [5,11] ns (time box R_1 in figure 5.6). This gives the number of pure randoms, N_{aaa}.

To get the final accidental correction, we add the first two results and then subtract the last one:

$$N^{acc.} = R_3 + R_4 - R_1. \tag{5.4}$$

5.3 Efficiencies

5.3.1 Tracking Efficiency, η_{track}

As discussed in subsection 5.1.1.2, the standard Hall A Analyzer poorly reconstructs events which have multi-tracks in the VDCs. We excluded these events from the main analysis but at the same time we don't know how many of them are actually good electron events. To correct for that, we introduced a correction factor in the name of tracking efficiency. To calculate the tracking efficiency, we used PID cuts to select a sample of good electrons, lets call this sample N_{PID}. Then from N_{PID} , we counted the number of

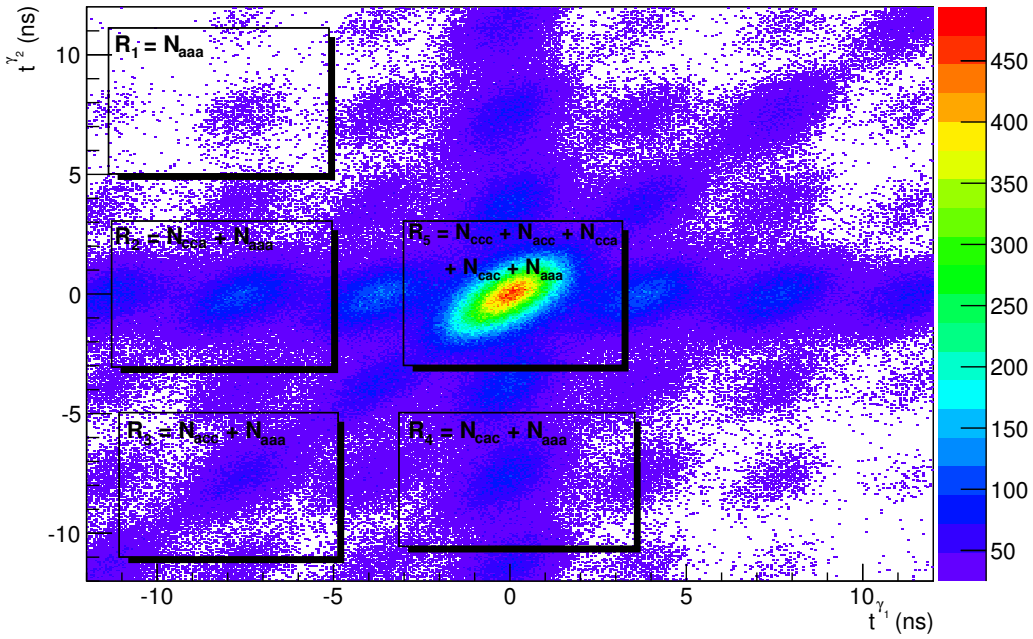

Figure 5.6: The time distribution of two photon events with respect to the scattered electron. Time corrections have been applied such that the time of each photon is relative to the detection of an electron in the spectrometer. The diagonal structure represents two photons in coincidence, of which some make up N_{acc}. The horizontal and vertical bands represent a case where an electron is in coincidence with one of the two photons only, some of which make up N_{cac}. Away from the vertical, horizontal and the diagonal bands, we have purely random events which are totally uncorrelated, N_{aaa}. The boxes show the time windows which were studied and their labels indicate the content of each time window in terms of the possible combinations of triple coincidences in each.

events with good tracks in the VDCs, call this sample N_{Gtrack}. The tracking efficiency was then calculated as:

$$\eta_{track} = \frac{N_{PID}}{N_{Gtrack}}. \tag{5.5}$$

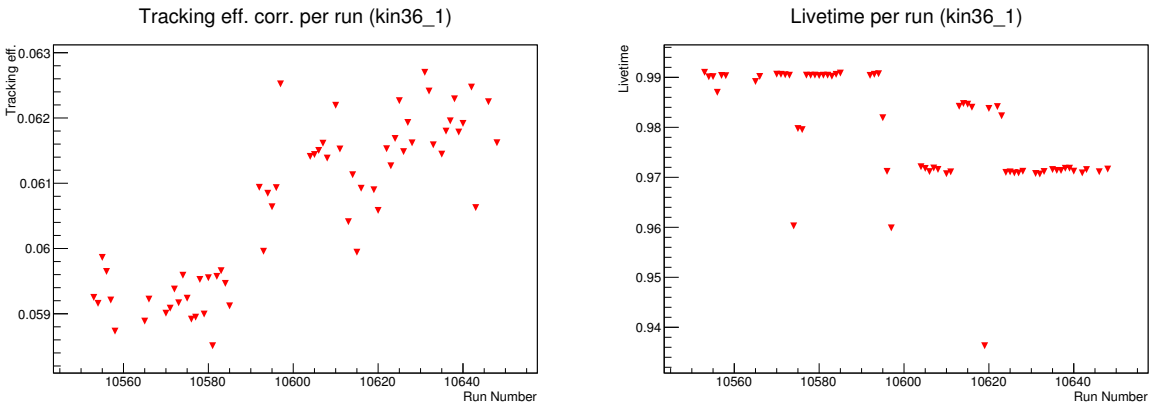

Figure 5.7: The tracking efficiency (left panel) and the livetime (right panel) as a function of run number. This kinematic was taken at 3 different beam currents and that is visible from the 3 distinct ”regions” in both the tracking inefficiency and livetime plots.

Since tracking efficiency is current dependent, it was calculated and corrected for on a run by run basis. The tracking inefficiency (1-η_{track}) for kin36_1 is shown as a function of run number in figure 5.7. In table 5.4 we show the average tracking efficiency for each kinematic.

5.3.2 Detector Efficiency

We had dedicated runs to study the efficiencies of different detectors at various points in time during data taking. To study the efficiency of a particular detector, we excluded it from a trigger and instead used other detectors around it to form a trigger. As an example, consider the set of detectors shown by the cartoon in figure 5.8. Suppose we want to measure the efficiency of detector 2. To do that we exclude detector 2 from the trigger and

record events which have fired detectors 1 and 3, call this set N_A. Out of the recorded events (N_A), we count how many have also fired detector 2, call this set N_B. The ratio of these two numbers gives us the efficiency of the detector:

$$\eta_{det.} = \frac{N_A}{N_B}. \tag{5.6}$$

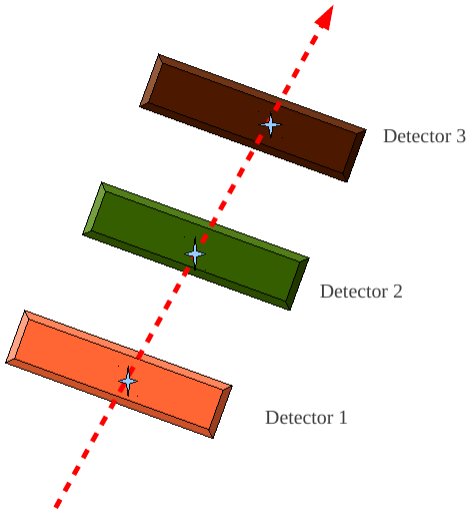

Figure 5.8: A cartoon showing an array of three detectors. To calculate the efficiency of say detector 2, we exclude it from the trigger and record events which have fired detectors 1 and 3. Out of the recorded events (seen by both 1 and 3), we count how many have also fired detector 2. The ratio of these two numbers give us the efficiency of the detector.

Since the trigger was formed by S2m and the gas Cherenkov, we discuss the efficiencies of these detectors in the following sections.

5.3.2.1 S2m Efficiency

To study the efficiency of the S2m scintillators, we triggered on the coincidence of the S0 scintillator and the gas Cherenkov and counted N_{S0Cer}. Then we counted how many of these events have also fired the S2m, N_{S0Cer_S2m}. The efficiency is then calculated as follows:

$$\eta_{S2m} = \frac{N_{S0Cer}}{N_{S0Cer\_S2m}}. \tag{5.7}$$

5.3.2.2 Cherenkov Efficiency

To study the efficiency of the gas Cherenkov, we triggered on the coincidence of the S0 and S2m scintillators and used the pion rejectors to count the number of good electrons N_{S0S2m}. Then we counted how many of these events have also fired the Cherenkov, N_{S0S2m_Cer}. We then calculated the efficiency as:

$$\eta_{Cer} = \frac{N_{S0S2m}}{N_{S0S2m\_Cer}}. \tag{5.8}$$

Both the gas Cherenkov and S2m detector efficiencies are summarized in table 5.4 for all kinematics.

5.3.3 Dead time

The DAQ system (detectors and the associated signal processing equipment) has some processing time for each event. This means that the DAQ is not always ready to accept incoming events. The amount of time it takes a detector to process an event is called the detector's dead time. During this time, the detector cannot "see" other events and a dead time correction factor becomes necessary to account for the number of events missed while the detector was processing an earlier event. The dead time is an intrinsic property of a detector but it can also be made worse by a high event rate.

To measure the dead time, we used a system of counting scalers. A scaler is an electronic device that records the accumulation of signals that occur too rapidly to be recorded individually. The scalers count the signals coming straight from the PMTs of the detectors and because they only count, they have no dead time compared to the other electronics which process the full data stream of an event. Two types of scalers were used during the experiment:

- Scalers which are continuously counting, we call these the raw scalers. The raw scalers give us a count which is not affected by the dead time.
- Scalers which count only when the DAQ is not busy. We call these the live scalers.

From these two scalers, dead time is calculated as:

$$DT = 1 - \frac{Live\ Scaler}{Raw\ Scaler} \tag{5.9}$$

The dead time correction factor is then given by:

$$\eta_{DT} = 1 + DT \tag{5.10}$$

Both the S2m and gas Cherenkov detectors had individual two copies of raw and live scalers each. The coincidence of these detectors also had two copies of raw and live scalers for dead time calculation. Since the dead time is a current (rate) dependent quantity and since the current would vary within a kinematic, the correction is done on a run by run basis. An example of the livetime as a function of run number is shown for kin36_1 in figure 5.7.

5.4 Integrated Luminosity ($\mathcal{L}$)

The integral of the luminosity is given by:

Table 5.4: Detector, tracking efficiencies and R-cuts per kinematic. The R-cut represents the number above which events were accepted. The last column is the virtual radiative correction factor introduced in chapter 4. The total number of accepted events is multiplied by the correction factors listed in this table to correct for the detector (or analysis) inefficiencies.

Kinematic	R-cut	Tracking (η_{track}) %	S2m (η_{S2m}) %	Cherenkov (η_{CER})	$\eta_{virtual}$ %
kin36_1	0.1	1.059	1.001	1.001	1.07
kin36_2	0.06	1.062	1.001	1.001	1.071
kin36_3	0.06	1.065	1.001	1.001	1.072

$$\mathcal{L} = \int \frac{d\mathcal{L}}{dt} dt \; = \; \frac{Q \cdot N_A \cdot \rho \cdot l}{e \cdot A_H}, \tag{5.11}$$

where:

- Q is the dead time corrected total charge of electrons incident onto the hydrogen target,
- N_A is Avogadro's number ($6.022 \cdot 10^{23}$ mol^{-1}),
- $\rho =$ 0.07229 g/cm^3 is the density of liquid hydrogen at 18 Kelvin and a pressure of 25 psi,
- l is the target length (15 cm),
- e is the electric charge ($1.602 \cdot 10^{-19}$ C) and
- $A_H =$ 1.0079 g/mol is the atomic mass of hydrogen.

Different runs may have been done at different currents and for different durations. This means the charge accumulated differs from one run to the next. Therefore, the total

charge accumulated in a kinematic is calculated on a run by run basis. The dead time corrections are also calculated and implemented likewise. The dead time corrected charged for all runs is then integrated to calculate the total luminosity.

5.5 Cross Section

We implemented the extraction method introduced introduced in Chapter 4 to obtain different response terms of the cross section. The data was divided into 12 bins in the angle ϕ (see definition in Chapter 1, Fig 1.13) and 5 bins in $t' = t_{min} - t$. A sample of the data is shown as a distribution in both ϕ and t' in figure 5.9.

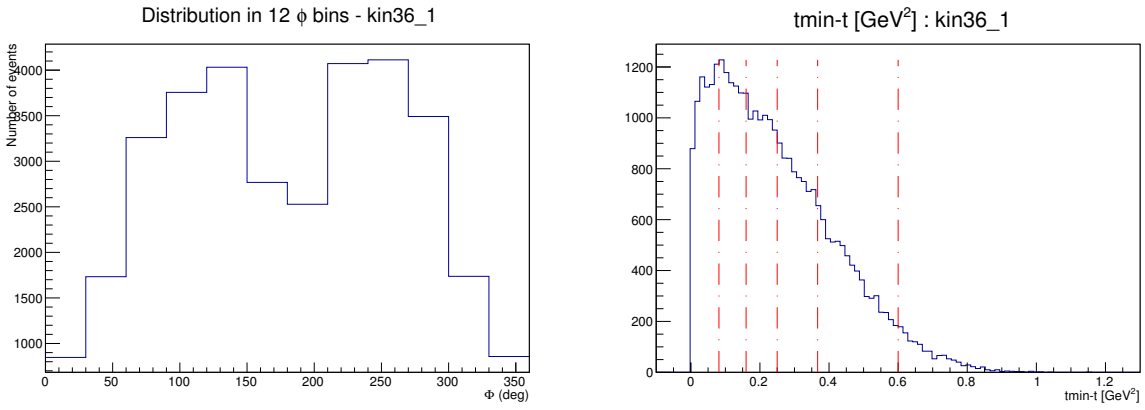

Figure 5.9: Final data sample after the event selection and accidental subtraction criteria. On the left panel is the data as a function 12 bins of the angle ϕ and the right panel shows the data as a function of 5 bins t.

5.5.1 Systematic Uncertainties

Systematic errors originate from instrumental sources and the systematics associated with the cross section extraction method. Our dominant systematic comes with the extraction method in the form the missing mass cuts to select exclusive events. Our

second most dominant is the systematic due to the lack of our understanding of the DIS cross section (luminosity and spectrometer acceptance) at the point of writing this document (Summer 2018). We present the different contributions to the systematics below and later summarize them in table 5.5. The final systematic error is a quadrature sum of all the listed systematic contributions.

5.5.1.1 DIS normalization systematic

Deep Inelastic Scattering (DIS) was discussed in chapter 1. DIS involves only the detection of the scattered electron using the HRS. The DIS cross section has been measured and reproduced over a range of kinematics world wide. Our kinematics also fall within these world measurements. Experimentally reproducing the DIS cross section with our data is an indication that we understand the luminosity and electron acceptance by the HRS. It is for this purpose that DIS data were acquired alongside the exclusive data. The DIS cross section can be extracted from the data by using the following formula:

$$\frac{d^2\sigma}{dx_B dQ^2} = \frac{N}{\mathcal{L}} \cdot \frac{1}{\Gamma_{DIS} \cdot \eta_{exp} \cdot \eta_{virt} \cdot \alpha}, \tag{5.12}$$

where N is the number of DIS events passing all analysis cuts, $\mathcal{L}$ is the integrated luminosity, η_{virt} is a term correcting for virtual radiative losses, η_{exp} is a term to correct for detector inefficiencies and Γ_{DIS} is the phase space through which the DIS events (N) are accepted in the spectrometer. The Γ_{DIS} term is estimated using a Monte Carlo simulation which was modified to a DIS simulation from an existing DVCS simulation package. We want to extract the DIS cross section at our nominal kinematics Q^2_{HRS} and x_B^{HRS}. However one needs to consider that the cross section varies within the spectrometer acceptance (as it does in the case of DVCS/DVMP). One also needs to consider that due to radiative effects, an event created out of the spectrometer acceptance can be detected by the spectrometer. This is most likely for DIS than it is for DVCS. To make the extracted cross

section comparable to the world measurements, a migration probability coefficient, α, that takes into account both effects, is applied.

As briefly mentioned above, the DIS cross section has been extensively measured for a wide range of kinematics. The cross section is parametrized by two structure functions F_1 and F_2. To compare our cross section to the world measurements (reference cross section) we used a cross section parametrization that is especially well adapted to our kinematics. The parametrization we are working with is based on electron-proton DIS scattering data from JLab's Hall C [98]. The Hall C data are compatible with our kinematics because they were measured in the kinematic ranges: $0 \leq Q^2 < 8$ GeV^2 and $1.1 \leq W < 3.1$ GeV and the cross section is known to 3% [98].

The DIS cross section extracted from our kin36_1 data was found to be systematically larger than the reference cross section by 11% as shown in Fig. 5.10. This discrepancy may be coming from either our extraction or the reference cross section or both. If the discrepancy comes from the reference cross section, then our source of error may be the radiative effects convoluted in the α term. Otherwise if the discrepancy comes from our extraction, our sources of error may be the detector efficiencies, the phase-space factor and the luminosity calculation. Up to the point of writing this document (Summer 2018), this discrepancy had not been resolved. To account for the lack of proper understanding of the cause for failing to reproduce the DIS cross section for our kinematics we apply the ±5.5% systematic to our extracted cross section. To implement this uncertainty, I have scaled down all the extracted DVMP cross section parameters by 5.5% and then assumed a ±5.5% normalization systematic to be added in quadrature with other systematics.

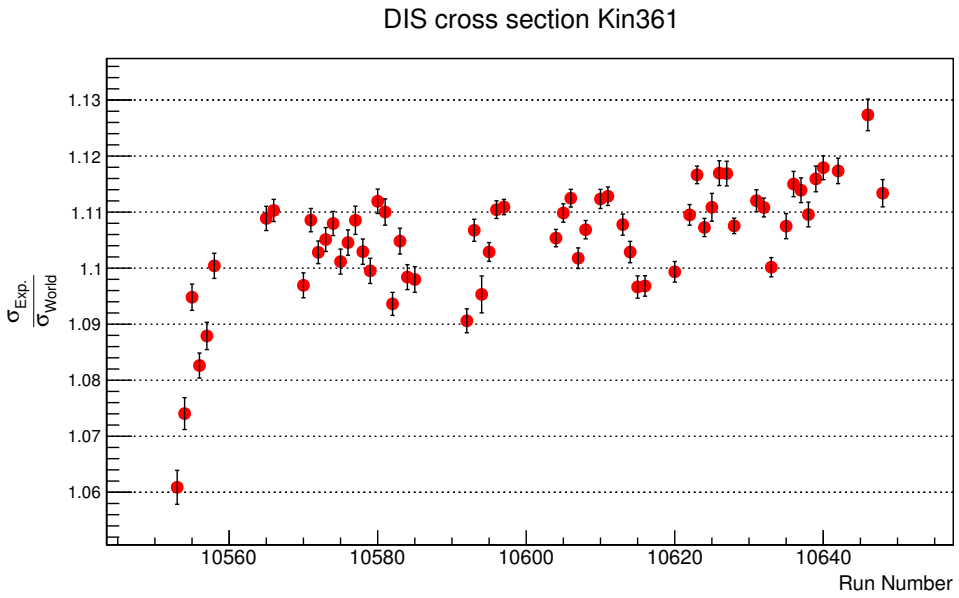

Figure 5.10: The ratio of the experimental DIS cross section ($\sigma_{Exp.}$) in kinematic setting kin36_1 (of experiment E12-06-114) to the world data (σ_{world}) in similar kinematics, as a function of run number. On average our DIS cross section is systematically 11% smaller than the world data. This discrepancy is an indication that we do not properly understand our luminosity and or the spectrometer's acceptance yet. We account for this by including this uncertainty as a systematic as discussed in the text. This figure was adapted from B. Karki in his report to the Hall A DVCS collaboration [99].

5.5.1.2 Exclusivity cut systematic

Systematics induced by the exclusivity cut arise because of semi-inclusive DIS (SIDIS) channels which contaminate the exclusivity distribution because of detector resolutions. Varying the exclusivity cut may vary the cross section because of the SIDIS channels, which are not simulated but contaminate the final sample of exclusive data. The amount of SIDIS contamination depends on the value of the missing mass cut.

The systematic error induced on the cross section by cutting on the proton missing mass and the π^0 reconstructed mass is evaluated by studying the variation of the extracted cross section terms as a function of the cuts. Our cross section is extracted at the optimal value of the cuts. To get an estimate of the systematic error, we take the difference between the cross section extracted with the optimum cuts and the cross section extracted at the extreme of stability. Figure 5.11 shows the behaviour of one of the extracted cross section parameters (σ_{LT}) in one $t_{min} - t$ bin as a function of the cuts in π^0 reconstructed mass and proton missing mass.

5.5.1.3 Summary of systematic errors

A list of the instrumental sources of systematic errors and their magnitudes is summarized in table 5.5. Since all the errors are independent of each other, they are later added in quadrature to propagate the final systematic error. The helicity-dependent cross section term has an additional systematic source from the beam polarization measurement.

Table 5.5: Experimental systematic errors for kin36_1.

Systematic	Value (%)
DIS normalization	5.5
Exclusivity cuts	6.6
Electron PID	1.0
Total quadratic (helicity-independent)	8.05
Beam polarization	2.2
Total quadratic (helicity-dependent)	8.34

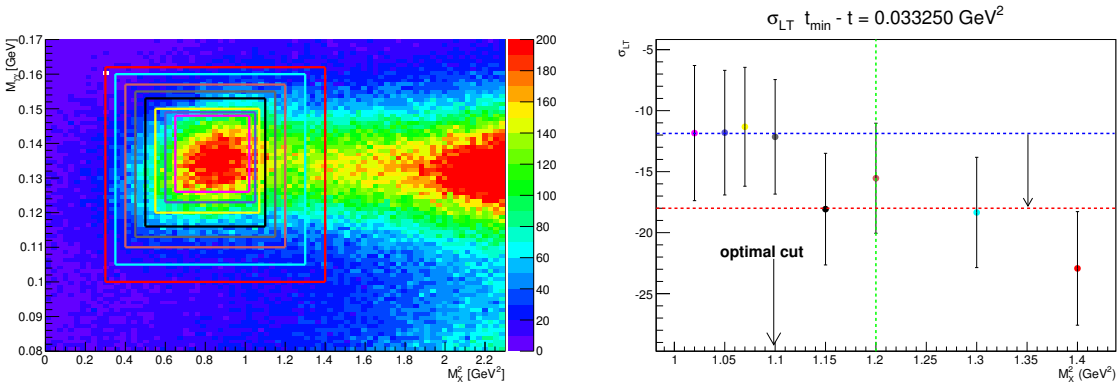

Figure 5.11: Propagation of uncertainty on the cross section as a result of cutting on the proton missing mass and reconstructed π^0 mass. The left panel shows a 2 dimensional plot of proton mass (horizontal axis) and π^0 mass (vertical axis). The rectangles in different colors mark the different cuts used to evaluate the systematic uncertainty. Each rectangle color corresponds to a point (same color as rectangle) on the right panel. Right panel: one $t_{min} - t$ bin of the extracted cross section parameter σ_{LT} as a function of the cuts shown on the left. The blue horizontal dotted line is the line of stability for this cross section, where the cross section is stable with respect to the value extracted with the optimal cuts. The green vertical dotted line is point beyond which the exclusivity of the experiment is not guaranteed. We estimate the systematic in this bin in $t_{min} - t$ as the difference between the stable region (blue line) and the extreme physics cut (green line).

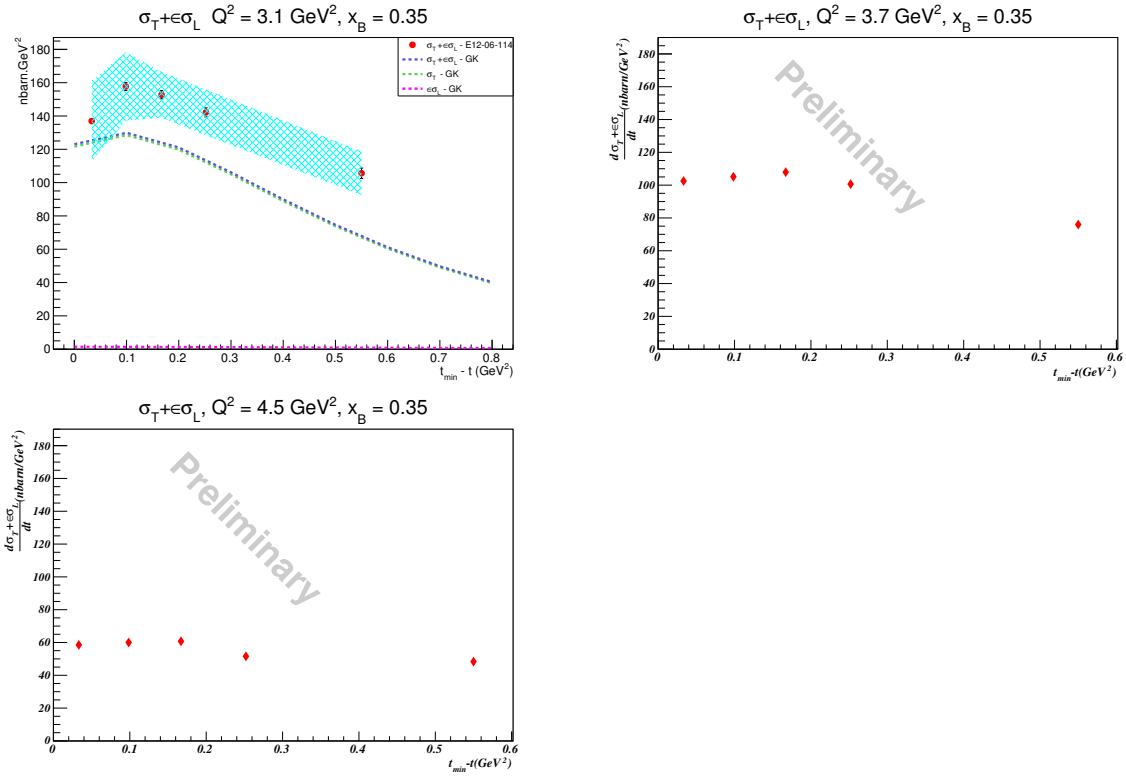

Figure 5.12: The extracted unseparated π^0 electroproduction cross section terms $\sigma_U = \sigma_T + \epsilon\sigma_L$. Top panel: results for kin36 (left) and kin36_2 (right). Bottom panel: results for kin36_3. The blue dashed lines show predictions GK model [73]. The shaded area shows the systematic precision as summarized in table 5.5 for each extracted cross section term.

5.5.1.4 Results and discussion

Results for the unseparated cross section $\sigma_U = \sigma_T + \epsilon\sigma_L$ are shown in Fig. 5.12. The π^0 has no charge and is spinless so coupling with a virtual photon is suppressed. The

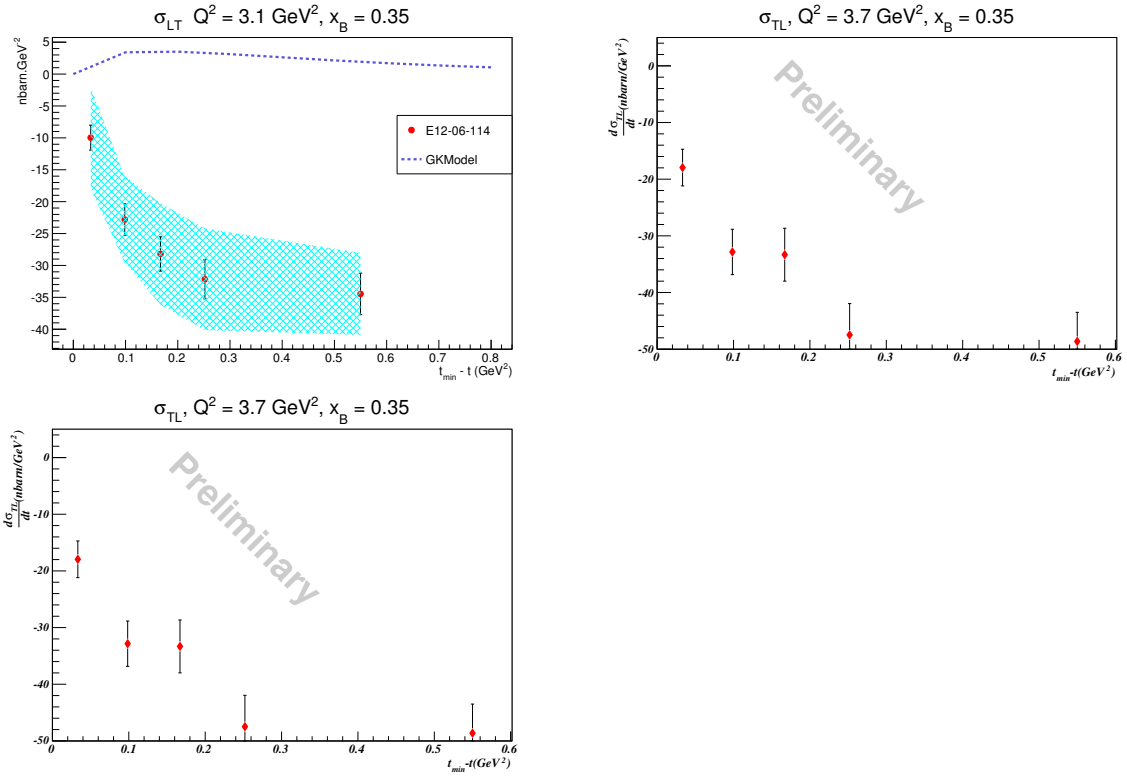

Figure 5.13: The extracted transverse-longitudinal interference π^0 electroproduction cross section terms σ_{LT}. Top panel: results for kin36 (left) and kin36_2 (right). Bottom panel: results for kin36_3. The blue dashed lines show predictions GK model [73]. The shaded area shows the systematic precision as summarized in table 5.5 for each extracted cross section term.

suppressed coupling to a virtual photon makes π^0 production to be free from a pion pole contribution, which when present boosts σ_L. Without the pion pole contribution the total π^0 cross section is predicted (by transversity GPD models [73]) to be dominated by σ_T. The Goloskokov-Kroll (GK) model [73] prediction for σ_U is also shown as the blue-dotted line on the same plot with our kin36_1 result. The prediction of the GK model for σ_T and $\epsilon\sigma_L$ is also shown further confirming the dominance of σ_T (transversity GPDs participation) over σ_L (chiral even GPDs participation). The GK model predicts the the

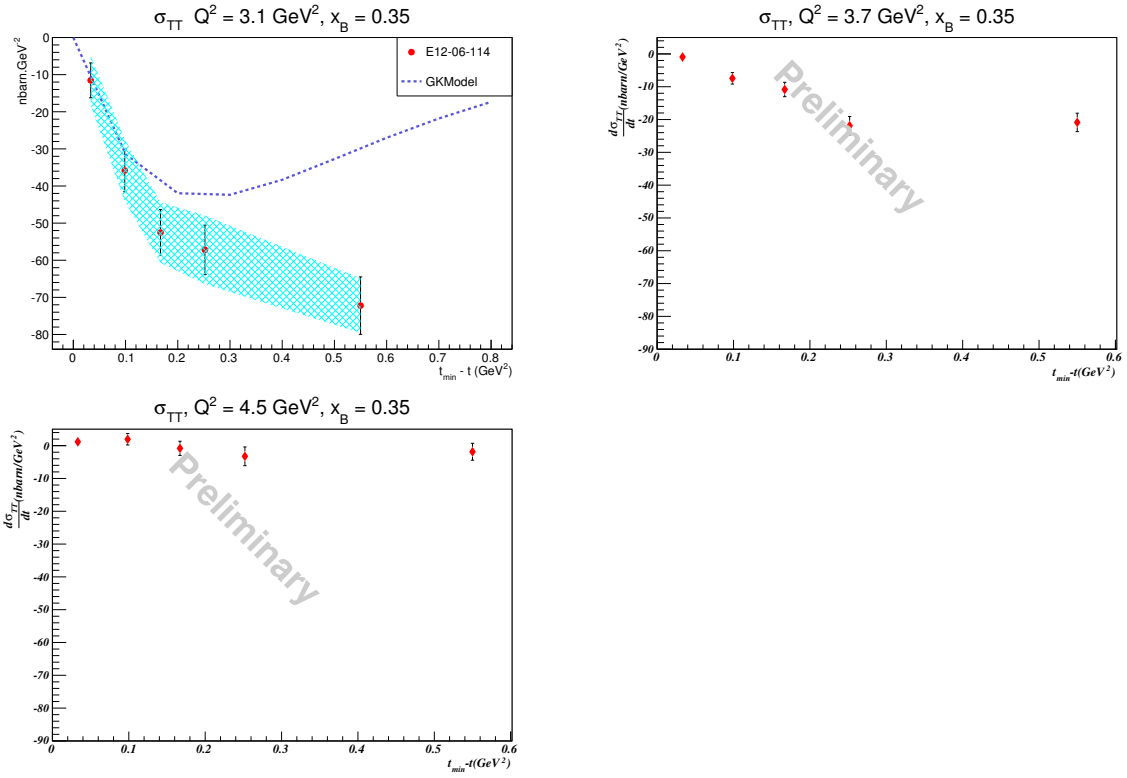

Figure 5.14: The extracted transverse-transverse interference π^0 electroproduction cross section terms σ_{TT}. Top panel: results for kin36 (left) and kin36_2 (right). Bottom panel: results for kin36_3. The blue dashed lines show predictions GK model [73]. The shaded area shows the systematic precision as summarized in table 5.5 for each extracted cross section term.

shape of the unseparated cross section fairly well. However, it fails to reproduce the cross section amplitude, underestimating it by about 20%. Our data is at a previously un-explored kinematic and its agreement with transversity GPD models adds to similar observations with existing data, however at slightly different kinematics. An existing measurement closest to our kinematic (kin36_1) was done by Bedlinskiy et al. (CLAS Collaboration) [43] at Q^2 = 2.71 GeV^2 and x_B=0.34 (see figure 1.15 in chapter 1). Even though at a lower Q^2, the CLAS result is in agreement with our data in terms of both the

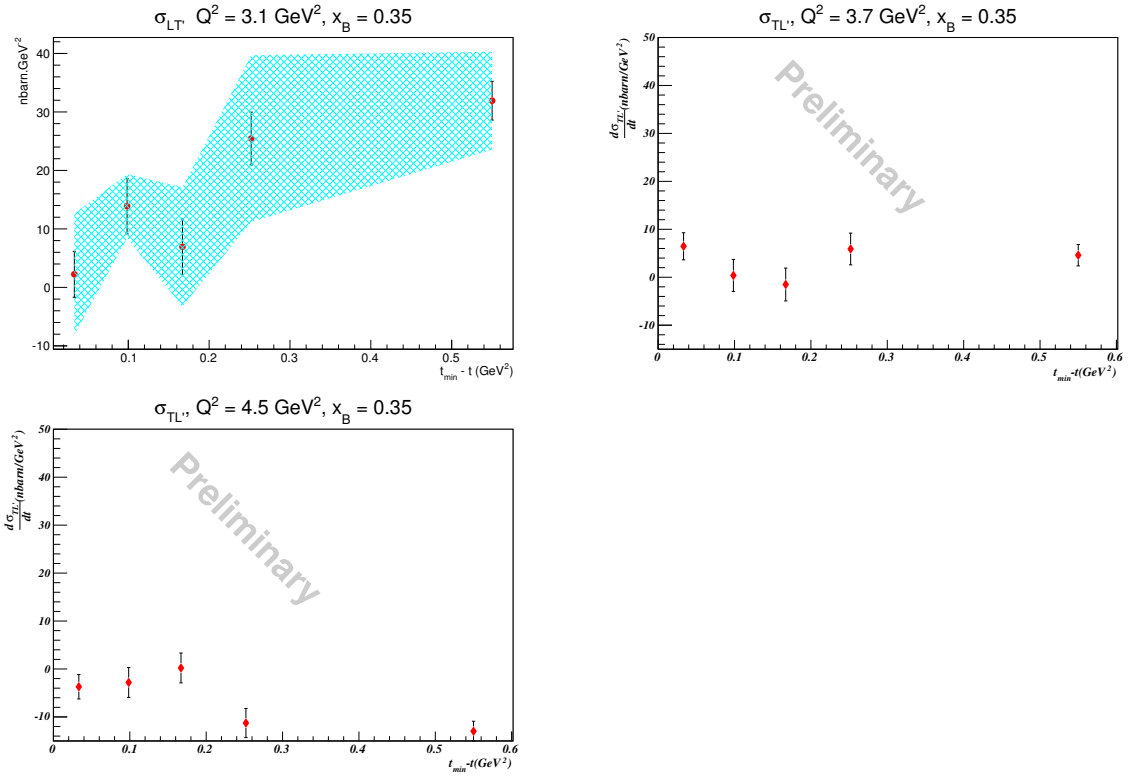

Figure 5.15: The extracted polarized response term for π^0 electroproduction cross section $\sigma_{LT'}$. Top panel: results for kin36 (left) and kin36_2 (right). Bottom panel: results for kin36_3. The shaded area shows the systematic precision as summarized in table 5.5 for each extracted cross section term.

order and shape of the cross section curve. σ_T and σ_L are predicted to decrease with increasing Q^2 and as a consequence their sum is expected to decrease too. Since our kinematic is at a higher Q^2 than that of the CLAS result, our cross section is smaller as expected. Preliminary results for the other two kinematics (kin36_2 and kin36_3) are also shown on the same plot. Even though we do not have model comparisons for these results, they are consistent with a decreasing cross section with an increasing Q^2.

Comparison with existing Hall A results is made difficult by the non-overlapping kinematics and the narrow range in $t_{min} - t$ for the older results. Comparing the sum of the

separated σ_L and σ_T terms from the most recent Hall A π^0 result [11] (see figure 1.17) with our unseparated result we find that we are in agreement in terms of the expected behaviour of the cross section magnitude at different Q^2 values. Since the results from Defurne et al. [11] were at a lower Q^2 their cross section is larger than ours as expected. The old results went further to separate the longitudinal and transverse contributions. Our data does not have the capability to separate the longitudinal and transverse terms of the cross section making it impossible to extract the independent contribution of each term to the cross section. Separation of the cross section terms requires that we have two different virtual photon fluxes' degrees of polarizations for the same kinematic point, i.e measuring the same kinematic point at two different beam energies. This could not be done because the driving experiment was DVCS cross section measurement instead of π^0 cross section measurement.

The transverse-longitudinal interference term (σ_{LT}) is shown in Fig. 5.13 and has a small but non-zero contribution. Transversity GPD models predict a small contribution by σ_L hence a small but positive interference term σ_{LT}, as shown in the figure. We however extract a negative (opposite sign to model predictions) value for this term. Moreover, our extracted interference term is about 8 times larger than the model prediction in absolute value. This suggests that the model is underestimating the contribution from the longitudinally polarized photons (σ_L). Our result is however consistent with the already existing Hall A results [11, 42] in terms of the sign of the cross section. We again show some preliminary results for the other two kinematics (kin36_2 and kin36_3) on the same plot. Like in the case of unseparated cross section terms, these results are consistent with a decreasing cross section with an increasing Q^2 forσ_{LT}.

The transverse-transverse interference term (σ_{TT}) is shown in Fig. 5.14 and we get a small but non-zero contribution. Since π^0 production is predicted by transversity GPD models to be mainly driven by transversely polarized virtual photons, the σ_{TT} term is

expected to be non-negligible. Compared to the predictions by the GK model, our result is in good agreement for $t_{min}-t$ below 0.17 GeV^2. Above $t_{min} - t = 0.17$ GeV^2 the model overestimates this term. Since σ_{TT} is connected to the transversity GPDs through equation 1.45 this implies that the contribution of the term $\bar{E}_T$ is overestimated in the model (compared to what the data shows). In the case where the handbag formalism was valid and transverse photons were suppressed, one would expect a negligible σ_{TT} contribution, especially relative to σ_{LT} but this is not the case. Compared to previous results [11, 42] our result is in agreement in terms of both a decreasing cross section amplitude with increasing Q^2 and decreasing $t_{min} - t$. Even though the old results have a narrow range in $t_{min} - t$, the trend continues in our wider momentum transfer arm. It is also interesting to note that in their kinematics, Defurne et al. [11] (see figure 1.17) also find the that GK model is consistently overestimating the σ_{TT} term. Preliminary results for the other two kinematics (kin36_2 and kin36_3) are also shown on the same plot (Fig. 5.14). Like in the case of the previous extracted cross section terms, these results are consistent with a decreasing cross section with an increasing Q^2 forσ_{TT}.

Lastly the polarized response $\sigma_{LT'}$ is shown in Fig. 5.15. This result is consistent with older Hall A results [42] in that it is found to be positive and increasing with $t_{min}-t$. We do not have a model comparison for this term at the moment and its interpretation in the GPD formalism is not well established.

Conclusion and Outlook

Generalized Parton Distributions are structure functions that describe the correlations between the longitudinal momentum fraction and the transverse spatial position of quarks and gluons inside the nucleon. GPDs provide a tool for accessing the 3D partonic structure of hadrons. By parametrizing the correlations between position and momentum of quarks and gluons, GPDs bring a wealth of information which form factors and parton distribution functions cannot independently offer. The connection of GPDs with quark orbital angular momentum also makes them relevant objects in the pursuit to resolve the proton spin crisis.

GPDs are measurable through deep exclusive processes like Deeply Virtual Compton Scattering (DVCS) and Deeply Virtual Meson Production (DVMP). DVCS is the cleanest tool to access GPDs. DVMP is a complimentary process through which different flavor GPDs can be accessed. Both DVCS and DVMP get their validation from factorization theorems which allow us to separate between the hard and the soft scattering scales in a perturbative QCD approach. It has been theoretically proven that in the Bjorken regime of large photon virtuality (Q^2) and large virtual photon-proton center of mass energy (W), these processes factorize into a hard-scattering part parametrized by Form Factors, a soft part of hadronic matrix elements parametrized by the GPDs, and in the case of meson production, a meson distribution amplitude (DA). DVCS and DVMP results are interpreted in the handbag approximation (formalism) of asymptotic freedom in perturbative QCD. According to the handbag formalism, the leading order amplitudes for these processes are expected to be mediated by longitudinally polarized virtual photons with a relatively suppressed transverse contribution. It is expected that at leading order only chiral-even GPDs participate, that is to say helicity flipping structure functions are not expected to participate until at least next to leading order. Earlier DVCS experiments,

however at lower photon virtualities Q^2, have hinted signs of the validity of the handbag formalism for photon production. A contradiction of the handbag formalism is observed with pseudoscalar meson, in particular π^0 and π^+, production data. The failure of the handbag formalism in the pseudoscalar case has inspired new models based on the participation of transversity (chiral-odd) GPDs at leading order through their coupling with the pion twist-3 Distribution Amplitude.

Experiment E12-06-114 in Hall A of Jefferson Lab was one of the first experiments to utilize the new 12 GeV upgrade at JLab to extend the kinematic reach of the GPD program in JLab. A wider energy range was useful in performing measurements as a function of a range of photon virtualities (Q^2) and hence pin down the validity of generalized parton distributions as the appropriate objects to parametrize the proton structure in the case of DVCS. In the case of DVMP, in particular π^0 production, there is a need to test the validity of the postulated presence of transversity GPDs at leading order. This experiment collected data capable of extracting both photon and π^0 electro-production cross sections over a range in Q^2 (3 to 9 GeV^2) and x_B (0.35 to 0.6). With a 15 cm liquid hydrogen target Hall A provides a high luminosity ($\sim 10^{37}$ cm^{-2}s^{-1}) for precision measurements. The experiment used Hall A's High Resolution Spectrometer (HRS) to detect the scattered electron with a precision of 10^{-4} in momentum and a dedicated DVCS electromagnetic calorimeter to detect photons with a moderate resolution of 4% in $\frac{\Delta E}{E}$. The proton was not detected but its missing mass was reconstructed using the measured electron and photon information.

In this thesis we have analyzed data at (Q^2, x_B) = (3.1 GeV^2,0.35) and extracted the π^0 electro-production cross section. We have extracted the cross section parameters $\sigma_T + \epsilon\sigma_L, \sigma_{LT}, \sigma_{TT}$ and $\sigma_{LT'}$ using a cross section parametrization by Dreschsel and Tiator [35]. Even though factorization has been theoretically proven for longitudinal photons only at this point, models based on transversity GPDs have been proposed and the

cross section results are confronted with one such model for interpretation. Compared to predictions with transversity GPD models by Goloskokov and Kroll (GK) [73] we find that the model fails to describe the data for all extracted parameters. Concerning the unseparated structure function term $\sigma_T + \epsilon\sigma_L$, the model predicts the shape and the order of magnitude well but it fails to predict the magnitude of the cross section, underestimating it by about 20%. Concerning the structure function σ_{TT}, the model predicts both the shape and amplitude of the cross section well for low values of $t_{min} - t$ (< 0.17 GeV^2) and fails above this point. The last term compared to the model is σ_{LT} and it is found to be in total disagreement with the data in terms of both the sign and the magnitude of the cross section. Even though the models do not convincingly describe the data, the fact that the unseparated cross section extracted from the data is larger than that predicted by the leading-twist handbag approximations means σ_L is indeed small compared to σ_T. This conclusion can also be made just from comparing the cross sections $\sigma_T + \epsilon\sigma_L$, σ_{TT} and σ_{LT}. This presence of a dominant σ_T over σ_L is a further confirmation that indeed the the pion twist-3 Distribution Amplitude couples with transversity GPDs. Our result shows some further hints that the DVMP transition is strongly mediated by transversely polarized virtual photons. This is in contradiction with the predictions of the handbag formalism of a dominant longitudinally polarized virtual photon mediation and from this we can conclude that we are still far from reaching the Bjorken regime for π^0 production. Our result is also compatible with existing measurements (from both Halls A and B of JLab) in terms of the shapes of the cross section curves, the size of the cross section and comparison with transversity models. The limitation of our result is that the data lacked the capability to separate the individual longitudinal σ_L and σ_T contributions to the cross section. In addition to quantifying the magnitude of each term, especially relative to the other, a separation of σ_L and σ_T would allow us to further test the scaling of these terms against the predictions of the handbag approximation. These terms are

predicted to scale as Q^{-6} for σ_L and Q^{-8} for σ_L once we reach the asymptotic freedom regime.

Two more data points were acquired at the same x_B but with a higher Q^2 of 3.5 and 4.47 GeV^2. Analysis for these two points is still in progress and we have only shown some preliminary results in this document. Once all the three Q^2 points analyzed we look forward to further tests of the handbag formalism for π^0 production. In addition to these data points, more data was taken at the x_B values: 0.48 and 0.6. These points were also scans in Q^2. Analysis of these data is also being done by a graduate student colleague and once analyzed, these data will also provide further test add to the wealth of knowledge and development of GPD models.

In the future, large acceptance vector meson electro-production cross section measurements with CLAS12 in Hall B of JLab are scheduled to collect data with the 12 GeV upgrade. These measurements will extend DVMP cross section data to perform a longitudinal-transverse cross section separation and evaluate the contribution of the transverse photons in the transition. With its large acceptance, CLAS12 is also going to be helpful in understanding other puzzles in the meson production channels such as the low W, ρ^0, ω cross section data [36]. The CLAS12 data will be measured in the valence quark regime, investigating kinematic points with x_B from 0.1 to 0.8, with Q^2 scans above resonance to 12 GeV^2.

Precision pseudoscalar meson cross section measurements are also scheduled to collect data with the JLab 12 GeV upgrade in Hall C using the High Momentum Spectrometer (HMS) and the Super High Momentum Spectrometer (SHMS) pair. These measurements are expected to run in the Fall of 2018. The data from these measurements will be useful in performing a longitudinal-transverse cross separation of the kaon electroproduction cross section and studying the scaling mechanism in the kaon

production channel. This experiment will also help understand the role of strangeness in GPD studies and the kaon form factor [100].

The Neutral Particle Spectrometer (NPS) collaboration is set to perform both DVCS and π^0 cross section measurements in Hall C of the 12 GeV upgraded JLab facility. The experiment will utilize the existing high momentum spectrometers in Hall C and an electromagnetic calorimeter (NPS) designed to measure high energy photons in a high background environment. The NPS will perform high precision measurements of the DVCS cross section in a wide kinematic coverage enabled by both the 12 GeV upgrade and the high momentum acceptance spectrometers [36]. Even though the main objective is to measure DVCS cross sections, π^0 electroproduction cross sections will also be measured and a longitudinal-transverse separation will be performed to test scaling properties [101].

The 12 GeV upgrade at JLab only offers DVMP measurement opportunities at the valence quark regime. To achieve a more complete partonic description of nucleon structure we also need to explore gluon and sea quark GPDs. The current JLab infrastructure does not have the necessary center of mass energy to reach the sea quark and gluon regime. The proposed Electron-Ion Collider (EIC) will be designed to reach a high center of mass energy and avail opportunities to study the role of gluons and sea quarks in determining nucleon structure and the accompanying dynamics. One example is the possibility to study exclusive ρ^0 and J/ψ production at high Q^2. This could open a window to disentangle the singlet quark and gluon GPDs and test QCD evolution [36]. The EIC will also provide opportunities to measure two mesons with a large rapidity gap between them and this could be an interesting tool to investigate GPDs for transversely polarized quarks [36, 102].

References

[1] K. Goeke, M.V Polyakov and M. Vanderhaegen, "Hard Exclusive Reactions and the Structure of Hadrons", Progress in Particle and Nuclear Physics, 47:401-515, 2001

[2] F. Wilczek, "Asymptotic freedom: From paradox to paradigm", Proc. Nat. Acad. Sci., 102:8403, 2005

[3] G. Dissertori, "The Determination of the Strong Coupling Constant", Adv. Ser. Direct. High Energy Phys., 26:113, 2016

[4] C. Muñoz Camacho, "Diffusion Compton profondément virtuelle dans le Hall A au Jefferson Laboratory", PhD Thesis, de l'Universite Paris VI, 2005

[5] J. Dudek *et al.*, "Physics opportunities with the 12 GeV upgrade at Jefferson Lab", Eur. Phys. J.A, 48:187, 2012

[6] DOE/NSF Nuclear Science Advisory Committee, "Reaching for the Horizon - The 2007 Long Range Planfor Nuclear Science", available online: `http://science.energy.gov/np/nsac/`

[7] O. W. Greenberg, "The Parton model", Compendium of Quantum Physics, Springer-Verlag, 255-258, 2009

[8] A. Airapetian *et al.* (HERMES Collaboration), "Measurement of the beam spin azimuthal asymmetry associated with deeply virtual Compton scattering", Phys. Rev. Lett., 87:182001, 2001

[9] C. Muñoz Camacho, A. Camsonne, M. Mazouz, C. Ferdi, G. Gavalian *et al.*, "Scaling Tests of the Cross Section for Deeply Virtual Compton Scattering", Phys. Rev. Lett., 97:262002, 2006

[10] H.S Jo *et al.*, "Cross Sections for Exclusive Photon electroproduction on the Proton and Generalized Parton Distributions", Phys. Rev. Lett., 115:212003, 2015

[11] M. Defurne *et al.* (Jefferson Lab Hall A Collaboration), "Rosenbluth Separation of the π^0 Electroproduction Cross Section", Phys. Rev. Lett., 117:262001, 2016

[12] R. De Masi *et al.* (CLAS Collaboration), "Measurement of e p $\rightarrow$ e p pi0 beam spin asymmetries above the resonance region", Phys. Rev. C, 77:042201, 2008

[13] M. Gorzellik (COMPASS Collaboration), "Measurement of the exclusive π^0 muonproduction cross section at COMPASS", arXiv:1702.06293 [hep-ex], 2017

[14] J. C. Bernauer, P. Achenbach, C. Ayerbe Gayoso, R. Bhm, D. Bosnar, L. Debenjak, M. O. Distler *et al.* (A1 Collaboration), "High-Precision Determination of the Electric and Magnetic Form Factors of the Proton", Phys. Rev. Lett., 105:242001, 2010

[15] E. Rutherford, “The scattering of α and β particles by matter and the structure of the atom”, Philosophical Magazine Series 6, 1911

[16] M. Guidal, H. Moutarde and M. Vanderhaeghen, “Generalized Parton Distributions in the valence region from Deeply Virtual Compton Scattering”, Rept. Prog. Phys., 76:066202, 2013

[17] X. Ji, “Generalized Parton Distributions”, Annu. Rev. Nucl. Part. Sci., 54:413-450, 2004

[18] M. Guidal, “Generalized Parton Distributions and deep virtual Compton scattering”, Prog. Part. Nucl. Phys. 61:89-105, 2008

[19] B. Guegan, “Study of Generalized Parton Distributions and Deeply Virtual Compton Scattering on the nucleon eith the CLAS and CLAS12 detectors at the Jefferson Laboratory”, PhD Thesis, Universite Paris-Sud, Rensselaer Polytechnic Institute, 2013

[20] M.N. Rosenbluth, “High Energy Elastic Scattering of Electrons on Protons”. Phys.Rev., 79:615619, 1950.

[21] C. F. Perdrisat, V. Punjabi and M. Vanderhaeghen, “Nucleon Electromagnetic Form Factors”, Prog. Part. Nucl. Phys., 59:694, 2007

[22] J. J. Krauth *et al.*, “The Proton Radius Puzzle”, arXiv:1706.00696v2, physics.atom-ph, 2017

[23] A. Accardi, L. T. Brady, W. Melnitchouk, J. F. Owens and N. Sato, “Constraints on large-x parton distributions from new weak boson production and deep-inelastic scattering data”, Phys. Rev. D, 93:11:114017, 2016

[24] M. Breidenbach, J. I. Friedman, H. W. Kendall, E. D. Bloom, and D. Coward *et al.*, “Observed behavior of highly inelastic electron-proton scattering”, Phys. Rev. Lett. 23, 1969

[25] A. V. Belitsky and A. V. Radyushkin, “Unraveling hadron structure with generalized parton distributions”, Phys. Rept., 418:1, 2005

[26] X.D. Ji, “Gauge-Invariant Decomposition of Nucleon Spin”, Phys. Rev. Lett., 78:4, 610-613, 1997

[27] M. Diehl, “Generalized parton distributions”, Phys. Rept., 388, 41-277, 2003

[28] G. R. Goldstein, J. O. Gonzalez Hernandez and S. Liuti, “Flexible Parametrization of Generalized Parton Distributions: The Chiral-Odd Sector”, Phys. Rev. D, 91:11:114013, 2015

[29] J.C. Collins, L.Frankfurt and M. Strikman, "Factorization for hard exclusive electroproduction of mesons in QCD", Phys. Rev. D, 56:2982, 1997

[30] J. C. Collins, D. E. Soper and G. F. Sterman, "Factorization of Hard Processes in QCD", Adv. Ser. Direct. High Energy Phys., 5:1, 1989

[31] A. Biselli *et al.*, "Deeply Virtual Compton Scattering with CLAS at 11 GeV", available online:
http://www.jlab.org/exp_prog/proposals/06/PR12-06-119.pdf

[32] A.V. Belistky, D. Muller and A. Kirchner, "Theory of deeply virtual Compton scattering on the nucleon", Nucl.Phys., B629, 323-392, 2002

[33] J.C. Collins and A. Freund, "Proof of factorization for deeply virtual Compton scattering in QCD", Phys. Rev. D, 59:074009, 1999

[34] M. Defurne *et al.*, "E00-110 experiment at Jefferson Lab Hall A: Deeply virtual Compton scattering off the proton at 6 GeV", Phys. Rev. C, 92:055202, 2015

[35] D. Dreschsel and L. Tiator, "Threshold pion photoproduction on nucleons", J. Phys. G: Nucl. Part. Phys. 18:449, 1992

[36] L. Favart, M. Guidal, T. Horn *et al.*, "Deeply virtual meson production on the nucleon", Eur. Phys. J., A52:158, 2016

[37] I. Bedlinskiy *et al.* (CLAS Collaboration), "Measurement of Exclusive π^0 Electroproduction Structure Functions and their Relationship to Transverse Generalized Parton Distributions", Phys. Rev. Lett., 109:112001, 2012

[38] T. Horn et al., "Determination of the Pion Charge Form Factor at Q^2 = 1.60 and 2.45 GeV^2", Phys. Rev. Lett., 97:192001, 2006

[39] S.V. Goloskokov and P. Kroll, "Transversity in hard exclusive electroproduction of pseudoscalar mesons", Eur.Phys.J., A47:112, 2011

[40] G.R. Goldstein, J. Osvaldo Gonzalez Hernandez, and S. Liuti, "Flexible Parametrization of Generalized Parton Distributions: The Chiral-Odd Sector", International Journal of Modern Physics Conference Series, 2013.

[41] A. Airapetian *et al.* (HERMES Collaboration), "Single-spin azimuthal asymmetry in exclusive electroproduction of π^+ mesons on transversely polarized protons", Phys. Lett. B, 682:345, 2010

[42] E. Fuchey, A. Camsonne, C. Munoz Camacho, M. Mazouz, G. Gavalian *et al.*, "Exclusive Neutral Pion Electroproduction in the Deeply Virtual Regime", Phys.Rev. C, 83:025201, 2011

[43] I. Bedlinskiy *et al.* (CLAS Collaboration), "Exclusive π^0 electroproduction at W > 2 GeV with CLAS", Phys.Rev. C, 90:025205, 2014

[44] G. R. Goldstein, J. O. Gonzalez Hernandez and S. Liuti, "Generalized Parton Distributions in the Chiral Odd Sector and Their Role in Neutral Meson Electroproduction", Int. Journal of Modern Physics: Conf. Series, 20, 2012

[45] M. Vanderhaeghen, P.A.M. Guichon and M. Guidal, "Deeply virtual electroproduction of photons and mesons on the nucleon: Leading order amplitudes and power corrections", Phys. Rev. D, 60:094017, 1999

[46] M. Defurne, "Photon and π^0 electroproduction at Jefferson Lab - Hall A", PhD Thesis, Universite Paris Suid, 2015

[47] C.E. Hyde, A. Radyushkin, and M. Guidal, "Deeply Virtual Exclusive Processes and Generalized Parton Distributions", J. Phys. Conf. Ser., 299, 012006-012029, 2013

[48] S. Yaschenko (On behalf of the HERMES Collaboration), "An overview of recent DVCS results at HERMES", Physics of Particles and Nuclei, 45:1, 173-175, 2014

[49] J. M. Laget,"Photoproduction of vector mesons at large transfer", Phys. Lett. B, 489:313, 2000

[50] A. Camsonne, C. Hyde, C. Muñoz Camacho and J. Roche *et al.*, "E12-06-114 Proposal Update to JLab PAC", available online:http://hallaweb.jlab.org/experiment/DVCS/

[51] C.W Leeman, D.R Douglas and G.A Krafft, "The Continuous Electron Beam Accelerator Facility: CEBAF at the Jefferson Laboratory", Annu. Rev. Nucl. Part. Sci., 51:413:50, 2001

[52] J. Alcorn *et al.*, "Basic Instrumentation for Hall A at Jefferson Lab", Nucl. Instrum. Meth., A522:294, 2004

[53] J. Dudek *et al*, Physics Opportunities with the 12 GeV Upgrade at Jefferson Lab, arXiv:1208.1244, 2012

[54] F. Gross, "Making the Case for Jefferson Lab", Journal of Physics: Conference Series, 299, 2011

[55] O. Glamazdin, E. Chudakov, R. Pomatsalyk, V. Vereshchaka and J. Zhang, "Status of the Hall A Møller Polarimeter", available online: `http://hallaweb.jlab.org/equipment/moller/docs/AnnualReport2012_Moller.pdf`

[56] O. Glamazdin and R. Pomatsalyk, "Moller Polarimetry for DVCS", available online: `https://www.jlab.org/indico/event/197/session/3/contribution/11/material/slides/0.pdf`

[57] D. Higinbotham, “Determination of the Beam Energy”, available online: https://www.jlab.org/indico/event/197/session/3/contribution/12/material/slides/0.pdf

[58] M. E. Christy, “HRS acceptance and optics study”, available online: https://hallaweb.jlab.org/news/talks/2017/2017-5-16Christy.pdf

[59] K. G. Fissum, W. Bertozzi, J. P. Chen, D. Dale, H. C. Fenker, J. Gao, A. Gavalya and S. Gilad *et al.*, “Vertical drift chambers for Hall A High Resolution Spectrometers”, Nucl. Instrum. Meth., A474:108, 2001

[60] A. Camsonne, “Experimental setup for Deeply Virtual Compton Scattering (DVCS) experiment in Hall A at Jefferson Laboratory”, PhD Thesis, Universite Blaise Pascal, 2005

[61] J. Roche, C. Hyde, B. Michel, C. Muñoz Camacho *et al.*, “E12-06-114 Proposal”, available online: http://www.jlab.org/exp_prog/proposals/06/PR12-06-114.pdf

[62] V. Breton *et al.*, “Application of neural networks and cellular automata to interpretation of calorimeter data”, Nucl. Inst. and Meth., A362:478, 1995

[63] W. R. Leo, “Techniques for Nuclear and Particle Physics Experiments”, Springer-Verlag, 1993

[64] A. Marti Jimenez, “Measurement of the photon electroproduction cross section at JLab with the goal of performing a Rosenbluth separation of the DVCS contribution”, PhD Thesis, Universitat de Valencia, 2014

[65] R. T. Jones *et al.*, “A bootstrap method for gain calibration and resolution determination of a lead-glass calorimeter”, Nucl. Instrum. Meth., A566:366, 2006

[66] G. D. Coughlan, and J. E. Dodd, “The ideas of particle physics”, Cambridge University Press, 1991

[67] M. Mazouz et al., “Deeply Virtual Compton Scattering off the Neutron”, Phys. Rev. Lett., 99:242501, 2007

[68] F. Georges, “Wavefrom analysis optimisation”, Private communication

[69] M. Vanderhaeghen, J. M. Friedrich, D. Lhuillier, D. Marchand, L. Van Hoorebeke and J. Van de Wiele, “QED radiative corrections to virtual Compton scattering”,Phys. Rev. C, 62:025501, 2000

[70] S. Agostinelli *et al.*, “Geant4 - a simulation”, Nucl. Instr. and Meth. in Physics, Research Section A: Accelerators, Spectrometers, Detectors and Associated Equipment, 506:3, 250-303, 2003

[71] R. Paremuzyan and M. Defurne, "Implementation of the Hall A DVCS calorimeter in GEANT4, (Technical report to DVCS collaboration", available online: https://userweb.jlab.org/rafopar/HallA/Calo/Calo Geant4.ps

[72] G. Hamad, "Using the R-Function to Study the High-Resolution Spectrometer (HRS) Acceptance for the 12 GeV Era Experiment E12-06-114 at JLab", Master Thesis, Ohio University, 2017

[73] S. V. Goloskokov and P. Kroll, "An Attempt to understand exclusive pi+ electroproduction", Eur. Phys. J., C65:137, 2010

[74] P.R. Bevington and D.K. Robinson, "Data Reduction and Error Analysis for the Physical Sciences 3^{rd} Edition", McGraw-Hill, 2003

[75] H. Rashad, "Event selection", Private Communication

[76] A. Johnson, "R-function and spectrometer acceptance", Private Communication

[77] C. Muñoz Camacho, "Experimental studies of the internal structure of the nucleon", Habilitation Thesis, de l'Universite Paris VI, 2014

[78] A. Radyushkin, "Double distributions and evolution equations", Phys. Rev. D, 59:014030, 1999

[79] M. Kirch, A. Manashov and A. Schafer, "Evolution equation for generalized parton distributions", Phys. Rev. D, 72:114006, 2005

[80] A. Freund, M. McDermott and M. Strikman, "Modeling generalized parton distributions to describe deeply virtual Compton scattering data", Phys. Rev. D, 67:036001, 2003

[81] A.V Efremov and A.V Radyushkin, "Factorization and Asymptotic Behaviour of Pion Form Factor in QCD", Phys. Lett. B, 94:2, 1980

[82] G.P Lepage and S.J Brodsky, "Exclusive processes in pertubative quantum chromodynamics", Phy. Rev. Lett. D, 23, 1980

[83] G. Altarelli and G. Parisi, "Asymptotic Freedom in Parton Language", Nucl. Phys. B, 126:298, 1977

[84] Y.L. Dokshitzer, "Calculation of structure functions of deep-inelastic scattering and e+e- annihilation by perturbation theory in quantum chromodynamics", Sov. Phys. JETP, 46:641, 1977

[85] V.N. Gribov, L.N. Lipatov, "Deep inelastic e p scattering in perturbation theory", Sov. J. Nucl. Phys. 15:438, 1972

[86] D. Muller, D. Robaschik, B. Geyer, F.-M. Dittes and J. Hosejsi, "Wave functions, evolution equations and evolution kernels from light ray operators of QCD", Fortsch. Phys., 42:101, 1994

[87] M. C. Kunkel *et al.* (CLAS Collaboration), "Exclusive photoproduction of π^0 up to large values of Mandelstam variables s, t and u with CLAS", arXiv:1712.10314 [hep-ex].

[88] M. M. Kaskulov, "Neutral pion electroproduction in $p(e, e'\pi^0)p$ above $\sqrt{s} > 2$ GeV", arXiv:1105.1993 [nucl-th], 2011

[89] H. Moutarde, B. Pire, F. Sabati, L. Szymanowski and J. Wagner, "On Deeply Virtual Compton Scattering at next-to-leading order", Few Body Syst., 55:339, 2014

[90] R. Dupre, M. Guidal, S. Niccolai and M. Vanderhaeghen, "Analysis of Deeply Virtual Compton Scattering Data at Jefferson Lab and Proton Tomography", Eur. Phys. J., A53:8:171, 2017

[91] M. Hattawy *et al.*. (CLAS Collaboration), "First Exclusive Measurement of Deeply Virtual Compton Scattering off ^{4}He: Toward the 3D Tomography of Nuclei", Phys. Rev. Lett., 119:202004, 2017

[92] H. Moutarde, "Extraction of the Compton Form Factor H from DVCS measurements at Jefferson Lab", Phys. Rev. D, 79:094021, 2009

[93] A. Danagoulian *et al.*, (Jefferson Lab Hall A Collaboration), "Compton-Scattering Cross Section on the Proton at High Momentum Transfer", Phys. Rev. Lett., 98:152001, 2007

[94] A. Gardestig, A. P. Szczepaniak and J. T. Londergan, "Separation of soft and hard physics in DVCS", doi:10.1142/9789812776211_0015 hep-ph/0209232

[95] S. Wallon, "Hard exclusive processes: Theoretical status", arXiv:0909.4052 [hep-ph], 2009

[96] E.W. Hughes, "Polarized Deep Inelastic Lepton-Nucleon Scattering: Inclusive Results", Nucl. Phys. B (Proceedings Supplements) 79 (1999)

[97] M. Mazouz, "Technical Report", available online: `https://hallaweb.jlab.org/dvcslog/Pion/131`

[98] M. E. Christy and P. E. Bosted,"Empirical fit to precision inclusive electron-proton cross- sections in the resonance region", Phys. Rev. C, 81:055213, 2010

[99] B. Karki, "Extraction of DIS cross section", Private communication

[100] T. Horn, G Huber *et al.*, "Approved Jefferson Lab experiment E12-07-105", available online:
http://www.jlab.org/exp_prog/proposals/07/PR12-07-105.pdf

[101] C. Muñoz-Camacho *et al.*, "Approved Jefferson Lab experiment E12-13-010", available online:
http://www.jlab.org/exp_prog/proposals/13/PR12-13-010.pdf

[102] DOE/NSF Nuclear Science Advisory Committee, "Reaching for the Horizon - The 2015 Long Range Planfor Nuclear Science", available online:
http://science.energy.gov/ /media/np/nsac/pdf/2015LRP/2015LRPNS_091815.pdf

Appendix A: Preliminary π^0 Electroproduction Cross Section for Kin36_1

In this section we show the results of the minimization procedure to extract the cross section. We have divided the data into five bins in $t_{min} - t$ and a further twelve bins in the angle between the hadronic and lepronic planes ϕ. For each bin in $t_{min} - t$ we show on the left panel the extracted total cross section as a function of ϕ together with a fit to the cross section. On the right panel we show a comparison of the experimental data and the prediction by the simulation.

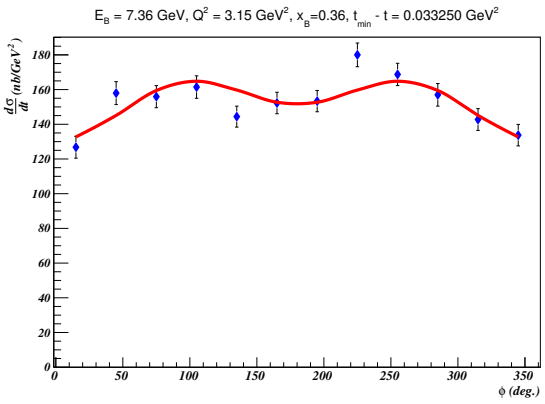

(a) $t_{min} - t = 0.03325$ GeV^2

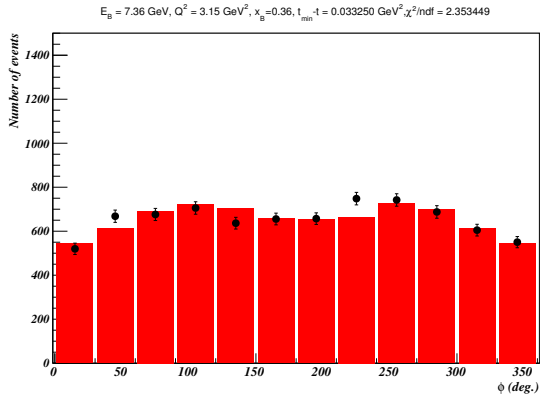

(b) $t_{min} - t = 0.03325$ GeV^2

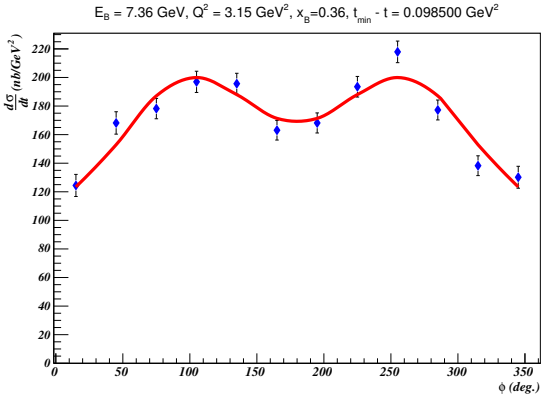

(c) $t_{min} - t = 0.0985$ GeV^2

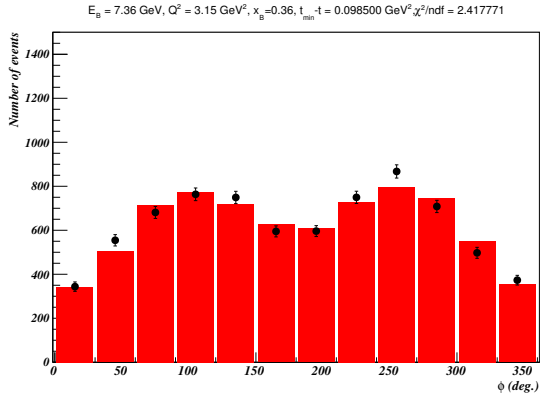

(d) $t_{min} - t = 0.0985$ GeV^2

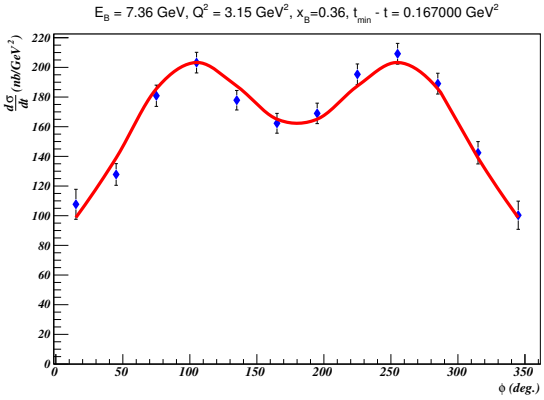

(e) $t_{min} - t = 0.167$ GeV^2

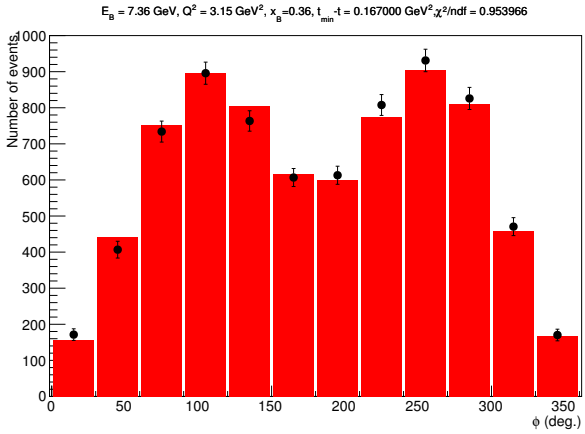

(f) $t_{min} - t = 0.167$ GeV^2

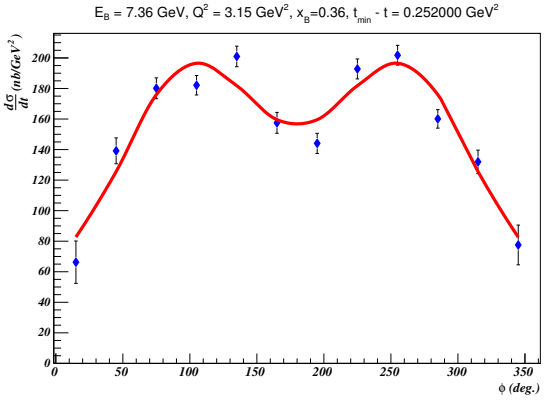

(g) $t_{min} - t = 0.252$ GeV^2

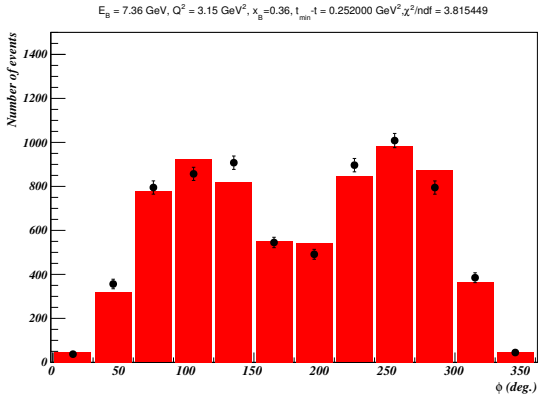

(h) $t_{min} - t = 0.252$ GeV^2

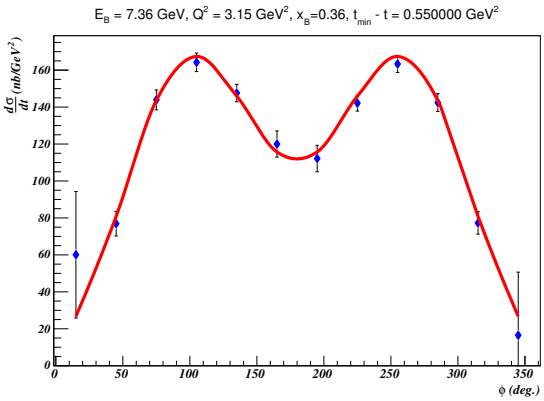

(i) $t_{min} - t = 0.0555$ GeV^2

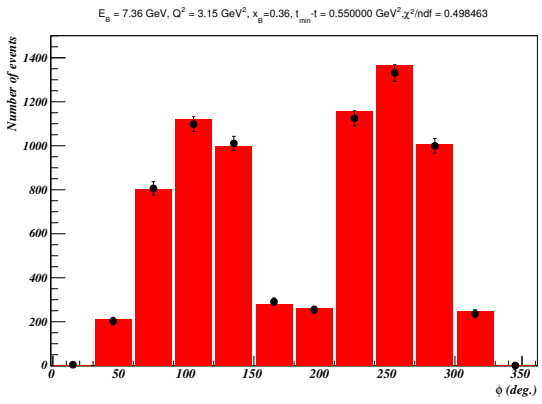

(j) $t_{min} - t = 0.055$ GeV^2

Figure 5.16: The total (unpolarized) cross section in each of the $t_{min} - t$ bins as a function of ϕ. The left panel shows the total cross section and the right panel shows a comparison of the experimental data and the number of events estimated by the simulation in each bin. Errors are statistical only.

Appendix B: Propagation of systematic errors induced by exclusivity cuts

In this section we show the results of the procedure to propagate systematic uncertainties due to the exclusivity cuts. For each extracted cross section term, we varied the exclusivity cuts and determined points at which the cross section started to vary significantly from that extacted with the "optimal" cuts. The different colors (or points) in each plot correspond to the exclusivity cuts demontrated in Fig. 5.11.

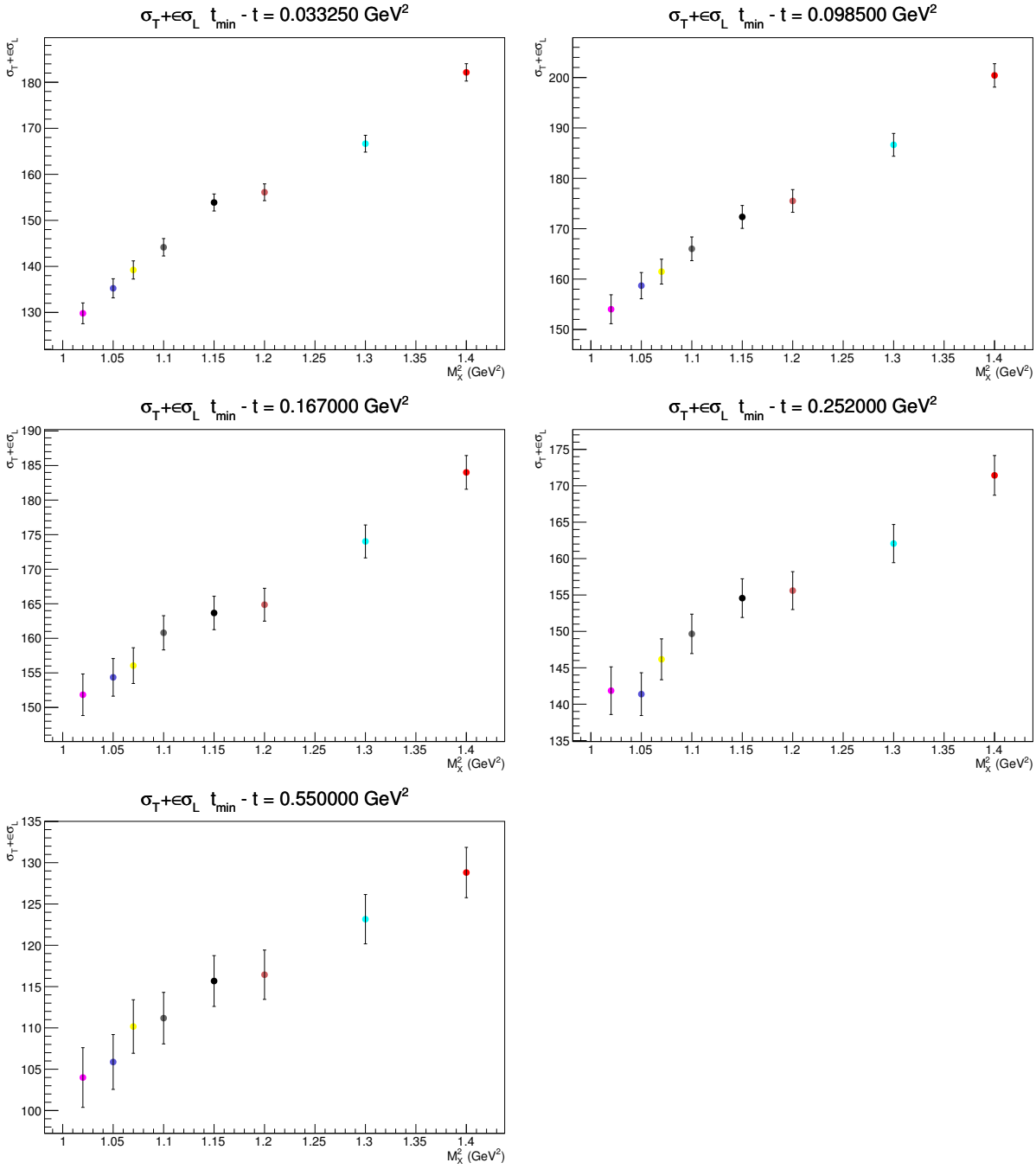

Figure 5.17: Extracted cross section parameter $\sigma_U = \sigma_T + \epsilon\sigma_L$ as a function of bins in t_{min} - t and cut in missing mass.

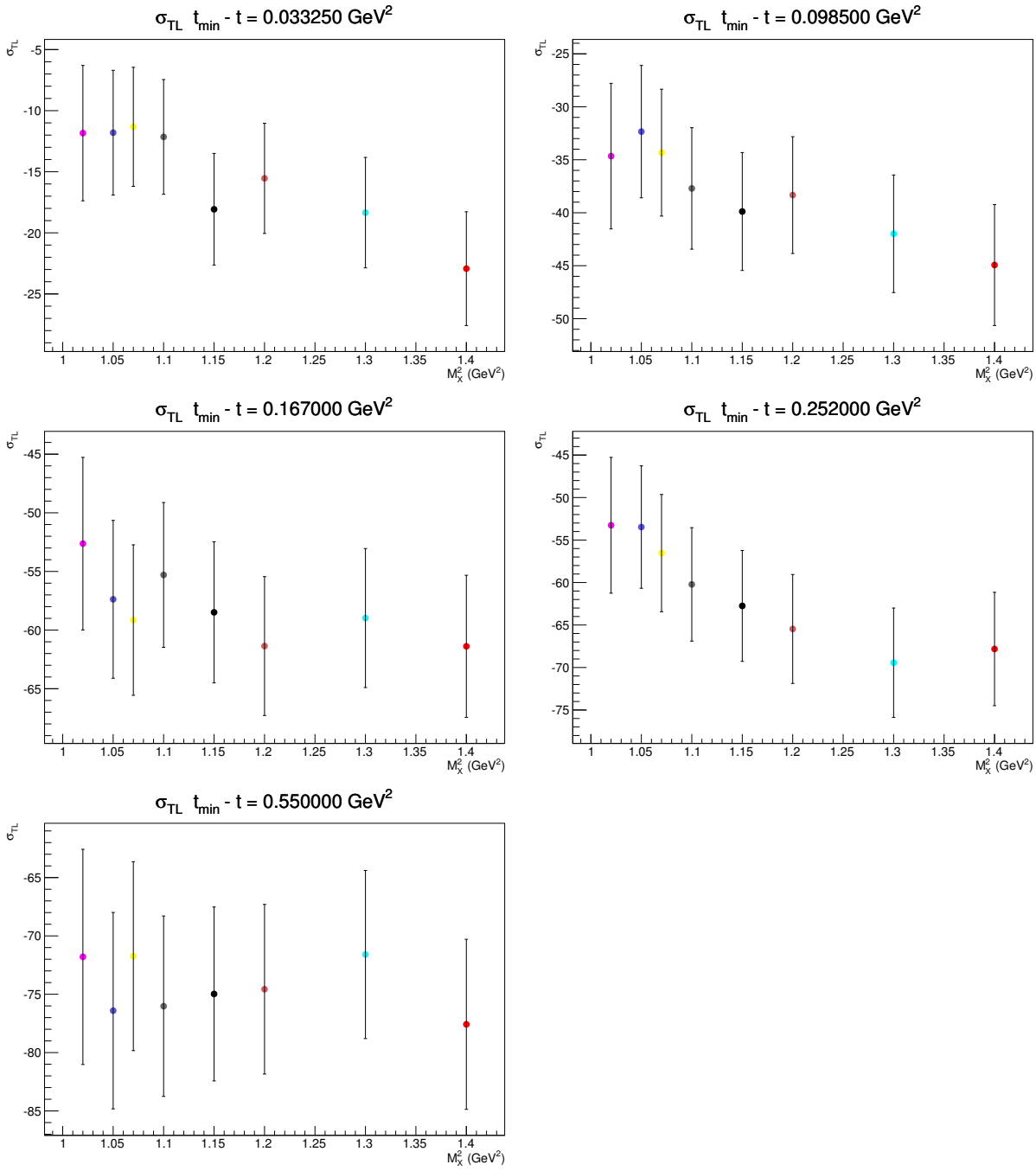

Figure 5.18: Extracted cross section parameter σ_{TL} as a function of bins in t_{min} - t and cut in missing mass.

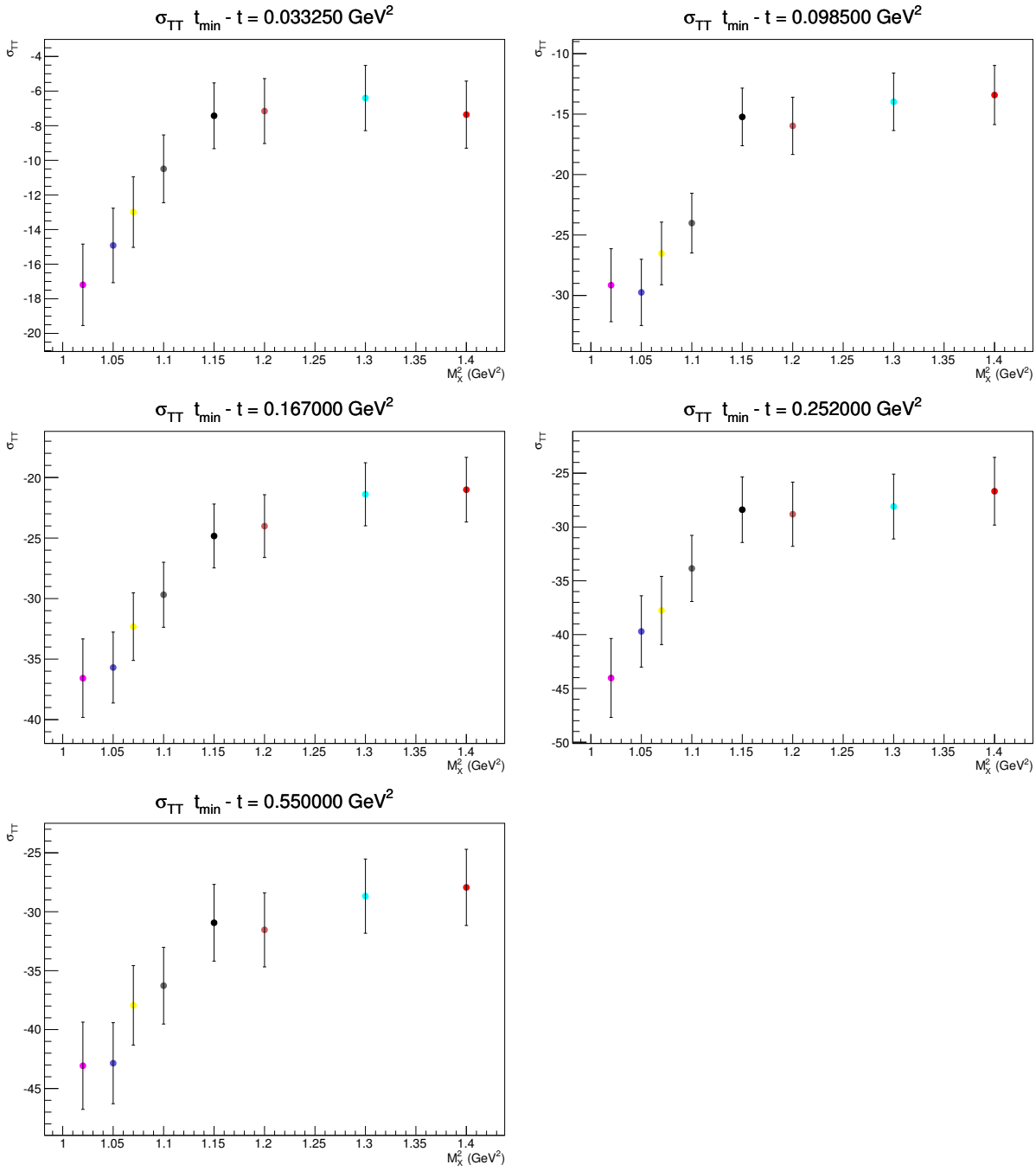

Figure 5.19: Extracted cross section parameter σ_{TT} as a function of bins in t_{min} - t and cut in missing mass.

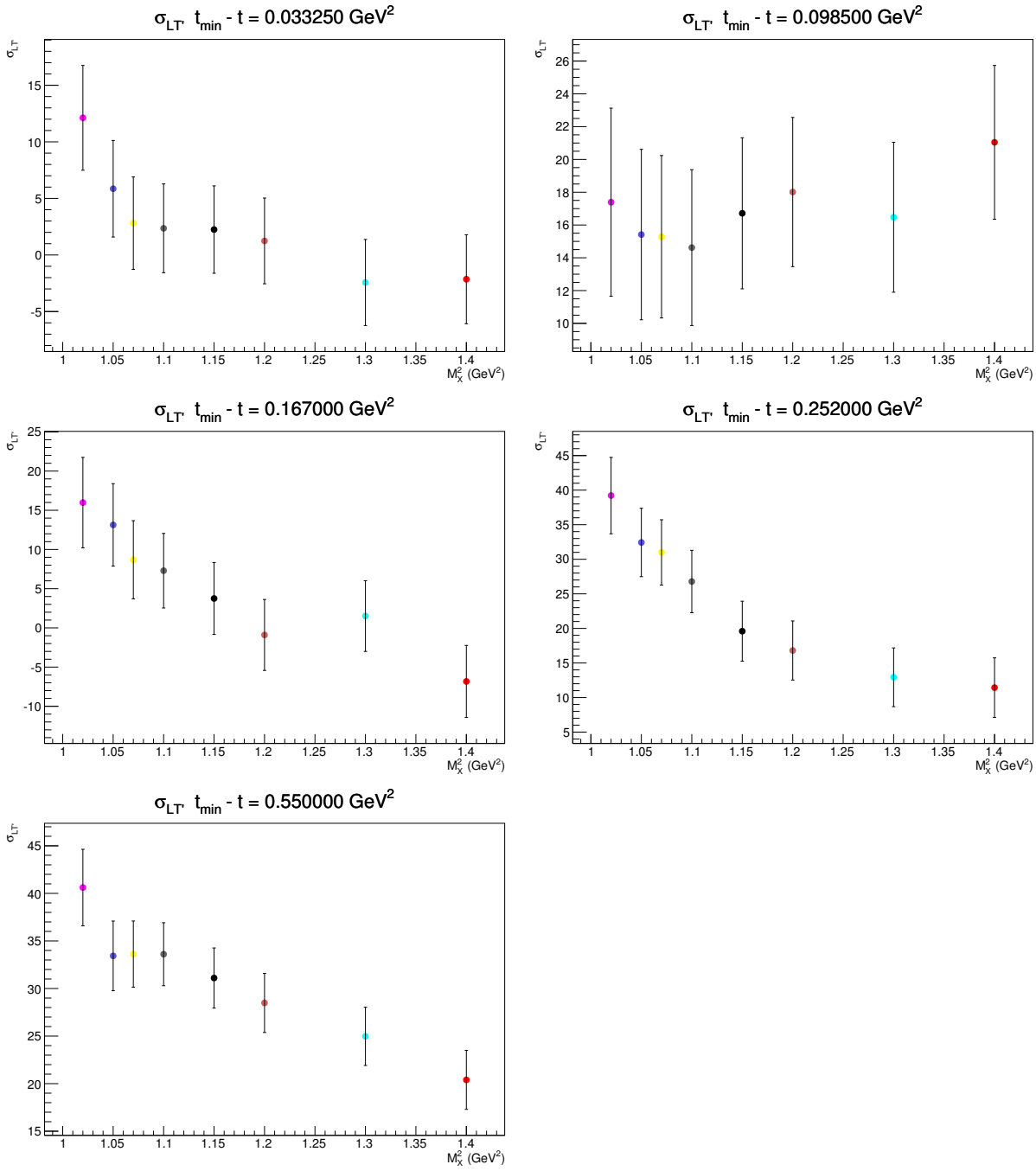

Figure 5.20: Extracted cross section parameter $\sigma_{TL'}$ as a function of bins in t_{min} - t and cut in missing mass.

Appendix C: Reprint Permissions and Licenses

1. Figs. 0.1, 2.6, 1.3, IOP Publishing, Open access, Creative Commons license: CC BY

2. Fig. 1.2, Elsevier, 2007, License date: Aug 02, 2018, License Number: 4400900573673

3. Figs. 1.5, 1.9, 1.10, 1.11, 1.12, 1.13, and 2.2, IOP Publishing, Order Date: 09/14/2018, Order License Id: 4427710281737

4. Figs. 1.6 1.7, 1.8, DO I: 10.1103/PhysRevD.93.114017, License date : 14-Sep-2018, License Number: RNP/18/SEP/007819

5. Figs. 1.22, 1.23, DO I: 10.1103/PhysRevLett.97.262002 , License date : 14-Sep-2018, License Number: RNP/18/SEP/007816

6. Fig. 1.16, DO I: 10.1103/PhysRevC.90.025205, License date : 14-Sep-2018, License Number: RNP/18/SEP/007828

7. Fig. 1.17, DO I: 10.1103/PhysRevLett.117.262001, License date : 14-Sep-2018, License Number: RNP/18/SEP/007820

8. Fig. 1.19, DO I: 10.1103/PhysRevC.77.042201, License date : 14-Sep-2018, License Number: RNP/18/SEP/007821

9. Fig. 1.20, DO I: 10.1103/PhysRevC.90.025205, License date : 14-Sep-2018, License Number: RNP/18/SEP/007827

10. Fig. 2.9, Elsevier, 2004, License date: Sep 14, 2018, License Number: 4427750049675

Thesis and Dissertation Services